Stony Brook University

Core-Shell and Monofaceted Nanocatalysts for Fuel Cells and Water Electrolysis

A Dissertation Presented

by

Yu Zhang

to

The Graduate School

in Partial Fulfillment of the

Requirements

for the Degree of

Doctor of Philosophy

in

Materials Science and Engineering

Stony Brook University

May 2015

Stony Brook University

The Graduate School

Yu Zhang

We, the dissertation committee for the above candidate for the

Doctor of Philosophy degree, hereby recommend

acceptance of this dissertation.

Dr. Radoslav Adzic – Dissertation Advisor
Senior Chemist, Chemistry Department, Brookhaven National Laboratory;
Adjunct Faculty, Materials Science and Engineering Department, Stony Brook University

Dr. Jia Wang – Chairperson of Defense
Chemist, Chemistry Department, Brookhaven National Laboratory;
Adjunct Faculty, Materials Science and Engineering Department, Stony Brook University

Dr. Gary Halada – Third Member of Academic Committee
Professor, Materials Science and Engineering Department, Stony Brook University

Dr. Oleg Gang – Outside Member
Group Leader, Center for Functional Nanomaterials, Brookhaven National Laboratory;
Affiliated Faculty, Chemistry Department, Stony Brook University

This dissertation is accepted by the Graduate School

Charles Taber
Dean of the Graduate School

Abstract of the Dissertation

Core-Shell and Monofaceted Nanocatalysts for Fuel Cells and Water Electrolysis

by

Yu Zhang

Doctor of Philosophy

in

Materials Science and Engineering

Stony Brook University

2015

Fuel cells and water electrolysis, with their economical and environmental benefits, are expected to become major clean energy technologies. Hydrogen fuel cells use hydrogen as the carbon-free fuel to generate electricity with high efficiency, and water electrolysis can produce hydrogen from water using solar or wind power. However, the large-scale commercialization of these technologies has been impeded by the high cost of Pt catalysts necessary for their operation. To overcome this problem, in this study, core-shell architectures and monofaceted nanocrystals have been developed as two main approaches for rational design of electrocatalyst materials with enhanced activity, selectivity and durability.

A series of bimetallic core-shell nanocatalysts having Ru core and Pt, Pd or Au shell (Ru@M, where M = Pt, Pd, Au) was synthesized using ethanol as the solvent and reducing agent. Their activities for the hydrogen evolution and oxidation reactions (HER-HOR) have been investigated in acid solution. It is found that Ru-Pt core-shell (Ru@Pt) nanocatalysts exhibited the highest HER-HOR activity among these bimetallic nanocatalysts. The optimal Pt shell thickness was determined by tuning the Ru to Pt atomic ratio. The key origin of improved

catalytic properties was the formation of an ordered lattice structural transition from Ru*(hcp)* to Pt*(fcc)* at the core-shell interface, which was verified by XRD and STEM, coupled with DFT calculations. *In situ* XAS measurements were performed to investigate the local structures of Ru@Pt nanocatalysts. The well-defined bilayer Ru@Pt nanocatalysts, with optimized structures and improved Pt utilizations, demonstrated superior activity and durability for the HER-HOR, along with enhanced carbon monoxide tolerance of fuel cells H_2 anodes. For the cathodic oxygen reduction reaction (ORR) in fuel cells, Pd-Pt core-shell (Pd@Pt) nanocatalysts with uniform and continuous Pt monolayer shell exhibited enhanced ORR activity in acid electrolyte. Further efforts in promoting the ORR activity were made by synthesizing Pt monolayer catalysts on hollow Pd and Pd-Au core nanoparticles.

Electrochemistry of faceted nanocrystals was started by studies of Au monofaceted nanocrystals, which were used as a platform to uncover the structure-dependent ORR selectivity in alkaline media of single-crystalline Au facets. Nanocrystals' surface cleanness and crystallinity were confirmed by electrochemical characterizations including cyclic voltammetry and by signature voltammetry curves for thallium underpotential deposition. ORR pathways on single-crystalline facets, including {111} on octahedra and {100} on cubes, were similar to their single-crystal counterparts. In stark contrast, a full-range 4e-ORR in alkaline solution was discovered on {310} facets of Au nanocrystal shaped as the truncated ditetragonal prism (TDP). From analysis of experimental results and DFT calculations, the combination of low-coordinated Au surface sites and the dioxygen-water co-adsorption were proposed to result in the observed selectivity of the ORR pathway on Au nanocrystal surfaces.

To God the Father and the Lord Jesus Christ,

To My Husband, Yu-Chi,

and

To My Parents

Table of Contents

List of Figures

List of Tables

Table 3.11 Co-adsorption of oxygen and water on Au {100} and Au {310} surfaces. $EbO2 + nH2O$ is the binding energy of O_2-H_2O co-adsorption (kJ mol^{-1}); $R_{O\text{-}O}$ is the oxygen-oxygen (O-O) bond length (Å) in O_2 molecule; $\Delta R_{O\text{-}O}$ is the $R_{O\text{-}O}$ elongation (%) in O_2; $R_{O1\text{-}H1}$, $R_{O1\text{-}H2}$, $R_{O2\text{-}H1}$ and $R_{O2\text{-}H2}$ are the hydrogen-oxygen (H-O) bond lengths (Å) in H_2O molecule, where *H1* is the H atom in H_2O forming the hydrogen bond with O_2, and *H2* is the H atom in H_2O not forming hydrogen bond with O_2; $\Delta R_{O1\text{-}H1}$ is the R_{O1}-H1 elongation (%) in co-adsorbed H_2O molecule; $R_{O\text{-}O}^{inter}$ is the inter-distance (Å) between O_2 and H_2O molecules. The DFT-calculated gas-phase value, 1.240 Å of O-O bond length in O_2 and 0.972 Å of H-O bond in H_2O, are used as the reference value to calculate elongation percentages. Abbreviations: D for diagonal, B for bridge, H for hollow, 1W for one H_2O molecule, 2W for two H_2O molecules. Here the colored configurations exhibit the highest binding energy compared to those with similar geometries, and are therefore considered as stable configurations and representatively displayed in Figure 3.44b. 155

List of Abbreviations

2D	Two-dimensional
2e	Two electron
3D	Three-dimensional
4e	Four electron
AA	Ascorbic acid
AEM	Anion exchange membrane
AFC	Alkaline fuel cell
ALD	Atomic layer deposition
BE	Binding energy
CA	Citric acid
CFR	Charge transfer resistance
CHP	Combined heat and power
CNT	Carbon nanotube
CPC	Cetylpyridinium chloride
CTAB	Cetyl-trimethylammonium bromide
CTAC	Cetyl-trimethylammonium chloride
CV	Cyclic voltammetry
DFT	Density functional theory
ECSA	Electrochemical active surface area
EDX	Energy dispersive X-ray spectroscopy
EELS	Electron energy loss spectroscopy
EG	Ethylene glycol
EIS	Electrochemical impedance spectroscopy
EXAFS	Extended X-ray absorption fine structure
FC	Fuel cell
fcc	Face-centered cubic
GDE	Gas diffusion electrode
GGA	Generalized gradient approximation

HAADF	High angle annular dark-field
hcp	Hexagonal close-packed
HER	Hydrogen evolution reaction
HFR	High frequency resistance
HOR	Hydrogen oxidation reaction
ICP-MS	Inductively coupled plasma mass spectrometry
IRA	Irreversible adsorption
M/C	Carbon-supported metal nanoparticles
MA	Mass activity
MEA	Membrane electrode assembly
ML	Monolayer
N@M	N-core M-shell
NNMC	Non-noble metal catalyst
NP	Nanoparticle
ORR	Oxygen reduction reaction
PAW	Projected augmented wave
PDF	Powder diffraction file
PEM	Proton exchange membrane
PEMFC	Proton exchange membrane fuel cell
PR	Polarization resistance
PROX	Preferential oxidation
PVP	Poly(vinyl pyrrolidone)
PW	Perdew-Wang
PZC	Potential at the point of zero charge
RDE	Rotating disk electrode
RHE	Reversible hydrogen electrode
rpm	Revolutions per minute
RRDE	Rotating ring disk electrode
SA	Specific activity
SAED	Selected-area electron diffraction

SEM	Scanning electron microscopy
SHE	Standard hydrogen electrode
SLRR	Surface limited redox reaction
STEM	Scanning transmission electron microscopy
TDP	Truncated ditetragonal prism
TEM	Transmission electron microscopy
TTAB	Tetradecyltrimethylammonium bromide
UPD	Underpotential deposition
VASP	Vienna ab-initio simulation package
WE	Water electrolysis
XANES	X-ray absorption near edge spectroscopy
XAS	X-ray absorption spectroscopy
XRD	X-ray diffraction

Acknowledgments

First and foremost, I praise the Lord and Savior Jesus Christ, for providing me this opportunity and granting me the capability to complete the work successfully, especially for giving me the opportunity to study gold, the precious and noble metal signifying the divine nature of God. Thank God for giving me wisdom, guidance and strength. In addition, I must also thank the Lord for the multiple blessings bestowed on me over the past few years.

I would like to thank my advisor Dr. Radoslav R. Adzic, for his expert guidance, support and tutelage throughout my Ph.D. program. His scientific intuition and expertise have been an immense inspiration to me. I would also like to thank my committee chair Dr. Jia X. Wang, for her patience and constant encouragement, and for her infectious enthusiasm and creativity. I am greatly honored to have the chance to learn from both of them. They introduced me into the field of electrochemistry and electrocatalysis, directed and supervised my research, and demonstrated dedication and diligent work ethic of scientists.

I would also like to express my deep gratitude and thanks to Dr. Gary Halada, and Dr. Oleg Gang, for taking the time to serve on committee. Their insightful comments and discussions suggestions have been invaluable to me in many areas.

I would also like to thank my colleagues, Dr. Kotaro Sasaki, Dr. Miomir Vukmirovic, Dr. Fang Lu, Dr. Hugh Isaacs, Dr. Meng Li, Dr. Kurian Kuttiyiel, Dr. Yun Cai, Dr. Wei-Fu Chen, Chiu-Hui Wang, Dr. Christopher Koenigsmann, Dr. Wei-Ping Zhou, Dr. Alex Harris, Dr. Kuanping Gong, Dr. David Buceta, Dr. YongMan Choi, Dr. Stoyan Bliznakov, Dr. Lele Duan, Zhixiu Liang, Dr. Liang Yu, Maria Roca-Ayats, Dr. Shijun Liao, Dr. Xiao-Qing Yang, Enyuan Hu, Haiqing Liu, Dr. Lijun Yang, Dr. Yan Li, Dr. Hua-Gen Yu, Dr. Javier Concepcion, Dr. Jue Hu, Dr. Fanke Meng, Katherine Elbert, Dr. Gu-Gon Park, Yan Xie, Zhong Ma, for offering invaluable assistance during my research.

I would like to express my sincere gratitude to my collaborators, Dr. Dong Su, Dr. Deyu Lu, Dr. Vyacheslav Volkov, Dr. Lijun Wu, Dr. Chao Ma, Dr. Yimei Zhu, Dr. Rui Si, Dr. Nebojsa S. Marinkovic, Dr. Wei An, Dr. Ping Liu, Dr. Yugang Zhang, Dr. Ping He, Dr. Siyu Ye, Dr. Katherine E. Ayers, Dr. Christopher B. Capuano, Morgan George, Dr. Julie Renner, Dr. Mingzhao Liu, Dr. Wenqian Xu, Dr. Sanjaya Senanayake, Dr. Dmitry Polyansky for their scientific expertise and technical support.

I gratefully acknowledge the faculty and staff from Stony Brook University, Dr. Dilip Gersappe, Dr. Artem R. Oganov, Dr. Jim Quinn, Dr. Charles Fortmann, Dr. Michael Dudley, Dr. Balaji Raghothamachar, Dr. T. A. Venkatesh, Dr. Andreas Mayr, Dr. Albert Tobin, Chandrani Roy, Lynn Allopenna, H. Deborah Michienzi, Shauntae Smith, Dr. Sanjay Sampath, Dr. Peter Khalifah, Dr. Carolyn Sofia, Prof. Lynne Barsky, Prof. Bonita Tobachnick, for their tutelage, support and assistance.

I am extremely grateful to all of my friends for their continuous encouragement and support. Special thanks to Dr. Bingfei Cao for her scientific insights, technical assistance, knowledge of crystallography and non-noble metal catalysts, and all the sharing and companion during these years, to Dr. Min Zhang, Erya Huang, Dr. Xiaonan Duan and Shangmin Xiong for their encouragement.

I would like to express profound appreciation to my beloved husband, Dr. Yu-Chi Hsieh, for his patience, understanding, constant support and encouragement. I am also grateful for the joyful scientific discussion and inspirational sharing with him.

I would like to thank my immensely supportive parents, for their continuous love and support throughout my Ph. D. career.

Finally, I would like to thank Materials Science and Engineering Department, Stony Brook University for the full scholarship. I appreciate the research sponsorship from US Department of Energy: Basic Energy Science, and Energy Efficiency and Renewable Energy.

Publications

Peer-Reviewed Journal Papers

1. Jia X. Wang, Chao Ma, YongMan Choi, Dong Su, Yimei Zhu, Ping Liu, Rui Si, Miomir B. Vukmirovic, Yu Zhang, Radoslav R. Adzic. *Journal of the American Chemical Society* 133, 13551-13557 (2011).
2. Fang Lu, Yu Zhang, Lihua Zhang, Yugang Zhang, Jia X. Wang, Radoslav R. Adzic, Eric A. Stach, Oleg Gang. *Journal of the American Chemical Society* 133, 18074-18077 (2011).
3. Yu Zhang, Chao Ma, Yimei Zhu, Rui Si, Yun Cai, Jia X. Wang, Radoslav R. Adzic. *Catalysis Today* 202, 50-54 (2013).
4. Yu-Chi Hsieh, Yu Zhang, Dong Su, Vyacheslav Volkov, Rui Si, Lijun Wu, Yimei Zhu, Wei An, Ping Liu, Ping He, Siyu Ye, Radoslav R. Adzic, Jia X. Wang. *Nature Communications* 4, 2466 (2013).
5. Miomir B. Vukmirovic, Yu Zhang, Jia X. Wang, David Buceta, Lijun Wu, Radoslav R. Adzic. *Journal of the Serbian Chemical Society* 78, 1983-1992 (2013).
6. Yu Zhang, Yu-Chi Hsieh, Vyacheslav Volkov, Dong Su, Wei An, Rui Si, Yimei Zhu, Ping Liu, Jia X. Wang, Radoslav R. Adzic. *ACS Catalysis* 4, 738-742 (2014).
7. Fang Lu[†], Yu Zhang[†], Deyu Lu, Dong Su, Mingzhao Liu, Yugang Zhang, Jia X. Wang, Radoslav R. Adzic, Oleg Gang. *Submitted*. ([†]Contributed equally)
8. Jia X. Wang, Yu Zhang, Christopher B. Capuano, Katherine E. Ayers. *Submitted*.
9. Yu-Chi Hsieh, Sanjaya D. Senanayake, Yu Zhang, Wenqian Xu, and Dmitry E. Polyansky. *Submitted*.
10. Yu Zhang, Yu-Chi Hsieh, Kotaro Sasaki, Nebojsa S. Marinkovic, Vyacheslav Volkov, Yimei Zhu, Jia X. Wang, Radoslav R. Adzic. *In Preparation*.

Conference Proceeding

1. Jia X. Wang, Ping He, Yu Zhang, Siyu Ye. *ECS Transactions* 64, 121-127 (2014).

Patent

1. Fang Lu, Oleg Gang, Yugang Zhang, Yu Zhang, Jia X. Wang. US Patent 2014/0106258, Apr. 17, 2014.

Chapter 1 INTRODUCTION

1.1 Fundamentals of Direct Energy Conversion in Fuel Cells and Water Electrolysis

Fossil fuels, such as petroleum, are the standard source of energy for transportation systems nowadays. However, these resources are non-renewable and their burning has severe environmental and climatic impacts.[1, 2] It is critical and important to reduce the use of fossil fuels and to develop alternative clean and sustainable energy sources. Thus, hydrogen has been considered as an alternative energy carrier in hydrogen economy scenario[3], because it is the source of clean energy with versatile applications. There are three main issues regarding the hydrogen economy − hydrogen production, storage and utilization[4]. Water electrolysis, using electricity to split water into hydrogen and oxygen, can produce hydrogen onsite with zero carbon footprint when integrated with a renewable energy technology[4, 5], such as solar or wind. Fuel cell can generate electricity by directly and efficiently converting the chemical energy of hydrogen to electricity. Water and potentially useful heat are the only byproducts. Powering the automotive vehicles by fuel cells could be pollution-free, which could provide great environmental benefits[6-8]. Fuel cells also have higher efficiencies compared to gasoline internal combustion engines[9]. Overall, a transportation system powered by hydrogen and fuel cells would bring significant economic and environmental benefits.

1.1.1 Fuel Cell (FC) Basics

A fuel cell is an electrochemical energy-conversion device that converts directly chemical into electrical energy. There are many types of fuel cells, but basic components and working principles are similar for all. A single fuel cell consists of two electrodes, an anode and a cathode in contact with an electrolyte between them. The electrolyte separates electronically the anode from the cathode, but provides ionic conduction. The circuit is closed externally by electronic conductors.

The fuel cell generates electrical current continuously provided a continuous supply of fuels and an oxidant is maintained. At the anode, the fuel, such as hydrogen, natural gas or methanol, is oxidized and produces electrons. While at the cathode, the oxidant, such as oxygen or oxygen from air, is reduced. The electrons produced at the anode are transferred to the cathode via the external circuit. The ions generated in reactions are ionic charge carriers that diffuse through the electrolyte from one electrode to the other to complete the redox reactions. Electrical energy is generated by the conversion of chemical energy of the fuel, via the redox reactions taking place at the electrode-electrolyte interface.

1.1.1.1 Classification of Fuel Cells

Based on the electrolyte used[10], fuel cells can be categorized into several types[9, 11] as shown in Table 1.1.

Table 1.1 Classification of fuel cells.

Fuel cell type	Electrolyte	Charge carrier	Operating temperature (℃)	Fuel	Applications
Alkaline fuel cell (AFC)	AEM[a]	OH^-	65 ~ 220	H_2	Military, space shuttle
Direct methanol fuel cell (DMFC)	PEM[b]	H^+	50 ~ 120	CH_3OH	Consumer electronic devices
Molten carbonate fuel cell (MCFC)	Mixture of molten alkali carbonate	CO_3^{2-}	~ 650	H_2, CO, CH_4, other hydrocarbons	Stationary power generation
Phosphoric acid fuel cell (PAFC)	H_3PO_4	H^+	150 ~ 220	H_2	Stationary power generation
Proton exchange membrane fuel cell (PEMFC)	PEM[b]	H^+	60 ~ 90	H_2	Automotive, CHP[c] systems
Solid oxide fuel cell (SOFC)	Yttria-stabilized zirconia	O^{2-}	600 ~ 1000	Gasoline	Stationary power generation

[a]AEM: Anion exchange membrane;

[b]PEM: Proton exchange membrane;

[c]CHP: Combined heat and power.

1.1.1.2 Proton Exchange Membrane Fuel Cell (PEMFC)

The proton exchange membrane (PEM) fuel cell, also called the polymer electrolyte

membrane fuel cell, has been extensively studied due to its simple structure, low operation temperature (~80 °C), high power density, and also because of their potential applications in automobiles and combined heat and power (CHP) systems. PEMFC uses PEM as the electrolyte, which only allows proton to pass through. A PEMFC stack consists of several elementary cells, which is known as the membrane electrode assembly (MEA). As shown in Figure 1.1, one MEA is composed of the PEM electrolyte sandwiched between the anode and the cathode. The use of a solid membrane electrolyte makes it possible to produce compact fuel cell, and it also facilitates simple management of heat and water produced.

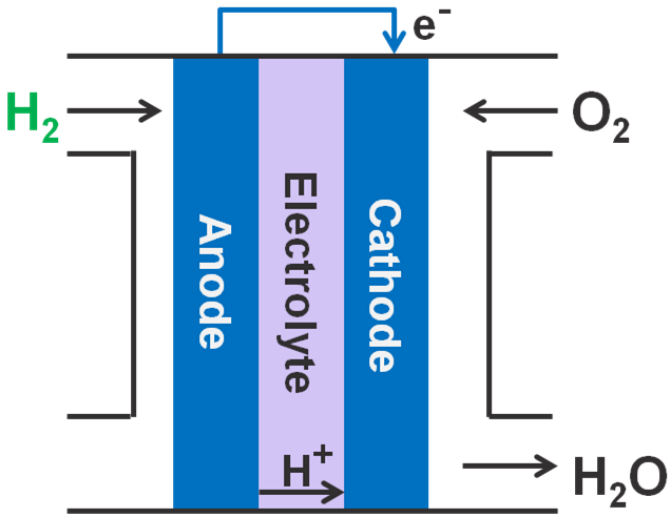

Figure 1.1 Basic scheme of a PEM fuel cell.

The PEM allows fast proton transfer, is insulating to electrons, and also acts as the gas barrier between cathode and anode. The most used and studied PEM in PEMFCs is Nafion membrane by DuPont. Nafion membrane consist of polytetrafluoroethylene (PTFE) backbone and sulfonic acid side chains ($–SO_3H$), as depicted in Figure 1.2. The hydrophobicity of PTFE

backbone helps to remove the product water out from the electrode, and to prevent the flooding issues. In contrast, the $–SO_3H$ group is ionically bonded, and therefore a SO_3^- ion is actually at the end of the side chain. The SO_3^- ion is highly hydrophilic, and can attach the protons for proton transfer.

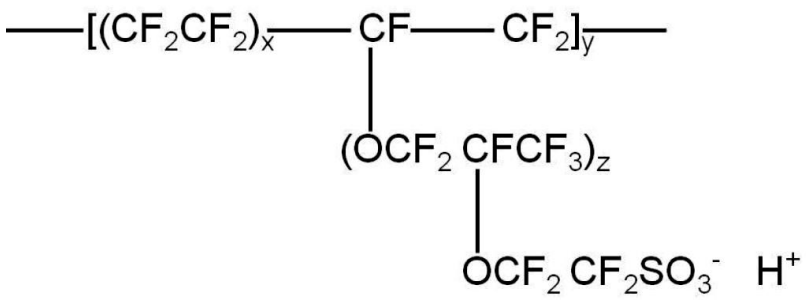

Figure 1.2 Structure of Nafion membrane by DuPont.

1.1.1.3 Alkaline Fuel Cell (AFC)

The AFC, as one of the oldest fuel cell types, was the first practical fuel cell operated by NASA in space mission. A renaissance of interest in AFCs has aroused because the expected lower total cost compared with PEMFCs[12, 13]. One major advantage of AFCs, compared to PEMFCs, is that the reaction rate of the ORR is higher in alkaline electrolyte than that in acid electrolyte[14]. The anion exchange membrane (AEM) has been developed as the electrolyte for AFC. The AEM only transfers OH^- anions produced at the cathode to the anode. Hydrogen and other organic fuels like methanol or ethanol can be used as the fuel at the anode side[15]. However, carbonates formation remain problematic for AFCs if air is used as the oxidant feed and fuel oxidation produces CO_2. The AEM with satisfactory anion conductivity along with chemical stability is vital in developing AFCs[16].

1.1.1.4 Performance of Fuel Cells

Figure 1.3 shows the typical polarization curve of a H_2/O_2 PEM fuel cell. The polarization curve is influenced by three factors: (i) kinetic loss, or activation loss; (ii) ohmic loss; (iii) concentration loss. Kinetic loss often is demonstrated as the rapid initial voltage drop at low overpotential. It is caused by the sluggish reaction kinetics on anode or cathode, reflecting the catalytic activity of electrode surfaces (the electrocatalysts). In a PEM fuel cell, the kinetic loss, especially the kinetic loss at the cathode, usually accounts for the major energy loss. Ohmic loss usually results from the resistance in the electrical circuit, including the resistance of electrode materials and electrolyte. Ohmic loss is typically depicted as the linear voltage drop with increasing current density. Concentration loss is usually associated with the decrease of the reactants' concentration on electrocatalysts surface at high overpotentials. At low currents, kinetic loss is dominant. At intermediate currents, ohmic loss is the major contributor to the performance loss. And at high currents, concentration loss due to limited mass transport of either reactants or products becomes crucial.

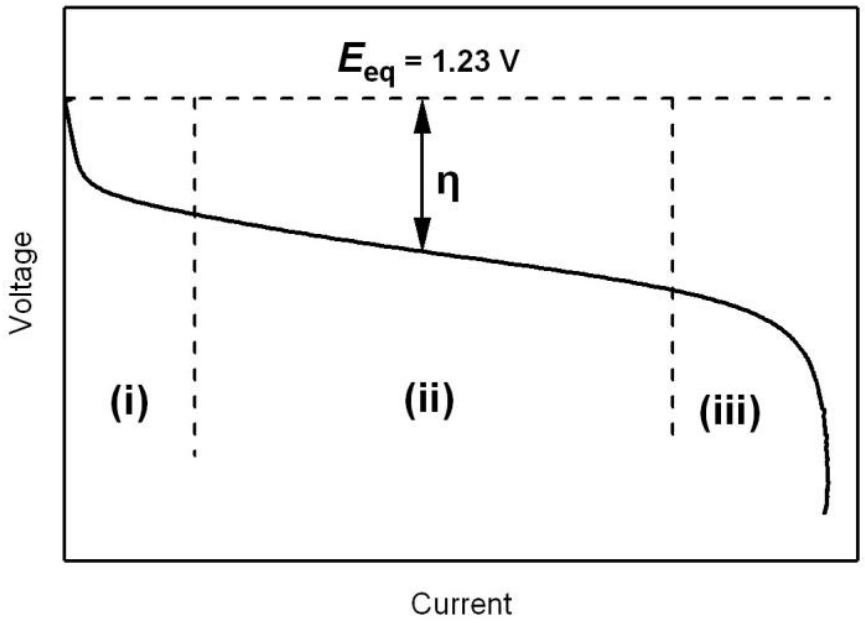

Figure 1.3 Typical polarization curve of a PEM fuel cell, showing the three influencing factors: (i) kinetic loss; (ii) ohmic loss; (iii) concentration loss.

1.1.2 Water Electrolysis (WE) Basics

As mentioned in the beginning of Section 1.1, hydrogen is considered as an ideal energy carrier for the future because it burns cleanly and it is renewable[4, 17]. On our planet, hydrogen is abundant. It exists bound in water and organic compounds[2]. Methods for hydrogen production include steam reforming, water electrolysis, photolysis, biological fermentation and others[2, 18]. Steam reforming from natural gas is currently the dominant method to produce hydrogen[19], which consumes the non-renewable energy resource, fossil fuels. Alternatively, electrolysis is a relatively efficient (>70%) and clean route[4, 20] to produce hydrogen from water, which is abundant on the earth[21]. The electrical current passing through the electrolyte splits water molecules into hydrogen and oxygen molecules[20]. About 4~5 % of the hydrogen worldwide is supplied by water electrolysis[19]. Furthermore, zero carbon footprint will be brought if the water

electrolyzers are integrated with and powered by a renewable energy technology[4, 5], such as solar or wind. Hydrogen generated in this manner can be stored, and used in fuel cells later to provide electricity on demand. One advantage of water electrolysis is that hydrogen can be produced and utilized onsite, without the need for transportation.

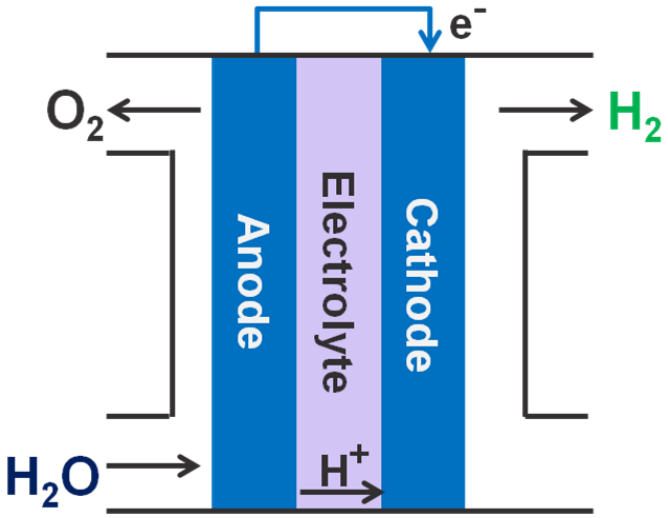

Figure 1.4 Basic scheme of a PEM water electrolyzer.

Two types of water electrolyzers are commercially available, which are anion exchange membrane (AEM) water electrolyzer and proton exchange membrane (PEM) water electrolyzer. Alkaline electrolysis technology is commercially mature for hydrogen production. However, the efficiency of alkaline water electrolysis is reduced, because of the incomplete prevention by the AEM of the cross diffusion of the gas products, and also because of the high ohmic loss across the AEM[19]. As a result, PEM water electrolysis has been developed to overcome these drawbacks of AEM water electrolysis. Figure 1.4 shows the basic scheme of a PEM water electrolyzer, which is composed of an electrolyte sandwiched between two electrodes, an anode

and a cathode. The commonly used electrolyte in PEM water electrolyzers is the polymer electrolyte membrane, such like Nafion.

The advantages of PEM water electrolysis include operation at high current density, good efficiency, and high output gas purity, as a result of some advantageous properties of the Nafion membrane including high proton conductivity and low gas crossover.[19] High cost of the components, and possibly low durability in corrosive acidic environment are some major problems, which prevent the wide commercialization of PEM electrolysis. The electrocatalysts with high efficiency and good long-term durability are therefore required, in order to develop the technology of PEM water electrolysis and to contribute to hydrogen based economy in future.

1.2 Electrocatalysis of FC and WE Reactions

1.2.1 Electrocatalysis of PEMFC and AFC

In PEMFCs, at the anode, the hydrogen oxidation reaction (HOR) occurs, where the fuel (H_2) is oxidized generating protons and electrons. The electrons and protons are transmitted to the cathode through the external circuit and the electrolyte, respectively. At the cathode, the oxygen reduction reaction (ORR) happens, wherein the oxidant (O_2) is reduced by the electrons and meets protons to form water. The reactions are similar in AFCs.

In acid electrolyte or PEMFCs, the overall reactions are:

Anodic HOR:

$$H_2 \rightarrow 2H^+ + 2e^- \tag{1.1}$$

Cathodic ORR:

$$O_2 + 4H^+ + 4e^- \rightarrow 2H_2O \tag{1.2}$$

Overall cell reaction:

$$2H_2 + O_2 \rightarrow 2H_2O \tag{1.3}$$

In alkaline electrolyte or AFCs, the overall reactions are:

Anodic HOR:

$$H_2 + 2\mathrm{OH}^- \rightarrow 2H_2O + 2e^- \tag{1.4}$$

Cathodic ORR:

$$O_2 + 2H_2O + 4e^- \rightarrow 4\mathrm{OH}^- \tag{1.5}$$

Overall cell reaction:

$$2H_2 + O_2 \rightarrow 2H_2O \tag{1.6}$$

Though water is always the final product, which is environmentally benign, for both the

PEMFC and AFC, water forms at the cathode in PEMFCs and at the anode in AFCs.

1.2.2 Electrocatalysis of PEM and AEM Water Electrolysis

The reaction mechanisms in water electrolysis can be seen as a reversed operation in hydrogen fuel cell[2]. At the cathode, the hydrogen evolution reaction (HER) occurs, wherein hydrogen is produced. At the anode, the oxygen evolution reaction (OER) occurs, wherein oxygen is generated.

In acid electrolyte or PEM water electrolyzers, the overall reactions are:

Cathodic HER:

$$2H^+ + 2e^- \rightarrow H_2 \tag{1.7}$$

Anodic OER:

$$2H_2O \rightarrow O_2 + 4H^+ + 4e^- \tag{1.8}$$

Overall cell reaction:

$$2H_2O \rightarrow 2H_2 + O_2 \tag{1.9}$$

In alkaline electrolyte or AEM water electrolyzers, the overall reactions are:

Cathodic HER:

$$2H_2O + 2e^- \rightarrow H_2 + 2\mathrm{OH}^- \tag{1.10}$$

Anodic OER:

$$4\mathrm{OH}^- \rightarrow O_2 + 2H_2O + 4e^- \tag{1.11}$$

Overall cell reaction:

$$2H_2O \rightarrow 2H_2 + O_2 \tag{1.12}$$

1.3 Hydrogen Evolution and Hydrogen Oxidation Reactions (HER-HOR)

1.3.1 HER-HOR Mechanisms

The mechanisms and kinetics of the hydrogen evolution reaction (HER) and hydrogen oxidation reaction (HOR) have been extensively studied[22-29]. There are three elementary steps for the HER-HOR on Pt catalysts[30, 31].

In acid electrolyte[30], the three elementary steps are:

Volmer reaction or discharge:

$$H^+ + e^- \leftrightarrow H_{ad} \tag{1.13}$$

Tafel reaction or recombination:

$$2H_{ad} \leftrightarrow H_2 \tag{1.14}$$

Heyrovsky reaction or reductive desorption:

$$H_{ad} + H^+ + e^- \leftrightarrow H_2 \tag{1.15}$$

In alkaline electrolyte[31], the three elementary steps are:

Volmer reaction or reductive adsorption:

$$\mathrm{H_2O} + e^- \leftrightarrow H_{ad} + \mathrm{OH^-} \tag{1.16}$$

Tafel reaction or recombination:

$$2H_{ad} \leftrightarrow H_2 \tag{1.17}$$

Heyrovsky reaction or reductive desorption:

$$H_{ad} + \mathrm{H_2O} + e^- \leftrightarrow H_2 + \mathrm{OH^-} \tag{1.18}$$

The kinetic of the HER-HOR can be described via two two-step pathways, either via the Volmer-Tafel or the Volmer-Heyrovsky pathway. The slower reaction determines the kinetics of HER-HOR and the property of polarization curves. From analyses of these polarization curves,

the molecular-level reaction mechanisms can be determined for various metals. HER-HOR are highly reversible with low activation barrier on Pt catalysts in acid solution, though the dependence of current on potential is asymmetric[32].

1.3.2 HER-HOR Electrocatalysts

Platinum black[33-35] and carbon-supported platinum nanoparticles (Pt/C)[26] have been used as HER-HOR catalysts. Several efforts have been done to reduce the Pt loading in HOR catalysts. Pt submonolayer catalysts on carbon-supported metallic Ru nanoparticles (Ru/C)[36, 37] have been synthesized using a spontaneous deposition technique[38, 39] and exhibited high activities for the HOR. The as-prepared 2D Pt islands or small 3D Pt clusters on Ru nanoparticles had an ultrahigh dispersion of Pt and therefore the more complete utilization of Pt atoms[40]. According to density functional theory (DFT) calculations, PtRu alloy is one of the alloys with optimum value of the free energy of hydrogen adsorption[41]. Also, nickel alloys[42], carbon nanotubes[43, 44], carbon electrodes modified with metalophthalocyanines[45], transition metal sulfides[46-48], transition metal nitrides[49, 50], transition metal carbides[51], Pt monolayer supported on transition metal carbides[52-54] have also been used as electrocatalysts for the HER.

1.4 Oxygen Reduction Reaction (ORR)

1.4.1 ORR Mechanisms

The reaction mechanisms for the ORR in acid and alkaline electrolytes are different, as listed in Table 1.2. Oxygen reduction is a multi-electron reaction, and usually includes several elementary steps. Depending on the mode of adsorption of O_2 on metal surfaces, different mechanistic steps will occur. The ORR can take place through four pathways[55, 56]: (i) a direct four-electron (4e) pathway, (ii) a two-electron (2e) pathway, (iii) a series 4e pathway, and (iv) an interactive pathway. In the direct 4e pathway, O_2 is directly and completely reduced to the final 4e-reduction product of H_2O (in acid electrolyte) or OH^- (in alkaline electrolyte). The 2e pathway generates H_2O_2 (in acid electrolyte) or HO_2^-. In the series 4e pathway, in exchange of 2e, O_2 is first reduced to the H_2O_2 (in acid electrolyte) or HO_2^- (in alkaline electrolyte) reaction intermediate, and then subsequently it is reduced to the final 4e-reduction product H_2O (in acid electrolyte) or OH^- (in alkaline electrolyte). In the interactive pathway, the diffusion of reaction intermediates from the series 4e pathway to the direct 4e pathway is operable. Both the direct and series 4e pathways are considered as the 4e pathway.

In acid electrolyte,

The direct 4e pathway:

$$O_2 + 4H^+ + 4e^- \rightarrow 2H_2O \tag{1.19}$$

The 2e pathway:

$$O_2 + 2H^+ + 2e^- \rightarrow H_2O_2 \tag{1.20}$$

The series 4e pathway:

$$O_2 + 2H^+ + 2e^- \rightarrow H_2O_2 \tag{1.21}$$

$$H_2O_2 + 2H^+ + 2e^- \rightarrow 2H_2O \quad (1.22)$$

Table 1.2 Reactant and products of the ORR in acid and alkaline electrolytes.

	Acid	Alkaline
Reactant	Oxygen (O_2)	Oxygen (O_2)
Proton donor	Proton (H^+) or hydronium ion (H_3O^+)	Water (H_2O)
2e reduction product	Hydrogen peroxide (H_2O_2)	Hydroperoxide ion (HO_2^-)
4e reduction product	Water (H_2O)	Hydroxide (OH^-)

In alkaline electrolyte,

The direct 4e pathway:

$$O_2 + 2H_2O + 4e^- \rightarrow 4OH^- \quad (1.23)$$

The 2e pathway:

$$O_2 + H_2O + 2e^- \rightarrow HO_2^- + OH^- \quad (1.24)$$

The series 4e pathway:

$$O_2 + H_2O + 2e^- \rightarrow HO_2^- + OH^- \quad (1.25)$$

$$HO_2^- + H_2O + 2e^- \rightarrow 3OH^- \quad (1.26)$$

Regarding the mechanism for ORR, there are three plausible models for oxygen adsorbed on metal surfaces[57], as depicted in Figure 1.5.

(i) Side-on interaction of O_2 with the metal (Griffith model);

(ii) End-on adsorption of O_2 through a single bond with the metal (Pauling model);

(iii) The bridge model with two bonds with two metal sites (Yeager model).

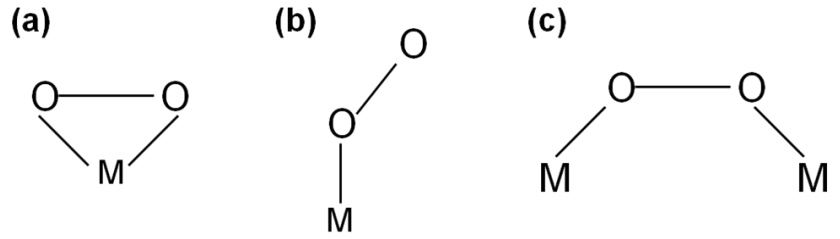

Figure 1.5 Possible configurations of O_2 interaction with a metal.

1.4.2 ORR Electrocatalysts in PEMFCs

The sluggish kinetics of the cathodic ORR and the high cost of Pt catalysts are two main obstacles to the large-scale commercialization of PEMFCs[8, 58-60].

Pure Pt catalysts have been fabricated with different shapes and morphologies, including nanowires[61-63], nanotubes[61, 64], hollow spheres[65]. Also various supports have been used for Pt nanoparticles, including carbon black[66], carbon nanotubes[67, 68], carbon aerogel[69] and mesoporous carbon[70, 71].

Recent efforts involved further lowering the Pt content in Pt-based electrocatalysts. The most commonly used method is to alloy Pt with transition metals, including Fe, Co, Ni, resulting in Pt_3Ni alloy[72-75], binary PtM/C (M=Cu,Co,Ni,Fe)[76-88] and ternary $PtNi_3M$/C (M=Cu,Co,Fe,Cr) nanoparticles[89]. Another recently developed method is to place a Pt monolayer[90, 91] as the outmost shell of nanocatalysts. This method leads to a numerous broad studies of the core-shell electrocatalysts. In addition, replacing Pt with less expensive materials in electrocatalysts has been studied. Among these catalysts, palladium is the most commonly used one, resulting in

catalysts including PdFe/C[92, 93] and PdCo/C[94].

Non-noble metal catalysts (NNMCs) have been studied as ORR electrocatalysts in PEMFCs, in order to further reduce catalyst cost[95-98]. So far the most promising non-noble metal catalysts are metallic complexes[99-103]. Other non-noble metal catalysts include transition metal oxides[104], nitrides[105-107] and chalcogenides[108], and carbon-based materials including carbon nanotubes and graphene[109].

1.4.3 ORR Electrocatalysts in AFCs

The Au {100} single-crystal facet has been considered as the most active catalyst for the ORR in alkaline electrolyte due to its low overpotential, even more active than polycrystalline Pt[110]. However, the complete 4e ORR only occurs on Au {100} within a limited potential range, beyond which the 2e ORR takes over. So currently Pt and Pt-based electrocatalysts are still regarded the most active nanocatalysts in alkaline electrolytes[111]. Silver-based catalysts have been studied as the replacement of Pt due to its relatively low cost and considerable high performance in alkaline electrolytes[112].

Non-noble metal catalysts (NNMCs), including binary manganese oxides[113, 114], perovskite oxides[115], and carbon-based materials, including carbon nanotubes and graphene[116-118], have also been studied as low-cost alternatives for the ORR in alkaline electrolyte.

1.5 Brief Review of Core-Shell and Monofaceted Nanocatalysts

1.5.1 Core-Shell Nanostructures *via* Atomic Layer Coating

Fabricating sub-nm-thick shell of the core-shell nanocatalysts is an effective approach for obtaining high surface area of active metals with tunable properties. The key to fully realize the potential of this approach in developing active, durable nanocatalysts at low cost is the method to produce atomically ordered core-shell nanostructures with tunable shell thickness in 1 ~ 3 monolayer range.

1.5.1.1 Coating with Limited Amount of Reductant

Underpotential deposition (UPD) is an electrochemical phenomenon involving the electrochemical hetero-epitaxial growth of metal adlayer on a foreign metal substrate at the underpotential. It allows for precise control of the surface coverage through the interactive adsorption between metal adatoms and adsorbates, and thus can be used for atomic layer coating. First, an atomic layer of a less noble metal is underpotentially deposited. Then, the pre-deposited metal monolayer, used as the reductant, is in contact with ions of a more noble metal forming an atomic layer of the more noble metal via galvanic replacement. The combination of the UPD process to coat the metal adlayer as reductant, with the subsequent galvanic replacement between the reductant metal adatoms and the noble metal ions produces the atomic layer coating of the noble metal. This combined process is a surface limited redox reaction (SLRR). An example[119] is that on the substrate of Au (111), a monolayer of underpotentially deposited Cu acted as the reductant. After the subsequent galvanic replacement with Pd^{2+} ions, a Pd monolayer was formed on substrate. Similarly a submonolayer of Pt or a bilayer of Ag was formed on substrate via

galvanic replacement of Pt^{4+} or Ag^{+} ions by Cu atoms since Cu ions have a +2 charge.

The coverage of obtained noble metal coating is determined by the initial coverage of the reductant atoms, and also by the charge conservation between reductant atoms and noble metal ions during galvanic replacement. Later by using Pt^{2+} ions instead of Pt^{4+} ions, together with Cu UPD, a Pt monolayer was coated on Pd (111) substrate and Pd nanoparticles[90]. Two or more monolayers of noble metal can be formed by repeating the SLRR process. Up to now, there are a large number of reports on the atomic layer coating of Pt and Pd by SLRR with Cu or Pb as reductant layer, summarized in Table 1.3.

Table 1.3 Summary of overlayer coating via metal UPD.

UPD metal	Coated metal	References
Cu	Pt	90, 91, 119-180
	Pd	94, 132, 140, 165, 166, 181, 182
Pb	Pt	171, 172, 183, 184
	Pd	181

Besides non-noble metal atoms, gas molecules can also be adsorbed on substrate and subsequently used for atomic layer coating. For example, hydrogen[185, 186] or carbon monoxide[187] adsorption was used for Pt coating. Similar to the electrochemical SLRR, some chemical reactions also use limited amount of reductant for atomic layer coating, such like hydrogen as reductant for Pt coating[188-191], and the combination of hydrogen and Cu as reducing agents for Pt coating[192].

Another coating technique utilizes limited amount of reductant is atomic layer deposition

(ALD). ALD is based on self-limiting chemical reactions between gaseous precursors and solid surfaces[193-197], different from its counterparts such as chemical vapor deposition (CVD) or physical vapor deposition (PVD) which are controlled by the supply of precursor sources. ALD can deposit highly uniform and conformal thin film coatings, including monometallic thin film (Pt[198-201], Pd[200, 202], Ru[203, 204], Ir[205], Rh[206]) and bimetallic thin film (RuPt[207], IrPt[208]). It can also deposit small (1~3 nm) and well dispersed nanoparticles on various supports for catalytic applications, including monometallic nanoparticles (Pt[209-215], Pd[210, 216-219], Ru[219], Ir[220, 221]), bimetallic alloy nanoparticles (RuPt[222], PtCo[223]). However, only very few examples of bimetallic core-shell nanoparticles synthesized by ALD have been reported (Pt@Pd[224]).

1.5.1.2 Seeded Epitaxial Growth

Controllable syntheses of core-shell bimetallic nanostructures are discussed in recent reviews[225-227]. Seeded growth, as a chemical and solution-phase synthesis method, was first employed to prepare monometallic nanoparticles with controlled size and shape[228-230], where nanoparticle seeds served as nucleation centers. Later seeded growth was also used to prepare bimetallic nanoparticles, where the metal seeds served as nucleation centers for the reduction of anther metal. Unlike the coating method using limited amount of the reducing agent but adequate amount of the metal precursors (Section 1.5.1.1), seeded epitaxial growth utilizes limited amount of the metal precursors, which are reduced by sufficient amount of the reductant. Table 1.4 lists some representative examples of conformal coating via the route of seeded growth.

Table 1.4 Some representative examples of conformal coating via seeded growth.

Shell	Core	Core size (nm)	Precursor	Solvent	Reducing agent	Stabilizer	Shell thickness	Ref
Pt	Pd nanoplates	50~100	H_2PtCl_6	Water	CA[a]	PVP[b]	1~2 nm	[231]
Pd	Pt nanocubes	9.5	K_2PdCl_4	Water	AA[c]	TTAB[d]	13.8 nm	[232]
Pt	Pd nanooctahedra	10~15	K_2PtCl_4	Water	CA[a]	PVP[b]	1~2 nm	[233]
Pd	Au nanooctahedra	~50	H_2PdCl_4	Water	AA[c]	CTAB[e]	~25 nm	[234]
Pd	Au tetrahexahedral nanocrystals	71	H_2PdCl_4	Water	AA[c]	CTAB[e]	3 nm	[235]
Pd	Ag nanoparticles	8	$Pd(NO_3)_2$	EG[f]	EG[f]	PVP[b]	1~10 ML	[236]

[a]CA: citric acid;

[b]PVP: poly(vinyl pyrrolidone);

[c]AA: ascorbic acid;

[d]TTAB: tetradecyltrimethylammonium bromide;

[e]CTAB: cetyl-trimethylammonium bromide;

[f]EG: Ethylene glycol.

Close lattice match, or small lattice mismatch has been suggested to be crucial for epitaxial conformal coating[225, 232]. A uniform Pt shell was coated on Pd nanoplates with hexagonal and triangular shapes[231], attributing to small lattice mismatch (0.85% for Pd and Pt) and the slow reduction rate for Pt. Uniform coating of Ag on Au seeds forming Au@Ag

nanoparticles (0.17% for Ag and Au) was also prepared by reducing $HAuCl_4$ with ascorbic acid in the presence of CTAB[237]. While the 4.08% mismatch for Au and Pt resulted in the formation of Pt@Au nanorods from anisotropic growth of Au on Pt nanocubes[232], or a rough polycrystalline Pt shell on shaped Au nanocrystals of cubes, octahedra and spheres[238]. However, by careful selection of reductants and surfactants and delicate control of reduction kinetics, conformal coating between two metals with large mismatch is operable. For example, thin Pd shells with a thickness of 3 nm were grown on Au tetrahexahedral (THH) nanocrystals resulting in Au@Pd THH nanocrystals[235].

Moreover, the reducing power of the reducing agent is also important in determining the reduction kinetics of shell metal. Using the mild reductant citric acid, an ultra-thin conformal Pt shell can be coated on Pd nanooctahedra[233], but a dense array of Pt branches were formed when the stronger L-ascorbic acid was employed as the reductant[239, 240], because the strong reducing power of L-ascorbic acid promoted the self nucleation of Pt in the solution[241].

Huang et al. have used Au octahedral nanocrystals as seeds for the growth of Pd shells by reducing H_2PdCl_4 with ascorbic acid in the presence of CTAB[234]. By progressively decreasing the amount of Au nanooctahedra seeds, i.e. by increasing the ratio of Pd shell to Au core, Au@Pd nanocrystals with different shapes can be produced. With increased shell-to-core ratio, the growth rates of Pd shell were expedited[234] bringing larger lattice strain build-up. The lattice strain was released through shape evolution of Au@Pd particles from the initial Au nanooctahedra, including octahedra, truncated octahedra, cuboctahedra, truncated cubes, and concave cubes. Lee et al. have reported the similar phenomenon that with a lower shell-to-core ratio, the resultant Au@Pd nanocrystals adopted the concave trisoctahedral shape of Au cores;

and the obtained Au@Pd nanocrystals had different shapes with a higher shell-to-core ratio[242].

1.5.2 Shaped or Monofaceted Metallic Nanocrystals

Synthetic strategies for controlling shapes of metallic nanocrystals have been developed in the past decade[243-246], which would facilitate studies of the correlation between catalytic activity and surface structure in this size regime[247-249]. Some shaped nanocrystals have only one kind of facet on their exposed surfaces, and therefore are known as monofaceted nanocrystals, while other shaped nanocrystals have at least two types of facets on their exposed surfaces. There are two main purposes of the electrochemical study on shaped metallic nanocrystals. One is to correlate the catalytic activity on nanoscale with that on single-crystal bulk surfaces; the other is to associate the catalytic activity on monofaceted nanocrystals with that on spherical nanocatalysts.

Table 1.5 lists the tentative summary of electrochemical measurements for shaped or monofaceted monometallic nanocrystals (Au, Pt and Pd) in literatures. The electrochemical measurements include three parts:

I. Electrochemical characterizations
    i. Cyclic voltammetry (CV)
    ii. Underpotential deposition (UPD) of metal (Cu, Pb or Tl) ions
    iii. Irreversible adsorption (IRA) of metal (Bi or Ge) ions
II. Cathodic reactions
    i. Oxygen reduction reaction (ORR)
III. Anodic reactions

i. Methanol oxidation reaction

ii. Formic acid oxidation reaction

iii. Ethanol oxidation reaction

iv. Glucose oxidation reaction

v. Ammonia oxidation

vi. CO electro-oxidation

Table 1.5 Summary of electrochemical measurements for shaped Au, Pt and Pd nanocrystals.

Electrochemical Measurements	Acid Electrolyte	Alkaline Electrolyte
Cyclic voltammetry	Au[170, 250-254], Pt[187, 255-263], Pd[249, 264-267]	Au[253], Pt[259, 260, 262], Pd[249, 264, 267]
Cu UPD	Pd[249, 268]	
Pb UPD		Au[269, 270]
Tl UPD	Pt[271]	
Bi IRA	Pt[258, 272, 273]	Pt[259]
Ge IRA	Pt[258, 272]	
ORR	Au[253], Pt[257], Pd[249, 264, 265]	Au[270, 274], Pd[249, 264, 267]
Methanol oxidation reaction	Pt[263]	Pd[267]
Formic acid oxidation reaction	Pt[271], Pd[249, 266, 268, 275]	Pd[267]
Ethanol oxidation reaction	Pt[255, 256]	Pd[266, 267]
Glucose oxidation reaction		Au[250, 269]
Ammonia oxidation		Pt[276]
CO electro-oxidation	Pt[187, 262], Pd[249, 264]	Pt[259, 260], Pd[264]

Albeit that such bottom-up synthetic approaches yield various monodisperse and well-shaped metallic nanocrystals, nevertheless, other surface-related concerns are brought up, such as

the elimination of the stabilizers and/or capping agents[277] used during synthesis which requires extraordinary cleaning procedures[278], as well as the surface structure fidelity after extensive post treatment. The removal of surfactants, including poly(vinyl pyrrolidone) (PVP)[144, 249, 267, 279, 280], oleylamine[280, 281], cetyl-trimethylammonium chloride (CTAC)[251], cetyl-trimethylammonium bromide (CTAB)[266, 282], polyvinyl alcohol[283], *n*-heptane[284] and sodium polyacrylate[259], has been discussed using various methods including electrochemistry[249, 267, 285], CO adsorption[266, 286], UV Ozone[287], oxygen plasma[288], H_2O_2 and concentrated H_2SO_4 [279]. Clean and well-ordered surfaces are essential for revealing their true catalytic behavior. Impurities, like surfactants, have detrimental effects by blocking the adsorption of reactants to the catalyst surface, which consequently inhibits the catalytic activities[289].

1.6 Aims and Objectives

1.6.1 Core-Shell Nanoparticle Strategies for Improving FC and WE catalysts

Platinum (Pt) is known as the best single metal catalyst for the anodic HOR and cathodic ORR in PEM fuel cells, and for the cathodic HER in PEM water electrolyzers. However, the high cost and low abundance of Pt are still the main obstacles to the large-scale commercialization of PEM fuel cells and water electrolysis. Therefore, the major goal of these electrocatalysis studies is to produce highly active, durable catalysts while minimizing the use of precious noble metals, especially Pt[8, 60]. An effective approach is to fabricate core-shell nanoparticles that have active, corrosion-resistant Pt atoms on the catalysts' surface, with tunable reactivity through their interactions with other metal cores to assure optimal catalytic performances[91, 149, 290].

Core-shell electrocatalysts for the HER-HOR in acid electrolyte

The HER-HOR are a pair of important reactions for carbon-free energy conversion, producing hydrogen in water electrolyzers and generating electrical power in hydrogen fuel cells. While Pt nanocatalysts are highly active for both the HER and the HOR, as indicated above, the scarcity and high cost of Pt impede the large-scale commercialization of these clean energy technologies[19, 291].

For the HOR at the anode of PEM fuel cells, a negligible potential loss was achieved with pure hydrogen using 50 μg cm^{-2} Pt nanoparticles[291, 292]. However, the challenge remains in employing inexpensive reformate hydrogen, wherein the ppm-level of carbon monoxide (CO) impurities can severely deactivate the Pt catalysts[293, 294]. In addition, though the anode operates at

relatively low potentials, its nanocatalysts must be dissolution resistant because of the high potentials experienced during startups and shutdowns[295, 296]. Therefore the main challenges are to develop low Pt loading electrocatalysts with high HOR activity, suitable tolerance to CO, along with high dissolution resistance.

For the HER at the cathode of PEM water electrolyzers, Pt loading <200 μg cm^{-2} remained elusive for the HER, without incurring a performance penalty in PEM water electrolyzers[297]. The major challenges for developing HER electrocatalysts are low Pt loading, retained or even enhanced HER activity, along with good durability.

In Section 3.1,[298] we investigated a series of bimetallic core-shell nanocatalysts having Ru core and Pt, Pd or Au shell (Ru@M, where M = Pt, Pd, Au), synthesized with ethanol, which is both the solvent and the reducing agent. By measuring their HER-HOR activities in correlation with chemical composition, shell thickness and loading using the hanging-strip GDE test method (Section 2.3.2), we identified the Ru@Pt nanocatalysts as the most active HER-HOR electrocatalysts in acid solution, among these core-shell nanocatalysts.

Next, in Section 3.2,[299-301] we optimized the Pt shell thickness of the Ru@Pt nanocatalysts. Because surface science studies of Pt thin films on Ru(0001) surfaces revealed a significant increase of CO binding energy on the Pt surface, from 0.99 eV on a monolayer to 1.21 eV on a bilayer, and about 1.30 ~ 1.35 eV for ≥ 3 monolayers[302], along with a remarkable variation of oxygen adsorption behavior on 1~3 monolayer thick Pt films[303]. These profound thickness-dependent effects suggest the need and the opportunity for advancing the CO tolerance and corrosion resistance via precisely controlling the thickness of well-defined Pt shells, without compromising the HER-HOR activity.

However, question arises whether a sharp and well-defined Ru-Pt core-shell interface is possible at the atomic level, because Ru and Pt have different crystalline structures, and also because Ru cores were considered disordered in previously synthesized Ru@Pt nanoparticles based upon the commonly observed weak Ru intensities in their X-ray diffraction (XRD) profiles[304, 305]. In Section 3.2, with in-depth characterizations and analyses of the Ru(*hcp*) to Pt(*fcc*) structural phase transition at the Ru-Pt core-shell interface, we also found that defect-induced partial alloying is the cause of Ru disordering, and therefore succeeded in fabricating single crystalline Ru@Pt nanoparticles with well-defined, energetically favorable *hcp* to *fcc* structural transition at the core-shell interface. This new level of atomic control in synthesis allowed us to use bilayer Ru@Pt nanoparticles as an advanced HER-HOR catalyst for practical applications in PEM fuel cells[299, 300] and water electrolyzers[301]. In addition, the local structures for bilayer Ru@Pt/C and commercial Pt/C were probed by *in situ* XAS measurements.

Core-shell electrocatalysts for the ORR in acid electrolyte

Recently, the Pt content in the Pt-based electrocatalysts has been greatly reduced via core-shell nanostructures consisting of a Pt shell on appropriate monometallic or alloy cores.[290, 306] Especially the highest Pt utilization along with enhanced activities and durability have been achieved in the Pt monolayer nanocatalysts with a one-atom-thick Pt shell,[91, 149, 307] where every Pt atom is on catalysts' surface and available for participating electrocatalytic reactions. Pd and Pd-Au alloy nanoparticles were shown to be suitable cores for the Pt monolayer catalysts having considerably enhanced Pt-mass activity for the ORR in acid solution[135, 140, 155].

In Section 3.3,[308] we placed Pt atomic layers on Pd nanoparticles to produce the Pd-Pt

core-shell nanocatalysts. The conformity and continuousness of Pt shells were verified by various characterization techniques, including X-ray diffraction (XRD), scanning transmission electron microscopy (STEM) with electron energy loss spectroscopy (EELS) and energy dispersive X-ray spectroscopy (EDX). The density functional theory (DFT) calculations also showed that two-dimensional growth is energetically favorable. The as-prepared Pt monolayer electrocatalysts exhibited high electrocatalytic performance toward the ORR.

In Section 3.4,[309] we explored the way of further enhancing the total-metal mass activity by employing hollow Pd and Pd-Au nanoparticles as cores for the Pt monolayer catalysts. The improved total-metal mass activity was attributed to the hollow-induced lattice contraction, in addition to the mass-saving geometry of hollow particles.

1.6.2 Monofaceted Nanocrystals for Investigating ORR Mechanisms in Alkaline Electrolyte

The surface atomic structures of metal catalysts play key roles in determining the kinetics and mechanisms of catalytic reactions[247, 310]. Bulk single-crystal surfaces have been employed extensively as model systems for studying the intrinsic correlations between surface atomic structures and various catalytic activities. In ORR, a complete four-electron (4e) ORR is preferred because of twofold efficiency of energy conversion in the comparison with the partial two-electron (2e) ORR[311]. The ORR has been investigated on many metal surfaces, wherein a majority of noble metals, such as platinum (Pt) and palladium (Pd), demonstrated to support the 4e-ORR pathway regardless of their surface atomic structures. On these noble metal surfaces exhibiting strong and dissociative interaction with the dioxygen (O_2) reactant, the 4e-ORR

activity is governed by desorption of reaction intermediates that allows releasing the occupied active sites. However, on bulk gold (Au) surfaces, the ORR in alkaline electrolyte is highly sensitive to the surface structure because of their weak interaction with O_2,[312-314] and with other reactants. A 2e reduction to hydroperoxide ions (HO_2^-) proceeds on most facets including Au {111}[315], whereas the complete 4e reduction to hydroxide ions (OH^-) only occurs on Au {100}[316] in a narrow potential region beyond which the 2e ORR takes over. A few studies further found that the high-index Au {910} and {11,1,1} facets with a large fraction of the {100} subfacet[317] exhibit the 4e-ORR performances similar to that on Au {100} in a confined potential range. But the full-potential-range 4e ORR has not been observed on Au single-crystalline surfaces yet.

In Section 3.5,[318] we have explored the ORR activity of three kinds of Au nanocrystals with polyhedral shapes, octahedron, cube, and truncated ditetragonal prism (TDP), which contain only one type of nanofacet per particle, {111}, {100} and {310}, respectively. Such surface tailoring of nanoscale objects permitted us probing the dependence of the ORR selectivity on Au surfaces with different facets. While the ORR behaviours on Au octahedra and Au cubes enclosed with {111} and {100} facets, respectively, are similar to those on the corresponding bulk Au single-crystal surfaces, the {310} nanofacets of Au TDPs exhibit the 4e ORR behaviour without reverting to a 2e ORR. Previous electrochemical[317] and spectroscopic[319] studies suggested hydroxyl (OH^-) adsorption as the primary reason for the structure-dependent ORR on Au. However, current models relying on OH binding[320, 321], which was derived from the past experimental discoveries, still cannot completely explain the ORR mechanism on Au in alkaline media and, especially, the characteristic 4e-to-2e ORR transition on Au {100}[321]. Our studies,

through the revealed relationship between nanofacet structure and ORR behaviour, shed light on the reaction mechanism/pathway, which is beneficial for the rational catalyst design. The observation of exceptional ORR performance on Au TDPs and its contrast with the more conventional behaviour of other shaped Au particles motivated us to re-investigate the ORR mechanism in alkaline solution by DFT calculations. We pose a new insight into the role of water in ORR selectivity on Au nanocrystal surfaces. O_2 and H_2O, as two essential and pervasive chemicals, are prominent in many areas of chemistry. However, the O_2-H_2O interplay on metal surfaces, as well as its effect on electrochemical process, is not clear. Our computational studies elucidate that the unique 4e ORR activity on Au surfaces is likely to arise from the O_2-H_2O coadsorption along with low-coordinated Au surface atoms.

Also, the work demonstrates a new platform for exploring model catalytic systems based on nanocrystals. Probing and optimizing the ORR behavior on Au surfaces require a precise control of the crystalline structures of Au surfaces. However, preparing perfect single-crystalline surfaces via conventional mechanical techniques, such as cutting and polishing, still remains comparatively challenging, since even minimal miscut may result in wide divergence of surface structure. Shape-controllable syntheses of metallic nanocrystals provide an alternative strategy for the fabrication of atomically tailored surface. In the past decade, a wide range of compositions, sizes and shapes have been achieved through various synthetic processes[243-246], which would help uncovering the effect of surface structure in this size regime[247-249] on catalytic activity. Nevertheless, such bottom-up synthetic approaches bring up challenges associated with the surface cleanness. For example, the elimination of the stabilizers and/or capping agents[277] used during syntheses requires extraordinary cleaning procedures[278], as well as the surface

structure might degrade after extensive post-treatment. Surfactants and ionic impurities, could detrimentally block the adsorption of reactants to the catalyst surface, and, consequently, inhibit the ORR activities[289]. Therefore, atomically intact and unpolluted surfaces obtained through appropriate synthetic procedures are critical for revealing the catalytic performance and understanding its mechanism.

Chapter 2 EXPERIMENTAL & TECHNIQUES

2.1 Syntheses of Carbon Supported Ru@M (M = Pt, Pd, Au) Core-Shell Nanoparticles

2.1.1 Syntheses of Carbon-Supported Ru Nanoparticles

The carbon-supported Ru nanoparticles were synthesized using ethanol as the solvent and the reducing agent. Firstly, 400 μmol $RuCl_3$ was dissolved in 100 mL anhydrous ethanol to form $RuCl_3$ ethanolic solution with the brown color. The $RuCl_3$ solution was refluxed with rigorous stirring for 1 h, in a three-neck round bottom flask immersed in the oil bath at 110 ℃. The color of the solution changed from brown to dark green. Secondly, 200 mg carbon powder (Ketjenblack EC-600JD) was disbursed in 60 mL ethanol by sonication for 30 minutes. The slurry was transferred into the flask with an additional 10 mL ethanol to assure a complete transfer. Then 1200 (= 3 × 400) μmol of 0.2 M NaOH aqueous solution was added dropwisely. The reaction mixture was refluxed at 110 ℃ (oil bath) for an additional 2 h. Thirdly, the reaction progress was checked by the color of supernatant. If it was not completely colorless, an additional 200 (= 0.5 × 400) μmol NaOH was added. The hot plate was turned off, allowing the mixture to cool slowly in the oil bath to room temperature. The mixture was filtered out, washed with water and ethanol, and dried at room temperature under vacuum. Then the carbon-supported Ru nanoparticles were annealed in H_2 at 450 ℃ for 1 h.

2.1.2 Syntheses of Ru@Pt Nanoparticles

In a typical synthesis of $Ru@Pt_{2ML}$ nanocatalysts, firstly, the annealed carbon-supported

Ru nanoparticles (400 μmol Ru) were dispersed in 120 mL ethanol. The mixture was refluxed in a three-neck round bottom flask at 110 ℃ (oil bath) for 1 h, and then cooled to 30 ℃. Secondly, 400 μmol of 50 mM H_2PtCl_6 ethanolic solution was added with the H_2PtCl_6 concentration in the reaction mixture being 1 to 4 mM. The mixture was heated to and refluxed at 80 ℃ (oil bath) for 2 h. Thirdly, the reaction progress was checked by the color of supernatant. After the solution color faded away, 800 (= 2 × 400) μmol of 0.2 M NaOH aqueous solution was added dropwisely. The mixture was cooled slowly in the oil bath to room temperature, filtered out, washed with water and ethanol, and dried for future use. In the synthesis of Ru@Pt_{1ML} nanocatalysts, 200 μmol H_2PtCl_6 was used instead.

2.1.3 Syntheses of Ru@Pd Nanoparticles

In a typical synthesis of Ru@Pd_{2ML} nanocatalysts, firstly, the annealed carbon-supported Ru nanoparticles (400 μmol Ru) were dispersed in 120 mL ethanol. The mixture was refluxed in a three-neck round bottom flask at 110 ℃ (oil bath) for 1 h, and then cooled to 25 ℃. Secondly, 400 μmol of Na_2PdCl_4 was mixed with 115 mL ethanol in another flat flask, and the mixture was stirred at room temperature for 1 h to assure the complete dissolution of Na_2PdCl_4. Then the Na_2PdCl_4 ethanolic solution was added with the Na_2PdCl_4 concentration in the reaction mixture being 1 to 2 mM. The mixture was heated to and refluxed at 55 ℃ (oil bath) for 2 h. Thirdly, 720 (= 1.8 × 400) μmol of 0.2 M NaOH aqueous solution was added dropwisely. The mixture was cooled slowly in the oil bath to room temperature, filtered out, washed with water and ethanol, and dried for future use. In the synthesis of Ru@Pd_{1ML} nanocatalysts, 200 μmol Na_2PdCl_4 was used instead.

2.1.4 Syntheses of Ru@Au Nanoparticles

In a typical synthesis of $Ru@Au_{2ML}$ nanocatalysts, firstly, the annealed carbon-supported Ru nanoparticles (400 μmol Ru) were dispersed in 260 mL ethanol. The mixture was refluxed in a three-neck round bottom flask at 110 ℃ (oil bath) for 1 h, and then cooled to 80 ℃ (oil bath). Secondly, 400 μmol of 100 mM $HAuCl_4$ ethanolic solution was added with the $HAuCl_4$ concentration in the reaction mixture being 1 to 1.5 mM. The mixture was heated to and refluxed at 105 ℃ (oil bath) for 1 h. Thirdly, after the solution color faded away, 800 (= 2 × 400) μmol of 0.2 M NaOH aqueous solution was added dropwisely. The mixture was cooled slowly in the oil bath to room temperature, filtered out, washed with water and ethanol, and dried for future use. In the synthesis of $Ru@Au_{1ML}$ nanocatalysts, 200 μmol $HAuCl_4$ was used instead.

2.1.5 Temperature Control

The temperature control in these solution-phase syntheses was realized by oil bath (silicone oil, high temperature, Alfa Aesar), and a magnetic stirrer (RCT basic, IKA) equipped with a temperature sensor (PT 1000.60, IKA). The temperatures mentioned here referred to the temperature setting of the magnetic stirrer. Because the reactor system was not closed and the boiling point of absolute ethanol is 78 °C, the temperature of ethanolic solution did not always equal to the temperature measured in oil bath (Figure 2.1). As shown in Figure 2.1, when the reaction temperature was set to be 80 °C, the real solution temperature was 70 °C and the solution was not boiling. When the reaction temperature was set to be higher than 95 °C, even though the solution temperature kept at 78 °C, the oil bath still provided extra heat energy to the

solution and stimulated the reaction kinetics.

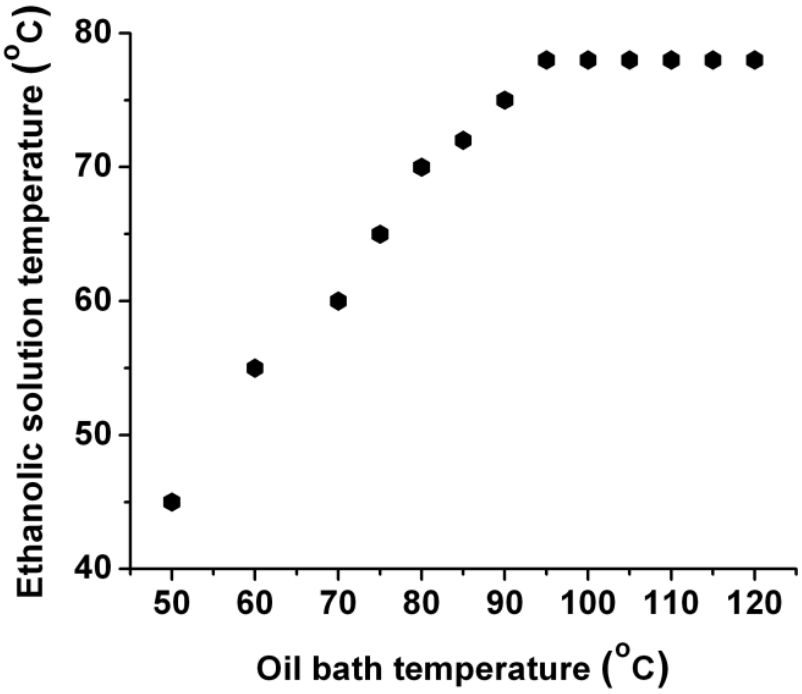

Figure 2.1 Ethanolic **s**olution temperature as a function of oil bath temperature. The temperature of ethanolic solution was measured by a thermometer inserted in the solution. The temperature of oil bath was measured by a temperature sensor connected to a magnetic stirrer. The oil bath temperature was controlled by settings of the magnetic stirrer. Anhydrous ethanol (200 proof) was used.

2.2 Syntheses of Carbon Supported Pd@Pt Core-Shell Nanoparticles

2.2.1 Preparation of Carbon Supported Hollow Pd and Pd-Au Nanoparticles

Pulse electrodeposited Ni nanoparticles were replaced galvanically by Pd and Pd-Au ions to obtain hollow Pd and Pd-Au nanoparticles, respectively. Typically, an aqueous suspension of Vulcan carbon powder (1 g L^{-1}) was prepared and sonicated in ice bath for 5 ~ 10 min. A 15 μL aliquot of the suspension was then pipetted onto the polished glassy carbon surface of a rotating disk electrode (5 mm diameter, 0.196 cm^2, Pine Instrument). After drying in air, the uniformity of the carbon thin film was inspected and there should be no visibly shining glassy carbon. The as-prepared thin-film electrode was immersed in a deaerated solution of 0.1 M $NiSO_4$ and 0.5 M H_3BO_3. A double potential pulse, t_1 /s at −1.4 V and t_2 /s at −0.8 V (vs. Ag/AgCl, 3M NaCl) was applied to deposit Ni nanoparticles on carbon support (Ni/C). Varying t_1 was used to vary the nucleation density of Ni particles, while varying t_2 altered the particle size. The integrated charge of each step varied from 1 to 5 mC, and from 1 to 7 mC, respectively. The open-circuit potential after electrodeposition was monitored and was stabilized in 10 min. Under the protective Ar atmosphere, the Ni/C electrode was then transferred, into a deaerated solution containing 0.5 mM $Pd(NH_3)_4Cl_2$ with or without $HAuCl_4$, where the galvanic replacement of Ni by Pd and Au took place. The reaction time was chosen in relation with both the Ni electrodeposition charges and the desirable shell thickness. The electrode was rotated in pure water at 1000 rpm for 1 min to get rid of the metal ions in the attached droplet before the immersion in a deaerated 0.1 M $HClO_4$ solution. Then 20 ~ 30 potential cycles from 0.05 to 1.1 V (vs. RHE) were applied at room temperature for a complete removal of the Ni atoms from inside the noble metal shells.

2.2.2 Pt Monolayer Coating *via* Cu Underpotential Deposition

Recently, platinum monolayer catalysts have been developed in Adzic's group[90, 91, 149]. A Cu monolayer is first formed on metal nanoparticles using underpotential deposition (UPD)[90, 322, 323], and is subsequently replaced galvanically by Pt ions to form a Pt monolayer[39, 119]. In a typical process, a Cu monolayer was underpotentially deposited on the nanocatalysts in a solution of 50 mM $CuSO_4$ and 0.10 M H_2SO_4. The electrode was subsequently immersed in a solution of 1.0 mM K_2PtCl_4 and 0.10 M H_2SO_4 to galvanically displace the Cu adatoms with $[PtCl_4]^{2-}$ ions. Then the electrode was rinsed with deionized water to remove excess $[PtCl_4]^{2-}$ ions.

2.2.3 Pt Monolayer Coating in Ethanol

In a typical synthesis of $Pd@Pt_{ML}$ core-shell nanoparticles, 30 mL anhydrous ethanol containing 60 mg Pd/C (30 wt%, 169.1 μmol Pd) was mixed with 50 mM ethanolic H_2PtCl_6 solution (63.4 μmol Pt, pH ~2, yellow) with rigorous magnetic stirring in a 3-neck round bottom flask at room temperature. After the mixture was confirmed to be uniform, it was heated to and refluxed at 80 °C for 1~2 h. Temperature was control by oil bath, and a magnetic stirrer equipped with a temperature sensor, as described in Section 2.1.5.

One end of the condenser was open to air and inert protective atmosphere was unnecessary during syntheses. The reaction progress was checked by the color of supernatant. After the solution color faded away, 126.8 (=2 × 63.4) μmol of aqueous 0.2 M NaOH solution was added with additional refluxing at 80 °C for 20 ~ 30 min, to ensure the complete reduction of Pt. Then the mixture was cooled down, filtered out, washed with water and ethanol, and dried at room temperature under vacuum.

2.3 Electrochemical Measurements

2.3.1 Rotating Disk Electrode (RDE) & Rotating Ring Disk Electrode (RRDE)

2.3.1.1 Preparation of Thin-Film Electrode

Carbon-supported nanocatalysts were dispersed in a solution of deionized water and isopropyl alcohol to make catalyst inks, typically in the concentration of 1 g L^{-1}. The ink was sonicated in the ice bath for 5 ~ 10 min. Then an aliquot of ink (10 to 20 μL) with desired amount of catalyst was pipetted on to a polished glassy carbon rotating disk electrode (5 mm diameter, 0.196 cm^2 electrode area, Pine Instrument). After drying in air, the uniformity of carbon thin film was inspected and there should be no visibly shining glassy carbon.

The thin-film electrode with Au nanoparticles was prepared by putting an aliquot of the aqueous nanocrystal suspension onto a polished electrode. A 5.0-mm diameter glassy carbon rotating disk electrode (RDE) (disk geometric area 0.196 cm^2, Pine Instrument), and a 5.61-mm diameter glassy carbon rotating ring disk electrode (RRDE) with a platinum ring (disk geometric area 0.247 cm^2, ring geometric area 0.186 cm^2, collection efficiency 37%, insulating ring-disk gap 320 um, Pine Instruments) were used in RDE and RRDE experiments, respectively. After drying in vacuum, the electrode was washed in ethanol and water prior to any electrochemical measurements.

2.3.1.2 Experimental Setup

All electrochemical treatments and measurements were performed with a Volta PGZ402 potentiostat (Voltalab, Radiometer Analytical) at room temperature. A Pt flag was used as the counter electrode. A leak-free (Ag/AgCl, 3M NaCl) electrode, or a leak-free (Hg/HgO, 1M

KOH) electrode, respectively, was used as the reference electrode for measurements in acid or alkaline solution. All potentials quoted in the paper were converted with respect to a reversible hydrogen electrode (RHE). The potential calibration of the reference electrode was conducted daily, by measuring the open circuit potential of the Pt flag in H_2-saturated electrolyte. All electrochemical experiments in alkaline solution were completed within 2 hours[324].

2.3.2 Gas Diffusion Electrode (GDE)

2.3.2.1 Preparation of Electrodes

Carbon-supported nanocatalysts were dispersed in a solution of deionized water, isopropyl alcohol, anhydrous ethanol and 10 wt% Nafion® to make catalyst inks. The dry mass of Nafion® is equal to 50~100 wt% of carbon support. [***Caution!*** *Deionized water and aqueous Nafion® were added before adding isopropanol or ethanol, because pouring alcohol on dry powder of carbon-supported metal nanocatalysts may cause sparks.*] The ink was sonicated in an ice bath for 5 ~ 10 min, and then mixed for at least 1 hour using MM 400 mixer (Mixer Mill, Retsch).

Catalyst inks were then applied onto a typical area of 1 cm × 1 cm at one end of the 1 cm × 4 cm carbon-paper strips of gas diffusion layer (Avcarb GDS1120, Fuel Cell Store) by brushing. The electrode area of 0.2 cm^2 was used in the measurements for Ru@Pt nanocatalysts in the long potential range where the current density exceeded 1.5 A cm^{-2}. After the solvents completely evaporated, the as-prepared gas diffusion electrodes (GDEs) were used as the working electrode in electrochemical measurements. The weight difference of carbon-paper strips before and after applying the inks was used to calculate the metal loading.

2.3.2.2 Experimental Setup

All electrochemical measurements were performed with a Volta PGZ402 potentiostat (Voltalab, Radiometer Analytical) at room temperature, using a three-electrode electrochemical cell. The electrolyte was 1 M $HClO_4$ solution. The GDE strip was held vertically, and the 1 cm^2 electrode area with catalysts was immersed in the electrolyte and positioned to face the counter electrode of a Pt flag. The distance between the working electrode of the GDE strip and the counter electrode of the Pt flag was kept the same to minimize the fluctuation of solution resistance. A leak-free Ag/AgCl (3M NaCl) electrode with a double-junction chamber (Cypress Systems) was used as the reference electrode, while all the potentials are quoted with respect to the reversible hydrogen electrode (RHE). The potential calibration of the reference electrode was conducted daily, by measuring the open circuit potential of the Pt flag in H_2-saturated electrolyte.

2.3.2.3 HER-HOR measurements

Traditionally, the rotating disk electrode (RDE) method was used for determining the HOR activities on smooth Pt crystal surfaces[325, 326] and on thin nanocatalyst films[40]. However, the RDE's limiting currents on the scale of mA cm^{-2} are insufficient for unambiguously determining the high HER-HOR activity on Pt in acids, as was later found by microelectrode measurements[327] and hydrogen pump experiments in PEM fuel cells[292, 328]. Other methods, such as using a porous electrode floating on the electrolyte solution, also were found effective in enhancing gas transport, and thus, were used in studying the intrinsic kinetics of the HOR and the oxygen reduction reaction on Pt nanocatalysts[329].

Less noticed was that the HER activity also is profoundly affected by gas transport, even though H_2 is the product, not the reactant as in the HOR. We illustrate this fact here by comparing the polarization curves measured on an RDE and a hanging strip of gas diffusion electrode (GDE). The latter affords us a feasible method to alleviate gas transport limits in solution electrochemical cells, and to quantify the HER-HOR activity by measured charge transfer resistance (*CTR*) at the reversible potential of 0 V.

As illustrated in the inset of Figure 2.2a, we coated catalysts on one side and at one end of a rectangular gas diffusion layer, and held such a strip vertically, with its catalyzed part immersed in an electrolyte solution. A Pt flag placed face-to-face with the GDE strip acted as the counter electrode. To make an easy comparison with the RDE method, we made a GDE sample with the same 0.2 cm^2 electrode area as the RDE. A remarkable enhancement in the rate of gas diffusion was directly evident by following the changes in the measured open-circuit potentials after switching the blanketing gas above the solution from Ar to H_2. The curves in Figure 2.2a show that a 90% decrease of the open-circuit potential from 0.88 to 0.088 V (zero is defined with a H_2-saturated solution) takes 7 seconds on a GDE, ten times quicker than on an RDE, illustrating the effectiveness in enhancing gas transport via microporous channels inside the GDE.

The impact of enhanced gas transport on the HER-HOR currents is huge as shown by the ohmic-loss-corrected polarization curves for the GDE and RDE in Figure 2.2b. While it is well known that starvation of reactant H_2 causes levelling off of the HOR current at a few mA cm^{-2} on the RDE, the comparison in Figure 2.2b further reveals that the HER current is also severely reduced on the RDE due to slow removal of the product, H_2. As an example, the HER current at

−8 mV on the GDE is 11-fold of that on the RDE; although this is less than the 80-fold for the HOR current at 8 mV, an-order-of-magnitude difference shows that the HER activity of a highly active catalyst may be significantly underestimated using the RDE method.

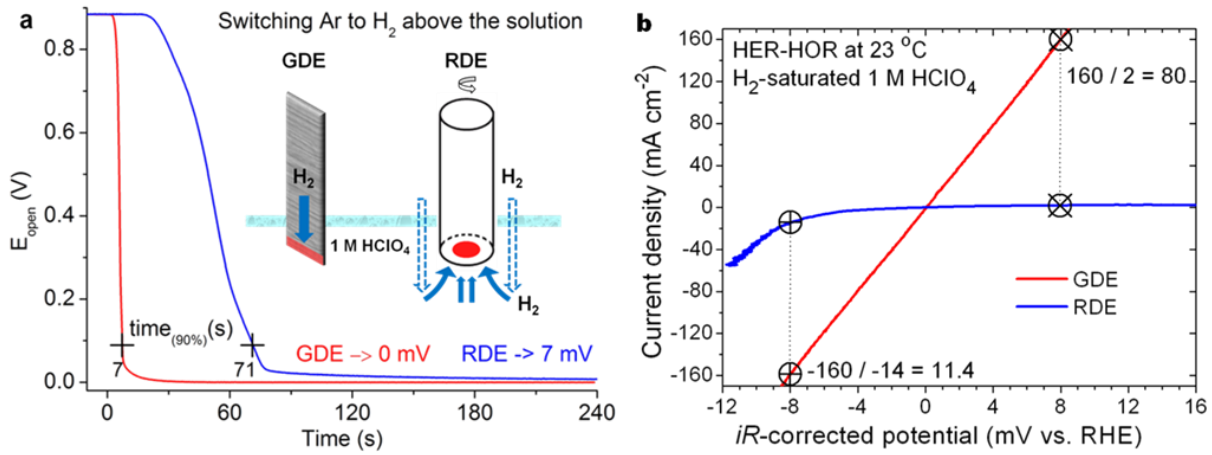

Figure 2.2 HER-HOR activity measured using hanging-strip GDEs in H_2-saturated 1 M $HClO_4$ at 23 ℃. (a) Open circuit potentials on a GDE and an RDE (2500 rpm) as a function of time, after the blanketing gas above the 1 M $HClO_4$ solution was switched from Ar to H_2. (b) HER-HOR polarization curves on a GDE and an RDE (2500 rpm), both having an electrode area of 0.2 cm^2 with the same amount of Ru@Pt catalysts (20 μg cm^{-2} Pt, 11 μg cm^{-2} Ru).

The linear, symmetric polarization on the GDEs near 0 V affords us a simple way to quantify the HER-HOR activity. Polarization curves for the HER-HOR were recorded using the hanging-strip GDE method, in H_2-saturated electrolyte at a sweep rate of 20 mV s^{-1}. [***Caution!*** *After measuring the hydrogen evolution and oxidation reactions on GDEs, the electrochemical cell should be purged with inert gas (e.g. Ar or N_2) until the increasing open circuit potential of the GDE stabilized, before taking the GDE out of the electrochemical cell, in order to avoid the burning of the carbon-paper GDE due to mixing of the hydrogen inside the porous GDE and the*

oxygen in the air.] For the polarization curves in the short potential range of −50 to 50 mV, the cathodic and anodic sweeps were almost identical and therefore were merged and averaged. Typically, the polarization resistance (*PR*) of the measured polarization curves at 0 V was determined by a linear fit within 20 mA cm^{-2}. Electrochemical impedance spectroscopy (EIS) measurements were carried out at a dc potential of 0 V with a sinusoidal wave perturbation of 20 mV and an ac frequency range of 10 kHz to 1 Hz. The high frequency resistance (*HFR*) was determined from the Nyquist plot of impedance spectra by the Z_{real} intercept at high frequencies, and was used to correct the *iR* drop in voltage of polarization curves. The charge transfer resistance (*CFR*) was calculated by the equation

$$CFR = PR - HFR \tag{2.1}$$

and was used to represent the HER-HOR activities of catalysts.

2.3.3 Oxygen Reduction Reaction (ORR)

2.3.3.1 Measurements

ORR measurements on RDE and RRDE respectively were carried out with a Volta PGZ402 potentiostat (Voltalab, Radiometer Analytical), and a CHI 700B electrochemical analyzer. During the RDE measurements, the disk potential was swept at 10 mV s^{-1} for the carbon-supported bimetallic core-shell or Pt nanocatalysts, or 50 mV s^{-1} for Au monofaceted nanocrystals. During the RRDE measurements for Au monofaceted nanocrystals, the disk potential was swept at 50 mV s^{-1}, while the ring potential was potentio-stated at 1.26 V versus RHE where peroxide oxidation occurred under diffusion control. The ORR measurements were performed in 0.1 M $HClO_4$ or 0.1 M NaOH solution. The electrolyte was saturated by oxygen

gas before the experiments and kept under a blanket of oxygen gas during the ORR measurements.

2.3.3.2 Calculation of Electron Transfer Number in ORR

From the RRDE measurements, the average number of electrons transferred per oxygen molecule (n) during the ORR can be determined by the following equation[330]:

$$n = 4\, i_D / (i_D + i_R / N) \tag{2.2}$$

where i_D is the disk current, i_R is the ring current, and N is the collection efficiency. Note that i_D and i_R are the currents (in units of mA), not the current densities (in units of mA cm^{-2}), on the disk and on the ring, respectively.

Alternatively, from RDE measurements, the electron transfer number (n) can calculated from the slopes of the Koutecky-Levich plots at different potentials. The Koutecky-Levich equation[331] is expressed as

$$j^{-1} = j_k{}^{-1} + j_L{}^{-1} = j_k{}^{-1} + B^{-1}\omega^{-1/2} \tag{2.3}$$

and

$$B = 0.62nFAD_{O_2}^{2/3}\nu^{-1/6}C_{O_2} \tag{2.4}$$

where j is the current density, j_k is the kinetic current density, j_L is the diffusion-limiting current density, n is the electron exchange number, F is the Faraday constant (96485 C mol^{-1}), A is the geometric area of the working electrode (0.196 cm^2 for the RDE, 0.247 cm^2 for the RRDE), and ω is the electrode rotation rate. The published values of the diffusion coefficient of O_2 ($D_{O_2} = 1.90 \times 10^{-5} cm^2 s^{-1}$)[317, 332], the kinetic viscosity of the solution ($\nu = 1.02 \times$

$10^{-2} cm^2 s^{-1}$ using $\nu = \frac{\eta}{\rho}$ [333] and $\eta = 1.027\ mPa\ s$, $\rho = 1.0039\ g\ cm^{-3}$ from Ref. [334]), and the concentration of dissolved O_2 ($C_{O_2} = 1.21 \times 10^{-3} mol\ L^{-1}$)[335] were used in the calculation. The standard diffusion-limiting current density can be calculated using the Koutecky-Levich equation.

If the ORR proceeds via the 2e pathway, i.e.

$$n = 2 \tag{2.5}$$

then the diffusion-limiting current density should be

$$j_L = 2.86\ mA\ cm^{-2} \tag{2.6}$$

If the 4e ORR occurs, i.e.

$$n = 4 \tag{2.7}$$

then the diffusion-limiting current density should be

$$j_L = 5.73\ mA\ cm^{-2} \tag{2.8}$$

2.4 X-ray Absorption Spectroscopy (XAS)

The X-ray absorption spectroscopy (XAS) measurements were carried out at the X18B and X19A beamlines at the National Synchrotron Light Source (NSLS), Brookhaven National Laboratory. Different sample preparation methods were employed. For *ex situ* measurements of solid powder samples, such as $RuCl_3$ salt, RuO_2 and carbon-supported nanocatalysts, they were dispersed and compressed onto an adhesive tape, and then installed on a holder with a window, through which X-ray impinged on the powder samples. For *ex situ* measurements of liquid samples, such as $RuCl_3$ and Ru^{n+} ethanolic solutions, they were injected into a holder through the hole at the top of the holder. And the window of the holder was then sealed by adhesive tapes and installed in a way that X-ray impinged on the liquid samples through the window. For the *in situ* XAS measurements of carbon-supported nanocatalysts, the nanocatalysts were pressed and sealed in an electrochemical cell as described elsewhere.[137] The electrolyte was 1 M $HClO_4$. A leak-free Ag/AgCl (3 M NaCl) electrode was employed as the reference electrode, but all the potentials in XAS measurements are given with respect to the reversible hydrogen electrode (RHE). All XAS measurements were conducted at the Pt L3-edge (11564 eV) or Ru K-edge (22117 eV) in the transmission mode at room temperature, with pure Ru and Pt metal foils measured in the reference mode simultaneously for the X-ray energy calibration and data alignment. Commercially available powders of $RuCl_3$ (technical, Aldrich) and RuO_2 (anhydrous, 99.9% metals basis, Alfa Aesar) were used as reference materials for Ru^{3+} and Ru^{4+}, respectively. Commercially available carbon-supported Pt nanocatalyst (45 wt%, Tanaka) was used as reference material in the *in situ* XAS measurements. The XAS data was processed and analyzed by Athena and Artemis software.[336]

2.5 Physical Characterizations

Transmission electron microscopy (TEM) images were taken with a JEOL 3000F TEM operating at 300 kV equipped with Gatan image filter system, or with a JEOL 1400 microscope operated at an accelerating voltage of 120 kV. The sample for TEM was prepared by drop casting the ethanolic suspension of nanoparticles on a carbon-coated copper grid (Lacey carbon support film, 300 mesh, Ted Pella Inc.). Scanning electron microscopy (SEM) characterization was conducted on a Hitachi S-4800 microscope. Concentration of polyhedral Au nanocrystals was quantified using the absorbance value at the surface plasmon resonance (SPR) maximum in UV-vis absorption spectra.

Scanning transmission electron microscopy (STEM) measurements were performed using the Hitachi HD2700C operated at 200 kV, equipped with a cold field emission electron source and a probe aberration corrector. The Z^n-contrast (Z is the atomic number and n is approximately 1.7)[337] STEM images were taken using a high angle annular dark-field (HAADF) detector, while elemental line scan and 2D mapping of nanoparticles were made with a high resolution Electron energy loss spectroscopy (EELS) detector (Gatan Enfina-ER). The Ru or Pd EELS signal from the EELS spectrum using a power-law background model and an integration window at the Pd $M_{4,5}$ edge.[338, 339] The energy dispersive X-ray spectroscopy (EDX) measurements carried out by the coupled Bruker SDD EDX detector was used to determine the elemental composition for individual nanoparticles. The STEM image simulations were carried out with our own computer codes running on GPU based on the multi-slice method with a frozen phonon approximation. The calculated STEM images were convoluted with a 0.15 nm FWHM Gaussian spread function for comparison with experiments.

Synchrotron X-ray diffraction (XRD) experiments were carried out on beamline X7B (λ = 0.3196 Å) of the National Synchrotron Light Source (NSLS) at Brookhaven National Laboratory. Lanthanum hexaboride (LaB_6) was used as the instrumental reference. Alternatively, X-ray powder diffraction (XRD) patterns were obtained from a D8 Advance X-ray diffractometer (Bruker, AXS) with a Bragg-Brentano geometry using Cu K_α radiation. The powder diffraction file (PDF) references were obtained by using JADE software.

The mass contents of metal nanoparticles on carbon support were determined using inductively coupled plasma mass spectrometry (ICP-MS) measurements, and energy dispersive X-ray spectroscopy (EDX) measurements equipped on a Hitachi S-4700 SEM.

2.6 Theoretical Calculations

2.6.1 Stacking Sequence of Pt Layers on Ru Substrate

The calculations were performed by using periodic DFT as implemented in the Vienna ab-initio simulation package (VASP)[340, 341]. Ion-core electron interactions were described using the projected augmented wave method (PAW)[342, 343], and the Perdew-Wang functional (GGA-PW91) within the generalized gradient approximation (GGA)[344, 345] was used to describe exchange-correlation effects. The cutoff energy of plane-wave basis set was 400 eV. The five- or six-layer slab models have four atoms in a (2 × 2) hexagonal array within each layer, and a vacuum of 12 Å between the slabs. The 9 × 9 × 1 k-points using the Monkhorst–Pack scheme[346] and first-order Methfessel–Paxton smearing[347] of 0.2 eV was employed in the integration to speed up the convergence. The conjugate gradient algorithm was used for optimization, allowing the convergence of 10^{-4} eV in total energy and 10^{-3} eV $Å^{-1}$ in Hellmann-Feynman force on each atom. All atoms were allowed to relax except those of the bottom two layers that were fixed at the *hcp* Ru bulk position with the optimized lattice constant of $a = b = 2.731$ Å and $c = 4.307$ Å. Simulated XRD spectra were obtained using Reflex module embedded in Materials Studio 5.5 by Accelrys[348] with X-ray source being a synchrotron beam ($\lambda = 0.3196$ Å) as in the experimental measurements, step size of 0.01 °, and Pseudo-Voigt broadening of 0.1 °.

2.6.2 Growth Mechanism of Pt Monolayer Shell on a Pd Nanoparticle

The calculations were performed by using plane-wave DFT as implemented in the Vienna ab-initio simulation package (VASP).[340, 341] Ion-core electron interactions were described using the projected augmented wave method (PAW)[342, 343], while Perdew-Wang functional

(GGA-PW91)[344, 345] within the generalized gradient approximation (GGA) was used to describe exchange-correlation effects. To investigate the growth mechanism of a Pd@Pt core-shell nanoparticle at affordable computational cost, we employed a hemisphere-like Pd_{174} nanoparticle model[308] based on a truncated octahedron, which contains typical {100} and {111} terraces and is nearly the half piece of a truncated octahedron Pd_{405} nanoparticle, placed in a large enough supercell to ensure no interactions between nanoparticles. Only Γ point was used for k sampling, and the cutoff energy of plane-wave basis set was 400 eV. The conjugate gradient algorithm was used in optimization, allowing the convergence of 10^{-3} eV in total energy and 0.05 eV $Å^{-1}$ in Hellmann-Feynman force on each atom. All atoms were allowed to relax except those of the bottom layer fixed along *z* direction. The binding energy (BE) of Pt was defined as

$$BE = E_{NP-n\times Pt} - E_{NP} - n \times E_{Pt} \quad (2.9)$$

where *n* was the total number of adsorbed Pt atoms, and $E_{NP-n\times Pt}$, E_{NP}, E_{Pt} was the total energy of Pt adsorbed on a Pd nanoparticle, a Pd nanoparticle, and a free Pt atom in gas phase, respectively.

2.6.3 Oxygen and Water Adsorption on Au Surfaces

The computational analyses were performed with the density functional theory under the generalized gradient approximation using the Perdew-Wang 91 (PW91) functional[36] and the projector augmented wave method[342, 343] implemented in the Vienna ab-initio simulation package (VASP)[341, 349]. We used a kinetic energy cutoff of 400 eV, and $6s^1$ and semi-core $5d^{10}$ electrons in Au were treated as the valence electrons. The lattice constant of 4.172 Å was obtained for bulk gold in PW91. The Au {111} (2 × 2 super cell), {100} (4 × 4 super cell) and {310} (4 × 3 super

cell) were modelled, respectively, by seven, seven, and nine layers of Au atoms. The O_2 on Au {111} was studied to verify the well-known results of physisorption, whereas vacuum layer of 12 Å was used to separate Au {111} slabs without fixing gold atoms. A 3 × 4 × 1 Monkhorst-Pack grid[346] was used to sample the Brillouin zone. For studies of O_2 on Au {100} and {310}, a vacuum layer of at least 17 Å was used to separate gold slabs. The bottom four layers in {100} and five layers in {310} were fixed during the structural optimization. The Brillouin zone of both systems was sampled by a 3 × 3 × 1 Monkhorst-Pack grid.

The binding energy of adsorbed O_2 is defined as

$$E_b^{O_2} = E_{complex} - E_{surface} - E_{O_2} \tag{2.10}$$

and the binding energy of co-adsorbed O_2 and H_2O is defined as

$$E_b^{O_2+nH_2O} = E_{complex} - E_{surface} - E_{O_2} - n \times E_{H_2O} \tag{2.11}$$

where $E_{complex}$, $E_{surface}$, E_{O_2} and E_{H_2O} are the total energy of the adsorbate-substrate system, the energy of the slab itself, the energy of the oxygen molecule in the gas phase, and the energy of the water molecules in the gas phase, respectively. *n* is the number of co-adsorbed H_2O molecules, and we considered cases where *n* = 1 or 2. The oxygen-oxygen bond length of 1.240 Å for oxygen molecule, and the hydrogen-oxygen bond length of 0.972 Å for water molecule were obtained in gas phase in PW91.

Chapter 3 RESULTS & DISCUSSION

3.1 Ru@M (M = Pt, Pd, Au) Core-Shell Nanocatalysts for Hydrogen Evolution and Oxidation in Acid Solution

A series of bimetallic core-shell nanocatalysts having Ru core and Pt, Pd or Au shell (Ru@M, where M = Pt, Pd, Au) was synthesized using ethanol as the solvent and reducing agent. The oxidation sate of Ru ions in ethanol during the syntheses was determined by X-ray absorption near edge structure (XANES) measurements. Catalytic activities of these bimetallic core-shell nanocatalysts for the hydrogen evolution and oxidation reactions (HER-HOR) have been investigated in acid solution.

3.1.1 Carbon-Supported Ru Nanoparticles

3.1.1.1 Synthesis Mechanism Using Ethanol as the Reducing Agent

We used the solvent ethanol as the reducing agent, without any other organic agents or metal templates, to fabricate Ru nanoparticles, and to coat them with metal atomic layers of Pt, Pd or Au (Section 2.1). The processes of metal deposition were manipulated via fine-tuning the reducing power of ethanol. In reacting with metal ions, ethanol itself is oxidized: First to acetaldehyde by removing two H atoms and then to acetic acid by adding one O atom, giving up two electrons at each step. Figure 3.1 shows the pH-dependent redox potentials for these two reactions. The more negative the value is, the higher is the reducing power. Therefore, the intermediate, acetaldehyde, is a less stable, stronger reductant than ethanol. This fact leads to a considerable activation barrier for the first step of ethanol oxidation; thus, noble-metal precursors

that have more positive reduction potentials than ethanol can be dissolved and uniformly mixed with the reductant without being reduced at ambient temperature. Adding water or an alkaline solution that affords a source of oxygen enables the second step, whilst increasing the pH facilitates both reactions. Thus, we can use temperature, H_2O, and pH as the tuning knobs to control the synthesis process. Compared with other synthesis methods, we found that simplicity leads to high reproducibility and scalability. The results, virtually 100% metal yield with ethanol as the sole solvent and reductant, clearly show the commercial value of the method.

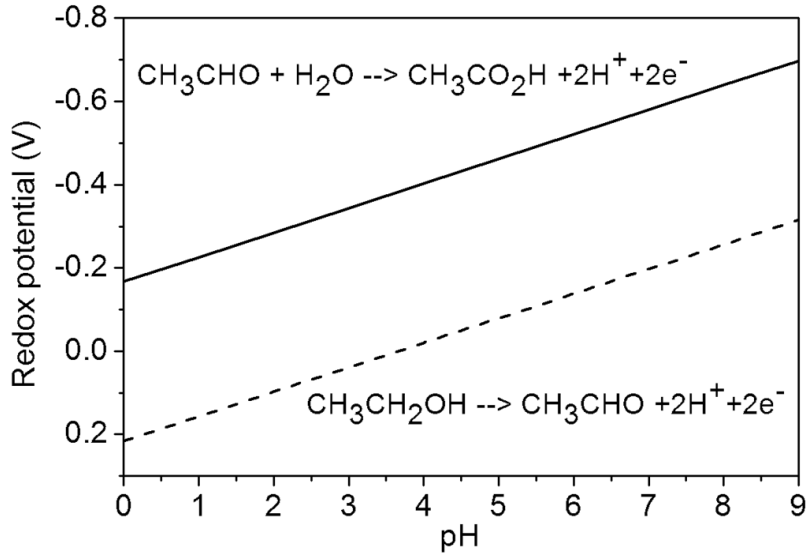

Figure 3.1 Standard redox potentials at 23 °C as a function of pH. The values at pH 7 are −0.197 V for ethanol/acetaldehyde and −0.58 V for acetaldehyde/acetate[350].

In synthesizing Ru nanoparticles, we first refluxed ethanol solutions containing $RuCl_3$ metal precursors (pH ~ 1) in an oil bath at 110 °C for 1 h. The color of the solution changed from brown (Ru^{3+}) to olive (Ru^{n+}) without the formation of Ru metal particles, while ethanol oxidation was limited to the first step due to the lack of oxygen source. A fast nucleation process then was

initiated by adding an aqueous alkaline solution to enable oxidation to acetic acid, resulting in the formation of Ru nanoparticles. The molar amount of OH^- is three times that of Ru^{3+} ions, which equals to the amount protons generated by the reaction at one proton per electron transfer. This condition eliminates the formation of any Ru hydroxide or oxide. The carbon-supported Ru nanoparticles were synthesized by adding either carbon powder (C) or carbon nanotubes (CNTs) before adding an aqueous alkaline solution. This synthetic route resulted in a uniform dispersion and strong bonding between the Ru and carbon supports. For fabricating atomically ordered core-shell nanoparticles, we further annealed the supported Ru nanoparticles in hydrogen at 350 ~ 500 °C to minimize lattice defects and the number of particles with diameters less than 2 nm.

3.1.1.2 Oxidation State of Ru Ions in Ethanol

During the synthesis of Ru nanoparticles, as shown in Figure 3.2a, firstly, the $RuCl_3$ salt was dissolved in anhydrous ethanol, forming brown $RuCl_3$ ethanolic solution. After refluxing at 110 ℃ for 1 h, the solution color turned from brown to olive green indicating the formation of Ru^{n+} ions. Then carbon powder and alkaline solution were added to promote the further reduction of Ru^{n+} ions, and to facilitate the growth of Ru nanoparticles on carbon support. From experimental observation, the Ru^{n+} ethanolic solution with an olive green color (denoted as olive Ru^{n+}) is known as an important stage to reach toward successful synthesis. In order to estimate the oxidation state of these olive Ru^{n+} ions, we carried out the X-ray absorption spectroscopy (XAS) measurements.

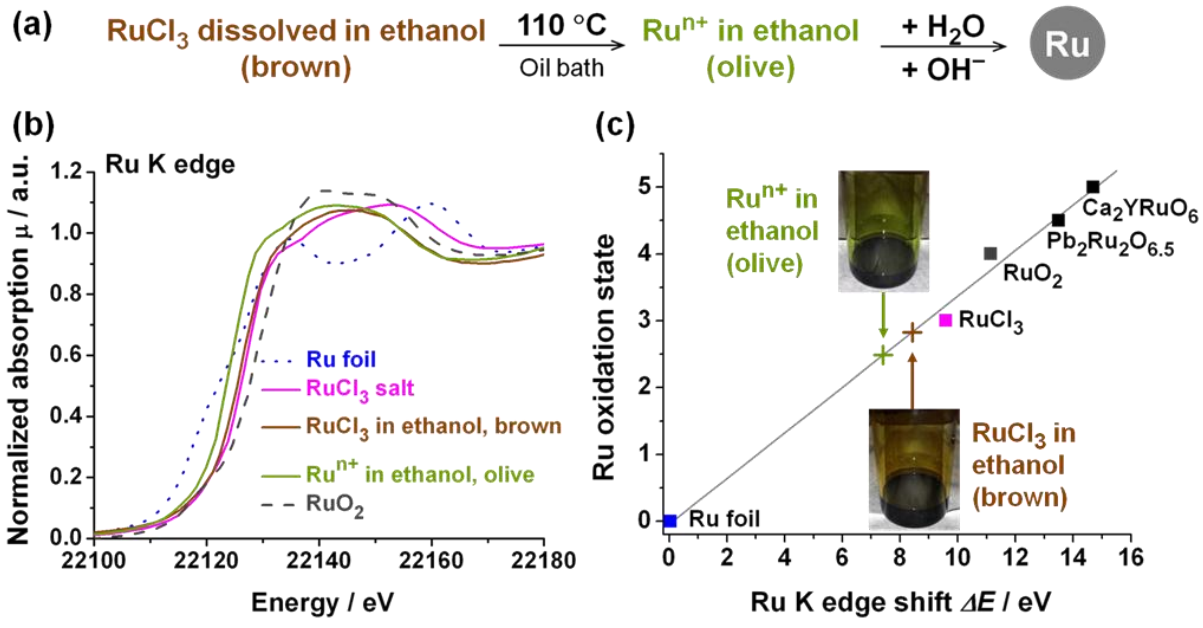

(d)

	Ru oxidation state
$RuCl_3$ dissolved in ethanol (brown)	2.8
Ru^{n+} in ethanol (olive)	2.5

Figure 3.2 Synthesis of Ru nanoparticles using the solvent ethanol as reducing agent. (a) Schematic illustration of the synthetic procedure of Ru nanoparticles. (b) XANES spectra at the Ru K-edge of $RuCl_3$ dissolved in ethanol with a brown color, Ru^{n+} ions in ethanol after heating with an olive color, as well as of reference materials for Ru foil, $RuCl_3$ salt and RuO_2. (c) The oxidation state of Ru in reference materials as a function of the energy shift ΔE of Ru K-edge, together with a linear fit (grey line) of reference materials including Ru foil, $RuCl_3$ salt and RuO_2 (data taken from (b)), $Pb_2Ru_2O_{6.5}$ and Ca_2YRuO_6 (data taken from reference [351]), used to estimate the Ru oxidation states in the brown $RuCl_3$ ethanolic solution (brown plus sign) and in the olive Ru^{n+} ethanolic solution (olive plus sign). Inset: pictures of the brown $RuCl_3$ and olive Ru^{n+} ethanolic solutions, respectively. (d) The Ru oxidation states in brown $RuCl_3$ and olive Ru^{n+} ethanolic solutions calculated from the linear fit in (c).

Figure 3.2b shows the Ru K-edge X-ray absorption near edge structure (XANES) spectra

of the brown $RuCl_3$ ethanolic solution and the olive Ru^{n+} ethanolic solution, along with the spectra of reference materials Ru^0 (Ru foil), Ru^{3+} ($RuCl_3$ salt) and Ru^{4+} (RuO_2). The K-edge of the brown $RuCl_3$ ethanolic solution is close to that of $RuCl_3$ salt, suggesting the average Ru oxidation state in the brown solution is close to 3+; While the K-edge of the olive Ru^{n+} ethanolic solution is positioned between those of Ru foil and $RuCl_3$ salt, suggesting that the average oxidation state of Ru in the olive solution is between 0 and 3+.

Here we employed an empirical method[351, 352] to determine the average oxidation state of Ru in these two ethanolic solutions, as shown in Figure 3.2c. The absorption edge energy of samples is determined by the edge inflection point, which is defined as the energy maximum of 1st derivative of the XANES spectrum, and the Ru K-edge shift ΔE is calculated with respect to 22117 eV of metallic Ru foil. Plotting the Ru oxidation state as a function of Ru K-edge shift allows for the linear fit to the data points. Two additional data points[351] of $Ru^{4.5+}$ ($Pb_2Ru_2O_{6.5}$) and Ru^{5+} (Ca_2YRuO_6) are added for more precise linear fit. Using the linear dependence of the oxidation state on the Ru K-edge shift, we calculated the average oxidation state of Ru in the ethanolic solutions (Figure 3.2d). The average Ru oxidation state in the brown $RuCl_3$ ethanolic solution is 2.8+, suggesting that the oxidation state of Ru in $RuCl_3$ salt decreases mildly after dissolving in ethanol. In contrast, the average oxidation state of Ru in the olive Ru^{n+} ethanolic solution is 2.5+, suggesting that the some of the Ru^{3+} ions are reduced by ethanol after heating the solution. These olive Ru^{n+} ions (n = 2.5) can serve as an advanced precursor, compared to the pristine brown $RuCl_3$, toward the reduction to Ru nanoparticles. The XANES results of Ru ethanolic solutions confirm the reduction of $RuCl_3$ by ethanol, the solvent and the reducing agent, during the synthesis of carbon-supported Ru nanoparticles.

3.1.2 Characterization of Ru@M Nanoparticles

Core-shell structured nanocatalysts can be synthesized using the carbon-supported Ru nanoparticles as the core particles. The shell can be coated on top of Ru cores employing the solvent ethanol as the reducing agent, and using H_2PtCl_6, Na_2PdCl_4 or $HAuCl_4$ as the metal precursor for the shell of Pt, Pd or Au, respectively. Different reduction temperatures were applied for different shell metals, in a way that the reduction temperatures were low enough to avoid the self-nucleation of the shell metal, and also were high enough to provide sufficient reducing power of ethanol toward the complete reduction of shell metal ions. These bimetallic core-shell nanoparticles having Ru core and Pt, Pd or Au shell (Ru@M, where M = Pt, Pd, Au), as illustrated in Figure 3.3a, are uniformly dispersed on carbon support, as shown in the transmission electron microscopy (TEM) images in Figure 3.3b. The powder X-ray diffraction (XRD) patterns (Figure 3.3c) exhibit both the hexagonal close-packed (*hcp*, space group *P63/mmc*) peaks from the Ru core, and the face-centered cubic (*fcc*, space group *Fm-3m*) peaks from the shell metal of Pt, Pd or Au, indicating the formation of the core-shell structure.

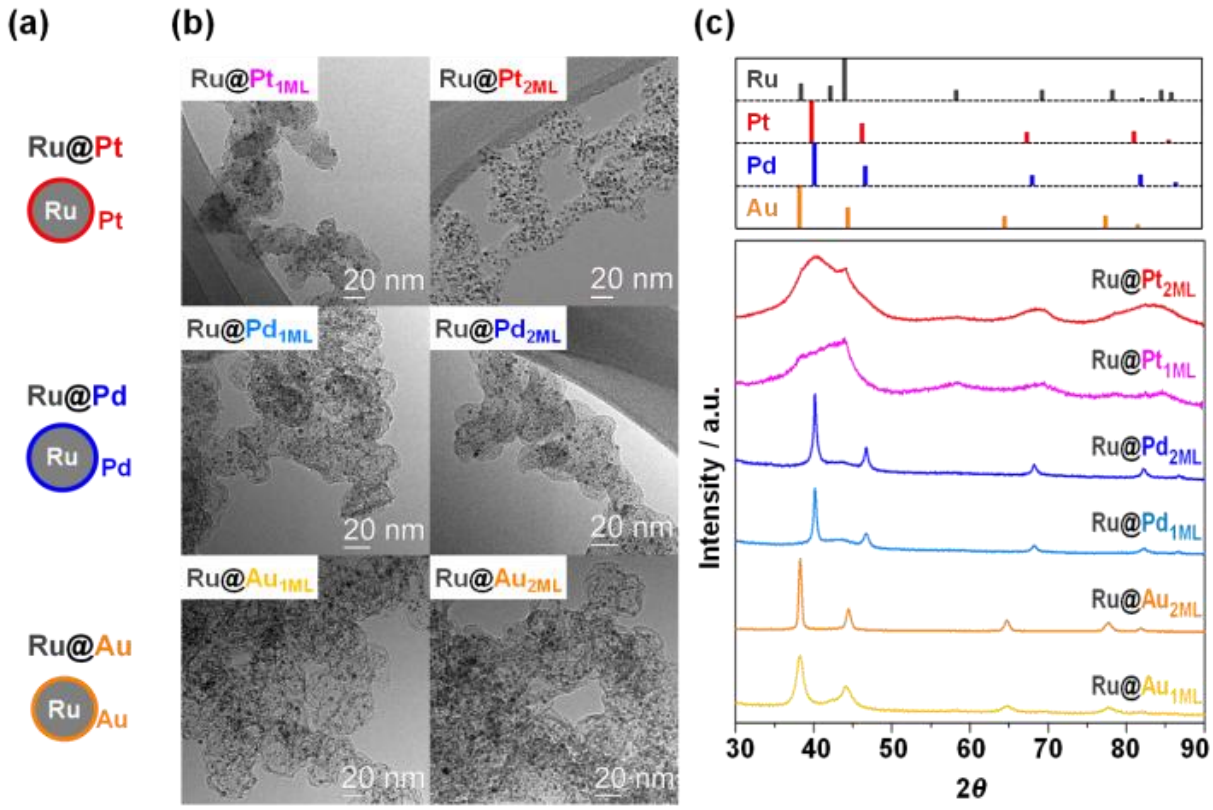

Figure 3.3 Structural characterization of carbon-supported Ru@M (M = Pt, Pd, Au) nanocatalysts. (a) Schematic illustration of the core-shell architectures. (b) TEM images and (c, bottom) Powder X-ray diffractograms of Ru@Pt, Ru@Pd and Ru@Au nanocatalysts with the shell thickness of one-monolayer (1ML) or two-monolayer (2ML). (c, top) Reference diffraction lines for Ru, Pt, Pd and Au.

3.1.3 HER-HOR Performance of Ru@M Nanocatalysts

It is known that the HER-HOR kinetics on noble metals, especially on Pt, are too fast to be accurately measured using the conventional rotating disk electrode (RDE) configuration, due to its intrinsic limitation of mass transport.[292, 327, 328, 353, 354] We have recently developed a hanging-strip method using the gas diffusion electrode (GDE) as the working electrode.[301] The

detailed experimental method is described in Section 2.3.2. Here we report the HER-HOR activities measured using the hanging strips of GDEs. We evaluated the electrochemical performance for the HER-HOR of three kinds of bimetallic core-shell nanocatalysts, including Ru@Pt, Ru@Pd and Ru@Au, in order to correlate the chemical composition to the electrocatalytic activity. Also we tested each kind of nanocatalyst with the one-monolayer (1ML) or two-monolayer (2ML) shell thickness, in order to take account of the effect of shell thickness.

First, we compared the electrocatalytic activities of different core-shell nanocatalysts with the shell metal loading around 20 ug cm^{-2} (Figure 3.4). The HER-HOR polarization curves in Figure 3.4a indicate that the Ru@Pt nanocatalysts produce much larger current density than the Ru@Pd and Ru@Au nanocatalysts. Among all the nanocatalysts, $Ru@Pt_{2ML}$ exhibits the highest activity with the current density of 2.5 mA cm^{-2} at the ultralow overpotential of 0.1 mV. Given that the larger current density at the same potential denotes the higher catalytic activity, the activity trend for these bimetallic core-shell nanocatalysts is Ru@Pt > Ru@Pd > Ru@Au, as observed from polarization curves (Figure 3.4a). From impedance spectra (Figure 3.4b), the same similar trend of Ru@Pt > Ru@Pd > Ru@Au can also been read, given that the smaller semi-circle radius in the $-Z_i$ direction ($-Z_i^{\max}$) corresponds to the higher activity. The perfect semicircle shape was not observed for impedance spectra, perhaps due to the uneven distribution of electric field and the slow kinetics of Ru@Au.

The electrochemical results are summarized in Figure 3.4c. Here we use the charge transfer resistance (*CTR*) measured at 0 V (vs. RHE) as the parameter to quantitatively evaluate the HER-HOR activity. The *CTR* can be considered as the reciprocal of slope of the *iR*-corrected polarization curves, and the lower *CTR* value represents the higher HER-HOR activity. As

shown in Figure 3.4c, with almost similar shell metal loading of 20 ug cm^{-2}, $Ru@Pt_{2ML}$ exhibits the highest activity with the lowest *CTR* of 0.04 Ω cm^2, which can be understood in the way that an overpotential of 0.4 mV is required to drive the current density of 10 mA cm^{-2}. And $Ru@Pt_{1ML}$ displays a slightly lower activity with the 0.06 Ω cm^2 *CTR*. $Ru@Pd_{1ML}$ and $Ru@Pd_{2ML}$ show *CTR*s around 8 Ω cm^2, corresponding to an overpotential of 8 mV in order to achieve 1 mA cm^{-2}, which are about 2 orders of magnitude lower than the activities of Ru@Pt. $Ru@Au_{1ML}$ and $Ru@Au_{2ML}$ demonstrate the activity with 3 and 3.6 orders of magnitude, respectively, lower than those of Ru@Pt.

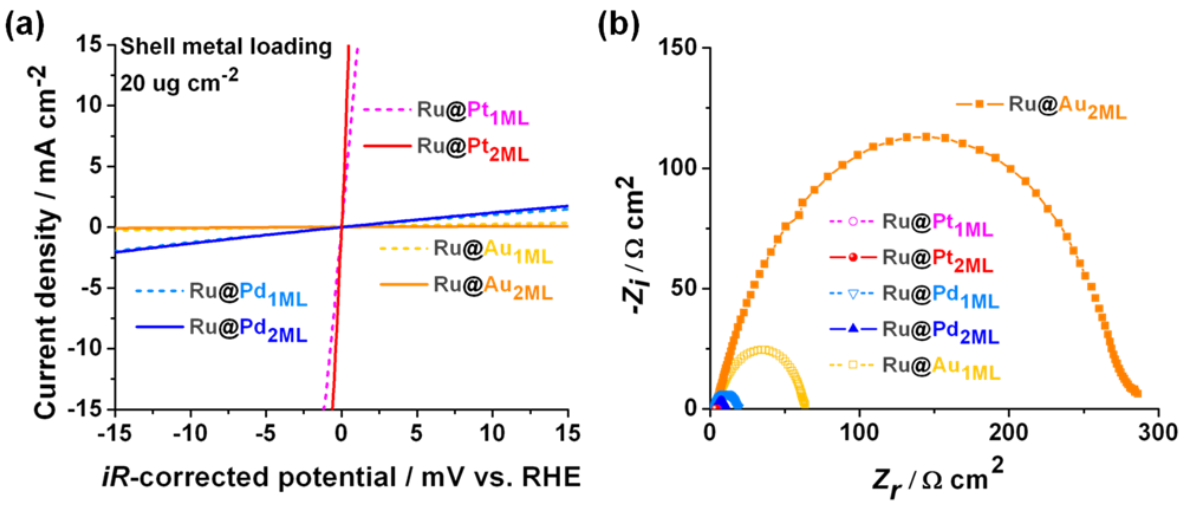

(c)	Shell metal loading/ug cm^{-2}	Ru loading/ ug cm^{-2}	*CTR*/Ω cm^2	*HFR*/Ω cm^2	$-Z_i^{max}$/Ω cm^2
Ru@Pt$_{1ML}$	20.5	21.2	0.06	4.70	0.02
Ru@Pt$_{2ML}$	19.6	10.1	0.04	3.83	0.01
Ru@Pd$_{1ML}$	19.3	36.7	8.82	2.92	6.21
Ru@Pd$_{2ML}$	19.8	18.8	7.54	3.63	3.07
Ru@Au$_{1ML}$	19.8	20.3	47.04	3.78	24.48
Ru@Au$_{2ML}$	20.0	10.3	175.14	3.02	112.90

Figure 3.4 HER-HOR activities of Ru@Pt, Ru@Pd and Ru@Au nanocatalysts, with one-monolayer (1ML) or two-monolayer (2ML) shell thickness, measured using the hanging-strip GDE method, in H_2-saturated 1 M $HClO_4$ at room temperature. (a) HER-HOR polarization curves measured at a sweep rate of 20 mV s^{-1}. (b) Nyquist plots showing electrochemical impedance spectra measured at 0 V (vs. RHE). (c) The summarized electrochemical results obtained from (a-b).

The representative polarization curves in the long potential range for three kinds of bimetallic core-shell nanocatalysts are presented in Figure 3.5. Ru@Au$_{1ML}$ shows the lower

activity toward both the HER and the HOR, compared with Ru@Pd_{1ML} (Figure 3.5a). The current densities of their HER-HOR polarization curves are within ±100 mA cm^{-2} at −200 ~ 600 mV. In stark contrast, Ru@Pt_{2ML} demonstrates the much larger current density of −400 ~ 1600 mA cm^{-2} at −20 ~ 180 mV (Figure 3.5b).

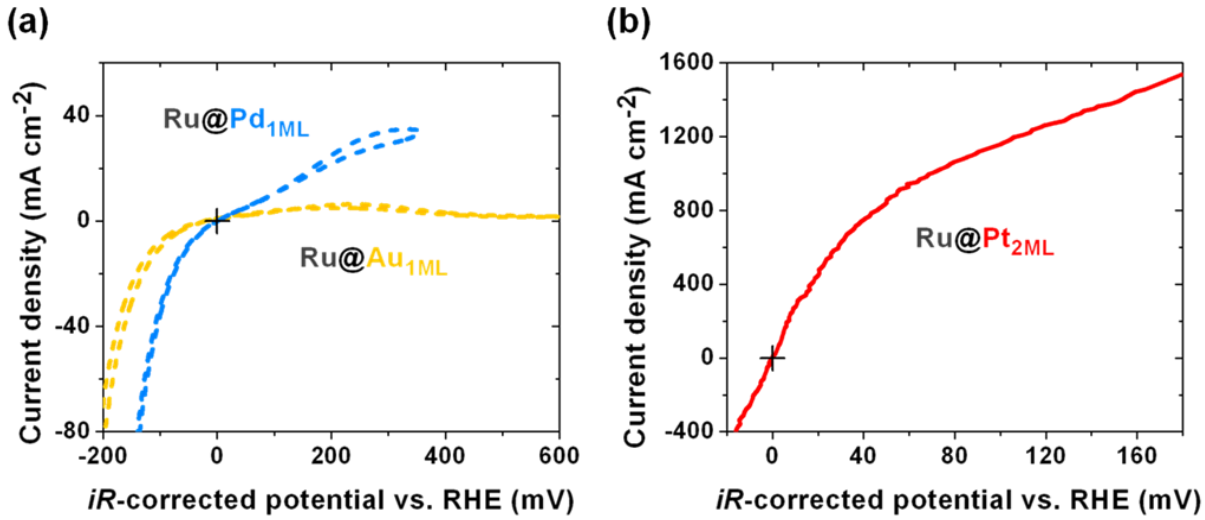

Figure 3.5 Representative HER-HOR polarization curves in the long potential range measured at 20 mV s^{-1} for (a) Ru@Pd and Ru@Au, and for (b) Ru@Pt. Shell metal loading was (a) 18.9 ug cm^{-2} Au for Ru@Au_{1ML}, 14.0 ug cm^{-2} Pd for Ru@Pd_{1ML}, and (b) 9.0 ug cm^{-2} Pt for Ru@Pt_{2ML}, respectively. The black plus sign marks the position of 0 mA cm^{-2} at 0 mV.

Next, we measured the HER-HOR activity, represented by *CTR*, for three kinds of bimetallic core-shell nanocatalysts with the 1ML or 2ML shell thickness with different shell metal loadings. Figure 3.6 shows the *CTR* as a function of the shell metal loading. The results in Figure 3.6 depict the general activity trend of Ru@Pt > Ru@Pd > Ru@Au, though the effect of shell thickness is not the same for nanocatalysts with different shell metals. For Ru@Pt nanocatalysts, Ru@Pt_{2ML} is more active, with lower *CTR*s, than Ru@Pt_{1ML}. Because Pt is known

as the most active metal for the HER-HOR, and the geometric and electronic effects from the underlying Ru substrate is excessive for $Ru@Pt_{1ML}$,[302] but is much released for $Ru@Pt_{2ML}$. For Ru@Pd nanocatalysts, $Ru@Pd_{1ML}$ and $Ru@Pd_{2ML}$ show very close activities, possibly due to the hydrogen absorption property of Pd which can overcome the geometric and electronic effects brought by the Ru substrate. For Ru@Au, $Ru@Au_{1ML}$ is more active than $Ru@Au_{2ML}$, which can be explained by the very low HER-HOR activity of Au, and the very weak binding of reactants or reaction intermediates on Au.

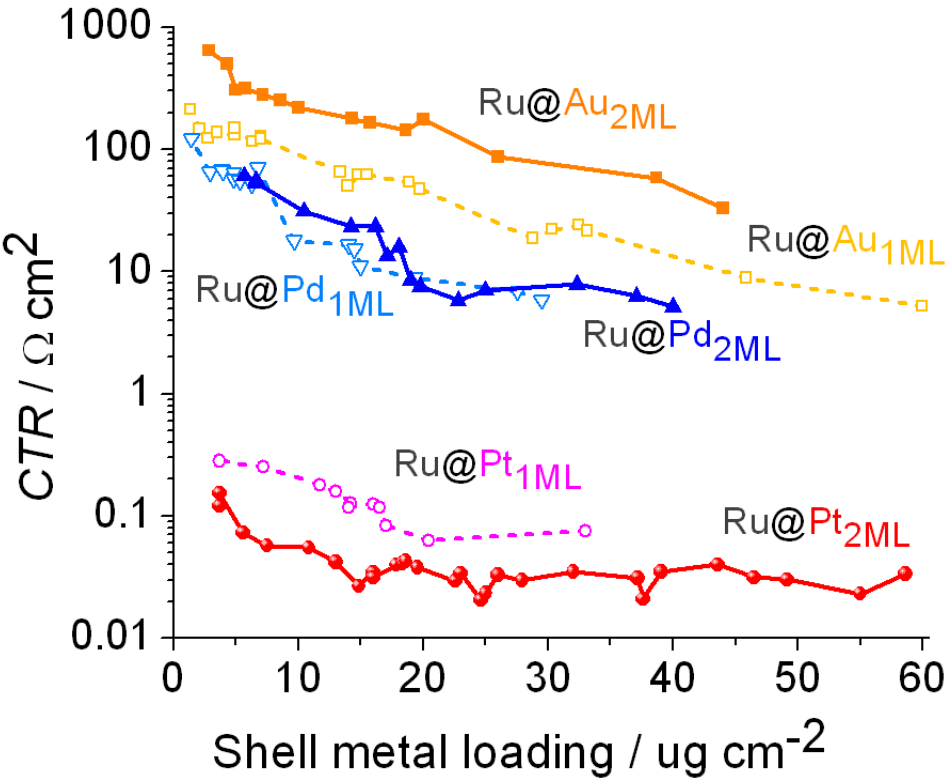

Figure 3.6 Charge transfer resistance (*CTR*) as a function of shell metal loading for Ru@Pt, Ru@Pd and Ru@Au nanocatalysts with 1ML or 2ML shell thickness, measured using the hanging-strip GDE method.

The results in Figure 3.6 clearly demonstrate the tremendously high HER-HOR activities of Ru@Pt nanocatalysts, especially $Ru@Pt_{2ML}$, which are 2~3.7 orders of magnitude higher than those of Ru@Pd and Ru@Au nanocatalysts. For $Ru@Pt_{2ML}$, the *CTR* as low as 0.04 Ω cm^2, corresponding to the required overpotential as low as 0.04 mV in order to drive the current density of 1 mA cm^{-2}, can be achieved with the minimum Pt loading of 20 ug cm^{-2}. Hence Ru@Pt nanocatalysts are identified as the most active HER-HOR electrocatalysts in acid solution, among the investigated bimetallic core-shell nanocatalysts.

3.1.4 Summary

A series of carbon-supported bimetallic core-shell nanocatalysts having Ru core and Pt, Pd or Au shell (Ru@M, where M = Pt, Pd, Au) was synthesized using ethanol as the solvent and the reducing agent. The XANES measurements were carried out to study the oxidation state of Ru during the synthesis, and the results of Ru ethanolic solutions confirm the reduction of $RuCl_3$ by ethanol, which is both the solvent and the reducing agent, toward the fabrication of Ru nanoparticles supported on carbon. The HER-HOR activities of these bimetallic core-shell nanocatalysts have been studied in acid solution as a function of chemical composition, shell thickness and loading. The Ru@Pt nanocatalysts are identified as the most active HER-HOR electrocatalysts in acid solution, among the investigated bimetallic core-shell nanocatalysts.

3.2 Ordered Ru@Pt Nanoparticles as HER-HOR Catalysts

In Section 3.1, we have successfully identified the carbon-supported Ru@Pt core-shell nanocatalysts as the most active HER-HOR electrocatalysts in acid solution, among the investigated series of bimetallic Ru@M (M = Pt, Pd, Au) core-shell nanocatalysts. In this section, we fine tuned the Ru to Pt atomic ratio toward the optimal Pt shell thickness. With the in-depth characterizations and analyses of the *hcp* to *fcc* structural phase transition at the Ru-Pt core-shell interface, we found that defect-induced partial alloying is the cause of Ru disordering, and so succeeded in fabricating single crystalline Ru@Pt nanoparticles with well-defined, energetically favorable *hcp* to *fcc* structural transition at the core-shell interface.

The significance of this achievement of structural perfection was demonstrated by the superior durability and excellent CO tolerance of the bilayer Ru@Pt nanocatalysts for the HOR in PEM fuel cells at ultra-low catalyst loadings (25 μg cm^{-2} Pt, 10 μg cm^{-2} Ru), which resolves the dilemma in using a dissolution-prone metal, ruthenium, for alleviating the deactivating effect of CO, opening the door for commercialization of low-temperature fuel cells that can use inexpensive reformates, H_2 with CO impurity, as the fuel. In addition, using the ordered bilayer Ru@Pt catalyst with total metal loadings <50 μg cm^{-2} for the HER in PEM water electrolyzers, we achieved uncompromised activity and durability compared to the baseline established with 3 mg cm^{-2} Pt black.

3.2.1 Well-Defined Ru@Pt Nanoparticles

In order to coat atomic layers of Pt on Ru nanoparticles, we used the H_2PtCl_6 ethanolic solution, which is stable at room temperature, as the precursor. In the absence of Ru

nanoparticles, Pt deposition on carbon did not occur below 100 °C. For the Ru@Pt nanoparticles fabricated with Pt coating temperature ≤ 80 °C, we verified the absence of Pt-only particles using the Ru:Pt atomic ratio of individual particles, determined by energy dispersive X-ray (EDX) spectroscopy equipped on the scanning transmission electron microscope. The optimal coating for seed-mediated Pt deposition on Ru occurred at 80 °C. This temperature is sufficiently low to avoid Pt nucleation, yet high enough to dominate Pt reduction via the oxidation of ethanol rather than of Ru. In an aqueous solution without reducing agents[355], Pt ions can be deposited through galvanic replacement of Ru, a metal that is less noble than Pt; this is an undesirable reaction as it could cause loss of Ru or result in Ru-Pt mixed shells[356]. At 80 °C, the $[PtCl_6]^{2-}$ ions usually had become colorless in 2~3 hours; we note that to ensure the completion of Pt deposition, an aqueous alkaline solution may be added up to twice molar amount of Pt precursors. After filtration, we confirmed, by energy-dispersive X-ray fluorescence measurements, that there were negligible amount of Ru and Pt ions left in the solutions.

The different crystalline structures of Ru(*hcp*) and Pt(*fcc*) allows us to distinguish whether the Ru-Pt core-shell boundary is well defined. Their distinctive XRD features were used in previous studies to distinguish the Ru@Pt core-shell nanoparticles, synthesized by using a sequential polyol process at 200 °C, from the RuPt alloy nanoparticles[304, 305]. We obtained a similar XRD profile for the Ru@Pt sample prepared with the as-synthesized Ru cores with 1:1 Ru:Pt atomic ratio (Figure 3.7a, orange curve). It differs from that for pure Pt nanoparticles (Figure 3.7a, red curve), by the notable intensity between the *fcc* Pt (111) and (200) peaks, originating from the *hcp* Ru (002) and (101) diffractions. Because of the relative weakness of the *hcp* diffractions, the Ru cores were considered to be highly disordered[305].

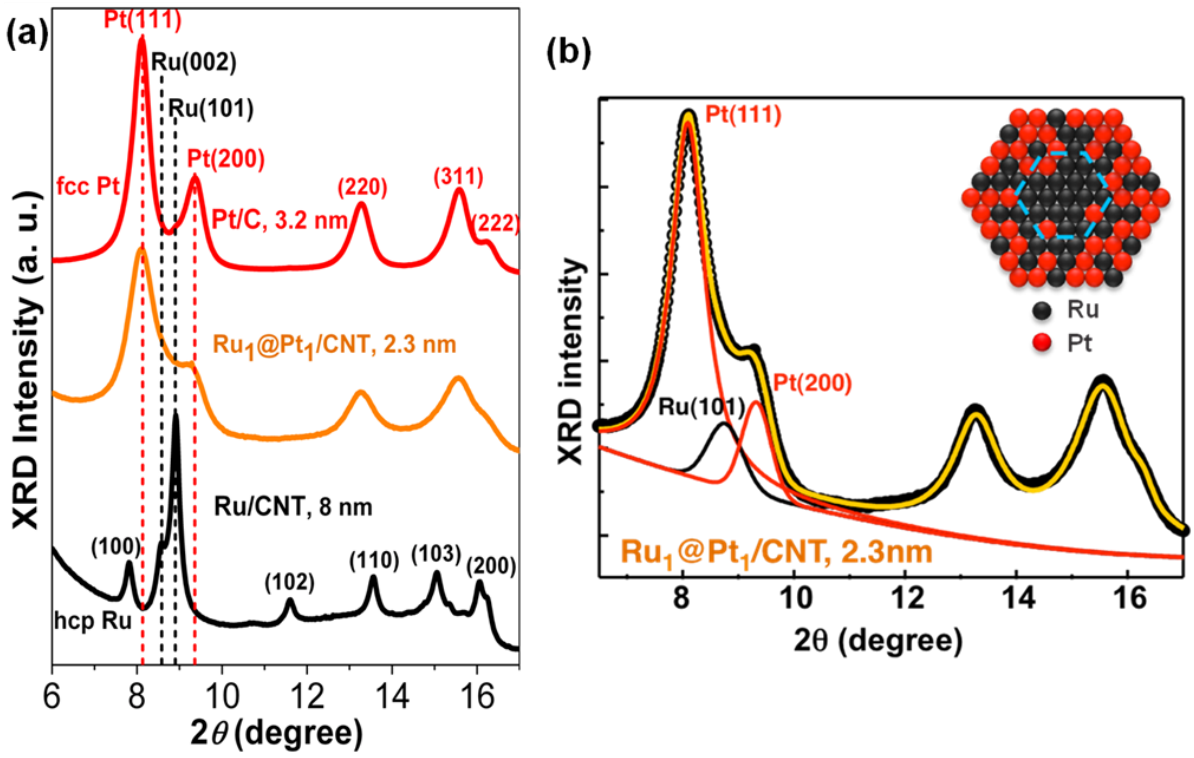

Figure 3.7 (a) Synchrotron XRD (λ = 0.3196 Å) diffractograms of bimetallic $Ru_1@Pt_1$ nanoparticles made with as-synthesized Ru cores supported on CNT (orange), in comparison with that of monometallic CNT-supported Ru (black) and carbon-supported Pt (red) nanoparticles. (b) XRD refinement (yellow line) to the *fcc*-dominant intensity profile (black circles, data taken from the orange curve in (a)) for the bimetallic $Ru_1@Pt_1$ nanoparticles made with as-synthesized Ru cores, based on Pseudo-Voigt function (the combination function of Gaussian and Lorentz functions) using the Trust-Region method. The black curve shows the shifted *hcp*-Ru(101) peak, and the red curves show the *fcc*-Pt(111) and *fcc*-Pt(200) peaks. Inset shows a schematic model of a partially alloyed particle that has a Ru-rich *hcp* core, marked by the blue dashed line, and a Pt-rich *fcc* shell.

We attribute the weak Ru diffraction to the formation of a Pt-rich shell on a Ru-rich core due to Ru-Pt partial alloying at the interface. Figure 3.7b shows the refinement of the XRD

profile for the Ru@Pt sample prepared with the as-synthesized Ru cores (Figure 3.7a, orange curve), wherein the strongest (101) peak for *hcp*-Ru is shifted to a position corresponding to a 1.3% lattice expansion from the bulk Ru lattice spacing of 2.056 to 2.082 Å. Since the mismatch in spacing between hexagonal layers for Pt to Ru is 5.8%, the ratio 1.3/5.8 = 0.22, yields an estimated Pt atomic content in a RuPt alloy based on Vegard's law[357]. This value is close to the Pt content in a Ru_5Pt alloy (1/6 = 0.17). For the 1.5 nm RuPt alloy nanoparticles, the dominant lattice structures were *hcp* and *fcc*, respectively, for a Pt content $\leq$ 17% (Ru_5Pt) and $\geq$ 50% (RuPt), with twined *fcc* found in between, e.g., 25% (Ru_3Pt)[358]. Thus, the observed expansion in the *hcp* structure likely reflects the maximum lattice expansion beyond which the *hcp to fcc* structural transition occurs. As illustrated in the inset of Figure 3.7b, partially alloyed nanoparticles with an inwardly decreasing Pt content (red dots) can account for the observed XRD feature: Weak and shifted *hcp* Ru diffractions from a small Ru-rich core (Pt $\leq$ 22%), and intense *fcc* diffractions from a Pt-rich shell that is thicker than the nominal value calculated for a well-defined core-shell structure.

Guided by the understanding that partial alloying occurred at the core-shell interface, we annealed the Ru nanoparticles before coating Pt to reduce lattice defects in the Ru cores, knowing that defect-mediated diffusion has a low energy barrier, and thus, promotes interlayer diffusion[359]. Remarkable improvements were observed with annealed Ru cores. We denote the carbon-supported Ru nanoparticles as Ru/C or Ru/CNT. With the Ru@Pt/CNT samples (1:1 atomic ratio, 4.5 nm average diameter), we obtained the *hcp*-dominant XRD profile (the blue curve in Figure 3.8), clearly indicating that the Ru cores were highly ordered. Higher dispersion and smaller particles were found on C than on CNT supports. The average sizes of nanoparticles

were obtained by TEM measurements (Figure 3.9).

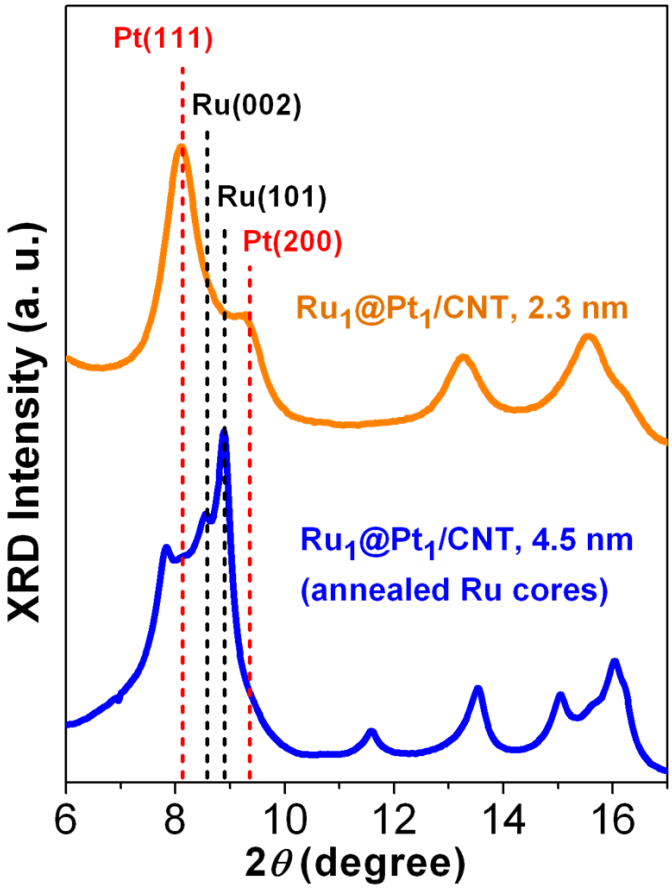

Figure 3.8 Synchrotron XRD diffractograms of CNT-supported bimetallic $Ru_1@Pt_1$ nanoparticles made with as-synthesized Ru cores (orange), and with annealed Ru cores (blue). λ = 0.3196 Å.

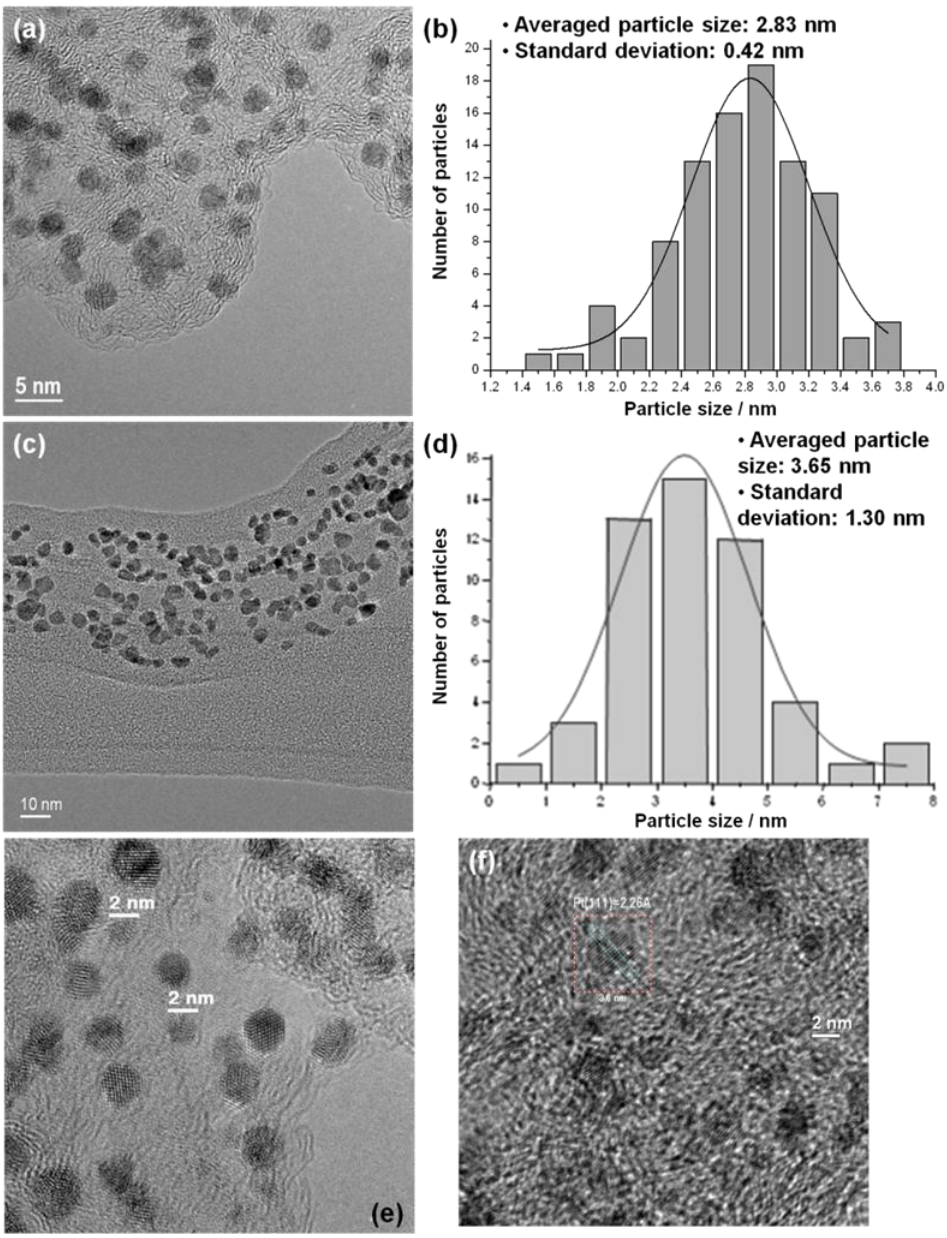

Figure 3.9 TEM images and particle size distribution of Ru@Pt nanoparticles. (a, c, e-f) TEM images of the $Ru_1@Pt_1$ core-shell nanoparticles made with (a, c, e) annealed Ru cores, and (f) with as-synthesized Ru cores. Carbon powder (a, e, f) and CNT (c) was used as the support for Ru@Pt nanoparticles. (b, d) Particle size distribution for carbon powder supported $Ru_1@Pt_1$ core-shell nanoparticles (a, b) and for CNT supported $Ru_1@Pt_1$ core-shell nanoparticles (c, d). The average particle size varies with annealing temperature and carbon supports.

Next, we verified the core-shell elemental distribution of individual particles at the atomic scale using various (scanning) transmission electron microscopy ((S)TEM) techniques including a high-angle annular dark field (HAADF)-STEM and electron energy loss spectroscopy (EELS). Figure 3.10a shows the intensity profiles in a line scan across a sphere-like Ru@Pt nanoparticle (Figure 3.10b), wherein the EELS signal for Ru indicates a 4.2 nm Ru core inside a 5.7 nm nanoparticle, as measured by the HAADF. The Pt shell is about three-monolayer thick, as is expected for 1:1 Ru@Pt nanoparticles with an average diameter of 5.5 nm. For another particle (Figure 3.10c), the HAADF-EELS 2D mapping (Figure 3.10d) shows a rather uniform Pt shell around the Ru core.

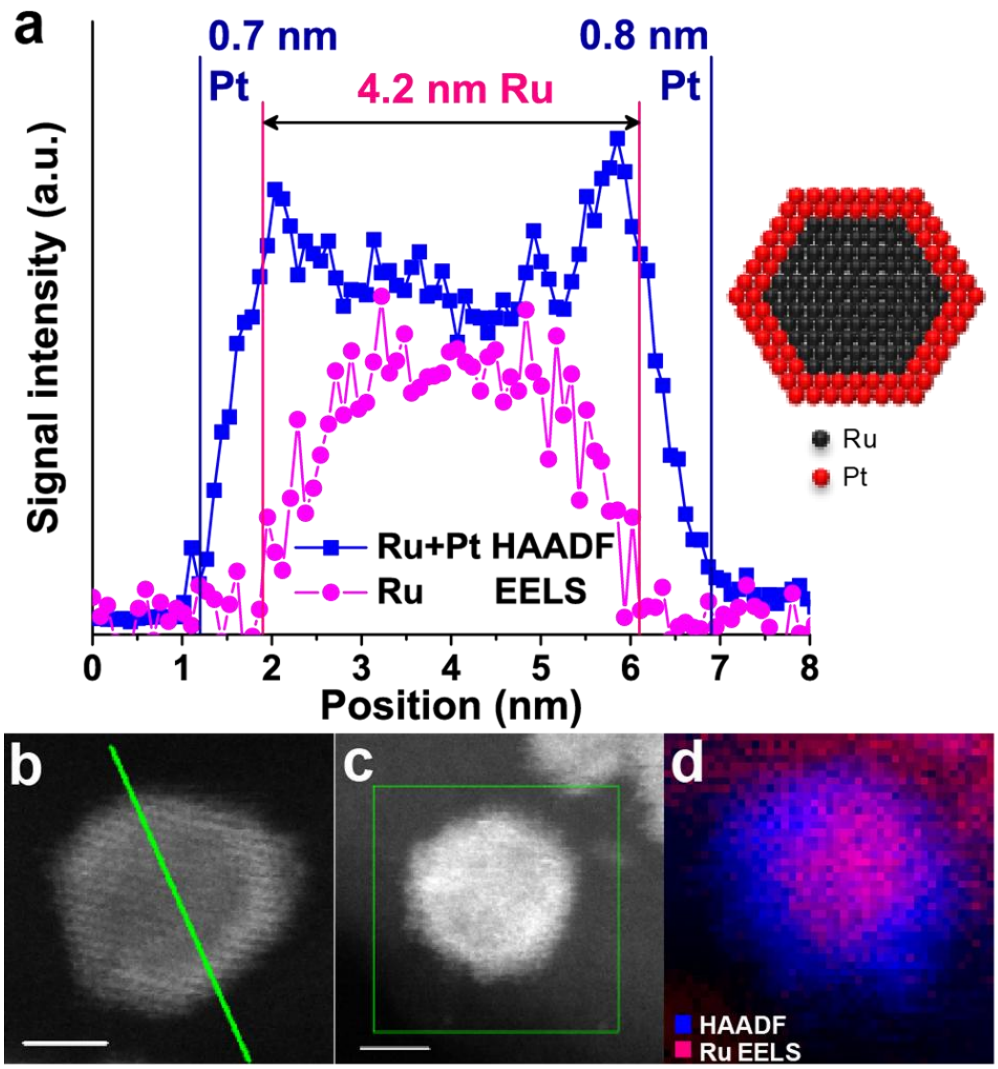

Figure 3.10 Well-defined Ru@Pt core-shell nanoparticles. (a) Line scan profiles of signals measured by HAADF-STEM and Ru EELS for an ordered Ru@Pt nanoparticle. The schematic model shows a well-defined core-shell particle. (b) STEM image for the particle measured by line scan in (a). Scale bar, 2 nm. (c) STEM image for the particle measured by 2D mapping in (d). Scale bar, 2 nm. (d) 2D mapping of an ordered Ru@Pt nanoparticle, which is attached on carbon at the top-right corner.

3.2.2 Varied Pt Shell Thickness

By adjusting the amount of the Pt precursor and average size of the Ru particles, we synthesized and structurally characterized the Ru@Pt samples with Pt shell thicknesses ranging from 1.0 to 2.3 atomic layers. The average Pt shell thicknesses were calculated from the particle size obtained by TEM measurements (for example, Figure 3.9) and Ru:Pt atomic ratio assuming a well-defined core-shell structure. For four Ru@Pt/C samples whose Pt:Ru atomic ratios were increased from 0.5 to 1.33, we show in Figure 3.11 the rise in intensities at the Pt peak positions, while the Ru diffraction intensities were normalized to that of the Ru core before the Pt coating (black curves). Even with Pt:Ru $\geq$ 1, the intensity at Ru(101) position is higher than at the Pt(200) position for particles less than 4 nm in diameter, which never was the case for previously synthesized Ru@Pt[304, 305, 355, 356]. These distinct features support our view that an atomically sharp core-shell boundary can be achieved for *hcp* Ru cores with *fcc* Pt shells, despite their different lattice structures.

Figure 3.12 shows *ex situ* XAS measurements of carbon-supported Ru@Pt nanoparticles with different Pt:Ru atomic ratios, in comparison with the reference materials of the metal and oxide forms of Pt and Ru, including Pt or Ru foil, PtO_2 or RuO_2. The EXAFS results at the Pt L3-edge (Figure 3.12c) demonstrate that the Pt-Pt contribution increases, while the Pt-O contribution decreases, with the increased Pt:Ru atomic ratio and therefore the thickened Pt shell. Likewise, as shown in Figure 3.12d, the Ru-Ru contribution increases with the increased Pt:Ru atomic ratio, suggesting the better protection of the Ru core from oxidation with the thicker Pt shell. The *in situ* XAS results of Ru@Pt nanoparticles will be discussed in Section 3.2.5.

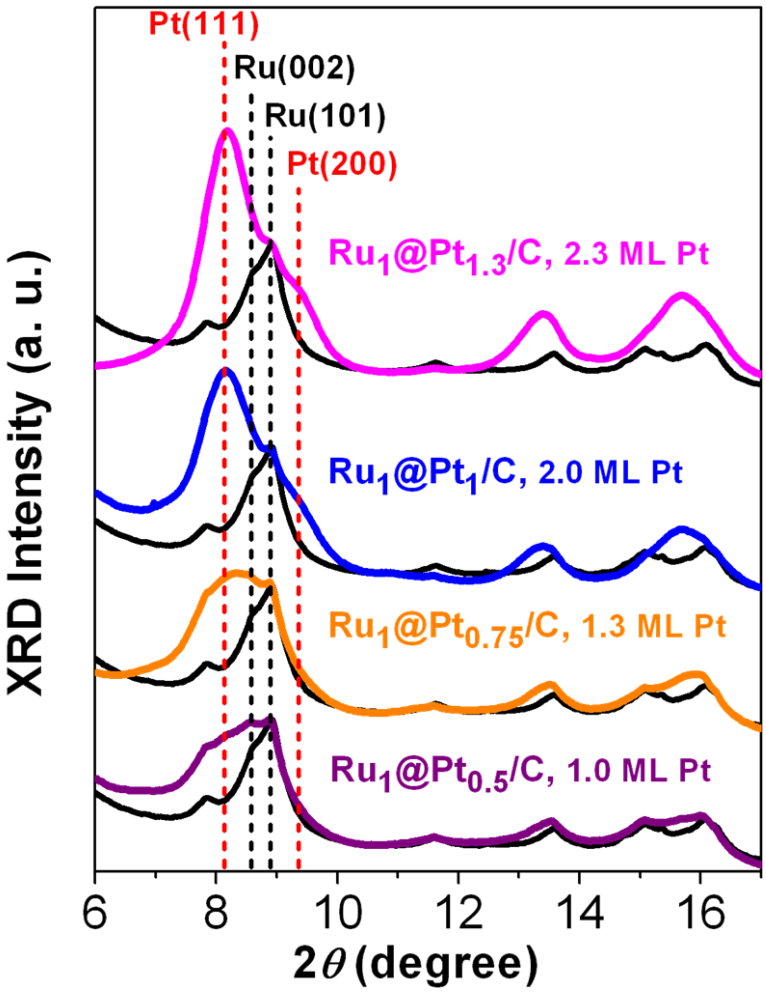

Figure 3.11 Synchrotron XRD diffractograms of ordered Ru@Pt nanoparticles with different Pt shell thickness. Ru@Pt/C samples were made with annealed Ru cores (black curve), and the Pt:Ru ratio increased from 0.5 to 1.33. The intensities of colored curves are normalized to the black ones at the Ru(101) position. λ = 0.3196 Å.

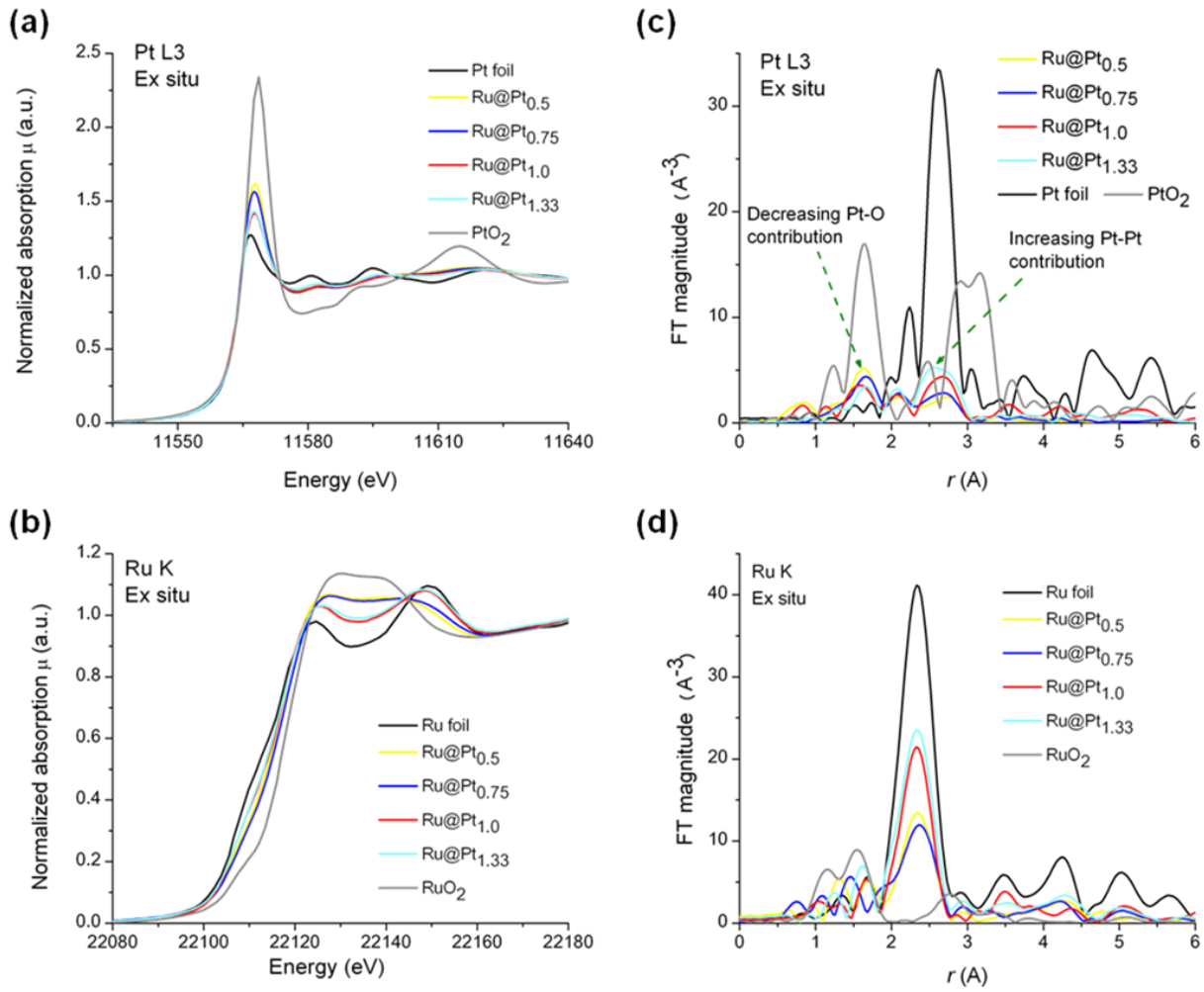

Figure 3.12 *Ex situ* XAS measurements of carbon-supported Ru@Pt nanoparticles with different Pt:Ru atomic ratios. (a, b) XANES spectra and (c, d) Fourier transformed magnitudes of the EXAFS data, measured at (a, c) Pt L3-edge and at (b, d) Ru K-edge. Also shown are spectra from reference materials of (a, c) Pt foil and PtO_2, (b, d) Ru foil and RuO_2.

3.2.3 Ordered Structural Transition at the Ru-Pt Core-Shell Interface

Ru(*hcp*) and Pt(*fcc*), both consist of closely packed planes of atoms, differing in their stacking sequence: The *hcp* layers cycle between two shifted positions, expressed as *ABAB*, whereas the *fcc* layers cycle between all three equivalent shifted positions, i.e., *ABCABC*. In

order to understand how Ru(*hcp*) and Pt(*fcc*) are compatible to form conformal core-shell structures given their different lattice structures and lattice constants, we studied the atomic structures at the Ru-Pt interface using X-ray diffraction and electron microscopic techniques, coupled with density functional theory (DFT) calculations.

First we carried out DFT calculations (Section 2.6.1) to assist analysis of lattice structure at the Ru-Pt core-shell interfaces. Focusing on the effect of the stacking sequence, we used slab models composed of four Ru layers and one or two Pt layers with a (2 × 2) hexagonal array within each layer. The atoms in the Pt layers and the top two Ru layers were relaxed. For a Pt monolayer, we found that the energy is slightly lower for the Ru(*ABAB*)-Pt(*C*) sequence (−33 meV) than for that of Ru(*ABAB*)-Pt(*A*), as shown in Figure 3.13.

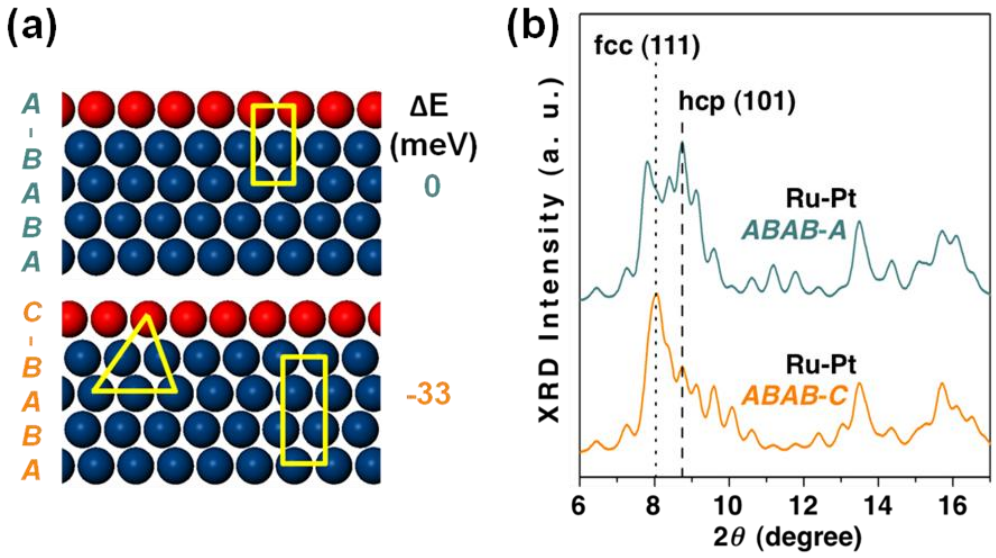

Figure 3.13 DFT models and simulated XRD for a Pt monolayer on Ru. (a) The side view of DFT slab models for a Pt monolayer (red) on four Ru hexagonal layers (blue) with four atoms in a (2 × 2) hexagonal in-plane cell. The ΔE is the energy difference between the two models. The *fcc-ABC* and *hcp-AB* sequences in the top three layers are highlighted, respectively, by the

yellow triangles and rectangles. (b) Simulated XRD using the top three layers illustrate the effect of stacking sequence on the relative intensities at the *fcc* (111) and *hcp* (101) positions.

Adding a second Pt layer with two choices for each type of monolayer creates four possible stacking sequences. The DFT calculations revealed that two of them have lower energies than the all-*hcp* Ru(*ABAB*)-Pt(*AB*) sequence. One is the Ru(*ABAB*)-Pt(*AC*) sequence (−160 meV); the other is the Ru(*ABAB*)-Pt(*CA*) sequence (−134 meV), as shown in Table 3.1. The side views of these structure models are depicted in Figure 3.14a. At the top, we show one partially alloyed model in which the Pt atoms were distributed among the top four layers with their Pt concentration varying from 3/4, 2/4, 2/4, to 1/4 (3D model in Figure 3.15). The energy for the Ru(*AB*)-RuPt(*ACBA*) partial-alloy model is much higher than those of the Pt bilayer models (e.g., 1000 meV relative to the Ru(*ABAB*)-Pt(*AB*) model), indicating that the Pt atoms preferentially stay on top of the Ru surfaces, consistent with the predication based on calculated surface segregation energies[360]. Driven by entropy and with the presence of steps on real surfaces, disordered were annealed surface alloys were observed when Ru(0001) crystals with a 0.5 to 1 Pt monolayer at temperatures between 800 and 1350 K[361]. For nanoparticles, interlayer diffusion can happen at even lower temperatures especially on defect-rich ones. When alloying occurs, the Ru(*AB*)-RuPt(*ACBA*) stacking sequence is more favorable by −250 meV than that of the Ru(*AB*)-RuPt(*ABAB*).

Table 3.1 Energy differences between different stacking sequences. The values are obtained using slab models in DFT calculations.

Stacking sequence models	ΔE (meV) vs. *ABAB* sequence
Ru-Pt monolayer	
ABAB-A	0
ABAB-C	−33
Ru-Pt bilayer	
Normal Ru hcp layers	
ABAB-AB	0
ABAB-AC	−160
ABAB-CA	−134
ABAB-CB	25
Top Ru layer shifted	
ABAC-BA	466
ABAC-AB	612
Ru-RuPt partial alloy	
AB-ACBA alloy vs. *ABAB-AB* bilayer	1000
AB-ACBA alloy vs. *AB-ABAB* alloy	−250

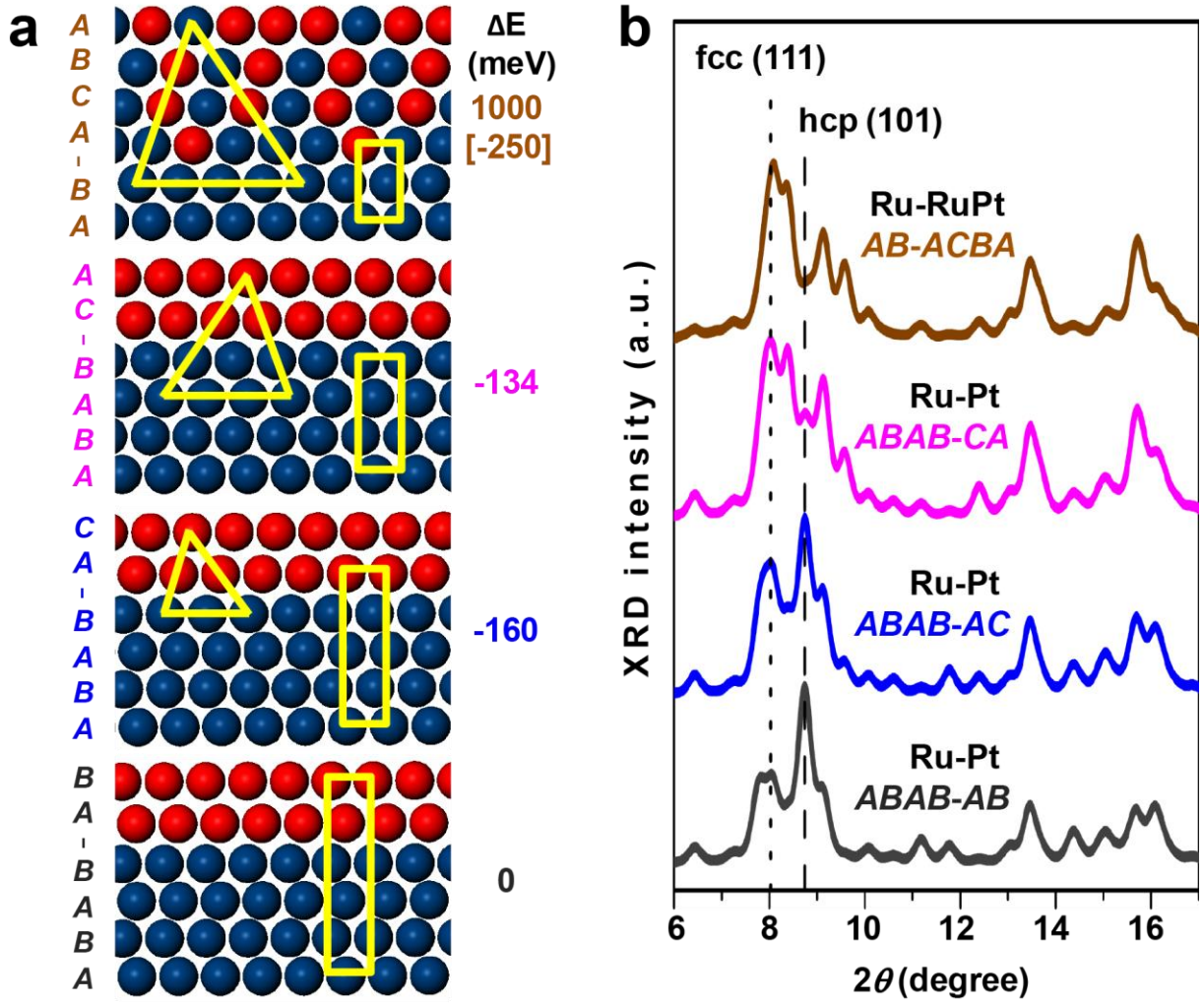

Figure 3.14 Optimized stacking sequences with simulated XRD. (a) Favorable stacking sequences for two layers of Pt (red) on four layers Ru (blue) slab models. The differences in energy, *ΔE*, are given relative to the bilayer model with the all-*hcp* sequence, Ru(*ABAB*)-Pt(*AB*), shown at the bottom. The additional *ΔE* value in square bracket for the partially-alloyed model at the top is with respect to the partially-alloyed model with all-*hcp* sequence, i.e., Ru(*AB*)-RuPt(*ABAB*). The numbers of layers involved in *fcc-ABC* and *hcp-AB* sequences are highlighted, respectively, by the yellow triangles and rectangles. (b) Simulated XRD using the structural models in (a) illustrating the effect of the stacking sequence on the relative intensities at the *fcc*-(111) and *hcp*-(101) positions. Atomic factors and the effects of lattice stain and particle size are not included.

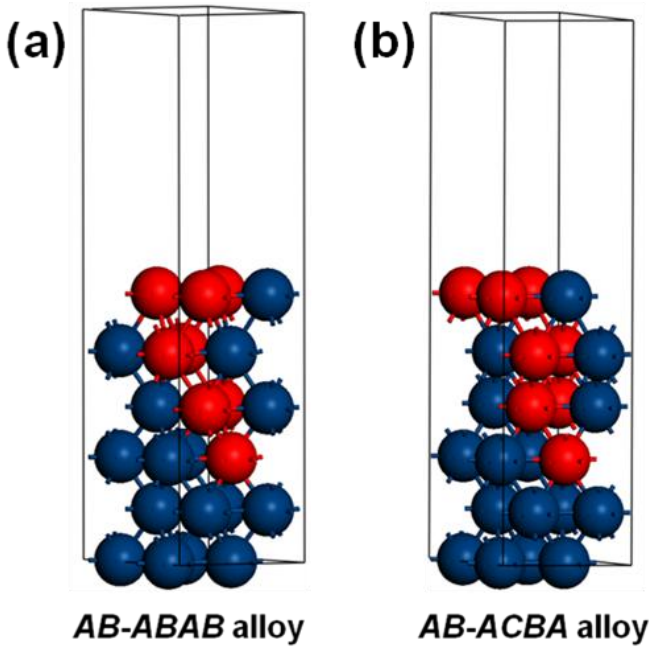

Figure 3.15 DFT slab models for Ru-Pt partial alloy. There are two layers of pure Ru (blue) and four layers of mixed Ru-Pt atoms. The layer contents of Pt (red) are 3/4, 2/4, 2/4 and 1/4 down from the top.

To characterize the structural models in Figure 3.14a, we drew the yellow rectangles to show how many layers have atoms at the same positions as the ones in the second layer below them. These layers are stacked in the *hcp*'s *ABAB* sequence. On the other hand, the yellow triangles mark how deep the triangular symmetry extends from the surface. The layers involved in the triangle are repeated every three layers, i.e., they follow the *fcc*'s *ABCABC* stacking sequence. Figure 3.14b shows that the simulated XRD intensities increase at the *fcc*-(111) position with the number of layers in the triangles, while the *hcp*-(101) intensity is associated with the number of layers in the rectangles. These results illustrate that the ratio of the *fcc*-(111) to *hcp*-(101) intensity varies with the lattice structure at the core-shell interface. Furthermore, a

partial alloy favors the *fcc* structure, and thus, causes the XRD to be more *fcc*-like, consistent with experimental observation (Figure 3.7, Figure 3.8).

Complementary to XRD that provides a global monitor of the core-shell lattice structure in the reciprocal space, we present below our real-space observations of the two most favorable DFT-optimized *hcp-fcc* interfaces for the bilayer-thick Ru@Pt samples. For the particles that have the crystallographic orientation shown in Figure 3.16a, the shifts in stacking sequence is denoted by the positions of the red dots with respect to the *hcp* sites marked by light blue circles in the "*C*" row and the one above it. The shift can involve one (left part) or two (right part) top layers. In other words, the first Pt layer can occupy either *C* or *A* site with little energy difference (33 meV), a fact that is supported by an experimental observation of Pt sub-monolayer islands in two orientations associated with *fcc* and *hcp* stacking sequence on the Ru(0001) single crystal surface[361]. We excluded the scenario wherein a Ru layer is shifted because the energy cost for such a shift is high, 466 or 612 meV (Table 3.1). In addition, the spacing of the Pt layer is visibly larger than that of Ru along the surface normal direction.

To verify the presence of these features on our synthesized bilayer Ru@Pt nanoparticles, we found the particles that exhibited the distinct fast Fourier transform patterns shown in Figure 3.16b, indicating that the close-packed crystalline planes are oriented normal to the imaging plane. Figure 3.16 c-d reveal that the atomic resolution STEM images of such oriented particles match well with the superimposed DFT-optimized structural models. For other facets, e.g., the one at the top-right corner of the image in Figure 3.16d, the lattice spacing of the top two layers is visibly expanded, supporting the presence of Pt shells about 2ML-thick on all facets.

In addition to the changes in atomic positions, we obtained evidence for the assigned Pt

layers by simulating the Z-contrast STEM image in Figure 3.16e, wherein the brightness of each dot represents the intensity associated with the number of electrons per atom (Z) and the number of atoms in the column (i.e., sample thickness). Since Z_{Pt} (78) is significantly higher than Z_{Ru} (44), the high STEM intensities near the edge of a sphere-like particle support a Pt shell. Along the line indicated in Figure 3.16e, the measured intensities (black circles) are well matched with a simulated curve (red line) in Figure 3.16f, using a Pt-bilayer model (Figure 3.17). If all the atoms were Ru, the intensity would be lower near the edge due to decreasing thickness of a sphere-like particle (blue line in Figure 3.16f). Based on the best match between the observed STEM image (Figure 3.16e) and the calculated one (Figure 3.16g), we assigned the Pt layers at the particle edge in Figure 3.16c, which shows that the bilayer Pt shell shifts down at the left following the curvature of the Ru core in an energetically favorable manner.

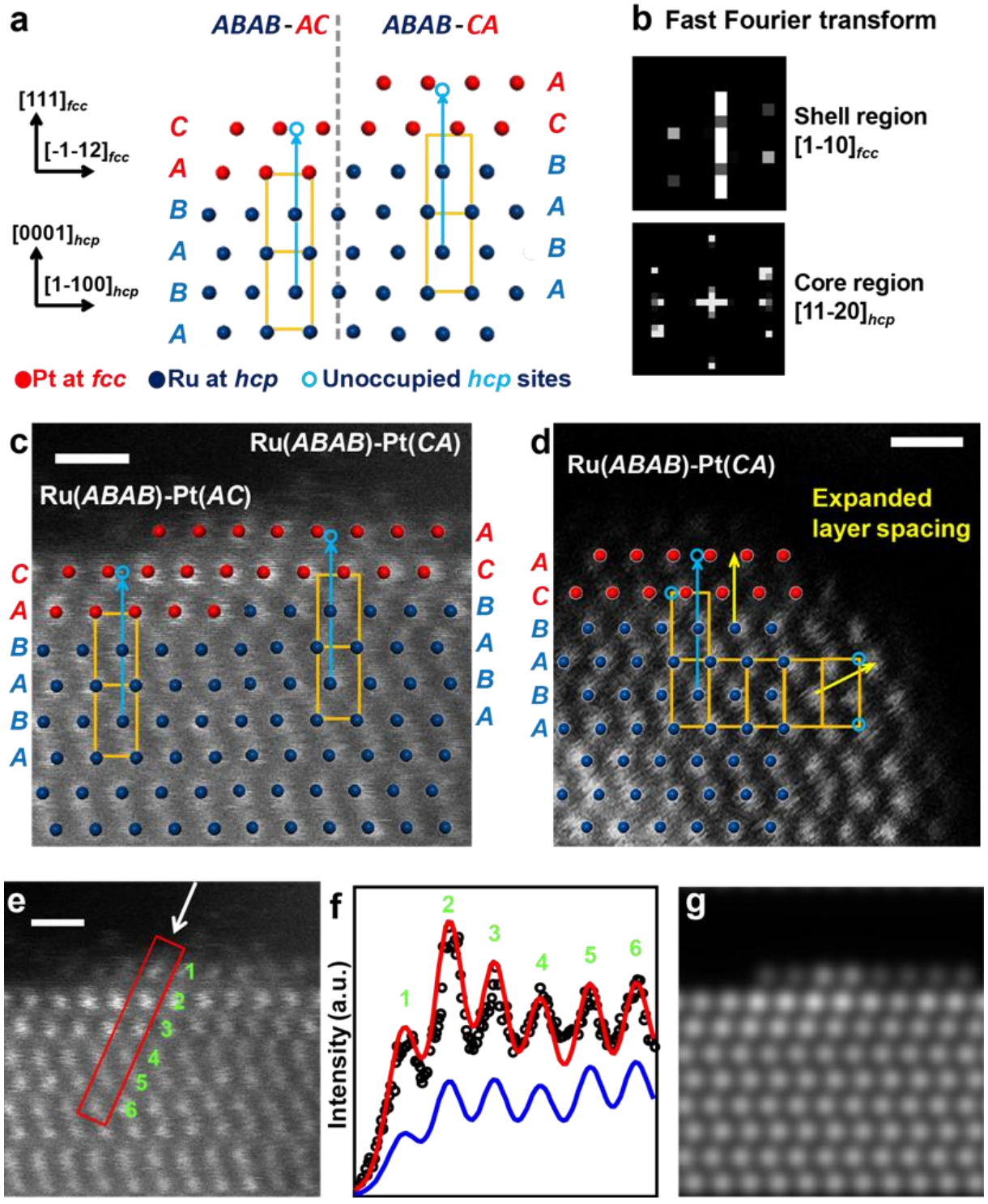

Figure 3.16 Ordered Ru(*hcp)-Pt(fcc)* phase transition at core-shell interfaces. (a) Orientation of crystallographic planes for the scanning transmission microscopy (STEM) image in (c), and two

DFT-optimized structural models for close-packed Pt bilayer on an Ru(0001) surface. (b) Fast Fourier transform of the image in (c). (c, d) HAADF-STEM images, superimposed with the DFT-optimized structural models (red and blue dots). Scale bar, 0.5 nm. The shifts from the *hcp* to the *fcc* lattice sites at the top one or two layers are indicated by yellow rectangles, light blue circles, and light blue arrows. The yellow arrows in (d) point to the expanded lattice spacing along the surface normal directions. (e) The same STEM image as in (c) for intensity analysis. Scale bar, 0.5 nm. (f) Intensity profile along the line indicated by the arrow in (e) (black circles) with calculated curves using Ru@Pt core-shell (red line) and all-Ru (blue line) models. (g) Calculated STEM image based on the Ru@Pt model shown in Figure 3.17.

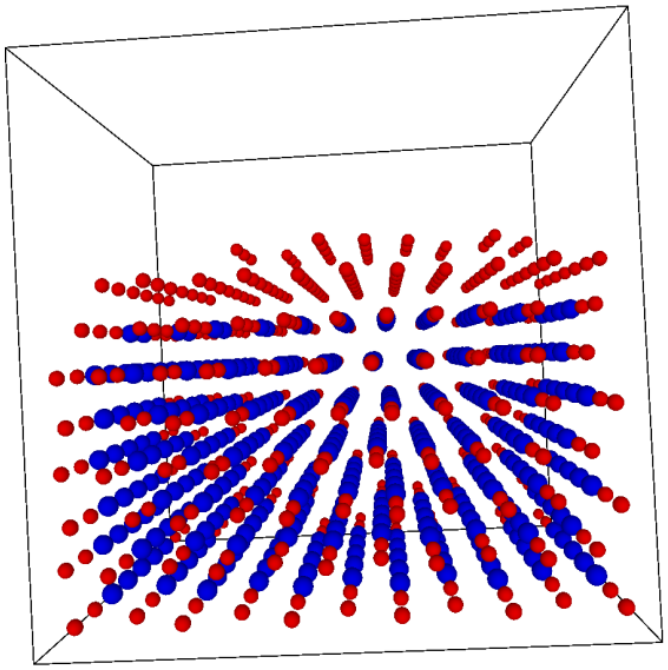

Figure 3.17 Ru@Pt structural model for simulating the image in Figure 3.16e. The top part is at the edge of the particle with two layers of Pt atoms (red). The left five columns of the third layer have three Pt atoms on the front and back, while all others have two Pt atoms at each end with Ru (blue) in the meddle. Other sides (left, right, and bottom) are truncated because the image simulated has particle edge only on the top.

While real-space evidence for the formation of single crystalline Ru@Pt nanoparticles with sharp, energetically favorable interfaces is provided, a question often rises on the representativeness of such particles because only a small portion of the nanoparticles are at the edge of carbon support and even fewer have the appropriate orientation for detailed analyses. Therefore, the correlation established between atomic-resolution STEM images for the ordered *hcp-fcc* phase transition and the non-diminishing Ru intensity in XRD is very helpful. The latter is a global probing technique more commonly available for charactering synthesized samples. We show next that structural perfection is vital for catalysts' stability and for tuning surface reactivity via the thickness of the Pt shell.

3.2.4 Catalytic Performances in Acid Electrolyte: Ru@Pt/C versus Pt/C

3.2.4.1 HER-HOR Activity Measured by GDEs

In order to determine the optimal Pt:Ru atomic ratio in the Ru@Pt catalysts, and the minimal Pt loading that is required for top performance, we measured the loading dependence of HER-HOR activity, represented by *CTR*, for four Ru@Pt catalysts with Pt:Ru atomic ratios ranging from 0.1 to 1.0, corresponding to Pt shell thickness varying from sub-monolayer to bilayer (two-monolayer). With Pt loadings up to 25 μg cm^{-2}, the best performance often was attained with the bilayer Ru@$Pt_{1.0}$ catalyst (red dots in Figure 3.18). For the bilayer Ru@$Pt_{1.0}$, the *CTR* as low as 0.04 Ω cm^2, corresponding to the required overpotential as low as 0.04 mV in order to drive the current density of 1 mA cm^{-2}, can be achieved with the minimum Pt loading of 20 ug cm^{-2}. The trend is illustrated by a calculated curve using *CTR* (Ω cm^2) = 0.4 / Pt loading (μg cm^{-2}). Due to the uncertainty level in determining the *HFR* (see the noise in Figure 3.19b for

highly active samples), we consider 0.04 Ω cm^2 as the minimal value that can be unambiguously determined in this study.

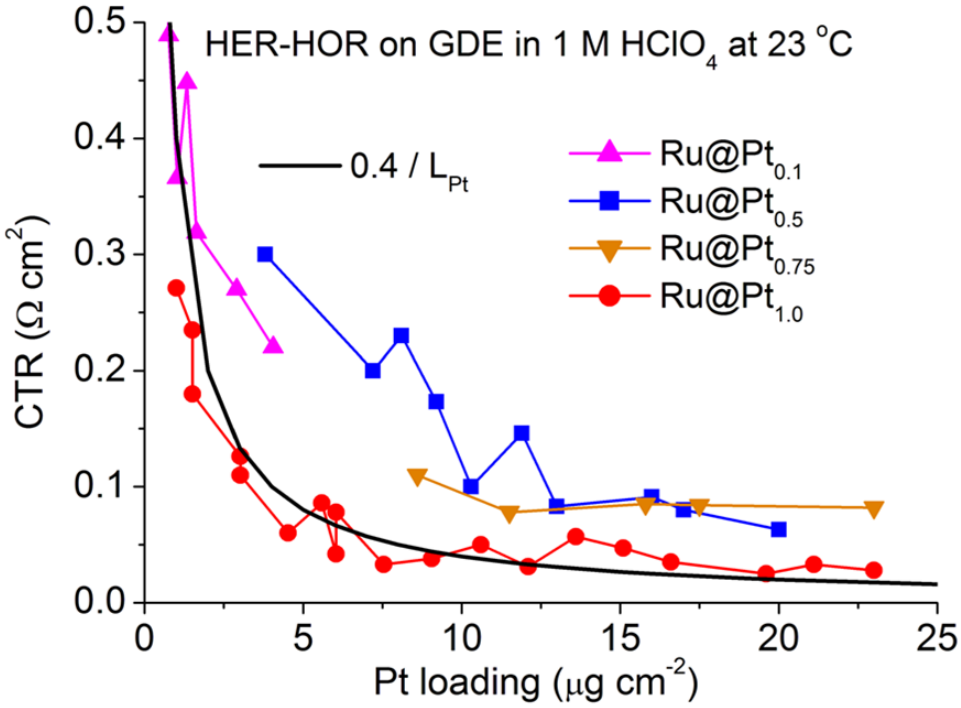

Figure 3.18 Charge transfer resistance (*CTR*) as a function of Pt loading for Ru@Pt nanocatalysts, with the Pt:Ru atomic ratio ranging from 0.1 to 1.0, measured using the hanging-strip GDE method in H_2-saturated 1 M $HClO_4$ at 23 ℃. The black line is calculated using 0.4 (Ω cm^2) divided by Pt loading (μg cm^{-2}).

Since the bilayer Ru@$Pt_{1.0}$, i.e. Ru@Pt_{2ML} nanocatalyst exhibits the highest HER-HOR activity among the investigated bimetallic core-shell nanocatalysts, the next intuitive subject to investigate is to compare the HER-HOR activity of our homemade carbon-supported Ru@Pt_{2ML} (denoted as Ru@$Pt_{1.0}$/C, or Ru@Pt_{2ML}/C), with the state-of-art carbon-supported Pt (denoted as Pt/C). Commercially available carbon-supported Pt nanocatalyst (50 wt%, TEC10E50E, Tanaka)

was used as reference material for HER-HOR measurements. The HER-HOR polarization curves of Ru@Pt_{2ML}/C and Pt/C demonstrate the similar current densities within the range of ±20 mA cm^{-2}. Their similar activity is signified by their similar *CTR*s of 0.04 Ω cm^2. Here we use the reciprocal of *CTR* as activity to be further normalized by Pt mass or Pt electrochemical surface area, in order to obtain the mass activity (MA_{Pt}) and specific activity (SA_{Pt}), as shown in Figure 3.19.

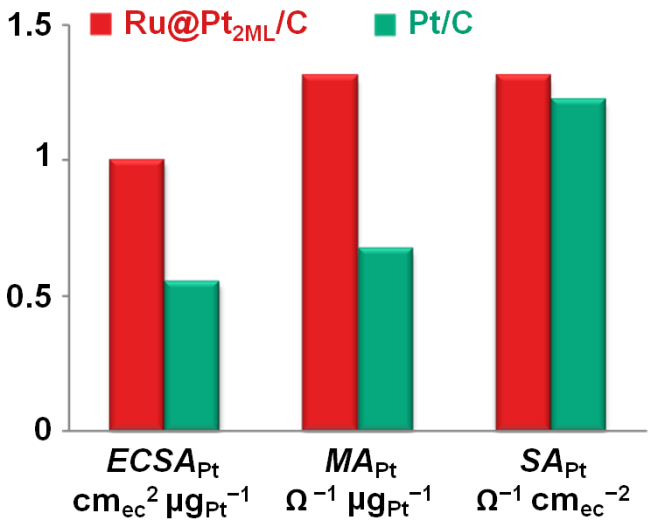

Figure 3.19 Comparison of the HER-HOR activities of Ru@Pt_{2ML}/C and commercial Pt/C, measured using the hanging-strip GDE method in H_2-saturated 1 M $HClO_4$, showing the Pt electrochemical surface area ($ECSA_{Pt}$), mass activity normalized by the mass of Pt (MA_{Pt}), specific activity normalized by the $ECSA_{Pt}$ (SA_{Pt}). The activity is represented by the reciprocal of *CTR*. Pt loading was 18.6 ug cm^{-2} for Ru@Pt_{2ML}/C, and 36.3 ug cm^{-2} for Pt/C.

Using commercial Pt/C catalysts, we obtained similar *CTR*s with the Pt loadings twice as those when the Ru@Pt_{2ML}/C catalyst was used, indicating a 50% reduction in Pt loading via the bilayer-thick core-shell structure. This 50% saving of the Pt loading can be attributed to the

roughly two-times Pt specific surface area in Ru@Pt_{2ML}/C (1.0 $cm^2\ \mu g^{-1}$) compared to that in Pt/C (0.56 $cm^2\ \mu g^{-1}$). These values were obtained by calculation using the average particle sizes and measured CO stripping charges[300]. Therefore these two catalysts exhibit almost similar specific activity for the HER-HOR.

It is also worth noting that hydrogen adsorption/desorption charge measured for the bilayer Ru@$Pt_{1.0}$ nanocatalyst is significantly less than that for the Pt nanocatalyst while their calculated surface areas are similar (Figure 3.20). This is caused by the influence of the Ru core on the Pt surface as it is known that adsorptions of H and OH are weakened on Ru-supported Pt films with ≤ 3-monolayer thickness.[302, 303, 362]

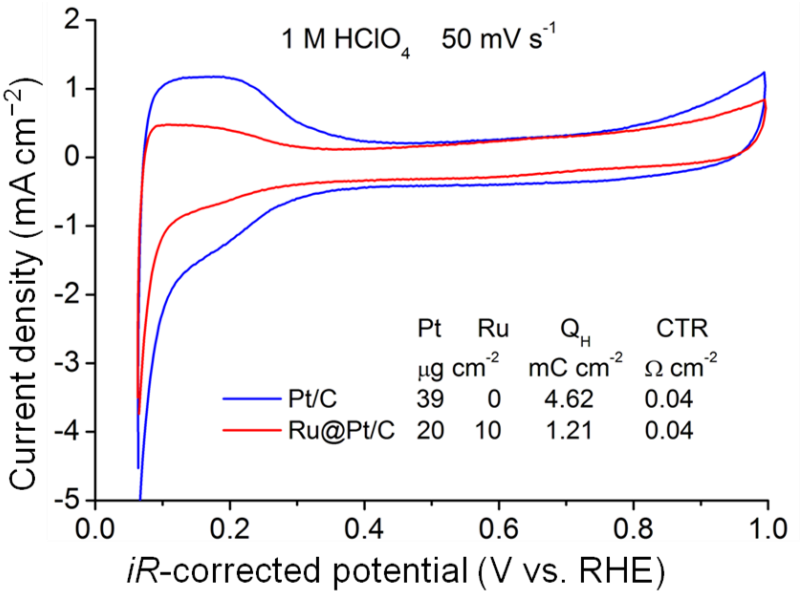

Figure 3.20 Cyclic voltammograms of bilayer Ru@Pt_{2ML}/C and commercial Pt/C catalysts, measured using the hanging-strip GDE method, in Ar-saturated 1 M $HClO_4$.

3.2.4.2 HOR Performance in Fuel Cells

For developing CO-tolerant HOR catalysts, ruthenium (Ru) was used to support spontaneous deposited sub-monolayer Pt[38, 39]. With Ru-Pt core-shell (denoted as Ru@Pt) nanoparticles with about 1~2 monolayer-thick shell, theoretical calculations and temperature programmed measurements showed preferential CO oxidation in hydrogen feeds on Ru@Pt nanoparticles compared to that of RuPt nano-alloys[304] and of Pt shells with other metal core[363]. Besides being a promoter of CO tolerance of Pt surface, Ru is less expensive than Pt, but it is prone to dissolution under oxidative conditions. Thus, our elaborating well-defined Ru@Pt nanoparticles with complete, uniform Pt shells opens an opportunity to achieve the CO tolerance and corrosion resistance needed for commercializing reformate-fed PEM fuel cells.

The significance of this achievement of structural perfection is demonstrated by the superior durability and excellent CO tolerance of the bilayer Ru@Pt nanocatalysts for the HOR in PEM fuel cells at ultra-low catalyst loadings (25 $\mu g\ cm^{-2}$ Pt, 10 $\mu g\ cm^{-2}$ Ru). The results hold great promise for using low CO-content reformates without much penalty in performance with the cost of catalyst comparable with that of the 50 ~ 100 $\mu g\ cm^{-2}$ Pt currently used for pure hydrogen fuel cells. This change would engender considerable savings in operating hydrogen fuel cells because the 2015 price target for hydrogen produced by reforming natural gas is $2 per kg H_2, viz., ~40% cheaper than pure hydrogen generated by water electrolysis at $3.5 per kg H_2.[364]

The performances of highly ordered Ru@Pt catalysts with low Pt loadings were assessed for the HOR in PEM fuel cells against CO tolerance and corrosion resistance at Ballard Power Systems, following the testing protocols for practical fuel cell applications. While the hydrogen

produced via steam reforming and the water gas shift reaction contains about 1% of CO, advances were made in lowering CO content to about 10 ppm via the preferential oxidation (PROX) reaction ($CO + 1/2O_2 \rightarrow CO_2$ in excess H_2)[365, 366], so triggering a renewed interest in developing CO-tolerant fuel cell catalysts. The target for using the hydrogen feed with 10 ppm CO is to assure that the CO-induced loss in performance is below 10%, or with air bleeding, it is reduced to < 1%. Air bleeding refers to injecting a small amount of air into the stream of anode fuel to promote the oxidative removal of adsorbed CO by forming CO_2.[367]

Figure 3.21a shows the polarization curves obtained in hydrogen PEM fuel cells without and with CO + air bleeding. The enhanced CO tolerance on the Ru@Pt core-shell catalyst that has lower total metal loading than the Pt/C baseline is verified by the doubling of the current at 0.65 V (0.51 vs. 0.25 A cm^{-2}) and by the smaller decrease in current from that with pure hydrogen (−41% versus −75%). For the other two core-shell catalyst samples tested with 1.5% air bleeding (Figure 3.21b), the current at 0.65 V is higher on $Ru@Pt_{1.0}/C$ than that on $Ru@Pt_{0.75}/C$ (0.52 versus 0.28 A cm^{-2}). The average Pt shell thicknesses for the Pt:Ru atomic ratios of 0.75, 1.0, and 1.33 are, respectively, about 1.3, 2.0, and 2.3 ML. For all the Ru@Pt samples, lattice contractions in the Pt shells ranged between −0.6% and −1.0% based on the XRD analyses, which are expected to weaken CO adsorption[304, 368]. Indeed, much weakened CO binding on the bilayer $Ru@Pt_{1.0}/C$ sample was observed by its lower potential of CO-stripping peak, compared with that on Pt/C (Figure 3.22). However, what weakens CO adsorption also lessens the adsorption of H and O species[303, 369], thereby lowering the HOR activity per site and the oxidative removal of CO. Therefore, a dedicated balance is needed to assure optimal performance. We achieved that goal by using well-defined core-shell structure with a tunable

shell thickness. With CO-containing H_2, the much better performance realized on bilayer Ru@Pt nanoparticles (solid red circles in Figure 3.21a and solid purple triangles in Figure 3.21b) compared with that on the monolayer Ru@Pt nanoparticles (open green triangles in Figure 3.21b) and on the Pt nanoparticles (solid blue squares in Figure 3.21a) illustrates the importance of structural perfection for fine-tuning surface reactivity. We note that the current at 0.65 V for the Ru@Pt/C sample with Pt loading of 25 μg cm^{-2} was reduced by less than half with the hydrogen containing CO than with pure hydrogen. Thus, the targeted <1% performance loss is likely achievable with total metal loading < 100 μg cm^{-2}, which is comparable to that currently used in the hydrogen fuel cell anode.

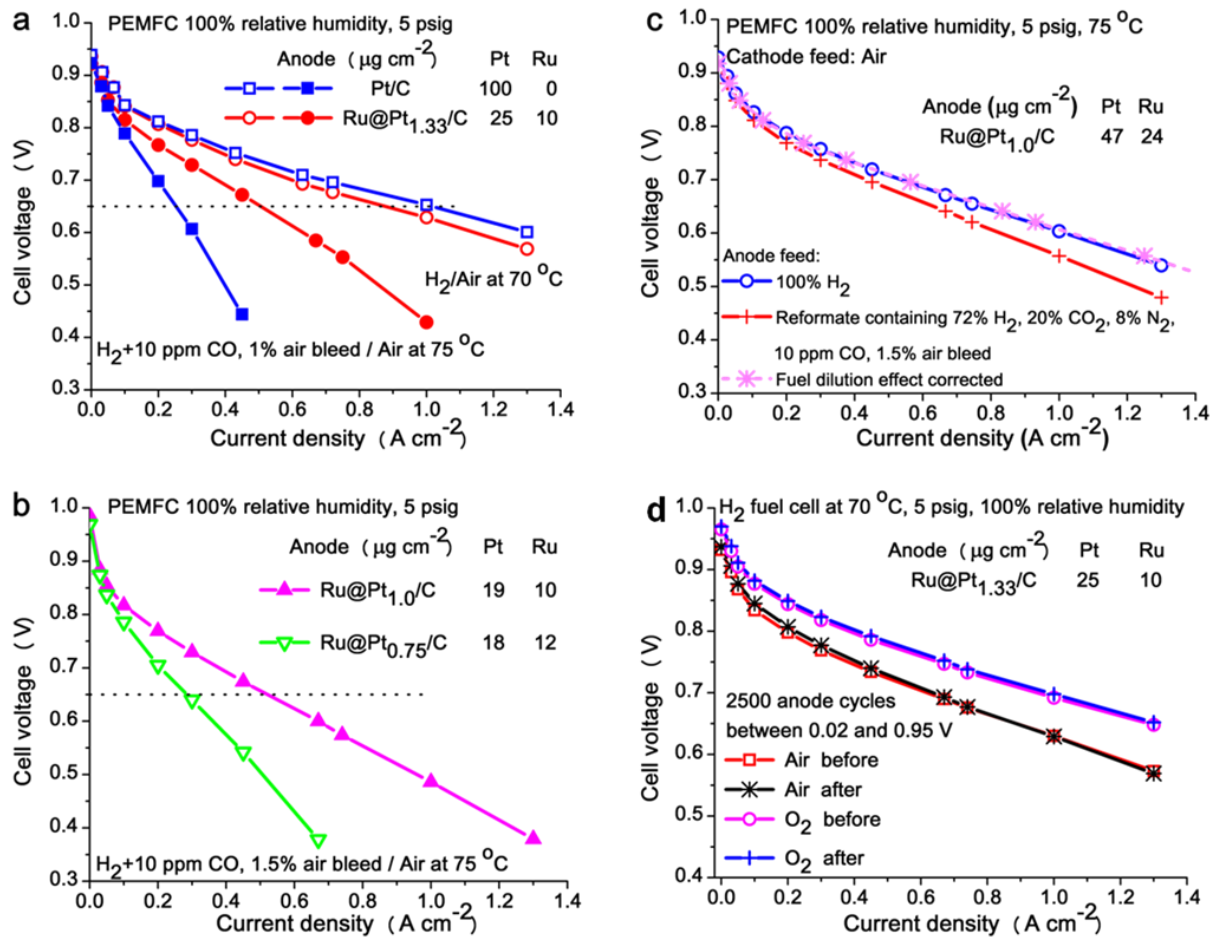

Figure 3.21 Performance of ordered Ru@Pt/C anode nanocatalysts in PEM fuel cells. (a) Polarization curves measured with pure hydrogen (open symbols), and hydrogen plus CO and air bleeding (solid symbols) at the anode. The cathode cathode gas was air. (b) Polarization curves measured with CO-containing hydrogen for two Ru@Pt/C samples with different Pt shell thicknesses. The dotted lines in (a) and (b) are to assist comparison of the current densities at 0.65 V. (c) Polarization curves obtained using an anode comprising bilayer Ru@Pt/C catalysts with pure hydrogen (blue circles) and reformate (red pluses) as the fuel. The curve with red crosses is generated by a correcting factor of 1/0.8 to account for the effects of fuel dilution. (d) Catalysts' stabilities after 2500 anode potential cycles measured with hydrogen at the anode, and air or oxygen at the cathode. The metal loadings for core-shell Ru@Pt catalysts were calculated using the catalysts' weights and metals' percentages based on the precursors used in syntheses with a 100% yield. The cathode Pt loading was 0.4 mg cm^{-2}.

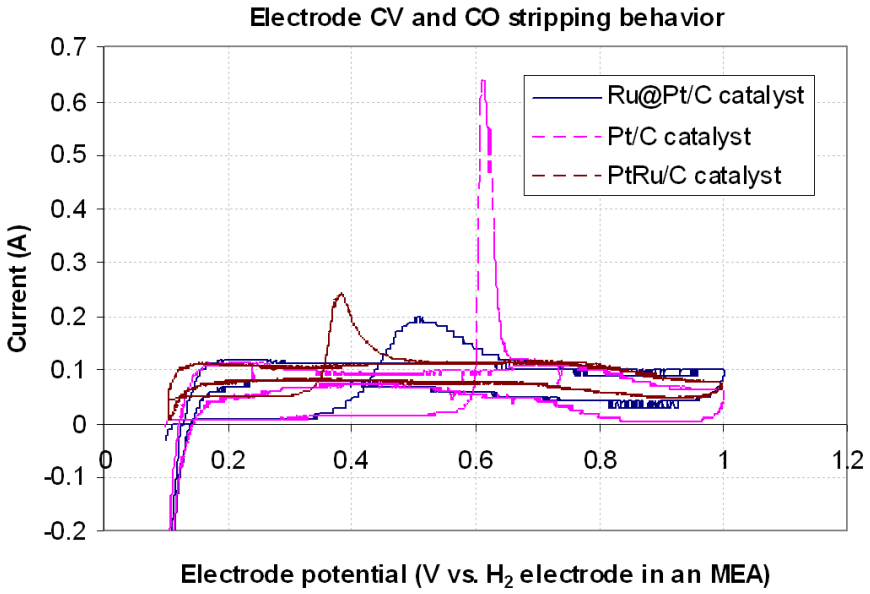

Figure 3.22 Anode's CO stripping behavior of the bilayer Ru@$Pt_{1.0}$/C, in comparison with those of conventional Pt/C and PtRu/C catalysts, measured in MEA after saturating CO adsorption on the catalysts' with 1% CO in N_2 and then with N_2 alone. The potential sweep rate was 20 mV s^{-1} and the cathode was under H_2 flow. The metal loading for the bilayer Ru@Pt/C electrode is 47 μg cm^{-2} Pt and 24 μg cm^{-2} Ru.

In order to study the fuel dilution effect, we prepared an anode GDE with bilayer Ru@Pt/C at 47% metal weight percentage, and tested its performance in PEMFC with a reformate comprising 72% H_2, 20% CO_2, 8% N_2, and 10 ppm CO with 1.5% air bleed as the anode fuel, to compared it to that with pure hydrogen as the anode fuel using Ballard Power Systems' standard protocols. Figure 3.21c shows that the two polarization curves differ only slightly, and their difference can be fully described by a constant factor in currents, as is evidenced by a curve generated by dividing the currents of the reformate polarization curve (red pluses) by 0.8 (red crosses) that matches the hydrogen polarization curve (blue circles) very well.

This fact favors the absence of losing active surface sites due to CO adsorption because otherwise the loss would have become bigger at higher currents, as usually seen. Combining this nearly perfect match over the entire curve with the dilution correcting factor not exceeding 1/0.72 for the 72% H_2 in the reformate, we concluded that the anode performance had no loss due to CO, and thus, met the target of a <1% CO-induced performance loss using a reformate containing 10 ppm CO with 1.5% air bleed. This result is significant because the loading of 0.047 mg cm^{-2} Pt and 0.024 mg cm^{-2} Ru are respectively 50% and 75% lower than the loading needed using conventional PtRu/C catalysts (i.e., 0.1 mg cm^{-2} Pt and 0.1 mg cm^{-2} Ru); Furthermore, the Pt loading is no more than the target for using conventional Pt/C with pure hydrogen.

Another important requirement for practical applications is corrosion resistance of the anode nanocatalysts. Although the anode operates at low potentials, metal dissolution and particle agglomeration may occur due to occasional high potentials at startup and shutdown or fuel starvation[370]. The problem is particularly detrimental for alloy RuPt/C catalysts, because Ru dissolves at lower potentials than does Pt, and furthermore, Ru ions can migrate through electrolyte membranes and be re-deposited at the cathode, so depressing its activity in oxygen reduction[371].

In order to check the corrosion resistance of the Ru@$Pt_{1.33}$/C sample, fuel cell accelerated stress tests (ASTs) for the anodes were carried out on MEAs with an active electrode area of 45 cm^2. During the AST, the fuel cell was alternated between operating (1 A cm^{-2}) and shutdown modes, with the anode potential cycled between ~0.02 V and ~0.95 V, and the cathode potential cycled between ~0.55 V and ~0.93 V.[372] After 2500 startup/shutdown cycles (~65 hours), there

was little change in the polarization curves shown in Figure 3.21d. This unaffected performance at the ultra-low Pt loadings signifies an excellent protection by the ordered Pt bilayer shells of the Ru cores and an enhanced stability of the Pt shells in comparison to Pt nanoparticles. We ascribe the latter effect to Ru-induced lattice contraction and the smooth morphology obtained both by the annealed Ru cores and by coating Pt under near equilibrium conditions to enhance the formation of energetically favorable structure. Previous studies have shown that the less reactive a surface is, the more corrosion resistant it is[143, 373]; low coordination sites (clusters, defects, vertices, edges) are prone to dissolution, and thus, need to be minimized[143, 373].

3.2.4.3 HER Performance in Water Electrolyzers

We tested the HER performance of the bilayer Ru@Pt nanocatalysts in PEM water electrolyzers at Proton OnSite. The test station had an integrated water purification module that maintained on-board conductivity near 18 MΩ cm. All operational tests were conducted at 50 ℃. A current-control Sorensen power supply was used to power the cell stack, with over-current protection set at 2.0 A cm^{-2}. The current was adjusted through the scan region and allowed to stabilize for 5 minutes before measuring cell potentials.

Among sixteen samples tested, the GDEs that performed similarly as the baseline had solution-tested CTR ≤ 0.08 Ω cm^2. Figure 3.23 show the results of a three-cell stack test. Two of the three cathodes were made with the Ru@Pt/C catalysts, and one with Pt black as the baseline. The polarization curves and time-dependent cell voltages were measured for each of the three cells. A lower cell voltage at a given current represents a higher HER activity. Equal activity to the baseline and excellent durability of the Ru@Pt catalysts are demonstrated by the polarization

curves in Figure 3.23a, and by the absence of rising voltage over 1200 hours at 1.8 A cm^{-2} as shown in Figure 3.23b. With the Pt loading about 30 μg cm^{-2}, these results demonstrated that the ordered Ru@Pt catalysts can reduce Pt content in PEM water electrolyzers to the same level as in the PEM fuel cells[299, 300].

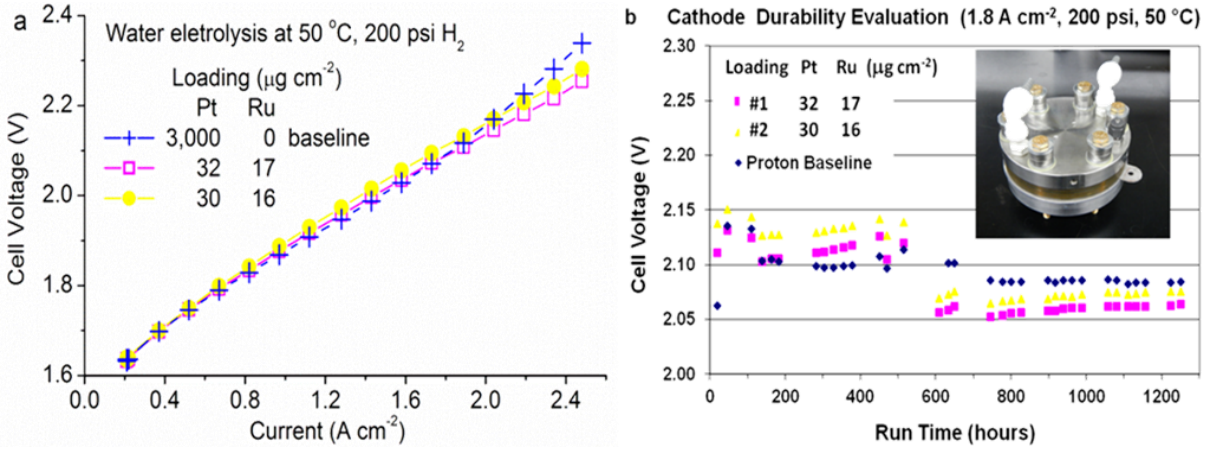

Figure 3.23 HER performance tests in PEM water electrolyzers. (a) Polarization curves and (b) voltage stabilities measured at 1.8 A cm^{-2} for two cathode samples made of the Ru@Pt core-shell catalysts and one made of Pt black catalysts as the baseline using a three-cell stack (inset of (b)).

3.2.5 *In Situ* XAS: Ru@Pt/C versus Pt/C

In Section 3.2.4, the well-defined bilayer Ru@Pt nanocatalyst demonstrated similar HER-HOR specific activity as the commercial Pt nanocatalyst in acid electrolytes. Here we explore the local structures of these two kinds of nanocatalysts probed by *in situ* XANES and EXAFS measurements, in order to elucidate their HER-HOR specific activities in acid media.

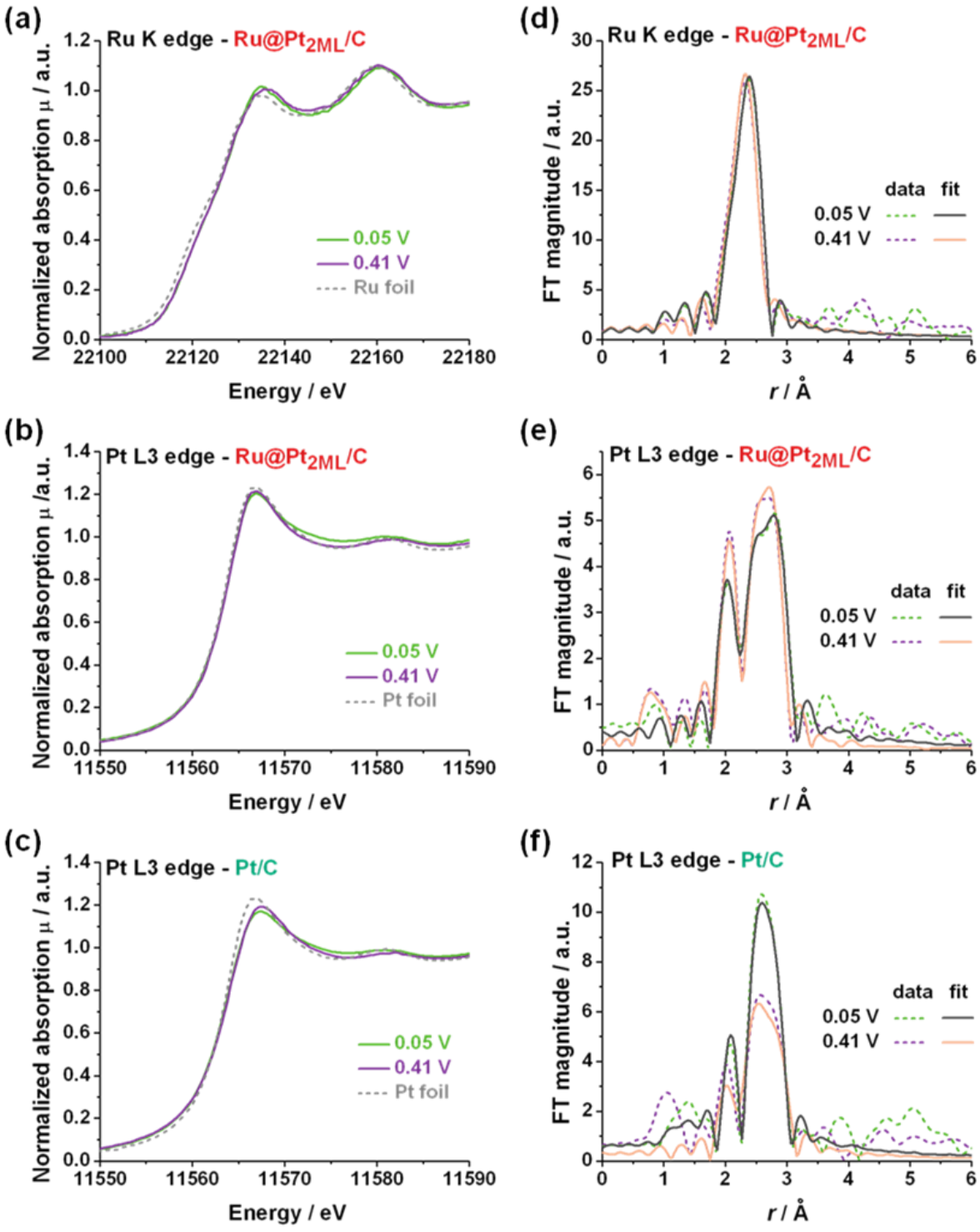

Figure 3.24 *In situ* XAS results of Ru@Pt_{2ML}/C and commercial Pt/C, measured in 1 M $HClO_4$ at potentials of 0.05 V and 0.41 V. (a-c) *In situ* XANES spectra (a) at the Ru K-edge and (b-c) at the

Pt L3-edge, of (a-b) Ru@Pt_{2ML}/C and (c) Pt/C. Also shown are spectra from reference materials of (a) Ru foil, and (b-c) Pt foil. (d-f) *In situ* EXAFS Fourier transformed magnitudes of the data (solid line) and of the first-shell fit (dotted line) (d) at the Ru K-edge and (e-f) at the Pt L3-edge obtained from (d-e) Ru@Pt_{2ML}/C and (f) Pt/C.

I*n situ* XANES spectra of Ru@Pt_{2ML}/C at the Ru K-edge (Figure 3.24a) and Pt L3-edge (Figure 3.24b) were measured in 1 M $HClO_4$ at the potentials of 0.41 and 0.05 V. The potential of 0.41 V was chosen because it is in the electrical double layer region of Pt, with the minimal interaction between the Pt surface with adsorbates including electrolyte anions and water.[36] The other potential of 0.05 V was chosen because it is in the hydrogen underpotential deposition (UPD) region of Pt, where the proton or hydronium ions from the acid electrolyte are adsorbed on the Pt surface. We did not purge H_2 into the *in situ* XAS cell at 0.05 V due to safety concerns.

The Ru K-edge spectra of Ru@Pt_{2ML}/C (Figure 3.24a) show negligible change at potentials of 0.41 and 0.05 V, suggesting that the electronic structure of the Ru core is not affected much by potentials. Also the Ru oxidation state in the Ru@Pt_{2ML}/C is considered to be metallic, because its edge energy of 22117.3 eV is very close to that of the Ru foil (22117 eV).

Figure 3.24 d-f display the Fourier transformed EXAFS spectra of Ru@Pt_{2ML}/C (Figure 3.24 d-e) and Pt/C (Figure 3.24f) at the Ru K-edge and Pt L3-edge at the potentials of 0.41 and 0.05 V, along with their fitted curves. We carried out the first-shell fit of the EXAFS data, and summarized the best-fit values of structural parameters in Table 3.2 and Table 3.3. EXAFS analysis of the Ru@Pt_{2ML}/C data was carried out by simultaneously fitting both the Ru K-edge and Pt L3-edge at the same time, with applying some constraints between the fitting parameters for bimetallic samples[374, 375], listed as follows.

(1) The Ru-Pt distance of the heterometallic bond is the same as measured from either end

$$R_{\text{Pt-Ru}} = R_{\text{Ru-Pt}} \tag{3.1}$$

(2) The bond length disorder parameter of the heterometallic bond between Ru and Pt are the same

$$\sigma^2_{\text{Pt-Ru}} = \sigma^2_{\text{Ru-Pt}} \tag{3.2}$$

(3) The coordination number ratio follows

$$R_{\text{Ru-Pt}} / R_{\text{Pt-Ru}} = x_{\text{Pt}} / x_{\text{Ru}} \tag{3.3}$$

where $x_{\text{Pt}} / x_{\text{Ru}}$ is the atomic ratio of Pt to Ru, and in the sample Ru@Pt_{2ML}/C

$$x_{\text{Pt}} / x_{\text{Ru}} = 1 \tag{3.4}$$

The fit results at 0.41 V can be used to understand the inherent local structure of Ru and Pt in the Ru@Pt_{2ML}/C, without specific adsorption of any reactants or reaction intermediates.

First, the coordination number ratio

$$N_{\text{Ru-Ru}} / N_{\text{Ru-Pt}} = 7.62 \tag{3.5}$$

which is much larger than the atomic ratio

$$x_{\text{Ru}} / x_{\text{Pt}} = 1 \tag{3.6}$$

Similarly the coordination number ratio

$$N_{\text{Pt-Pt}} / N_{\text{Pt-Ru}} = 6.72 \tag{3.7}$$

which is also much larger than the atomic ratio

$$x_{\text{Pt}} / x_{\text{Ru}} = 1 \tag{3.8}$$

These results indicate that Ru and Pt tend to segregate to different regions instead of forming random alloy, suggesting the formation of core-shell structure.

Second, the total coordination number of Ru atoms is

$$N_{\text{Ru-M}} = N_{\text{Ru-Ru}} + N_{\text{Ru-Pt}} = 10.29 \quad (3.9)$$

which is larger than that of Pt atoms

$$N_{\text{Pt-M}} = N_{\text{Pt-Pt}} + N_{\text{Pt-Ru}} = 9.22 \quad (3.10)$$

suggesting that Ru atoms are segregated into the core, and Pt atoms are segregated to the shell at the particle surface.

Third, the obtained coordination numbers of Ru@Pt_{2ML}/C are close to those of the infinite slab, with reasonable shrinkage due to the finite size effect of nanoparticles. In the infinite slab condition, assuming two Pt monolayers on a six-layer Ru slab, the coordination numbers should be

$$N_{\text{Pt-Ru(slab)}} = 1.5 \quad (3.11)$$

$$N_{\text{Pt-Pt(slab)}} = 9 \quad (3.12)$$

$$N_{\text{Ru-Ru(slab)}} = 11.5 \quad (3.13)$$

and

$$N_{\text{Ru-Pt(slab)}} = 0.5 \quad (3.14)$$

In the nanoparticle case, the average coordination number $N_{\text{Ru-Ru(particle)}}$ is 9.26 for Ru@Pt_{2ML} nanoparticle with the diameter of 2.8 nm (Figure 3.9) and two-monolayer Pt shell, estimated using the hcp cluster model by Glasner and Frenkel[376]. Overall these obtained results of coordination numbers provide evidence to the formation of two-monolayer of Pt shell on Ru nanoparticles.

As shown in Table 3.2 and Table 3.3, at the potential of 0.41 V, the obtained Pt-Pt bond length for Ru@Pt_{2ML}/C is 2.726 Å, which is 0.024 Å shorter than the Pt-Pt bond of 2.751 Å for

Pt/C. It is known, both experimentally and theoretically, that the adsorption of small adsorbates, such as H_2 and CO, are weakened on the Pt overlayer supported on Ru substrate, compared to the adsorption on Pt surface, due to the combination of electronic and geometric effects of Ru substrate.[302, 303, 362] The significant shortening of the Pt-Pt bond length we obtained at 0.41 V for Ru@Pt_{2ML}/C, compared to that for Pt/C, is consistent with such weak adsorption.

Table 3.2 Summary of in situ EXAFS first-shell fit results for carbon-supported Ru@Pt_{2ML} nanocatalyst.

Potential/V vs. RHE	Path	N	R/Å	σ^2 ($\times 10^{-4}$)/Å^2
0.41	Pt-Ru	1.19 ± 0.25	2.683 ± 0.002	7.6 ± 0.3
	Pt-Pt	8.02 ± 0.43	2.726 ± 0.006	7.7 ± 0.3
	Ru-Ru	9.10 ± 0.41	2.661 ± 0.006	4.7 ± 0.1
	Ru-Pt	1.19 ± 0.25	2.683 ± 0.002	7.6 ± 0.3
0.05	Pt-Ru	1.01 ± 0.19	2.702 ± 0.018	6.9 ± 0.2
	Pt-Pt	7.72 ± 0.35	2.745 ± 0.005	7.1 ± 0.1
	Ru-Ru	9.06 ± 0.39	2.664 ± 0.005	5.0 ± 0.1
	Ru-Pt	1.01 ± 0.19	2.702 ± 0.018	6.9 ± 0.2

Table 3.3 Summary of in situ EXAFS first-shell fit results for commercial carbon-supported Pt nanocatalyst.

Potential/V vs. RHE	Path	N	R/Å	σ^2 ($\times 10^{-4}$)/Å^2
0.41	Pt-Pt	8.48 ± 0.86	2.751 ± 0.014	7.8 ± 0.4
0.05	Pt-Pt	10.42 ± 0.72	2.750 ± 0.012	7.3 ± 0.3

However, at the potential of 0.05 V, the obtained Pt-Pt bond length for $Ru@Pt_{2ML}/C$ is 2.745 Å, which is only 0.005 Å shorter than the 2.750 Å bond length for Pt/C. Such a negligible compression of Pt-Pt bond could account for the similar HER-HOR specific activity for $Ru@Pt_{2ML}/C$ and Pt/C, yet the slightly squeezed Pt-Pt bond length for $Ru@Pt_{2ML}/C$ might contribute to the weakened CO adsorption together with the accordingly enhanced tolerance to the CO impurity for the HOR in PEM fuel cells[299, 300].

The insignificant shortening of the Pt-Pt bond at 0.05 V for $Ru@Pt_{2ML}/C$ compared to Pt/C can also be understood from the H adatoms on Pt. There are mainly two kinds of H adatom on Pt. One is the H atom adsorbed at atop sites, H_{atop}, originated from the dissociation of H_2 or H_2O, which is the active reaction intermediate for both the HOR and HER.[377] The other is the H atom adsorbed at bridge or *fcc*-hollow sites, also known as the underpotentially deposited hydrogen (H_{UPD}), derived from proton reduction[29]. On Pt surfaces, or on the Pt/C, the active species H_{atop} has lower coverage than the inactive H_{UPD}. Though the H_{UPD} does not directly contribute to the reaction, its major role is that the lateral repulsion between H adatoms can facilitate desorption of the H_{atop} intermediate and therefore release the occupied active Pt sites. In contrast, on the Pt overlayer supported on Ru substrate, for example on the $Ru@Pt_{2ML}/C$, the shortened Pt-Pt bond causes the weakened H adsorption at all the sites, including the adsorption of H_{atop} and H_{UPD}. The weakened H_{atop} adsorption could result in the weaker HER-HOR activity. But there is another opposite factor − the weakened lateral repulsion[29] resulted from the weaker H_{UPD} adsorption (Q_H ratio of 3.8 in Figure 3.20) could in turn increase the adsorption of the active H_{atop}. Ultimately, the net effect of these two contrary factors on the HER-HOR activity is negligible. This can be proved by the similar HER-HOR activity for $Ru@Pt_{2ML}/C$ and Pt/C

measured using the hanging-strip GDE method (Section 3.2.4.1). Moreover, the similar specific activity toward the HER-HOR for Ru@Pt_{2ML}/C and Pt/C, measured using the hanging-strip GDE method, corroborates with the very close apparent activation barrier determined for Ru@Pt_{2ML}/C[301] with the reported values for Pt surfaces[325, 378], and is also consonant with the similar HER-HOR performance for these two electrocatalysts measured in PEM fuel cells (Section 3.2.4.2) and water electrolyzers (Section 3.2.4.3).

3.2.6 Summary

We demonstrate herein a case wherein lattice defects must be minimized for achieving desirable nanostructures, while advantages have been taken of the lattice defects and relative diffusivities of two elements to fabricate hollow nanomaterials[309, 379]. The drastic effect of lattice defects on diffusion rate in bulk materials was noted in the 1940s[359]. Just a few per million empty sites makes vacancy exchange the dominant mechanism for inter-diffusion at the interface of two metals, because the barrier is much lower than that of direct exchange or rotation. While interlayer mixing occurred in Ru@Pt nanoparticles synthesized using a sequential polyol process at 200 °C[304, 305], our 80 °C coating of Pt in ethanol on 450 °C-annealed Ru cores produced single crystalline Ru@Pt core-shell nanoparticles with tunable Pt shell thicknesses as confirmed by complementary XRD and microscopy measurements. This is because the number of defects in Ru nanoparticles is reduced by annealing at 450 °C compared to those as-synthesized at 200 °C, and the interlayer diffusion rate is further lowered by coating Pt at 80 °C versus 200 °C.

In summary, Ru-Pt partial alloying is not inevitable for core-shell nanoparticles with different crystal structures, and highly-ordered Ru@Pt nanoparticles with designed shell

thickness can be reliably produced by a fine-tuned synthetic method using ethanol as the solvent and reductant. This new level of atomic control in synthesis allowed us to use bilayer Ru@Pt nanoparticles as an advanced HER-HOR catalyst for practical application in PEM fuel cells and water electrolyzers. Using the hanging-strip GDE test method, $Ru@Pt_{2ML}/C$ demonstrated almost similar HER-HOR specific activity as commercial Pt/C. The high HER-HOR activities of bilayer $Ru@Pt_{2ML}$ were shown by $\leq 0.04\ \Omega\ cm^2$ *CTR* at 0 V in 1 M $HClO_4$ at 23 °C with Pt loading $\leq 20\ \mu g\ cm^{-2}$. We attribute the ultralow *CTR* with ultralow Pt loading primarily to the high Pt surface area per Pt mass of the well-defined Ru@Pt core-shell catalysts. In addition, the significantly enhanced CO tolerance and the superior stability for the HOR at the H_2 anode in fuel cells at ultralow catalyst loadings, in comparison with commercial Pt/C, show the promise of using a well-ordered core-shell structure to resolve the dilemma in using dissolution-prone metals for alleviating the CO poisoning effect. Moreover, the top-level performance for the HER in water electrolyzers is verified by comparison with well-established baseline of commercial Pt catalyst over 2.4 A cm^{-2} current range and stability over 1200 hours.

The local structures for $Ru@Pt_{2ML}/C$ and Pt/C were probed by *in situ* XAS measurements. The considerable compression of Pt-Pt bond at 0.41 V for $Ru@Pt_{2ML}/C$ is consistent with the weakening of adsorbate binding for Pt overlayer on Ru in literatures; While the unsubstantial contraction of Pt-Pt bond at 0.05 V for $Ru@Pt_{2ML}/C$ could contribute to the infinitesimal influence of Ru core on the Pt shell for the HER-HOR activity. Therefore, present results suggest that $Ru@Pt_{2ML}/C$ nanocatalyst, with almost half of the Pt loading for Pt/C, holds promise as a high performance HER-HOR electrocatalyst in enabling the large scale commercialization of PEM water electrolyzers and fuel cells.

3.3 Carbon-Supported Pd@Pt Nanocatalysts for Oxygen Reduction

While aerobic alcohol oxidation catalyzed heterogeneously by metal catalysts has been extensively investigated for the synthesis of valuable chemical precursors and intermediates[380, 381], the ethanol oxidation catalyzed by metal nanoparticles can be employed for the epitaxial growth of Pt monolayer on the metal particles. Ethanol, a non-toxic liquid that can be produced from renewable sources,[382] was employed as both reducing agent and solvent in the syntheses. In a typical synthetic procedure, ethanol oxidation was catalyzed by the Pd core nanoparticles and consequently generated electrons. These electrons were then utilized in the reduction of $[PtCl_6]^{2-}$ ions to Pt atoms, which were coated on core nanoparticles forming atomic Pt layers.

3.3.1 Physical Characterization

Carbon-supported palladium (Pd) nanoparticle was employed as the core to support Pt monolayer shell. After the Pt coating process in ethanol (Section 2.2.3), such Pd@Pt core-shell nanoparticles were observed to be evenly dispersed on carbon support, shown by the transmission electron microscopy (TEM) image (Figure 3.25a). Their crystal structure is confirmed to be face-centered cubic (*fcc*, space group *Fm-3m*) by X-ray diffraction (XRD) (Figure 3.25b), and by selected-area electron diffraction (SAED) (Figure 3.25c). The similar crystal structure (*fcc*), and the small lattice mismatch (0.85%) between Pt (0.39236 nm) and Pd (0.38903 nm)[334] are beneficial for Pt to coherently match the lattice structure of Pd core and to form a pseudomorphic shell.[189]

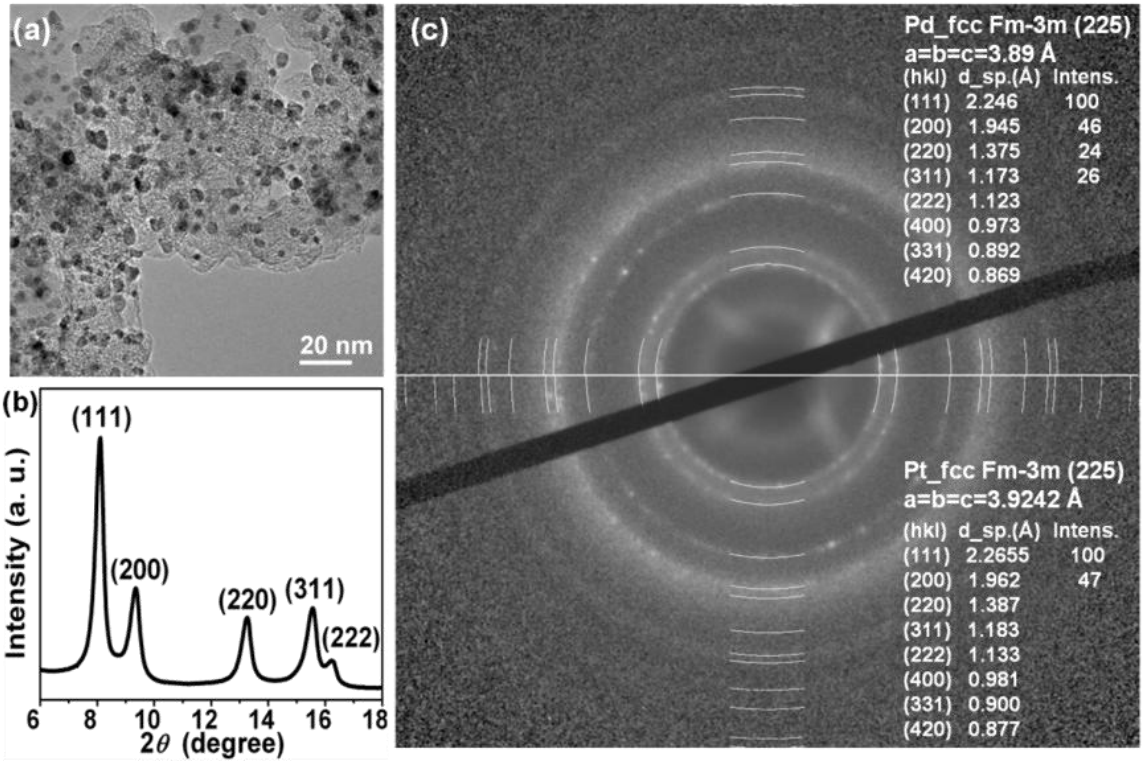

Figure 3.25 Morphology and crystal structure of Pd@Pt_{ML} sample. (a) TEM image where the average size is 3.73 nm, (b) Synchrotron XRD (λ = 0.3196 Å) diffractogram. (c) SAED pattern, superimposed with the standard profiles of diffraction rings for Pd (top) and Pt (bottom).

3.3.2 Pt Monolayer Coating in Ethanol

The exclusive deposition of Pt atoms on Pd cores is verified by the two-dimensional (2D) intensity mapping (Figure 3.26a) of high-angle annular dark field (HAADF) image (blue) with electron energy-loss spectroscopy (EELS) signal of Pd (red) using scanning transmission electron microscopy (STEM) technique. In addition, the Pt/(Pt+Pd) atomic ratios were determined by energy dispersive X-ray spectroscopy (EDX) equipped on the STEM for individual particles (Figure 3.26 b-d). No particles were found without the existence of Pd, indicating that the self-nucleation of Pt has been effectively inhibited. For two distinct samples

(red dots and blue squares in Figure 3.26e) with different amounts of H_2PtCl_6 precursor in syntheses, the measured Pt/(Pt+Pd) atomic ratios decreases with the increasing particle sizes. The trend primarily follows the curves calculated for Pt monolayer (Pt_{ML}) and bilayer (Pt_{2ML}) shells on Pd cores, respectively (solid and dash lines in Figure 3.26e). The calculation was based on a cuboctahedron model and the normal distribution of particle size (Section 3.3.3). These results denote that simply increasing the amount of H_2PtCl_6 precursor could correspondingly increase the thickness of conformal Pt shells.

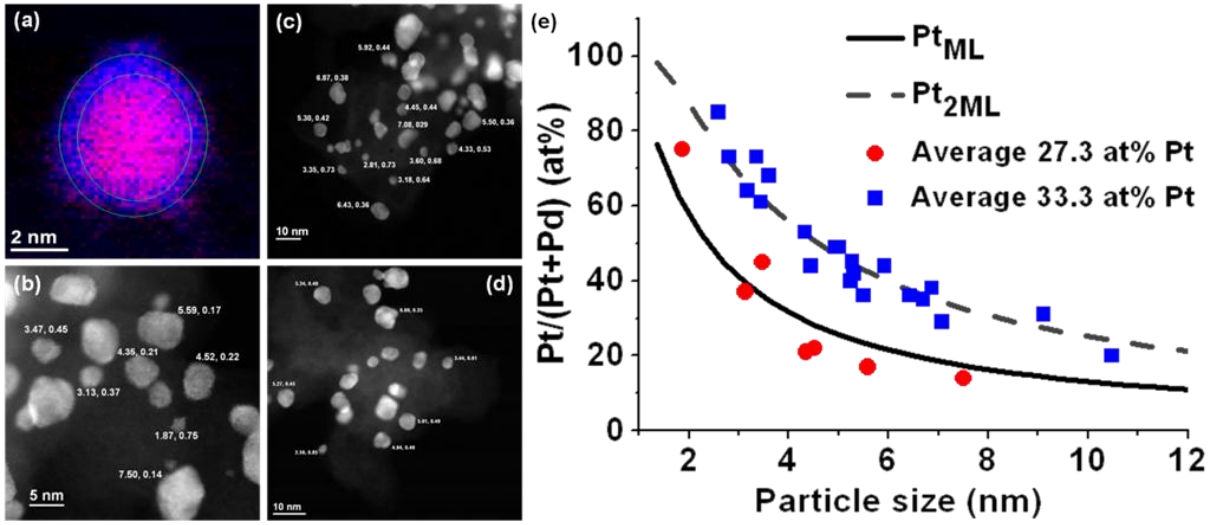

Figure 3.26 (a) STEM-HADDF image (blue) overlapping Pd-EELS signal (red) for a representative Pd@Pt core-shell nanoparticle. (b-d) Representative HADDF image of Pd@Pt_{ML} (b) and Pd@Pt_{2ML} (c-d) nanoparticles. Individual particles are marked by (s, r) where s is the particle size and r is the Pt/(Pt+Pd) atomic ratio determined by EDX equipped on a STEM. (e) The EDX-determined Pt/(Pt+Pd) atomic ratio as a function of particle size for two distinct samples. The data for the Pd@Pt_{ML} sample (red dots) were measured from the area shown in (b), and the Pd@Pt_{2ML} data (blue squares) were from (c-d). The lines are the calculated curves for Pt_{ML} (solid) and Pt_{2ML} (dash) on Pd nanoparticles.

The uniform coating of Pt shells is partly attributed to the optimal reaction temperature of 70 ℃, which has been chosen considering three aspects. First, in 1~5 mM ethanolic H_2PtCl_6 solutions, Pt nucleation didn't occur until the solution temperature was higher than 78 ℃, which is also the boiling point of ethanol. Second, the reducing power of ethanol at 70 ℃ was sufficient to reduce Pt (IV) to Pt (0) in the presence of Pd nanoparticles. The complete reduction of $[PtCl_6]^{2-}$ is signalled by the color of H_2PtCl_6 solution fading from pristine yellow to colorless during the coating process. The nearly 100% yield is also verified by the good agreement between metal compositions in final products measured by inductively coupled plasma mass spectrometry (ICP-MS) and by EDX equipped on a scanning electron microscope (SEM), with those calculated from the precursor amounts used in syntheses (Table 3.4). Third, at 70 ℃ the reduction of Pt ions was dominated by the oxidation of ethanol rather than the oxidation of Pd atoms. Without a reducing agent, Pt atoms can be deposited via the galvanic displacement of Pd because Pd has a lower reduction potential than Pt.[383-385] That process could lead to either a small loss of Pd if the Pd ions remained in the solution at the end of synthesis or a Pd-Pt partially alloyed shell if oxidized Pd was reduced back by ethanol.

Table 3.4 Calculated compositions of synthesized Pd@Pt_{ML} core-shell nanoparticles, compared to those determined by ICP-MS and SEM-EDX. 60 mg 30wt% Pd/C and 63.4 μmol H_2PtCl_6 were used in the synthesis. Results suggested a Pt coating yield > 95%, and a Pd loss < 5%.

	Pd (wt%)	Pt (wt%)	Pd:Pt (at)
Calculated from precursor amounts	24.9	17.1	2.67
Determined by ICP-MS	26.1	18.0	2.65
Determined by SEM-EDX	/	/	2.64

3.3.3 Calculation of Atom Numbers in Pd@Pt Core-Shell Nanostructures

Based on an cuboctahedron model,[386] we calculated the Pt/(Pt+Pd) atomic ratios for individual Pd@Pt core-shell nanoparticles as a function of the particle size. Around a single central atom, the cuboctahedron cluster is formed by onion-like concentric atomic layers. In our calculation, the central atom was counted as the first shell, *i.e.*

$$m = 1 \tag{3.15}$$

for one single atom, where *m* is the number of shells.

The total number of atoms, *N*, as a function of the total number of atomic layers, *m*, was expressed as

$$N(m) = \frac{1}{3}(2m-1)(5m^2-5m+3) \tag{3.16}$$

We note that *N* and *m* consider both Pd atoms at the core and Pt atoms at the shell for a Pd@Pt core-shell nanoparticle. And the number of surface atoms, N_s, *i.e.* the number of atoms at the *m*-th shell, was expressed as

$$N_s(m) = 10m^2 - 20m + 12 \tag{3.17}$$

For Pd@Pt_{ML} nanoparticles with a 1 monolayer Pt shell, the Pt/(Pt+Pd) atomic ratio equaled the numeric ratio of surface atoms to total atoms

$$\frac{Pt}{Pt+Pd} = \frac{N_s(m)}{N(m)} = \frac{10m^2-20m+12}{\frac{1}{3}(2m-1)(5m^2-5m+3)} \tag{3.18}$$

For Pd@Pt_{2ML} nanoparticles with a two-monolayer Pt shell, the Pt/(Pt+Pd) atomic ratio equaled the numeric ratio of atoms at the *m*-th and the *(m−1)*th shell to total atoms. In addition, the number of atoms at the *(m−1)*th shell for a cluster of *m* complete shells equaled the number

of surface atoms for a cluster of (*m−1*) complete shells, $N_s(m-1)$, because each shell had the same geometrical shape.[387]

$$\frac{Pt}{Pt+Pd} = \frac{N_S(m)+N_S(m-1)}{N(m)} = \frac{(10m^2-20m+12)+[10(m-1)^2-20(m-1)+12]}{\frac{1}{3}(2m-1)(5m^2-5m+3)} \quad (3.19)$$

The diameter of the entire particle was estimated to be

$$d(m) = 0.45 \times m \quad (3.20)$$

The particle size distribution was assumed to follow the normal distribution, and the probability of one particular particle size can be expressed as

$$f(d) = \frac{1}{\sigma\sqrt{2\pi}} e^{-\frac{(d-\mu)^2}{2\sigma^2}} \quad (3.21)$$

where μ was the mean particle size and σ was the standard deviation. μ and σ were determined by TEM measurements.

Then all the *N(m)* and $N_s(m)$ were weighed by multiplying with the corresponding *f(d)*, and thus the Pt/(Pt+Pd) atomic ratio can be expressed as a function of particle size.

3.3.4 DFT Calculations on the Growth Mode of Pt Monolayer Shell

To better understand the growth mode of Pt monolayer shell on Pd nanoparticles at atomic level, we performed DFT calculations (Section 2.6.2). A hemisphere-like Pd_{174} nanoparticle model was employed to represent a ~2.2 nm sphere-like truncated octahedral Pd_{405} nanoparticle (Figure 3.27a) containing {111} and {100} facets, which are typical exposing facets for small fcc metal nanoparticles[148, 239]. Our previous studies demonstrated the capability of such a hemisphere model to well interpret the experimental electrochemical activities of core-shell nanoparticles.[72, 73] We first calculated the binding energy (BE) of a single Pt atom adsorbed at

different sites of the Pd nanoparticle in order to understand nucleation at the very early stage of Pt growth. The lower the BE is, the more preferable is the site. The results exhibit that a Pt atom prefers the 4-fold hollow site on Pd {100} facets (BE = −5.01 eV, step **1** in Figure 3.27a), followed by the 3-fold hollow site on Pd {111} facets (−4.28 eV at an *fcc* site, −4.20 eV at an *hcp* site, step **5**), then the bridge site at {111}/{111} edges (−3.75 eV), and at last the bridge site at {100}/{111} edges (−3.04 eV). In addition, a Pt adatom at the vertex site spontaneously moves to the {111}/{111} edge site during the geometry optimization. Therefore, the deposited Pt atom is likely to nucleate on the {100} or {111} terraces (steps **1** and **5**) rather than at edges.

Next, we studied the Pt growth mode after initial nucleation by comparing the BEs of Pt adatoms forming small Pt clusters on the {100} or {111} facets of Pd nanoparticle. A Pt_4 planar was employed to model the ordered Pt structure formed on Pd {100} facets, wherein each Pt atom sat at the most stable 4-fold hollow site. The Pt growth on Pd from an adatom to a 2D tetramer is highly exothermic releasing an energy of −15.13 eV (step **2** in Figure 3.27a), suggesting that the 2D growth of Pt on Pd {100} is energetically preferred. It also shows that the further growth from Pt_4 to Pt_5 favors the formation of a 2D planar rather than a 3D cluster by 1.51 eV (steps **3** vs. **4**), due to the formation of additional strong Pt-Pt and Pt-Pd bonds. Similar phenomena were observed for Pd {111} facets as well (steps **6**, **7** and **8**), though energetically the Pt growth on Pd {111} are less preferential than that on {100} facets (steps **7** vs. **3**).

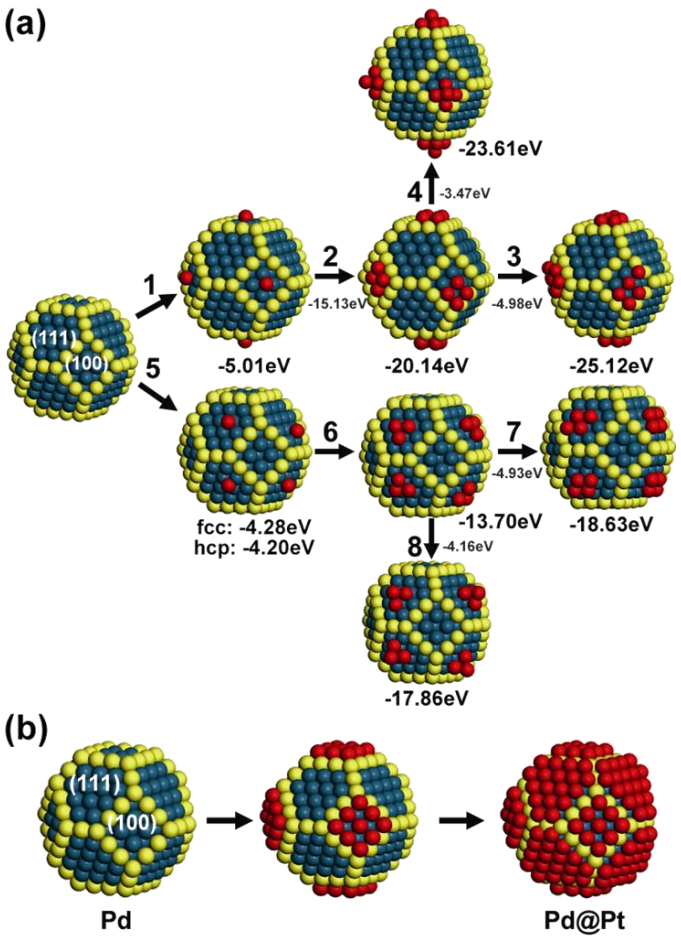

Figure 3.27 (a) DFT-calculated binding energies (BEs) of Pt atoms (red) on {100} and {111} terraces of a Pd nanoparticle represented by a sphere-like truncated octahedron Pd_{405} nanoparticle model with a 2.2 nm diameter. BEs are shown in eV per facet. (b) Proposed growth scheme for sphere-like truncated octahedral Pd@Pt core-shell nanoparticles, based on the calculated BEs shown in (a). Color scheme: Dark blue for Pd atoms on terraces, yellow for Pd atoms at edges and vertices, red for Pt atoms.

Considering all the DFT results discussed above, we propose a growth scheme for the sphere-like truncated octahedral Pd@Pt core-shell nanoparticles (Figure 3.27b). The growth of Pt shell starts from the formation of an ordered Pt monolayer on Pd {100} facets, followed by the closure of an ordered Pt monolayer on Pd {111}. A similar growth mode has been proposed

recently for a ~1.7 nm Pt@Cu core-shell nanoparticle.[388] Overall, our DFT-calculated results clearly demonstrate that the epitaxial layer-by-layer growth of Pt is thermodynamically favorable on Pd nanoparticles, and hence the elevated temperature during syntheses should facilitate the formation of a uniform and complete Pt shell on Pd cores.

3.3.5 ORR Activity in Acid Solution

The electrochemical performances of Pd@Pt_{ML} and Pd@Pt_{2ML} samples were measured using the RDE technique in 0.1 M $HClO_4$ solution at room temperature. Electrochemical surface area (ECSA) was calculated using the integrated hydrogen-desorption charges from the cyclic voltammetry (CV) curves assuming 0.21 mC cm^{-2}.[389] The ORR polarization curves were measured at 10 mV s^{-1} with a 1600-rpm rotation rate. The kinetic currents at 0.9 V was calculated from the ORR polarization curves using

$$j_k = j / (1 - j / j_L) \quad (3.22)$$

where j was the measured current at 0.9 V and j_L was the diffusion limiting current below 0.5 V. The obtained kinetic current was further normalized to ECSA, and metal mass (Pt mass or total metal mass) to calculate specific activity (SA) and mass activity (MA), respectively.

Table 3.5 summarizes the ORR activities for Pd@Pt_{ML} and Pd@Pt_{2ML} samples, compared with those for commercial carbon-supported Pt catalyst (45.4 wt% Pt/C, TKK). The core-shell Pd@Pt samples exhibit enhanced activities than Pt/C. For example, the Pt mass activity (MA_{Pt}) of 0.64 A mg^{-1} obtained on the core-shell Pd@Pt_{ML} catalyst, is 2.9 times that of the Pt/C catalyst (0.22 A mg^{-1}, Figure 3.29). These electrochemical results indicate that the synthetic approach using the solvent ethanol as the reductant is an effective scale-up route to fabrications of Pt

monolayer catalysts with enhanced ORR activities.

Table 3.5 Mass activities and specific activities for $Pd@Pt_{ML}$ and $Pd@Pt_{2ML}$, in comparison those for with commercial Pt/C, derived from the ORR kinetic currents at 0.9 V (vs. RHE).

	Pt/C	$Pd@Pt_{ML}$	$Pd@Pt_{2ML}$
Pt/(Pt+Pd) (at%)	/	27.3	33.3
Pt (wt%)	45.4	17.1	18.1
Pd (wt%)	/	24.9	19.7
MA_{Pt} ($A\ mg^{-1}$)[a]	0.22	0.64	0.62
$MA_{Total\text{-}Metal}$ ($A\ mg^{-1}$)[b]	0.22	0.26	0.30
SA ($mA\ cm^{-2}$)[c]	0.48	0.58	0.70

[a]MA_{Pt}, mass activity normalized by the mass of Pt. [b]$MA_{Total\text{-}Metal}$, mass activity normalized by the total mass of metals including Pt and Pd. [c]SA, specific activity normalized by the electrochemical surface area.

Besides good catalytic activities, the $Pd@Pt_{ML}$ sample also exhibited exceptional durability after pulse-potential stability test. As shown in Figure 3.28, after 5000 cycles of potential pulses (10 s at 0.6 V and at 1.0 V each), the ORR polarization curve remained unchanged, and the cyclic voltammetry curve showed negligible loss of ECSA. The excellent durability is attributed to the uniform and complete Pt monolayer shell.

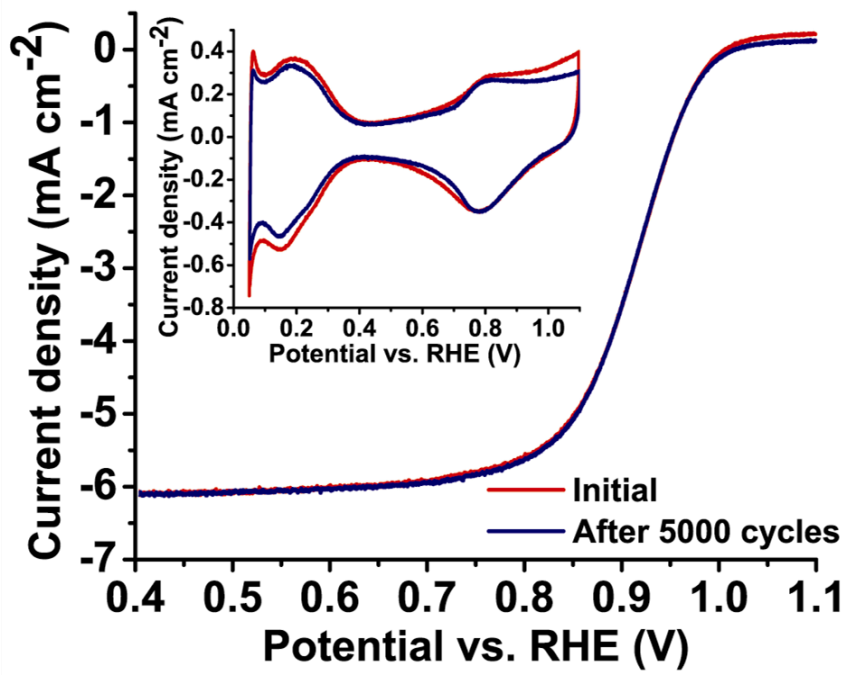

Figure 3.28 ORR polarization (10 mV s^{-1}, 1600 rpm) and cyclic voltammetry (inset) curves (50 mV s^{-1}) obtained in 0.1 M $HClO_4$ solutions on a $Pd@Pt_{ML}$ sample, before (red) and after (blue) 5000 potential-pulse cycles of 0.6 V (10 s) - 1.0 V (10 s).

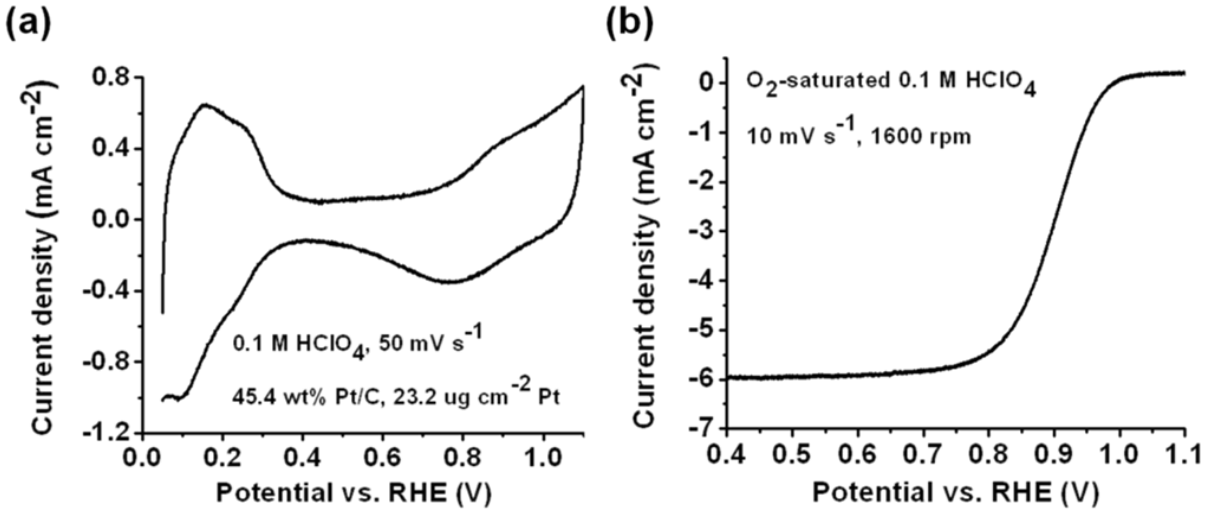

Figure 3.29 (a) Cyclic voltammetry and (b) ORR polarization curves obtained in 0.1 M $HClO_4$ solutions on commercial 45.4 wt% Pt/C.

3.3.6 Summary

In conclusion, we have demonstrated a surfactant-free and high-yield chemical route for coating of Pt atomic layers on Pd nanoparticles, which ensures high reproducibility and scalability. The conformity and continuousness of Pt shells were verified by various characterization techniques. The DFT calculations also showed that two-dimensional growth is energetically favorable. The uniform and complete Pt coating is promoted by the coating process with slow kinetics in ethanol, and the reaction temperature of 70 °C rather than room temperature. The strategy illustrated here could be applicable to the fabrication of other bimetallic or multimetallic core-shell nanoparticles for various applications.

3.4 Hollow Pd-Based Core Supported Pt Monolayer Catalysts for Oxygen Reduction

In Section 3.3, Pd@Pt core-shell nanocatalysts were fabricated, and they exhibited enhanced ORR activity in acid electrolyte. In this section, further efforts in promoting the ORR activity were made by synthesizing Pt monolayer catalysts on hollow Pd and Pd-Au core nanoparticles.

3.4.1 Fabrication of Hollow Nanoparticles

Figure 3.30 depicts the synthetic route to obtain Pt monolayer catalysts supported on hollow Pd-Au cores. Ni nanoparticles, having diameters less than 9 nm, generated by pulse electrodeposition, were well dispersed on carbon support (Figure 3.31a). In the absence of oxygen, partial galvanic replacement of Ni atoms by mixed Pd and Au ions yielded noble-metal shells on Ni particles, which further formed Pd-Au hollow particles upon dissolution of the remaining Ni in acidic solutions at room temperature, as described in the experimental process in Section 2.2.1.

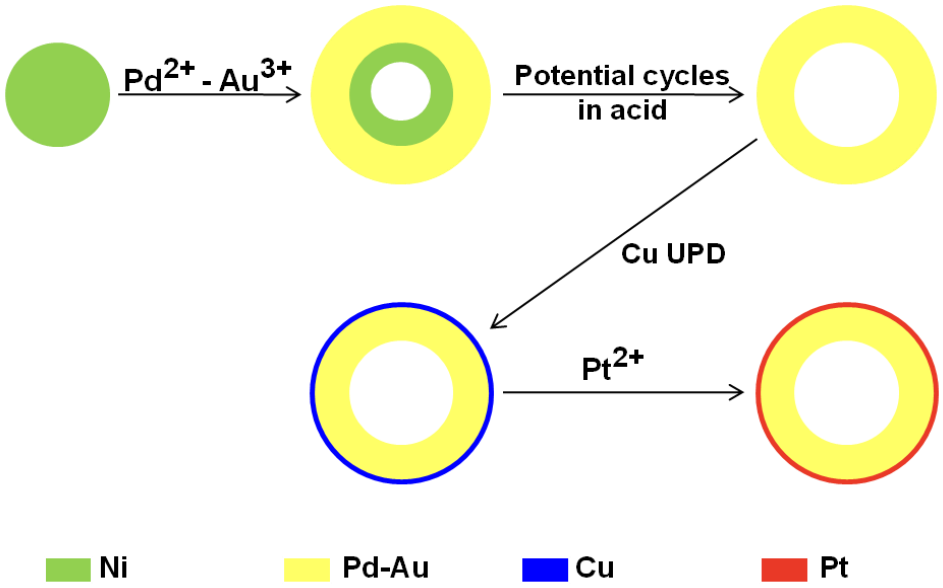

Figure 3.30 Sketch of the procedure for fabricating Pt monolayer catalysts on Pd-Au hollow nanoparticles (Pd_xAu(hollow)@Pt_{ML}).

Figure 3.31 b-d show TEM images of the Pt monolayer catalysts made with as-prepared hollow Pd-Au cores, denoted as Pd_xAu(hollow)@Pt_{ML} catalysts, where x is the atomic ratio of Pd to Au. The high-resolution image in Figure 3.31c also reveals the catalysts' polycrystalline structure. No Ni was detected in the samples by ICP-MS, suggesting the more easily complete removal of Ni than Cu as sacrificial templates to produce hollow nanostructures[390].

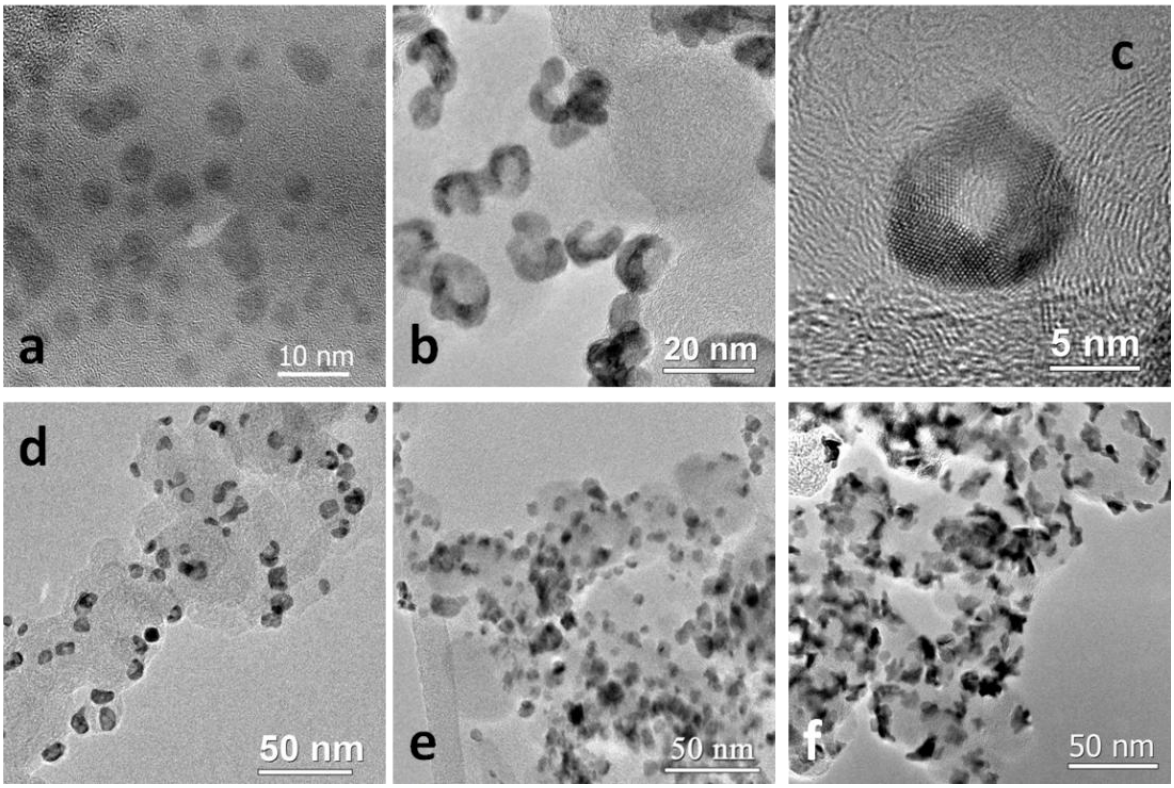

Figure 3.31 TEM images of carbon-supported (a) pulse-electrodeposited Ni nanoparticles, (b-c) $Pd_{20}Au(hollow)@Pt_{ML}$ nanoparticles fabricated using Ni nanoparticles as templates, (d) $Pd_{10}Au(hollow)@Pt_{ML}$ nanoparticles fabricated using Ni nanoparticles as templates, (e) $Pd@Pt_{ML}$ nanoparticles, and (f) pulse-electrodeposited Pt nanoparticles.

3.4.2 ORR Activity in Acid Solution

The ORR activity and electrochemical surface area (ECSA) of the catalysts were measured in 0.1 M HClO4 solutions after 5000 step potential cycles between 0.6 and 1.0 V (vs. RHE, 5 s at each potential) to represent the quasi-stabilized activities. Electrochemical surface area (ECSA) was calculated using the integrated hydrogen-desorption charges from the cyclic voltammetry (CV) curves assuming 0.21 mC cm^{-2}.[389] Kinetic currents at 0.9 V were calculated from the ORR polarization curves using equation

$$j_k = j / (1 - j / j_L) \quad (3.23)$$

The obtained kinetic current was further normalized to ECSA and metal mass (Pt mass, Pd + Pt mass, or total-metal mass) to calculate specific and mass activities, respectively.

Figure 3.32 shows that similar ORR polarization curves were obtained for the hollow $Pd_{20}Au$(hollow)@Pt_{ML} catalyst and the solid electrodeposited Pt/C catalyst, while their voltammetry curves differ significantly. The H adsorption/desorption charge at low potentials and the OH adsorption/desorption charge at high potentials are both smaller on the hollow sample than on the Pt/C(solid) sample because of three reasons. (i) The catalyst loading is lower on the hollow sample. This also leads to a higher mass activity on the hollow sample, even when similar activities are found from polarization curves for both hollow and solid samples. (ii) The hollow sample has smaller specific surface area due to a larger average particle size (9 nm for the hollow sample versus 4 nm for the solid sample)[391]. (iii) The smooth and contracted surface of the hollow sample adsorbs less H and OH because the high-coordination sites on smooth terraces are less reactive than the low-coordination sites at edges and defects. Although these reasons suggest that calculating the ESA with the same H desorption charge density of 0.21 mC cm^{-2} for the hollow sample results in a smaller value than the geometric Pt surface area, we use this method for reporting the specific activity since it has become a conventional method and serves the purpose of representing the less reactive Pt surface is more conductive to the desorption-limited ORR.

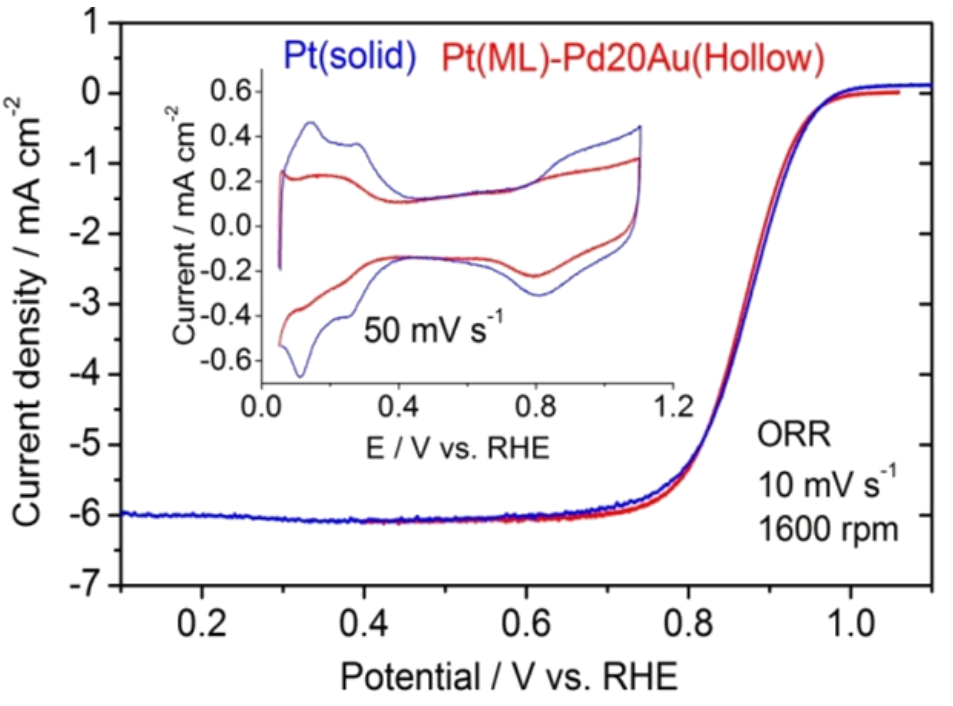

Figure 3.32 ORR polarization and voltammetry (inset) curves in O_2-saturated and deaerated 0.1 M $HClO_4$, respectively, for hollow $Pd_{20}Au$(hollow)@Pt_{ML} nanocatalyst (loading: 1.4 ug cm^{-2} Pt, 3.9 ug cm^{-2} total metal) (red) made using electrodeposited Ni templates, and for solid Pt/C nanoparticles (loading: 14.3 ug cm^{-2} Pt) (blue) made by electrodeposition.

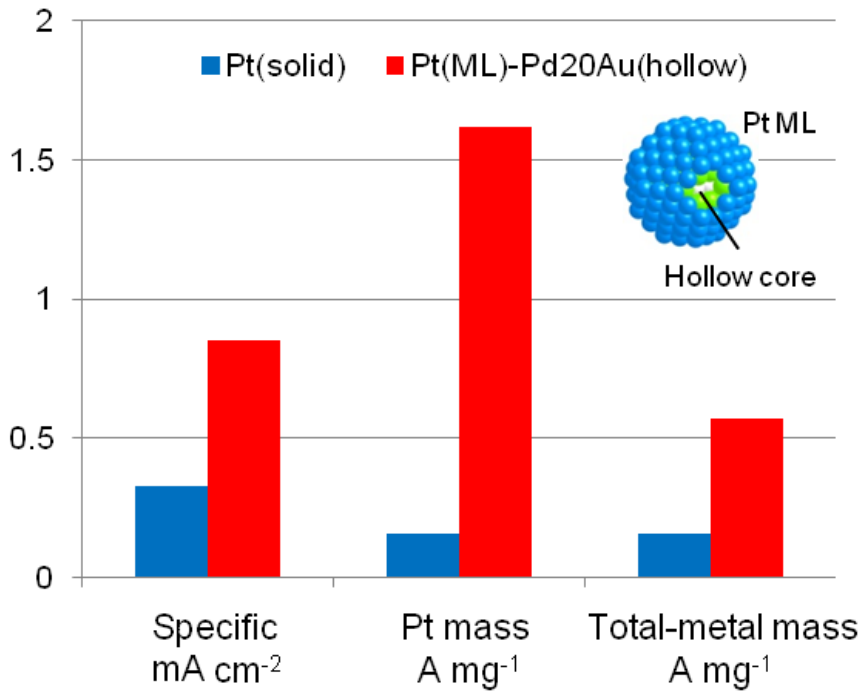

Figure 3.33 Comparison of the ORR specific and mass activities derived from the kinetic currents at 0.9 V (vs. RHE) in Figure 3.32 for hollow $Pd_{20}Au$(hollow)@Pt_{ML} nanocatalyst (red) made using electrodeposited Ni templates, and for solid Pt/C nanoparticles (blue) made by electrodeposition.

Figure 3.33 compares the specific and mass activities determined from the ORR kinetic currents at 0.9 V (vs. RHE). The $Pd_{20}Au$(hollow)@Pt_{ML}/C sample yielded a total-metal mass activity of 0.57 A mg^{-1}, which was 3.5 times that of solid Pt/C nanoparticles fabricated by pulse electrodeposition (0.16 A mg^{-1}). The comparison is made between our hollow-core sample and the sample of pulse-electrodeposited solid Pt nanoparticles on carbon support, in order to illustrate that the enhanced activities are not due to the full exposure of all the electrodeposited metal particles to the electrolyte, while the commonly used benchmark, a commercial Pt/C catalyst thin film directly put on the electrode, might have some metal particles that are buried

inside and not in contact with the electrolyte.

Table 3.6 Specific and mass activities for the ORR derived from the kinetic currents at 0.9 V in O_2-saturated 0.1 M $HClO_4$, for carbon-supported Pt monolayer catalysts on hollow Pd-based nanoparticles, compared to those on solid Pt/C catalyst made using pulse electrodeposition.

Samples	SA ($mA\ cm^{-2}$)[a]	MA_{Pt} ($A\ mg^{-1}$)[b]	MA_{Pt+Pd} ($A\ mg^{-1}$)[c]	$MA_{Total\text{-}Metal}$ ($A\ mg^{-1}$)[d]
Pt monolayer catalysts on hollow Pd-based cores supported on carbon				
$Pd(hollow)@Pt_{ML}/C$	0.90	1.50	0.45	0.45
$Pd_{20}Au(hollow)@Pt_{ML}/C$	0.85	1.62	0.61	0.57
$Pd_{10}Au(hollow)@Pt_{ML}/C$	0.94	1.15	0.45	0.41
Electrodeposited Pt nanoparticles on carbon				
Pt/C	0.33	0.16	0.16	0.16

[a]SA, specific activity normalized by the electrochemical surface area. [b]MA_{Pt}, mass activity normalized by the mass of Pt. [c]MA_{Pt+Pd}, mass activity normalized by the mass of Pt and Pd. [d]$MA_{Total\text{-}Metal}$, mass activity normalized by the total mass of metals including Pt, Pd and Au.

Table 3.6 summarizes the specific and mass activities for the ORR on several samples. All the hollow-core samples, including $Pd(hollow)@Pt_{ML}/C$, $Pd_{20}Au(hollow)@Pt_{ML}/C$ and $Pd_{10}Au(hollow)@Pt_{ML}/C$, displayed enhanced total-metal mass activities ($MA_{Total\text{-}Metal}$), ranging from 0.41 to 0.57 A mg^{-1}. The best $MA_{Total\text{-}Metal}$ value of 0.57 A mg^{-1}, obtained on the $Pd_{20}Au(hollow)@Pt_{ML}/C$ sample, is 2.2 times that of the Pt monolayer catalyst on solid Pd cores (0.26 A mg^{-1} for $Pd@Pt_{ML}$, Table 3.5). The value of 0.26 A mg^{-1} for $Pd@Pt_{ML}$ is consistent with

the activity values in reference [373] measured under similar conditions, though it may differ from other literature values for Pt monolayer catalysts on solid Pd nanoparticles. Various measurement conditions, including but not limited to sweep rates, rotation frequencies, temperature, composition and concentration of electrolytes, metal loadings on electrodes and the potential used to determine kinetic currents, could impose effects on the final values for specific and mass activities for the ORR.

3.4.3 Morphological Effects and Lattice Contraction

We ascribe the enhanced Pt mass and total-metal mass activities of Pt monolayer catalysts supported on hollow cores to the smooth surface morphology and hollow-induced lattice contraction. The rounded and smooth surface morphology of the Pt monolayer catalyst supported on hollow Pd-based cores is evident in comparing the TEM images for $Pd_{10}Au$(hollow)@Pt_{ML} particles (Figure 3.31d) with that for solid Pd@Pt_{ML} nanoparticles (Figure 3.31e), and that for a solid Pt/C sample made by pulse electrodeposition (Figure 3.31f). In addition, lattice contraction was found for Pt monolayer on hollow cores by X-ray diffraction (XRD) measurements, consistent with the previous discovery of hollow-induced lattice contraction on hollow Pt particles[392]. Synchrotron XRD experiments were carried out at beamline X7B (λ = 0.3196 Å) of the National Synchrotron Light Source (NSLS) at Brookhaven National Laboratory. The fitted parameters (lattice constant and particle size) were obtained through a Rietveld refinement. As shown in Figure 3.34, diffraction peaks shift to higher angles for the Pt monolayer catalyst with Pd_9Au(hollow) core compared to that with Pd_9Au(solid) and Pd(solid) cores, indicating a smaller lattice spacing was induced by hollow cores.

The low-coordination sites at edges and defects are known to bind oxygen more strongly than the high-coordination sites do, and are prone to dissolution[393, 394]. Previous studies have shown that the ORR kinetics on Pt surface is limited by the O and OH desorption rate at high potentials[395-397]. Smooth surface reduces the site-blocking by oxygen-containing species, and thus, enhances the activity and durability for the ORR[143, 373]. Demonstrated by the density functional theory calculations, the binding energy for reactive adsorbates varies with the electronic structure (d-band center) of the catalyst, and thus, affects the surface reactivity[398, 399]. Compressive strain induced by lattice mismatch weakens oxygen binding and has been attributed to the observed enhancement for the ORR on core-shell nanocatalysts[72, 77, 153, 400, 401]. The lattice contraction induced by the hollow structure provides an alternative route to fine tuning oxygen binding characteristics on catalysts' surface toward better ORR activities.

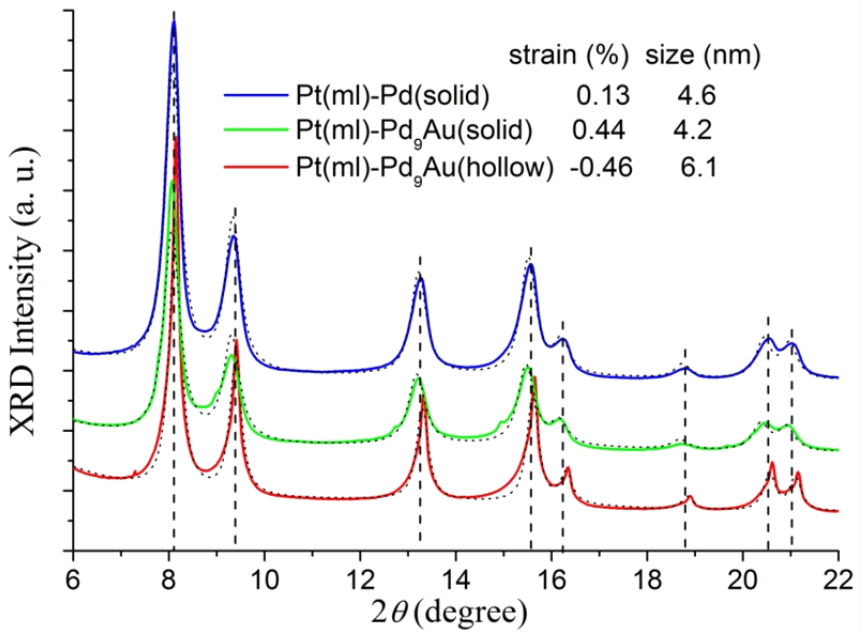

Figure 3.34 Synchrotron XRD diffractograms for three Pt monolayer catalysts on Pd(solid) (blue, top), Pd_9Au(solid) (green, middle), and Pd_9Au(hollow) (red, bottom) cores. The dotted lines are

the fits, yielding the average particle diameters and lattice constants. The lattice strains listed are calculated with respect to the lattice constant of bulk Pt (3.923 Å).

3.4.4 Formation Mechanism for Hollow Structures

The possible formation mechanism for hollow nanostructures was proposed based on galvanic replacement[402-404] and Kirkendall effect[379, 405, 406]. Galvanic replacement reaction occurs spontaneously in a solution phase when atoms of one metal meet ions of another metal having a higher reduction potential[407]. Kirkendall effect is a nonreciprocal atomic diffusion process occurred through vacancy exchange in a diffusion couple[359]. The imbalanced atomic fluxes of counter-flowing atoms with different diffusivities will be balanced by a compensating "vacancy wind" that blows in a direction opposite to the net mass flow[408].

The formation of hollow structures in these systems was governed by both galvanic replacement and Kirkendall effect. The driving force for the galvanic replacement reaction is the reduction potential difference between two metals[409]. While in the Kirkendall diffusion process the net flux of compensating vacancies is proportional to the diffusivity difference[408]. In principle, metal ions with higher reduction potentials than that of Ni^{2+}/Ni (−0.257 V vs. standard hydrogen electrode, SHE) can replace Ni atoms and form a thin shell on the surface of Ni templates. If these metals diffuse slower than Ni, vacancies will be generated inside core-shell nanostructures, and they may coalesce into a single void (hollow structure) or multiple voids (porous structure).

In comparison with Pt[392], we found that hollow structures were more difficult to form with Pd or Au ions alone when using Ni nanoparticles as sacrificial templates. Better results were

obtained using a mixed solution of $Pd(NH_3)_4Cl_2$ and $HAuCl_4$ to galvanically replace Ni. Typical TEM images of the $Pd_{20}Au$(hollow)@Pt_{ML}/C and $Pd_{10}Au$(hollow)@Pt_{ML}/C samples with hollow cores are shown in Figure 3.31b and Figure 3.31d, respectively. The melting temperatures[334] for Au (1337 K), Ni (1728 K), Pd (1828 K), and Pt (2045 K) suggest that (1) Ni diffuses slower than Au, and (2) Ni-Pd diffusivity differs less than Ni-Pt [410-413]. Hollow Au particles cannot be made with Ni templates because when the remaining Ni atoms dissolve, the faster diffusing Au atoms fill the vacancies inside resulting in solid Au particles. A Ni-Pd core-shell particle may not yield a hollow Pd particle because the diffusivity difference between Ni and Pd is not large enough to create sufficient vacancies to form hollows.

Adding Au ions in Pd solutions may mediate the diffusion process and promote the formation of hollow particles. In the Pd-Au mixed solution, since the standard reduction potential of the $AuCl_4^-$/Au redox couple (1.002 V vs. SHE) is higher than that of the $Pd(NH_3)_4^{2+}$/Pd couple (0.902 V vs. SHE)[414], Au ions will be preferentially reduced instead of Pd ions and deposited on the surface of Ni templates as a thin shell. The imbalance between the outward flux of faster-diffusing Ni-Au atoms and the inward flux of slower-diffusing Pd atoms will get compensated by an inward flux of vacancies. The vacancies will then supersaturate and coalesce into a single void. On the shell surface, the Ni atoms that flowed out will spontaneously dissolve because of their lower reduction potential, while the Au atoms will remain intact because of their higher reduction potential. The broken or open shells in Figure 3.31b and Figure 3.31d can be explained by preferential reaction along certain directions[415].

3.4.5 Summary

We have fabricated Pt monolayer catalysts on hollow Pd and Pd-Au cores that were made using pulse electrodeposited Ni nanoparticles as sacrificial templates. The hollow architecture of the Pd-Au particles was achieved by the delicate balance between galvanic displacement and Kirkendall effect in controlling reaction kinetics. The smooth surface morphology and lattice contraction, as well as the mass-saving resulted from the hollow structure, have accordingly enhanced the electrocatalysts' total-metal mass activities for the ORR up to 0.57 A mg^{-1}. This is 2.2 times that of 0.26 A mg^{-1} for a Pt monolayer catalyst on solid Pd cores, and 3.5 times that of 0.16 A mg^{-1} for solid Pt nanoparticles made by pulse electrodeposition. This synthetic strategy can be applied to other core-shell systems for the formation of metallic or bimetallic, double- or multi-layered, hollow or porous nanostructured electrocatalysts.

3.5 ORR in Alkaline Solution on Au Monofaceted Nanocrystals

Four-electron oxygen reduction reaction (4e-ORR), as a key high-performance pathway in energy conversion, has been sought after in numerous investigations of metal surfaces over the last decades. Although the surfaces of most noble metals, e.g. platinum and palladium, demonstrate the full-potential-range 4e-ORR, this is not the case, till now, for gold (Au) surfaces. Such experimental absence of full-range 4e-ORR on Au has consequently restricted elucidating the ORR mechanisms on metal surfaces. Herein we employed Au nanocrystal surface as a platform to reveal the ORR pathways on a series of single-crystalline facets, including {111} on octahedra, {100} on cubes, and {310} on truncated ditetragonal prism (TDP) nanocrystals. In contrast to the octahedral and cubic Au nanoparticles that show catalytic behaviors similar to their single-crystal counterparts, we discovered a full-range 4e-ORR on gold {310} facets of Au TDP nanocrystals in alkaline solution. Combining our experimental results with density functional theory calculations, we propose that the combination of the low-coordinated Au surface sites and the dioxygen-water co-adsorption results in the observed selectivity of the ORR pathway on Au nanocrystal surfaces. Our studies demonstrate that catalytic performance can be tailored by shaping nano-objects through the realization of specific atomically defined facets.

3.5.1 Synthesis and Characterization of Au Nanocrystals

Our solution-phase synthesis methods[318, 416] permitted creating monofaceted nano-objects (octahedra, cubes, TDPs) with a narrow size distribution, and with a high-fidelity terminating surface. The typical employed synthesis procedures yield single-crystalline nanoparticles with clean surfaces after a simple washing, so enabling us to precisely probe the ORR behaviors on

the nanofacets. In shape-controlling synthesis of Au nanocrystals, we used the multi-step procedure to prepare various polyhedral nanocrystals with edge lengths above 40 nm. The Au octahedra were formed in an aqueous solution of cetylpyridinium chloride (CPC), via reducing the $AuCl_4^-$ ions by ascorbic acid at 25 ℃. The surfactant CPC is weakly adsorbed, and accordingly, removing it to obtain clean Au surfaces does not require harsh treatments[416, 417]. We ensured sufficient protection of the {111} facets during the growth of Au octahedra by using a high concentration of the surfactant (CPC), and a low concentration of the reducing agent (ascorbic acid)[418, 419]. For preparing the Au cubes, we added KBr and raised the reaction temperature to 32 ℃. In synergy with CPC, the cationic surfactant with Br^- counter-ions stabilizes the {100} facets, in a way similar to that of the surfactant cetyl-trimethylammonium bromide (CTAB)[420]. The Au TDPs were obtained by adding HCl and a small amount of Ag^+. A monolayer of Ag may form on Au, serving as a short-lived facet-blocking adsorbate during a crystal growth[416]. Since the amount of reducing agent is less than that required for the complete reduction of all the metal ions present, the Ag monolayer is removed via galvanic replacement by the excess Au ions at the end of synthesis. Energy dispersive X-ray spectroscopy (EDX) analysis confirmed that no trace of Ag was left on the final TDP surface (Figure 3.35). While previously we prepared the Au TDPs at 25 ℃,[416] we found in this study that raising the temperature to 50 ℃ can speed up the synthesis without compromising quality. The yields of all three types of Au nanocrystals are higher than 95%, and the standard deviations in particle size distribution are below 4% (Table 3.7).

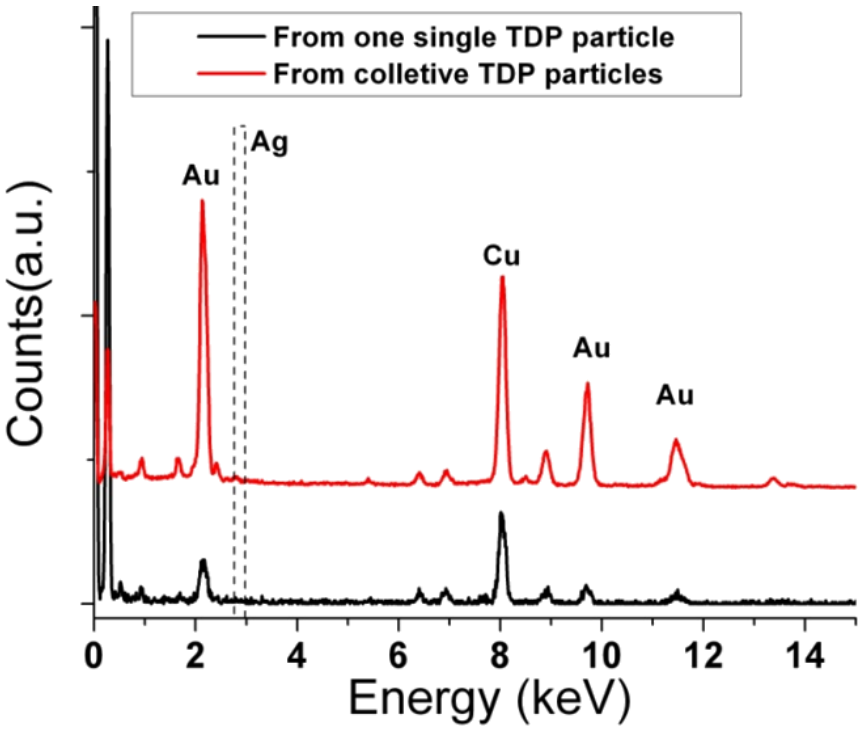

Figure 3.35 EDX analysis on the collective Au TDPs and the individual Au TDP, respectively. The peak of Cu comes from the grid substrate. The results demonstrate that no trace of Ag is observed from the synthesized TDP surfaces.

The high uniformity of particle sizes and shapes assures that these nanocrystals assemble readily into ordered, densely packed structures. The scanning electron microscopy (SEM) images, shown in Figure 3.36, reveal that the packing types are primarily determined by the particle shapes. For example, the Au octahedra (~42 nm edge length, Figure 3.36a_2) with eight {111} faces (Figure 3.36a_3) assemble only via incomplete face-to-face contact with their neighbors: the bottom layer forms a simple hexagonal arrangement biased by a flat substrate surface (Figure 3.36a_2). Then, a Minkowski-like structure forms after a few staggered layers, which increases the density of three-dimensional packing[421] as depicted in Figure 3.36a_1. Au cubes with six {100} faces (Figure 3.36b_3) have an average edge length of ~48 nm (Figure

3.36b_2) and form closely packed layers with in-plane square symmetry (Figure 3.36 b_1-b_2). The Au TDPs enclosed by twelve {310} facets (Figure 3.36c_3) with the long edge ~45 nm act like spheres, and thus, assemble into a quasi-hexagonal packing structure within the layer (Figure 3.36 c_1-c_2).

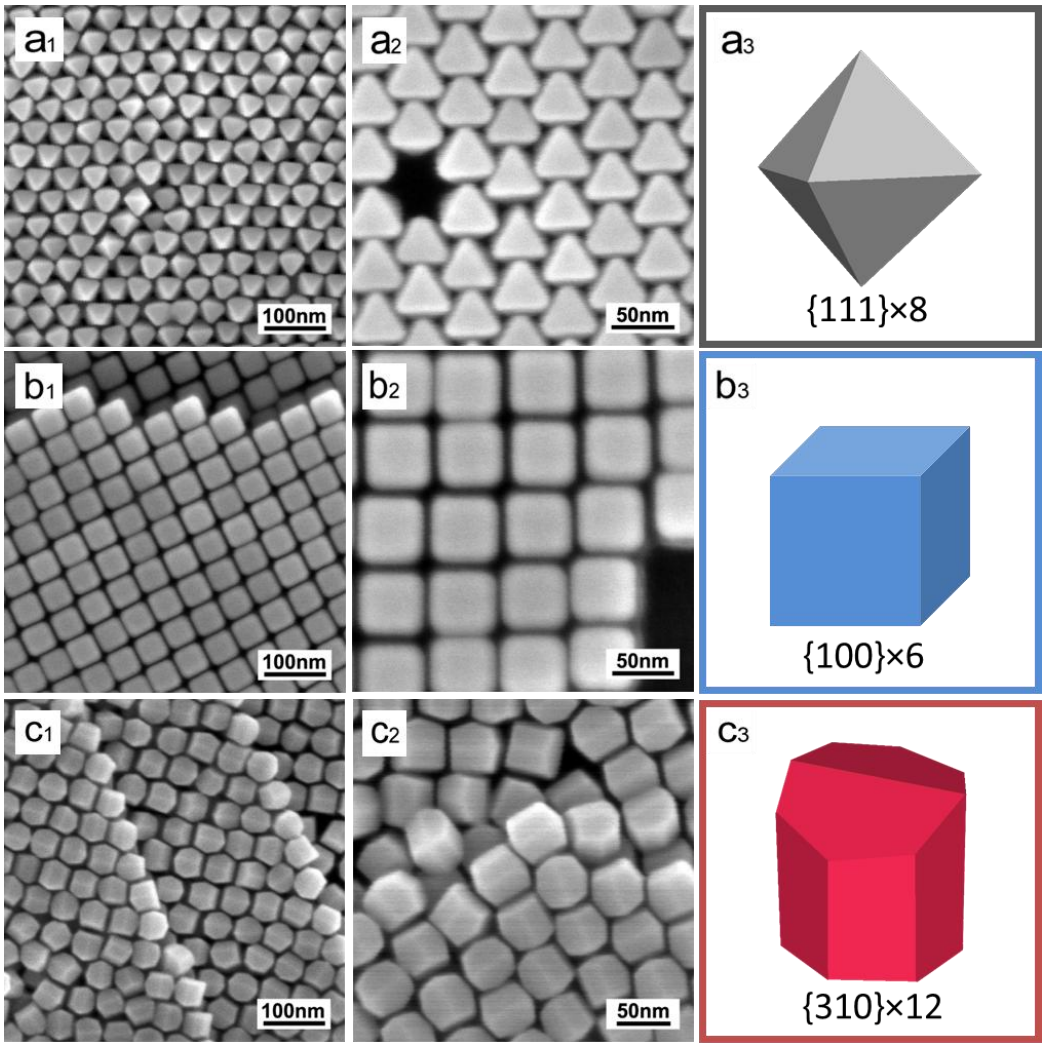

Figure 3.36 Self-assembly of Au nanocrystals. (a_1-c_1) Typical large-area SEM images of Au nanocrystals. (a_2-c_2) Locally magnified SEM images of Au nanocrystals. (a_3-c_3) Schematic representation of nanocrystals' polyhedral shapes. (a) Au octahedral nanocrystals. (b) Au cubic nanocrystals. (c) Au TDP nanocrystals.

Table 3.7 Average edge lengths (L), size distribution standard deviations (σ), and yields of Au cubic, octahedral, and TDP nanocrystals.

Nanocrystal shape	Edge length L (nm)	Size distribution standard deviations σ (%)	Yield (%)
Cube	48	2.6	96
Octahedron (small)	42	2.4	95
Octahedron	62	3.3	95
TDP	45	3.7	96

We further characterized the atomic lattice structures of these mono-faceted nanocrystals using transmission electron microscopy (TEM) and selected area electron diffraction (SAED). In Figure 3.37, TEM images of multiple (a_1-c_1) and single (a_2-c_2) particles of Au octahedra (a), cubes (b), and TDPs (c) are shown with the SAED patterns (a_3-c_3) obtained from the corresponding single particles. The sharp diffraction dots in the characteristic SAED patterns confirm the nanocrystals' single crystallinity.

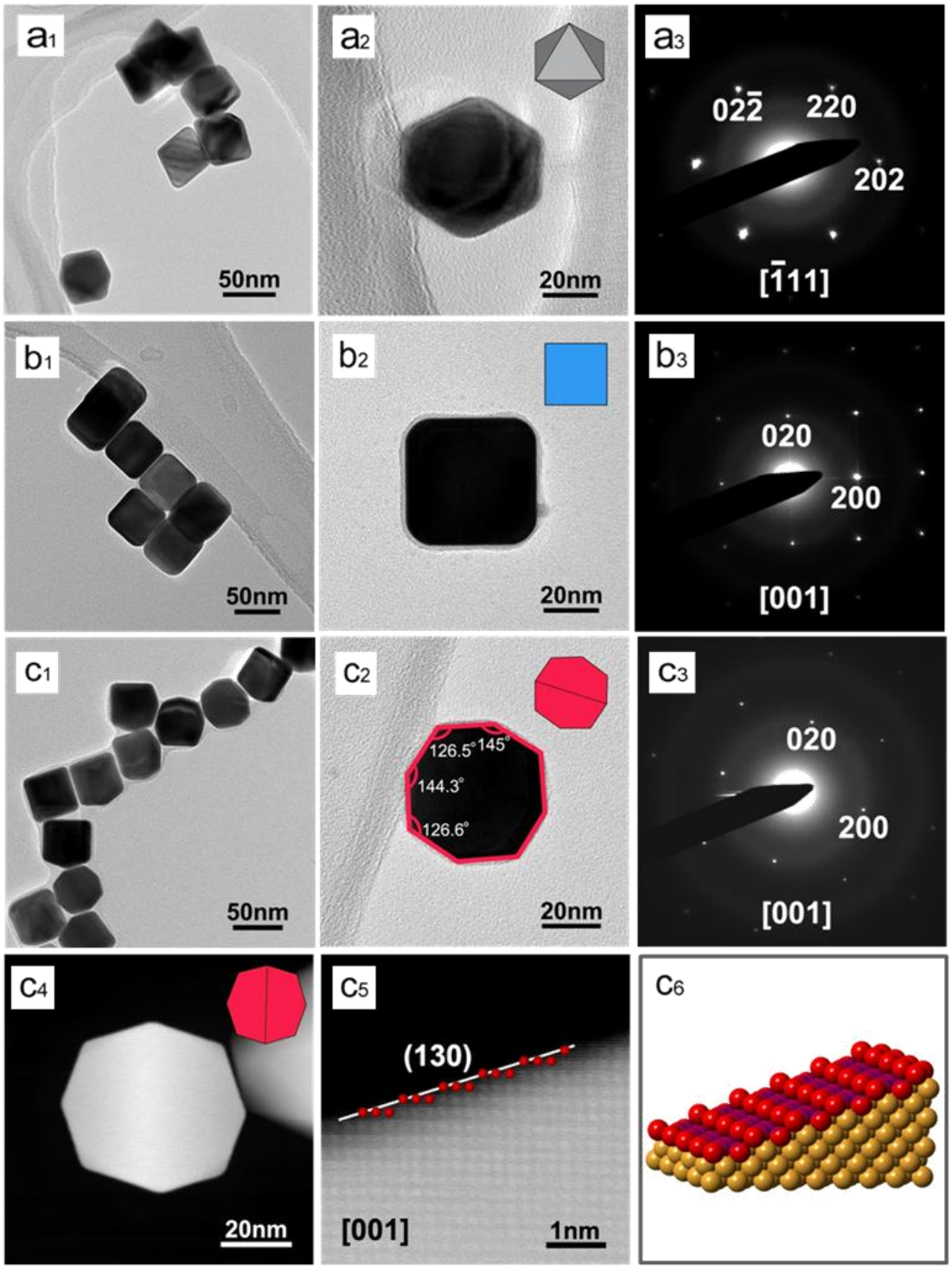

Figure 3.37 Structural characterization of Au nanocrystals. (a_1-c_1) TEM images of multiple Au nanoparticles, (a_2-c_2) TEM images of single Au nanoparticles, and (a_3-c_3) SAED pattern for Au nanocrystals of (a) octahedra, (b) cubes and (c) TDPs. (c_4) STEM image of a single Au TDP

nanoparticle. (c_5) High-resolution HAADF-STEM image of the TDP surface, showing its {110} and {100} sub-facets. (c_6) Tilt-view atomic model of the {310} facet. The red and yellow spheres, respectively, represent surface- and bulk-atoms.

The Au TDP nanocrystals are bounded by twelve high-indexed {310} facets that can be considered as a stepped surface with the vector sum of one {110} facet, and two {100} facets (Figure 3.37c_6). Typically, when viewed along the [001] direction, the projection profile of TDP appears di-tetragonal, while the correspondingly measured inner angles are close to those calculated from the ideal TDP model with {310} side facets. Orienting the Au TDPs along the axis of the [001] zone can drive their {310} facets parallel to the electron beam, so allowing us to directly observe the atomic arrangement by the high-resolution scanning TEM (STEM) with a high-angle annular dark field (HAADF) detector. As displayed in Figure 3.37c_5, the sub-facets of the {110} and {100} planes clearly are present in the {310} facet oriented in the [100] direction, matching well the atomic model (Figure 3.37c_6).

3.5.2 Electrochemical Characterization

To evaluate the electrochemical behaviors of the three types of Au nanocrystals in alkaline electrolyte, the nanocrystals were drop-casted onto glassy carbon electrodes followed by washing. We have conducted electrochemical measurements for all nanocrystal types, and the color-coded curves are shown in Figure 3.38 accordingly to the color scheme of SEM images (Figure 3.38d). The surface cleanness and crystallinity of these mono-faceted nanocrystals were tested by signature cyclic voltammograms and thallium under-potential deposition (Tl UPD) on well-ordered surfaces.

3.5.2.1 Cyclic Voltammetry

The cyclic voltammograms in deaerated 0.1 M NaOH (Figure 3.38e) show that the surface oxidation of Au occurs above 1.2 V for both cubes (blue) and TDPs (red) in positive potential sweeps, wherein a small peak around 1.0 V on the cubes could be related to the reconstruction lifting on Au {100}[422]. Also, we did not observe any anodic peak below 1.2 V on the TDPs even in the first potential cycle, thus confirming that the surface is free of Ag and organic species.

3.5.2.2 Tl Underpotential Deposition

We carried out Tl underpotential deposition (UPD) measurements to acquire additional electrochemical characteristics, because Tl monolayer and co-adsorbed Tl^{+}-OH^{-} adlayer phases are very sensitive to the structure and quality of Au single-crystal surfaces, and the phase transition between these two phases generates sharp voltammetry peaks. The Tl UPD curves (Figure 3.38f) obtained for octahedra (dark grey) and cubes resemble those on the corresponding well-oriented clean Au {111}[423] and {100}[424] bulk single-crystal surfaces, albeit with broadened peaks due to influences from the edges and corners of nanoparticle facets. Above 0.9 V, the rising anodic currents for all three types of nanocrystals signal the vanishing of ordered coadsorbed Tl^{+}-OH^{-} adlayer[423]. The observed characteristic phase-transition features of the Tl UPD curves demonstrate the high quality of the facets for all synthesized nanocrystals.

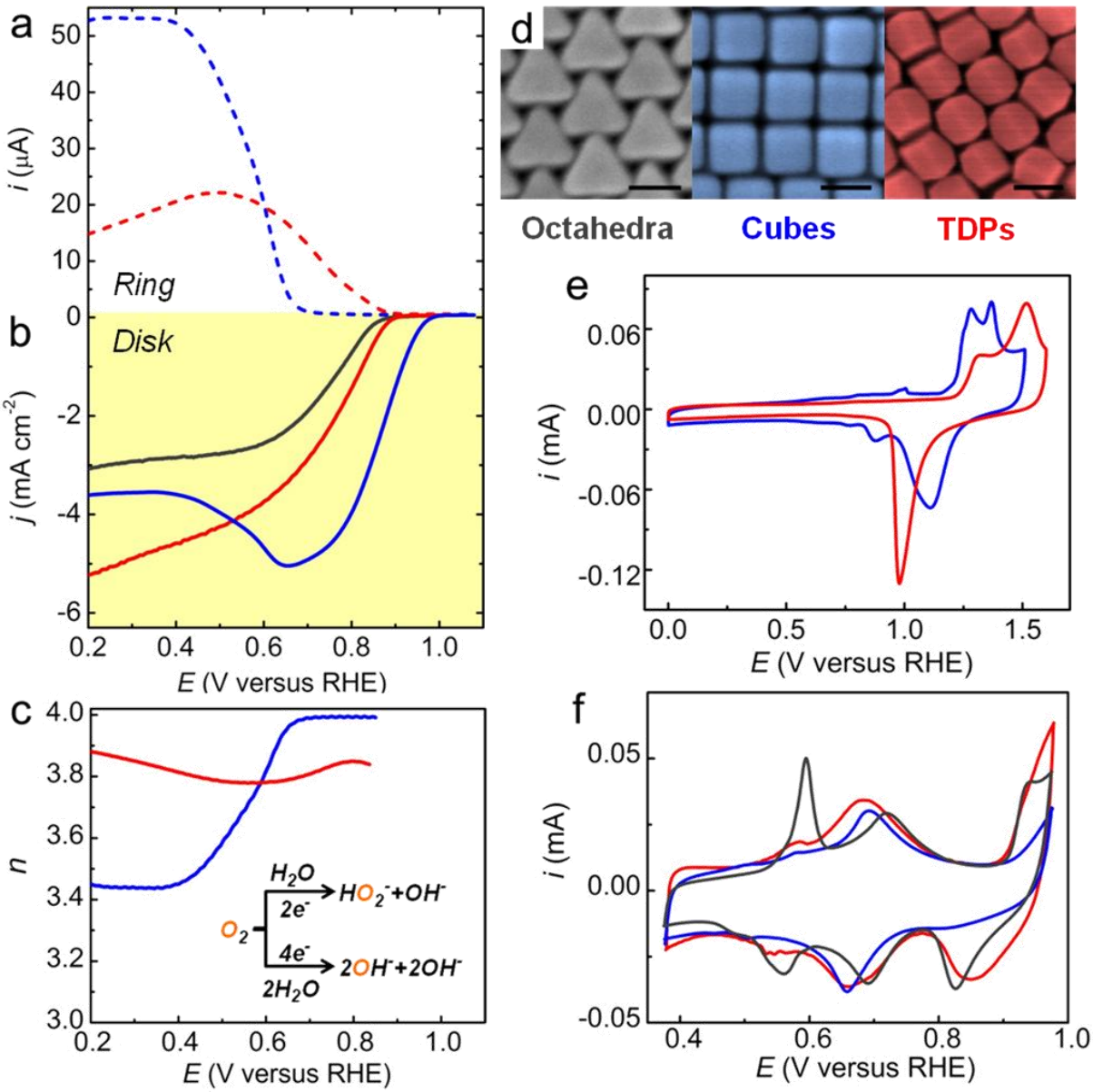

Figure 3.38 Oxygen reduction reaction on various Au nanocrystals. (a) Ring currents measured from RRDE technique for Au cubes, and TDPs in O_2-saturated 0.1 M NaOH. The ring potential was constant at 1.26 V versus RHE. (b) Disk current densities for octahedra, cubes and TDPs in O_2-saturated 0.1 M NaOH at 50 mV s^{-1} and 1600 rpm, obtained with RRDE configuration for cubes and TDPs and with RDE configuration for octahedra. (c) Average number of transferred electrons (*n*) during the ORR as a function of potential, on cubes and TDPs, calculated from the fraction of disk- to ring-flux in (a) and (b). The inset shows the 2e- and 4e-pathways for the ORR in alkaline electrolyte, where the color scheme of oxygen atoms illustrates the two oxygen

sources. (d) False-color SEM images of Au nanocrystals used for the ORR measurements: Octahedra, cubes and TDPs. Scale bar: 50 nm. (e) Cyclic voltammograms of cubes and TDPs in deaerated 0.1 M NaOH at 50 mV s^{-1}. (f) Thallium (Tl) underpotential deposition (UPD) curves of octahedra, cubes and TDPs in deaerated 5 mM $TlNO_3$ + 0.1 M NaOH at 50 mV s^{-1}. Colour scheme: Au octahedra (dark grey), cubes (blue) and TDPs (red).

The characteristic sharp twin peaks near 0.6 V on Au {111} single crystal correspond to the first-order phase transition from a closely packed Tl monolayer to an incommensurate aligned hexagonal phase, and the broad peak centered at 0.73 V is associated with the continuous coadsorption of Tl^+ and OH^-.[423] Easily-handled treatment of nano-facets in our case allowed us to investigate the correlation between electrocatalytic properties and size effect in nanoscale, which would bring nature-bored features unexpected from bulk materials. Here we studied the size effect of octahedra by Tl UPD. As shown in Figure 3.39, by decreasing the edge length from 62 nm of octahedra (Figure 3.40) to 42 nm of small octahedra (Figure 3.36 a_1-a_2), the featured sharp twin peaks near 0.6 V are lowered and their amplitudes become close to that of the broad peak centered at 0.73 V.

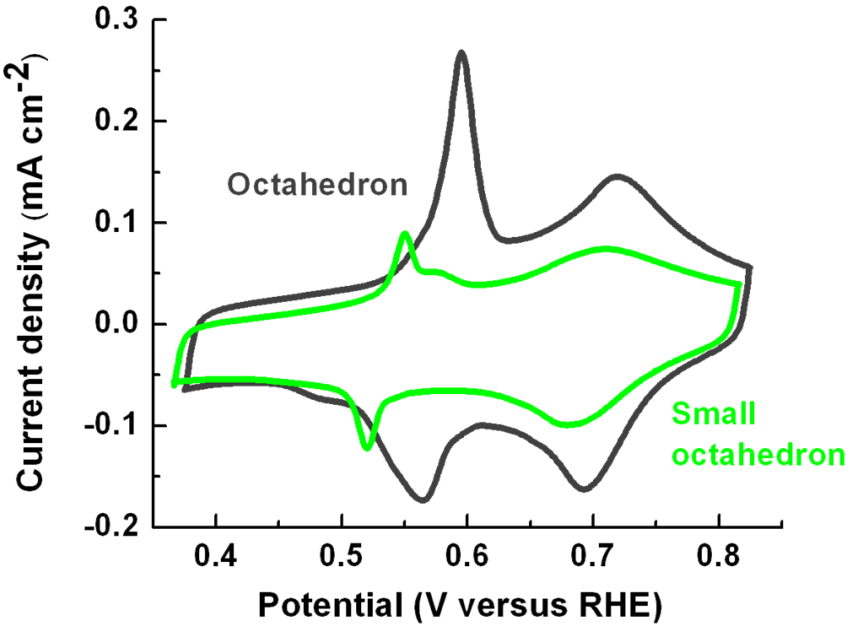

Figure 3.39 Size effect of Au octahedral nanocrystals investigated by Tl UPD. Voltammetry curves for Tl UPD in deaerated 5 mM $TlNO_3$ + 0.1 M NaOH solutions on Au nanocrystals of octahedra (62 nm edge length, black) and small octahedra (42 nm edge length, green). Sweep rate is 50 mV s^{-1}.

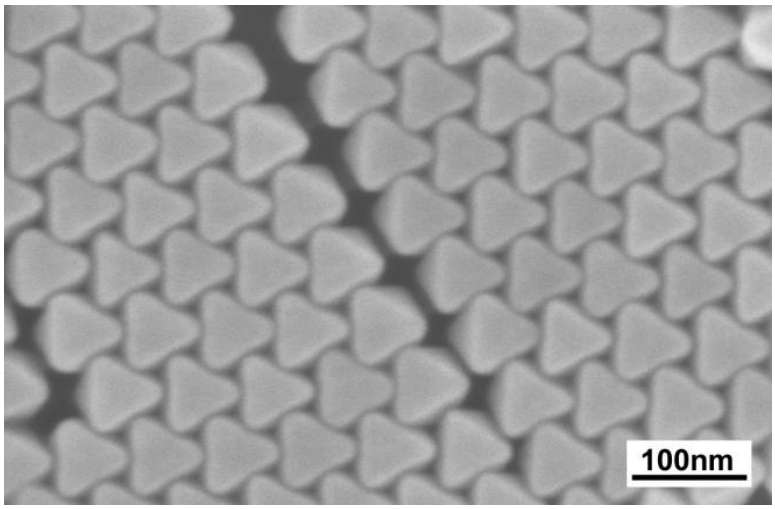

Figure 3.40 SEM image of Au octahedra with the average edge length of 62 nm.

First, the effective surface atom numbers were calculated from Tl UPD charges, as shown in Table 3.8. The Tl UPD charge was calculated only from the sharp peaks at around near 0.6 V. Its coverage was

$$0.21 = 0.75 - 0.54 \tag{3.24}$$

Because the sharp peaks on Au {111} single crystal corresponded to the first-order phase transition from a closely packed Tl monolayer to an incommensurate aligned hexagonal phase[423], while the coverage of the closely packed Tl monolayer was 0.75 and the coverage of the incommensurate aligned hexagonal phase was 0.54.

Table 3.8 Surface atom numbers calculated using Tl UPD charges.

	Edge length L (nm)	Charge (μC cm^{-2})	Coverage	Surface Au atoms (nmol)
Octahedra	62	190.410	0.21	1.842
Small octahedra	42	88.851	0.21	0.860

Then, the theoretical surface atom numbers calculated from atom cluster models, and the results are shown in Table 3.9. Au nanocrystals of 1.5E−14 mol octahedra and 2.5E−14 mol small octahedra were put on the RDE for electrochemical measurements, respectively. The surface atom numbers of Au octahedra were calculated using the octahedron cluster model[425] as a function of the particle size. Around a single central atom, the octahedron cluster is formed by onion-like concentric atomic layers. And the central atom is counted as the first shell here, *i.e.*

$$m = 1 \tag{3.25}$$

for one single atom, where *m* is the number of shells.

The total number of atoms, *N*, as a function of the total number of atomic layers, *m*, is expressed as

$$N(m) = \frac{1}{3}m(2m^2 + 1) \tag{3.26}$$

And the number of surface atoms, N_s, *i.e.* the number of atoms at the *m*-th shell, equals the difference between the total atom numbers for a cluster of *m* complete shells and for one of *(m−1)* complete shells, because each shell has the same geometrical shape[387].

$$N_s(m) = N(m) - N(m-1) = \frac{1}{3}m(2m^2 + 1) - \frac{1}{3}(m-1)[2(m-1)^2 + 1] \tag{3.27}$$

And the edge length of the entire particle *L* was estimated to be

$$L = 0.25 \times (m - 1) \tag{3.28}$$

Table 3.9 Surface atom numbers calculated using octahedron cluster model.

	Edge length *L* (nm)	Particle (mol)	*m*	N_s per particle	Surface Au atoms (nmol)
Octahedra	62	1.5E−14	249	123505	1.853
Small octahedra	42	2.5E−14	169	56785	1.420

The effective surface atom numbers calculated from Tl UPD charges (Table 3.8) and the theoretical surface atom numbers calculated from atom cluster models (Table 3.9) are very close for octahedra (62 nm edge length). While the discrepancy calculated by the two methods for small octahedra (42 nm edge length) can be explained by the high edge-to-surface ratio and the

consequent weak capability for Tl adsorption[426]. The study on the size effect demonstrates the resemblance for confined nanocrystals to the extended single crystal could be further improved by increasing the particle size and consequently decreasing the edge-to-surface ratio.

Overall, the excellent conformity of electrochemical characteristics, including cyclic voltammetry and Tl underpotential deposition, on the Au nanoscale octahedra and cubes with those on their bulk single-crystal counterparts validates our use of nanocrystals as model systems for correlating Au surface structures and ORR behaviors.

3.5.3 ORR Activity in Alkaline Solution

We probed the ORR activities of Au nanocrystals using the techniques of rotating disk electrode (RDE) and rotating ring disk electrode (RRDE) in O_2-saturated 0.1 M NaOH. The ORR currents on the disk electrode (Figure 3.38b) for the octahedra and cubes, consonant with other groups' results[271, 274], emulate those on the Au {111} and {100} single-crystal surfaces[317], respectively. The Au octahedra show the lowest onset potential (0.88 V), and a mass-transport limiting current of -3 mA cm^{-2} at 0.2 ~ 0.6 V, demonstrating that the octahedron is the least active of these three facets and catalyzes only the 2e ORR. In contrast, Au cubes and TDPs exhibit currents exceeding the maximum for the 2e ORR on octahedra, suggesting that the 4e ORR occurs. Thus, we performed the RRDE measurements to analyze the ORR selectivity and to quantify the average number of electrons transferred per O_2 molecule on Au cubes and TDPs.

As shown in the inset to Figure 3.38c, the 2e-ORR pathway in alkaline electrolyte leads to the production of HO_2^-. Using an additional ring electrode, the RRDE method detects the oxidation current of HO_2^- concomitantly produced via the 2e ORR on the disk electrode. For Au

cubes, with decreasing potentials (or increasing overpotentials), the rise of the ring current of HO_2^- oxidation (blue, Figure 3.38a) coincides with a decrease in the disk current (Figure 3.38b) from the maximum around 0.6 V to the plateau near the mass-transport limiting current (−3 mA cm^{-2}, see Section 2.3.3.2). The same behavior was observed with single-crystal Au {100}[317], clearly suggesting that the major ORR pathway switches from 4e to 2e around 0.6 V. Surprisingly, on Au TDPs, both a smaller ring current (red, Figure 3.38a) and a larger disk current (Figure 3.38b) are found than those on cubes, although at relatively low potentials. The RRDE polarization curves at different rotation rates are shown in Figure 3.41.

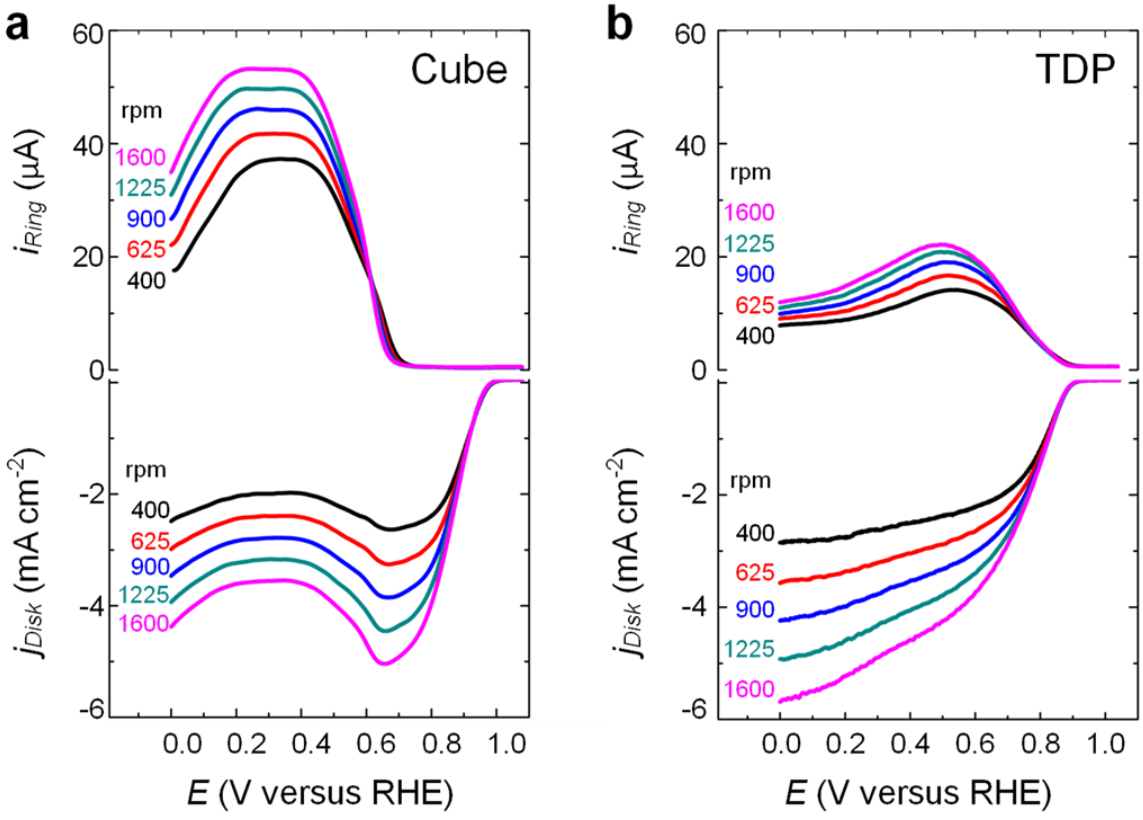

Figure 3.41 RRDE polarization curves of Au cubic (a) and TDP (b) nanocrystals in O_2-saturated 0.1 M NaOH at different rotation rates indicated. The disk potential was swept at 50 mV s^{-1},

while the ring potential was constant at 1.26 V vs. RHE. The curves measured at 1600 rpm were shown in Figure 3.38 a-b.

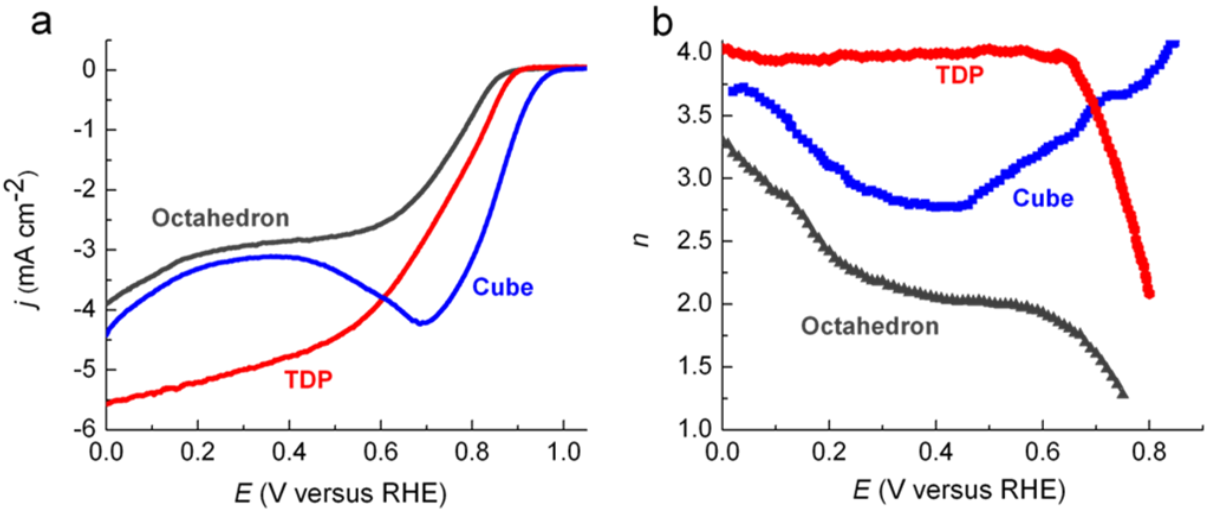

Figure 3.42 ORR performance and electron transfer number of Au nanocrystals measured by RDE. (a) RDE polarization curves of Au octahedra (dark grey), cubes (blue) and TDPs (red) in O_2-saturated 0.1 M NaOH solutions at 1600 rpm. Sweep rate is 50 mV s^{-1}. (b) Average number of electrons transferred per O_2 molecule (n) during ORR as a function of potential, on Au octahedra (dark grey), cubes (blue) and TDPs (red), calculated from slopes of Koutecky-Levich plots at different potentials (Figure 3.43 b, d, f).

The number of transferred electrons, calculated by the equation (Section 2.3.3.2)

$$n = 4\, i_D / (i_D + i_R / N) \qquad (3.29)$$

as a function of potential (Figure 3.38c) demonstrates that while a distinct 4e-to-2e switch occurs on Au cubes, the almost 4e ORR over the entire potential region takes place on TDPs, which was not previously seen on any Au bulk single-crystal surfaces. Alternatively, the electron transfer number (Figure 3.42) could be calculated by the Koutecky-Levich equation using the RDE results at different rotation rates (Figure 3.43).

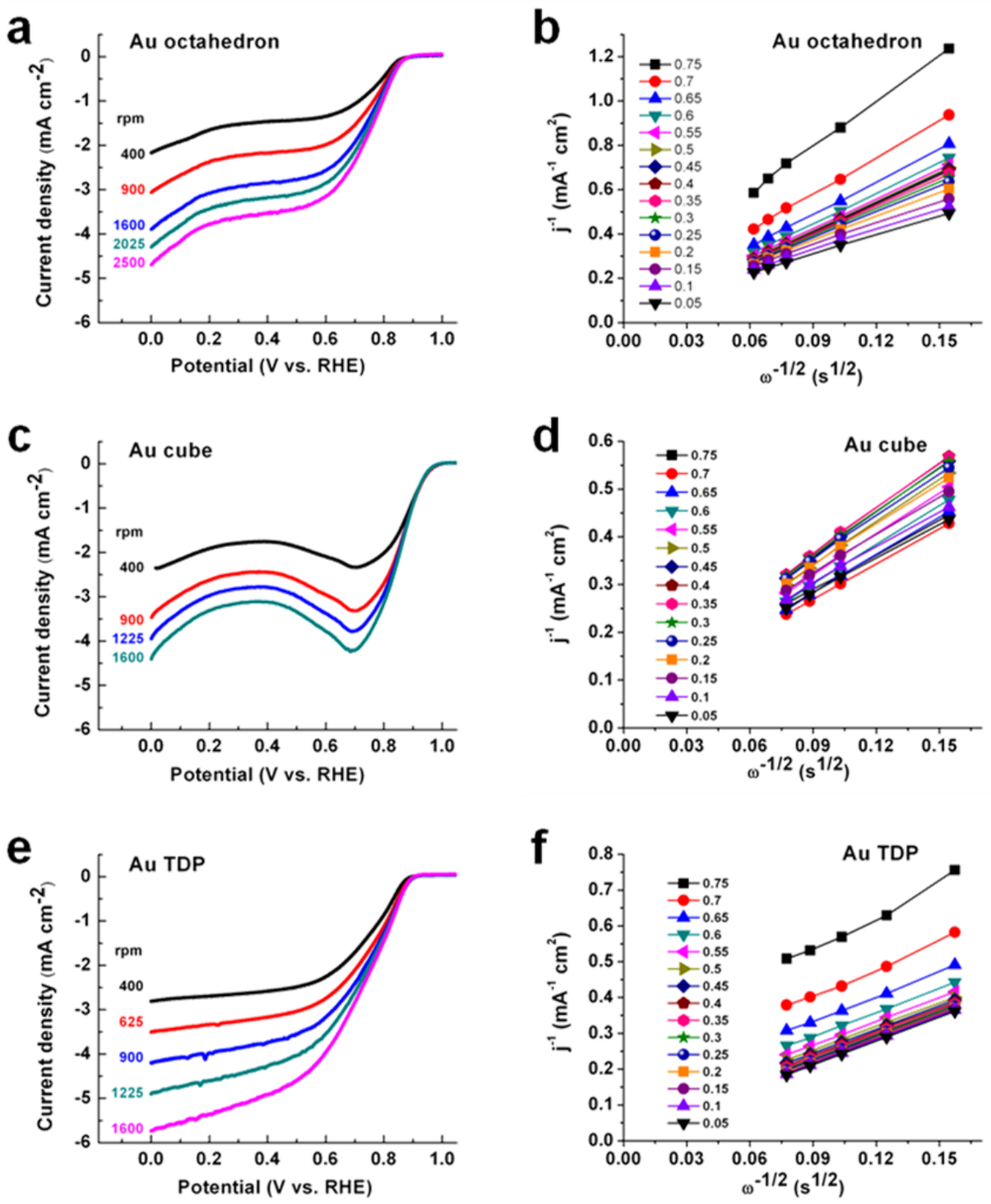

Figure 3.43 ORR performance of Au nanocrystals measured by RDE. (a, c, e) RDE polarization curves of the Au (a) octahedral, (c) cubic, and (e)TDP nanocrystals in O_2-saturated 0.1 M NaOH at different rotation rates indicated. Seep rate is 50 mV s^{-1}. (b, d, f) Koutecky-Levich plot at different potentials (V vs. RHE) obtained from (a, c, e) respectively.

The exceptional observation of the 4e ORR over a wide potential region on Au TDPs calls for further exploration of the structure-activity correlations and the underlying ORR mechanism by DFT calculations, as we discuss in the next section.

3.5.4 ORR Mechanisms Investigated by DFT Calculations

One major function of catalysts is to promote the bond breaking in reactants[427]. For the ORR (Figure 3.38c inset), the selectivity toward the 4e or 2e pathway is determined by the catalyst's propensity to break the oxygen-oxygen (O-O) bond in O_2.[428] The O-O bond dissociation causes the reaction to proceed via the 4e pathway with OH^- as the final product in alkaline electrolyte; however, if the O-O bond is not broken, then the 2e-ORR pathway is realized. The O-O bond breaking is especially essential for the 4e ORR on Au, because Au is known to adsorb O_2 weakly[312-314] with a very high O_2 dissociation barrier compared to other transition metals[320, 429]. Therefore, we use the relative O-O bond elongation from the gas-phase value as the primary criterion to assess the structure-activity correlations.

We first studied computationally O_2 adsorption on three Au surfaces to understand the adsorbate-substrate effects (Section 2.6.3). Three bi-dentate binding motifs (Figure 3.46, Table 3.10), including bridge, diagonal and hollow modes, were considered to identify the active adsorption sites toward the 4e ORR. In general, surface sites with lower coordination are more reactive, and interact with adsorbates more strongly[430]. Our DFT calculations on three types of discussed Au facets confirmed this trend. Figure 3.44a illustrates that the close-packed {111} surface has 9 nearest neighbors around each atom in the top atomic layer, and the coordination

number falls to 8 on {100}, and to 6 on {310} edges. At the bridge site, O_2 is weakly physisorbed on Au {111} (dark grey hollow circle in Figure 3.44b), retaining the original O-O bond length ($R_{O\text{-}O}$) of a gas-phase O_2 molecule. Thus, this confirms that the close-packed Au surface is catalytically incapable to break the O-O bond, in line with previous DFT studies[431, 432]. In contrast, the strong O_2-Au interaction at bridge sites on {100} and {310} results in a weakening of the O-O bond, illustrated by the $R_{O\text{-}O}$ stretched by ~8.5% (blue and red hollow circles in Figure 3.44b), which can facilitate the O-O bond breaking for a complete 4e ORR. Moreover, a major structural difference is observed for the diagonal mode between {100} and {310}, where O_2 is physisorbed on {100} with an unperturbed $R_{O\text{-}O}$, but O_2 strongly interacts with the under-coordinated edge atoms on {310} with the $R_{O\text{-}O}$ elongated by 8.1%, which indicates a significant weakening of O-O bond at the diagonal site on {310} compared to {100}. Overall, the 2e-only ORR on Au {111} is attributed to its weak O_2-Au interaction, whereas the enhanced O_2 adsorption on the lower-coordinated {310} surface compared to {100}, particularly the activation of the diagonal mode, contributes to the wide-range 4e ORR on {310}.

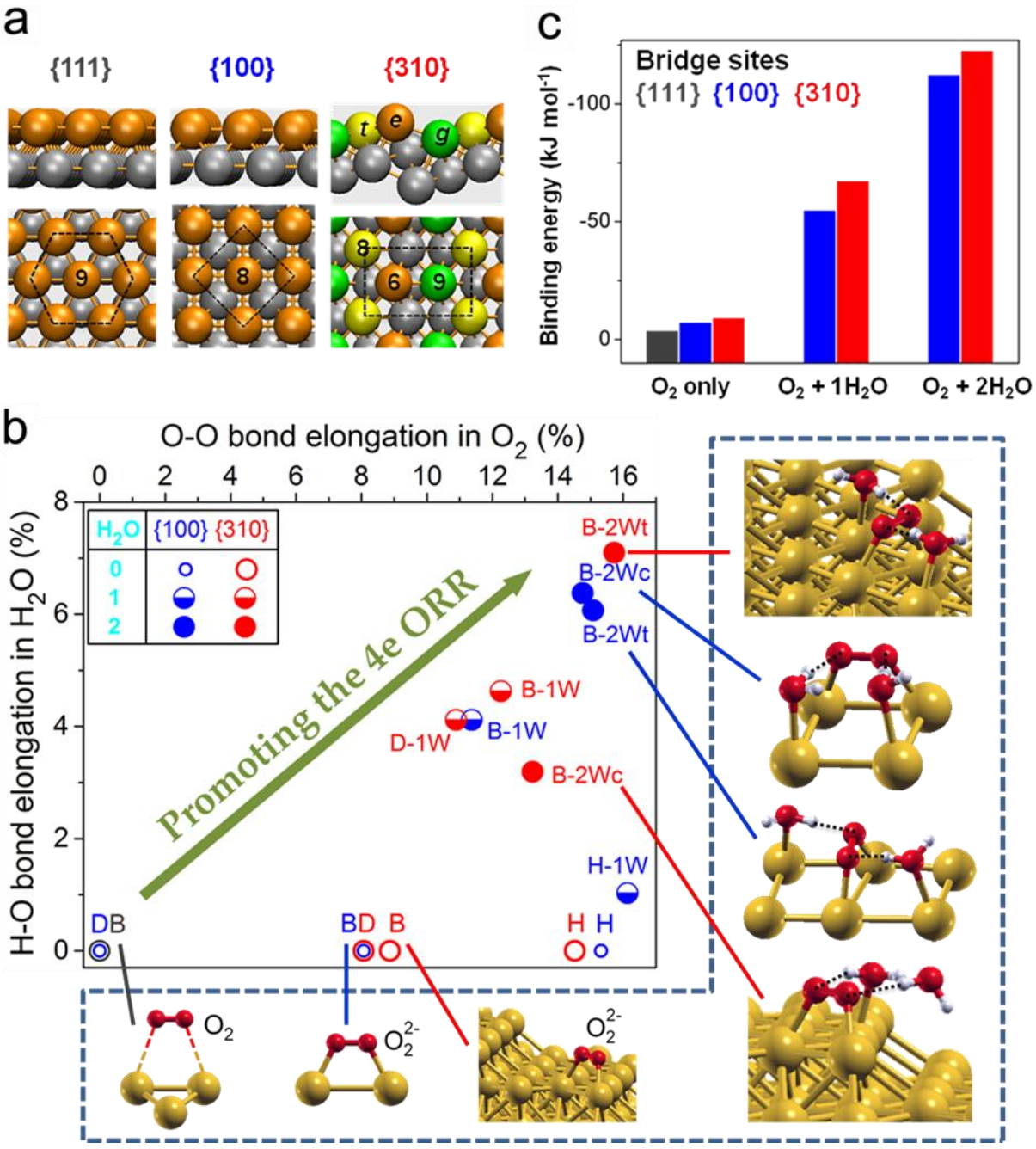

Figure 3.44 Co-adsorption of oxygen and water on Au surfaces. (a) Schematic side view (upper) and top view (lower) of lattice structures of Au surfaces showing coordination numbers for surface atoms. Outmost surface atoms on {111} and {100}: orange; Those on {310} at edge (*e*): orange, terrace (*t*): yellow, groove (*g*): green; Bulk atom: grey. The detailed side view of Au {310} is displayer in Figure 3.45. (b) The H-O bond elongation versus the O-O bond elongation

for adsorbed H_2O and O_2, respectively, in respect of different Au facets: {111} (dark grey), {100} (blue) and {310} (red), without (hollow circle) or with one H_2O (1W, semi-hollow circle) or two H_2O (2W, solid circle) molecules. The bond elongation is calculated with respect to the bond length of 0.972 Å and 1.240 Å respectively in the DFT-calculated gas-phase H_2O and O_2. The table in the top-left corner defines the symbols. Abbreviations: D for diagonal, B for bridge, H for hollow, 1W for one H_2O molecule, 2W for two H_2O molecules, c for *cis* configuration with two H_2O molecules on the same side of adsorbed O_2, t for *trans* configuration with two H_2O molecules on the opposite sides of adsorbed O_2. Three bottom-left-side configurations (from left to right): O_2 adsorption at bridge sites on Au {111}, {100}, and {310}. Four right-side configurations: O_2-$2H_2O$ co-adsorption configurations on Au {100} (marked by blue lines) and {310} (marked by red lines). (c) The binding energies (kJ mol^{-1}) of adsorbed O_2 and of co-adsorbed O_2-H_2O at bridge sites on Au {111} (dark grey), {100} (blue), and {310} (red) surfaces.

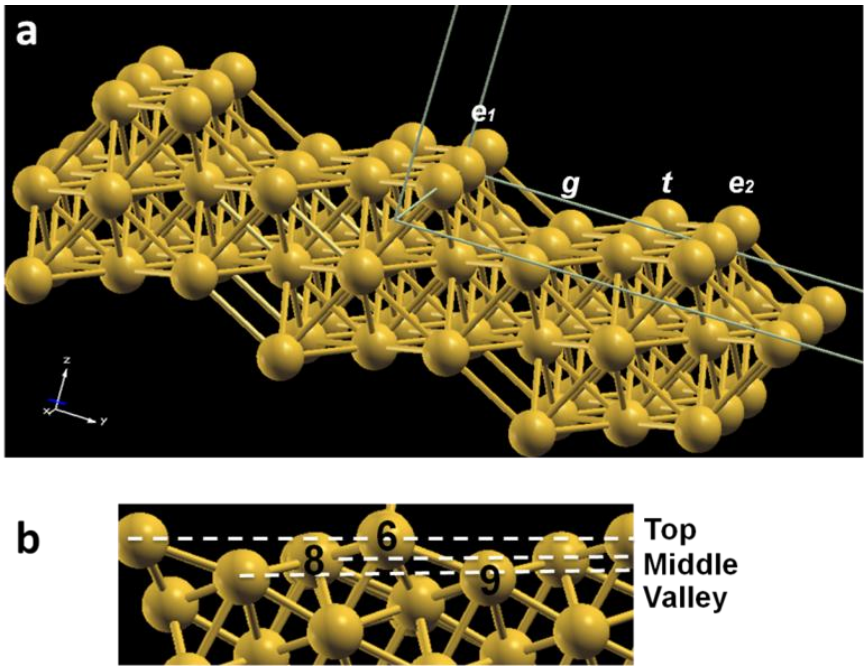

Figure 3.45 Side view of Au {310} surface. (a) Four Au surface atoms are marked as e_1 (top edge), *g* (groove), *t* (terrace) and e_2 (bottom edge). Atom e_1 and e_2 are the step atoms and have the identical environments. (b) Coordination numbers for surface atoms. Edge (*e*) atom has 6

coordination number and is the outmost surface atom, terrace (*t*) atom has 8 coordination number and lies in the middle position, groove (*g*) atom has 9 coordination number and locates in the lowest position (valley) of surface atoms.

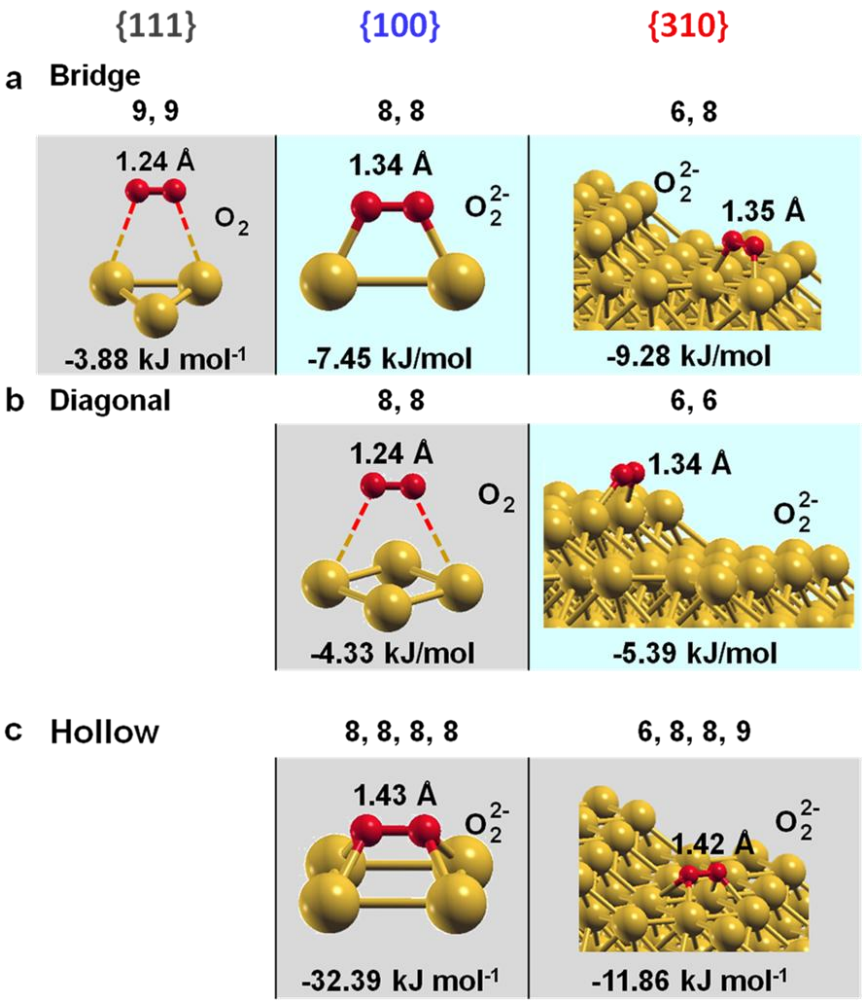

Figure 3.46 O_2 adsorption on Au {111} (dark grey), {100} (blue), and {310} (red) surfaces, with corresponding coordination numbers of Au atoms. (a) Bridge sites, (b) diagonal sites; (c) hollow sites. The figure also shows the binding energies (kJ mol^{-1}), oxygen-oxygen (O-O) bond lengths (Å) and charge states of adsorbed O_2.

Table 3.10 O_2 adsorption in the bidentate configuration on Au {111}, {100} and {310}. $E_b^{O_2}$ is the binding energy (kJ mol^{-1}); $R_{O\text{-}O}$ is the oxygen-oxygen (O-O) bond length (Å); $R_{O\text{-}Au1}$, $R_{O\text{-}Au2}$, $R_{O\text{-}Au3}$ and $R_{O\text{-}Au4}$ are the oxygen-gold (O-Au) bond lengths (Å); M is the magnetic moment (μ_B). The DFT-calculated gas-phase value 1.240 Å of O-O bond length in O_2 is used as the base value to calculate elongation percentages. Only stable configurations with negative E_b are shown.

	Sites		$E_b^{O_2}$ (kJ mol^{-1})	$R_{O\text{-}O}$ (Å)	$\Delta R_{O\text{-}O}$ (%)	$R_{O\text{-}Au1}$ (Å)	$R_{O\text{-}Au2}$ (Å)	$R_{O\text{-}Au3}$ (Å)	$R_{O\text{-}Au4}$ (Å)	M (μ_B)	Charge State
{111}	Bridge		−3.88	1.24	0.00	3.54				1.97	O_2
{100}	Hollow		−32.39	1.43	15.32	2.30				0	O_2^{2-}
	Bridge		−7.45	1.34	8.06	2.17				0	O_2^{2-}
	Diagonal		−4.33	1.24	0.00	3.60				1.96	O_2
{310}	Hollow	$g\text{-}e_2$	−11.86	1.42	14.52	2.38	2.28	2.32	2.27	0	O_2^{2-}
	Bridge	$t\text{-}e_2$	−9.28	1.35	8.87	2.19	2.13			0	O_2^{2-}
	Diagonal	$e_1\text{-}e_1$	−5.39	1.34	8.06	2.20	2.20			0	O_2^{2-}

However, if we consider only O_2 adsorption, it remains puzzling why the 4e ORR is highly potential-dependent on Au {100}, while it is potential-independent on {310}. Here, we propose to account for the influence of specifically co-adsorbed water on the 4e ORR behavior. Since water is another reactant for the ORR in alkaline media, also because such co-adsorbed water can act as the main proton donor to O_2 for the ORR[431, 433] and other reactions catalyzed by Au[434-436]. All the calculation results are listed in Table 3.11, Figure 3.48 and Figure 3.49. Our calculation demonstrates that with co-adsorbed H_2O, the $R_{O\text{-}O}$ of O_2 is further stretched for each configuration on {100} and {310} compared to the situation where only O_2 is adsorbed (Figure 3.44b), consistent with the case of Pt {111}[437, 438]. For example, at bridge sites on {100} (blue),

the O-O bond is elongated by 8.1% without co-adsorbed H_2O (hollow circle), but by 11.4% with one co-adsorbed H_2O (semi-hollow circle), and by ~14.9% with two co-adsorbed H_2O molecules (solid circles), indicating that the effectively co-adsorbed H_2O could constructively activate the O-O bond, and facilitate O_2 dissociation required for the 4e ORR.

In addition to the O-O bond elongation in O_2, the stretching of the H-O bond in H_2O can occur, and this could confirm the harmonious interaction between co-adsorbed O_2 and H_2O. For example, the intramolecular H-O bond in H_2O is stretched by 4.1% with one H_2O, and by ~6.2 % with two H_2O molecules when O_2 is co-adsorbed at bridge sites on {100}. Most co-adsorption configurations with two H_2O molecules exhibit large stretches for both O-O and H-O bonds, except for the B-2Wc configuration on {310}. In this case, one H_2O is adsorbed on the Au edge atom, while the other H_2O desorbs from the surface after relaxation (see the bottom one of the right-side configurations in Figure 3.44b). Such arrangement for two H_2O molecules may contribute to the low ORR onset potential on {310}. In contrary, for all other three modes with two H_2O, when both H_2O molecules are adsorbed on Au (see the top three ones of right-side configurations in Figure 3.44b), the largest stretches for both O-O and H-O bonds are obtained among all the calculation results, implying that the effectively co-adsorbed H_2O instead of bulk water could constructively activate the O-O bond, and facilitate O_2 dissociation required for the 4e ORR.

On Au {100}, the shorter distances between co-adsorbed O_2 and H_2O in the bridge configurations, 2.57 ~ 2.66 Å (Figure 3.47), than 3.10 Å in the hollow configuration, result in the larger H-O bond elongation in H_2O, 4.1 ~ 6.2 % at bridge modes, versus 1.0% at hollow mode, and also induce larger increase in O-O bond elongation with respect to the situation without any

co-adsorbed H_2O (Figure 3.44b, Table 3.10, Table 3.11). These effects support the co-adsorption configurations at bridge sites as the most active configuration, although the hollow configuration has the largest O-O bond elongation in the absence of H_2O co-adsorption.

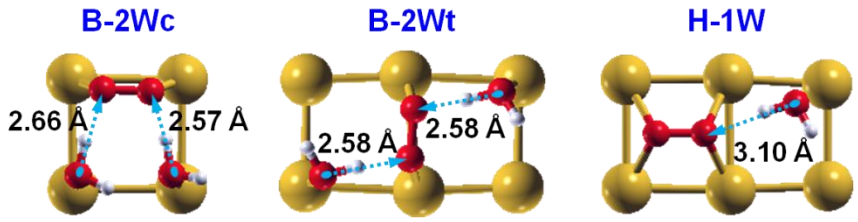

Figure 3.47 Top views of the distance between interacting oxygen atoms in co-adsorbed O_2 and H_2O on Au {100} surface. Abbreviations: B for bridge, H for hollow, 1W for one H_2O molecule, 2W for two H_2O molecules, c for *cis* configuration, t for *trans* configuration.

Furthermore, the trend of stronger interaction with lower coordination also is observed for the O_2-H_2O co-adsorption. The co-adsorption binding energies on {310} generally are higher than those on {100} with the similar number of co-adsorbed H_2O molecules (Figure 3.44c). The weaker O_2-H_2O co-adsorption on {100} would render to the variation of external applied potential resulting in the 4e-to-2e ORR transition. In contrast, the stronger and, therefore, more stable O_2-H_2O co-adsorption on {310} would support the potential-independent 4e-ORR behavior. Overall the observed ORR activities on three types of Au nanocrystal surfaces are explicable using the calculation results from the O_2-H_2O co-adsorption configuration. We attribute the observed 4e-ORR to the O_2-H_2O co-adsorption dominantly occurring at bridge sites on {100} and {310}, and the full-potential-range 4e ORR on the {310} to the stronger O_2-H_2O co-adsorption on {310} than on {100}.

Table 3.11 Co-adsorption of oxygen and water on Au {100} and Au {310} surfaces. $E_b^{O_2+nH_2O}$ is the binding energy of O_2-H_2O co-adsorption (kJ mol^{-1}); $R_{O\text{-}O}$ is the oxygen-oxygen (O-O) bond length (Å) in O_2 molecule; $\Delta R_{O\text{-}O}$ is the $R_{O\text{-}O}$ elongation (%) in O_2; $R_{O1\text{-}H1}$, $R_{O1\text{-}H2}$, $R_{O2\text{-}H1}$ and $R_{O2\text{-}H2}$ are the hydrogen-oxygen (H-O) bond lengths (Å) in H_2O molecule, where *H1* is the H atom in H_2O forming the hydrogen bond with O_2, and *H2* is the H atom in H_2O not forming hydrogen bond with O_2; $\Delta R_{O1\text{-}H1}$ is the R_{O1}-H1 elongation (%) in co-adsorbed H_2O molecule; $R_{O\text{-}O}^{inter}$ is the inter-distance (Å) between O_2 and H_2O molecules. The DFT-calculated gas-phase value, 1.240 Å of O-O bond length in O_2 and 0.972 Å of H-O bond in H_2O, are used as the reference value to calculate elongation percentages. Abbreviations: D for diagonal, B for bridge, H for hollow, 1W for one H_2O molecule, 2W for two H_2O molecules. Here the colored configurations exhibit the highest binding energy compared to those with similar geometries, and are therefore considered as stable configurations and representatively displayed in Figure 3.44b.

Mode		$E_b^{O_2+nH_2O}$ (kJ mol^{-1})	$R_{O\text{-}O}$ (Å)	$\Delta R_{O\text{-}O}$ (%)	$R_{O1\text{-}H1}$ (Å)	$\Delta R_{O1\text{-}H1}$ (%)	$R_{O1\text{-}H2}$ (Å)	$R_{O2\text{-}H1}$ (Å)	$R_{O2\text{-}H2}$ (Å)	$R_{O\text{-}O}^{inter}$ (Å)	
{100}	B-1W-inward	−55	1.381	11.37	1.012	4.12	0.975			2.645	
	B-1W-outward	−53.36	1.377	11.05	1.011	4.01	0.974			2.653	
	H-1W-parallel	−56.75	1.440	16.13	0.982	1.03	0.975			3.100	
	H-1W-perpendicular	−51.9	1.430	15.32	0.977	0.51	0.975				
	H-1W-perpendicular-close	−54.17	1.430	15.32	0.988	1.65	0.973				
	B-2W-*cis*-inward	−112.48	1.423	14.76	1.034	6.38	0.973	1.015	0.985	2.575	2.659
	B-2W-*cis*-outward	−98.61	1.419	14.44	1.022	5.14	0.975	1.022	0.975	2.616	2.616
	B-2W-*trans*-inward	−110.06	1.427	15.08	1.031	6.07	0.974	1.031	0.974	2.582	2.582

	B-2W-*trans*-outward	−107.11	1.422	14.68	1.031	6.07	0.974	1.031	0.974	2.578	2.578
{310}	D-1W-asymmetrical	−59.25	1.375	10.89	1.012	4.12	0.975			2.625	
	D-1W-symmetrical	−40.23	1.367	10.24	0.981	0.93				2.876	
	B-1W	−67.41	1.392	12.26	1.017	4.63	0.974			2.627	
	B-2W-*cis*-edge/bulk(down)	−117.71	1.404	13.23	1.003	3.19	1.007	0.995	0.974	2.705	2.799
	B-2W-*cis*-edge/bulk(up)	−109.93	1.396	12.58	1.019	4.84	0.973	1.006	0.975	2.625	3.936
	B-2W-*cis*-terrace/bulk	−103.43	1.400	12.90	0.998	2.67	1.005	0.996	0.979	2.763	2.787
	B-2W-*trans*-edge/terrace	−122.71	1.435	15.73	1.041	7.10	0.974	1.025	0.975	2.558	2.662

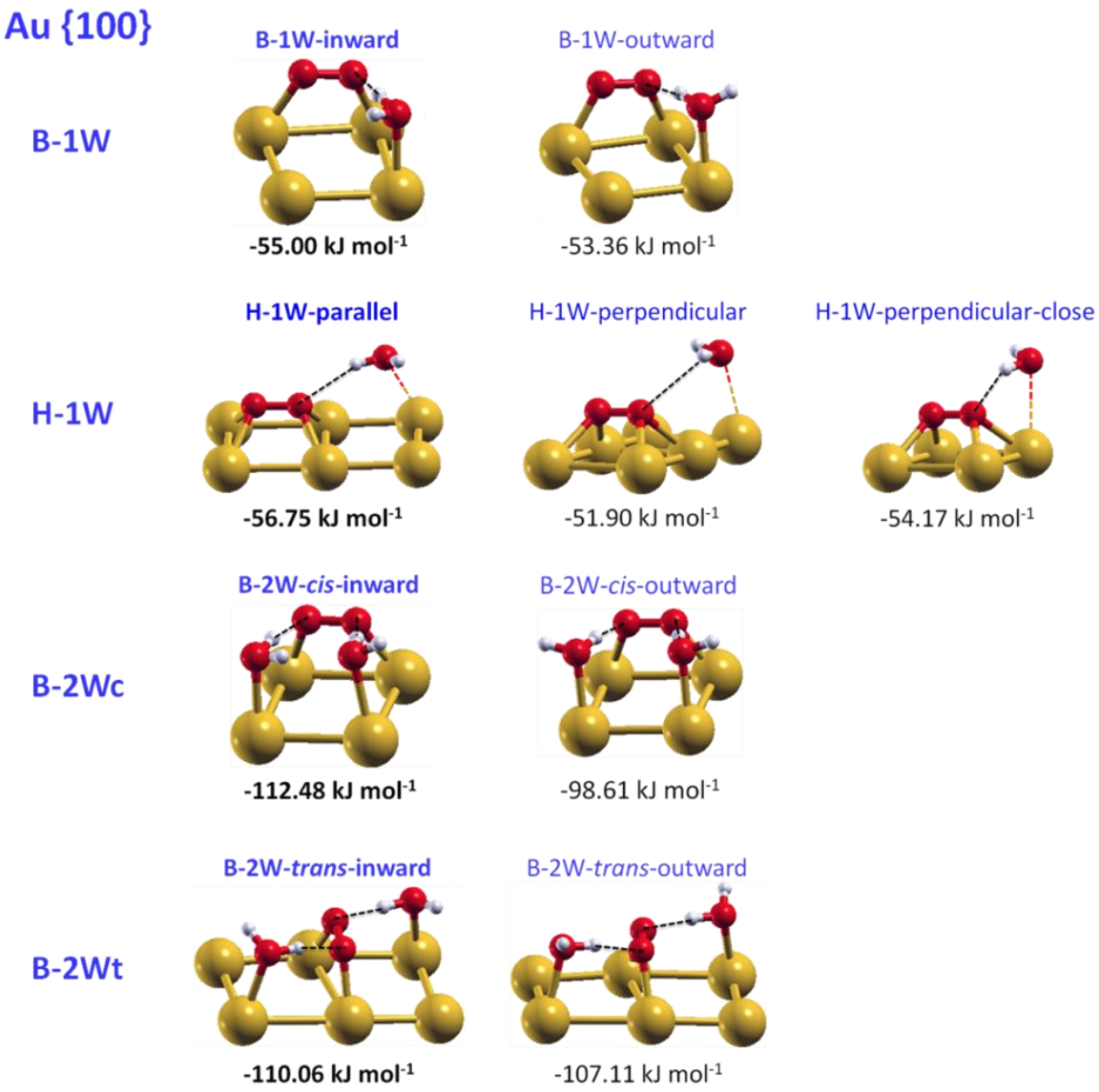

Figure 3.48 Co-adsorption of water and oxygen on Au {100} surface. The parameters of these configurations are listed in Table 3.11. The black dash lines represent hydrogen bonds. Here the bold configurations exhibit the highest binding energy compared to those with similar geometries, and are therefore representatively displayed in Figure 3.44b. In some configurations, the H_2O molecule becomes desorbed after relaxation. Abbreviations: B for bridge, H for hollow, 1W for one H_2O molecule, 2W for two H_2O molecules, c for *cis* configuration with two H_2O molecules on the same side of adsorbed O_2, t for *trans* configuration with two H_2O molecules on the opposite sides of adsorbed O_2.

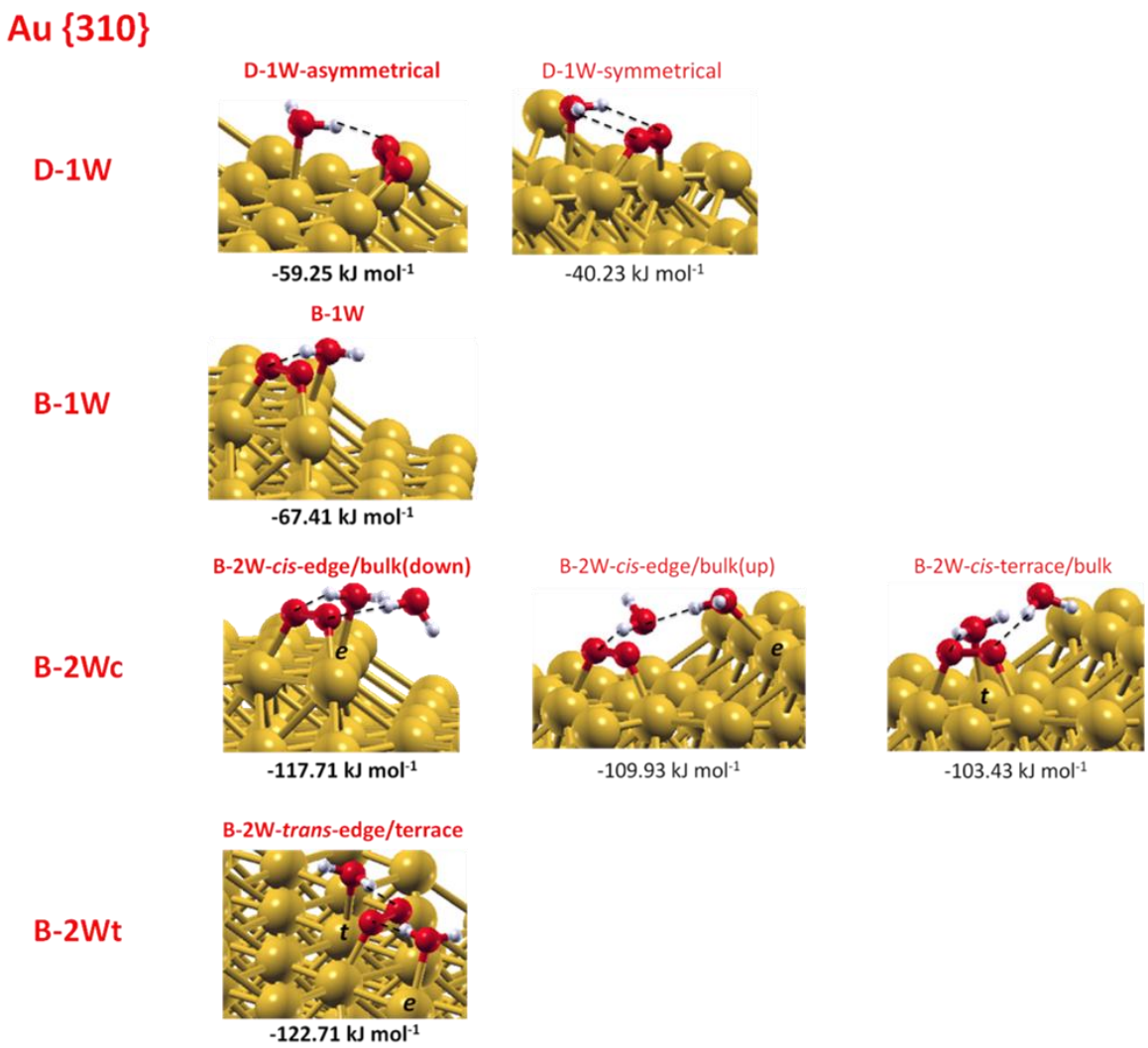

Figure 3.49 Co-adsorption of oxygen and water on Au {310} surface. The parameters of these configurations are listed in Table 3.11. Here the bold configurations exhibit the highest binding energy compared to those with similar geometries, and are therefore representatively displayed in Figure 3.44b. In some configurations, the H_2O molecule becomes desorbed after relaxation. Abbreviations: D for diagonal, B for bridge, 1W for one H_2O molecule, 2W for two H_2O molecules, c for *cis* configuration with two H_2O molecules on the same side of adsorbed O_2, t for *trans* configuration with two H_2O molecules on the opposite sides of adsorbed O_2.

3.5.5 Summary

In conclusion, we generated several types of gold shaped nanocrystals, including octahedra, cubes and TDPs, which are correspondingly enclosed by atomically well-defined nanofacets, {111}, {100}, and {310} respectively. We observed that the ORR behaviors on Au octahedra and cubes are similar as those on corresponding single-crystal surfaces. Astonishingly, Au {310} nanofacet catalyzes the 4e ORR over a wide potential range; such effect was not observed on any Au single-crystalline surfaces in the past. These high-quality single-crystalline gold nanocrystals with differently expressed atomic arrangements of their surface can serve also as model systems to understand the nature of the ORR in alkaline solution. Combined with DFT calculations, we proposed that the O_2-H_2O co-adsorption mechanism plays a critical role in the observed 4e-ORR activities on {100} and {310} facets. The ease of attaining single-crystalline surfaces using gold nanocrystals provides new opportunities for gaining an in-depth understanding of the mechanisms of catalytic reactions, thereby opening up new strategies for the rational design of catalyst materials.

Chapter 4 CONCLUDING REMARKS

Here are the summary and main conclusions of this dissertation:

(I) A series of carbon-supported bimetallic core-shell nanocatalysts having Ru core and Pt, Pd or Au shell (Ru@M, where M = Pt, Pd, Au) have been synthesized, using ethanol as the solvent and the reducing agent. The XANES measurements confirm the reduction of $RuCl_3$ by ethanol, which is both the solvent and the reducing agent. These catalysts have high activity and stability for HER and HOR. The HER-HOR activities of these bimetallic core-shell nanocatalysts in acid solution have been correlated with catalysts' chemical composition, shell thickness, and loading. The Ru@Pt nanocatalysts are identified as the most active HER-HOR electrocatalysts in acid solution, among the investigated bimetallic core-shell nanocatalysts.[298]

The Ru-Pt partial alloying can be avoided for core-shell nanoparticles with different crystal structures, and highly-ordered Ru@Pt nanoparticles with designed shell thickness can be reliably produced by a fine-tuned synthesis method using the solvent ethanol as the reducing agent. This new level of atomic control in synthesis facilitates use of bilayer Ru@Pt nanoparticles as an advanced HER-HOR catalyst for practical applications in PEM fuel cells and water electrolyzers. Using the hanging-strip GDE test method, $Ru@Pt_{2ML}/C$ showed similar HER-HOR specific activity as commercial Pt/C. The high HER-HOR activities of bilayer $Ru@Pt_{2ML}$ are facilitated by $\leq 0.04\ \Omega\ cm^2$ *CTR* at 0 V in 1 M $HClO_4$ at 23 °C with Pt loading $\leq$ 20 $\mu g\ cm^{-2}$. We attribute the ultralow *CTR* with ultralow Pt loading primarily to the high Pt surface area per Pt mass of the well-defined Ru@Pt core-shell catalysts. In addition, the significantly enhanced CO tolerance and the superior stability for the HOR at the H_2 anode in fuel cells at ultralow catalyst loadings in comparison with commercial Pt/C show the promise of

using a well-ordered core-shell structure to resolve the dilemma in using dissolution-prone metals for alleviating CO poisoning effect. Furthermore, the $Ru@Pt_{2ML}$ catalyst has a top-level performance for the HER in water electrolyzers, verified by comparison with well-established baseline of commercial Pt catalyst over 2.4 A cm^{-2} current range and stability over 1200 hours. Therefore, the present results suggest that the $Ru@Pt_{2ML}$/C nanocatalyst, with almost half of the Pt loading for Pt/C, holds promise as a high performance HER-HOR electrocatalyst in enabling large-scale commercialization of PEM fuel cells[299, 300] and water electrolyzers[301].

(II) Pt monolayer catalysts have been fabricated on Pd nanoparticles as ORR electrocatalysts in acid solution, via a surfactant-free and high-yield chemical route using the solvent ethanol as the reductant. The conformity and continuousness of Pt shells were verified by XRD, STEM together with EELS and EDX techniques. The DFT calculations also showed that the two-dimensional growth of Pt atomic layers on Pd substrate is energetically favorable. The uniform and complete Pt coating is promoted by the coating process with slower kinetics and the reaction temperature of 70 °C rather than room temperature. The core-shell Pd@Pt nanocatalysts exhibit enhanced activities than the commercial Pt/C electrocatalyst.[308]

In order to further enhance the total-metal mass activity for the ORR in acid media, hollow Pd and Pd-Au cores have been prepared, using the pulse electrodeposited Ni nanoparticles as sacrificial templates, to serve as the core particles for Pt monolayer catalysts. The hollow architecture of the Pd-Au particles was achieved by the delicate balance between galvanic displacement and Kirkendall effect in controlling reaction kinetics. The smooth surface morphology and lattice contraction, as well as the mass saving resulted from the hollow structure, have accordingly enhanced the electrocatalysts' total-metal mass activities for the ORR

up to 0.57 A mg^{-1}. This is 2.2 times that of 0.26 A mg^{-1} for a Pt monolayer catalyst on solid Pd cores, and 3.5 times that of 0.16 A mg^{-1} for solid Pt nanoparticles made by pulse electrodeposition.[309]

(III) Several types of Au monofaceted nanocrystals, including octahedra, cubes and TDPs, which are correspondingly enclosed by atomically well-defined nanofacets, {111}, {100}, and {310} respectively, have been prepared to study the structure-dependent ORR selectivity in alkaline solution. The ORR behaviors on Au octahedra and cubes were found similar to those on corresponding single-crystal surfaces. Astonishingly, Au {310} nanofacet catalyzes the 4e ORR over a wide potential range; such effect was not observed on any Au single-crystalline surfaces in the past. These high-quality single-crystalline gold nanocrystals with differently expressed atomic arrangements of their surface can serve also as model systems to understand the nature of the ORR in alkaline solution. Combined with DFT calculations, we propose that the O_2-H_2O coadsorption mechanism plays a critical role in the observed 4e-ORR activities on {100} and {310} facets. The ease of attaining single-crystalline surfaces using gold nanocrystals provides new opportunities for gaining an in-depth understanding of the mechanisms of catalytic reactions, thereby opening up new strategies for the rational design of catalyst materials.[318]

BIBLIOGRAPHY

1. P. Moriarty, D. Honnery. The Problems We Face. *Rise and Fall of the Carbon Civilisation*. Springer London, 2011, pp 1-13.
2. B. Sørensen. Hydrogen. *Hydrogen and Fuel Cells*. Academic Press: Burlington, 2005, pp 5-111.
3. S. Dunn. Hydrogen futures: toward a sustainable energy system. *International Journal of Hydrogen Energy* 2002, **27**(3)**:** 235-264.
4. S.A. Sherif, F. Barbir, T.N. Veziroglu. Wind energy and the hydrogen economy--review of the technology. *Solar Energy* 2005, **78**(5)**:** 647-660.
5. K.E. Ayers, L.T. Dalton, E.B. Anderson. Efficient Generation of High Energy Density Fuel from Water. *ECS Transactions* 2012, **41**(33)**:** 27-38.
6. 2020 visions. *Nature* 2010, **463**(7277)**:** 26-32.
7. R.F. Service. TRANSPORTATION RESEARCH Hydrogen Cars: Fad or the Future? *Science* 2009, **324**(5932)**:** 1257-1259.
8. F.T. Wagner, B. Lakshmanan, M.F. Mathias. Electrochemistry and the Future of the Automobile. *The Journal of Physical Chemistry Letters* 2010, **1**(14)**:** 2204-2219.
9. M. Winter, R.J. Brodd. What are batteries, fuel cells, and supercapacitors? *Chemical Reviews* 2004, **104**(10)**:** 4245-4269.
10. http://www1.eere.energy.gov/hydrogenandfuelcells/mypp/pdfs/fuel_cells.pdf
11. L. Carrette, K.A. Friedrich, U. Stimming. Fuel Cells: Principles, Types, Fuels, and Applications. *ChemPhysChem* 2000, **1**(4)**:** 162-193.
12. F. Bidault, D.J.L. Brett, P.H. Middleton, N.P. Brandon. Review of gas diffusion cathodes for alkaline fuel cells. *Journal of Power Sources* 2009, **187**(1)**:** 39-48.
13. M. Zhiani, H.A. Gasteiger, M. Piana, S. Catanorchi. Comparative study between platinum supported on carbon and non-noble metal cathode catalyst in alkaline direct ethanol fuel cell (ADEFC). *International Journal of Hydrogen Energy* 2011, **36**(8)**:** 5110-5116.
14. N. Ramaswamy, S. Mukerjee. Fundamental Mechanistic Understanding of Electrocatalysis of Oxygen Reduction on Pt and Non-Pt Surfaces: Acid versus Alkaline Media. *Advances in Physical Chemistry* 2012, **2012**.
15. E.H. Yu, X. Wang, U. Krewer, L. Li, K. Scott. Direct oxidation alkaline fuel cells: from materials to systems. *Energy & Environmental Science* 2012, **5**(2)**:** 5668-5680.
16. G. Merle, M. Wessling, K. Nijmeijer. Anion exchange membranes for alkaline fuel cells: A review. *Journal of Membrane Science* 2011, **377**(1–2)**:** 1-35.
17. M. Ni, M.K.H. Leung, D.Y.C. Leung, K. Sumathy. A review and recent developments in photocatalytic water-splitting using TiO2 for hydrogen production. *Renewable and Sustainable Energy Reviews* 2007, **11**(3)**:** 401-425.
18. A. Haryanto, S. Fernando, N. Murali, S. Adhikari. Current Status of Hydrogen Production Techniques by Steam Reforming of Ethanol: A Review. *Energy & Fuels* 2005, **19**(5)**:** 2098-2106.
19. M. Carmo, D.L. Fritz, J. Mergel, D. Stolten. A comprehensive review on PEM water electrolysis. *International Journal of Hydrogen Energy* 2013, **38**(12)**:** 4901-4934.

20. I. Dincer. Technical, environmental and exergetic aspects of hydrogen energy systems. *International Journal of Hydrogen Energy* 2002, **27**(3)**:** 265-285.
21. R. Kothari, D. Buddhi, R.L. Sawhney. Studies on the effect of temperature of the electrolytes on the rate of production of hydrogen. *International Journal of Hydrogen Energy* 2005, **30**(3)**:** 261-263.
22. N.M. Markovic, C.A. Lucas, V. Climent, V. Stamenkovic, P.N. Ross. Surface electrochemistry on an epitaxial palladium film on Pt(111): surface microstructure and hydrogen electrode kinetics. *Surface Science* 2000, **465**(1-2)**:** 103-114.
23. V. Stamenkovic, N. M. Markovic, P.N. Ross Jr. Structure-relationships in electrocatalysis: oxygen reduction and hydrogen oxidation reactions on Pt(111) and Pt(100) in solutions containing chloride ions. *Journal of Electroanalytical Chemistry* 2001, **500**(1-2)**:** 44-51.
24. M.W. Breiter. Reaction mechanisms of the H2 oxidation/evolution reaction. *Handbook of Fuel Cells*. John Wiley & Sons, Ltd, 2003.
25. S.A. Vilekar, I. Fishtik, R. Datta. Kinetics of the Hydrogen Electrode Reaction. *Journal of the Electrochemical Society* 2010, **157**(7)**:** B1040-B1050.
26. W. Sheng, H.A. Gasteiger, Y. Shao-Horn. Hydrogen Oxidation and Evolution Reaction Kinetics on Platinum: Acid vs Alkaline Electrolytes. *Journal of the Electrochemical Society* 2010, **157**(11)**:** B1529-B1536.
27. J.K. Norskov, T. Bligaard, A. Logadottir, J.R. Kitchin, J.G. Chen, S. Pandelov, U. Stimming. Trends in the Exchange Current for Hydrogen Evolution. *Journal of the Electrochemical Society* 2005, **152**(3)**:** J23-J26.
28. V. Stamenković, N.M. Marković. Oxygen Reduction and Hydrogen Oxidation Reactions on Pt(111) and Pt(100) in Solutions Containing Copper Ions. *Langmuir* 2001, **17**(8)**:** 2388-2394.
29. J.X. Wang, T.E. Springer, P. Liu, M.H. Shao, R.R. Adzic. Hydrogen oxidation reaction on Pt in acidic media: Adsorption isotherm and activation free energies. *Journal of Physical Chemistry C* 2007, **111**(33)**:** 12425-12433.
30. J.X. Wang, T.E. Springer, R.R. Adzic. Dual-pathway kinetic equation for the hydrogen oxidation reaction on Pt electrodes. *Journal of the Electrochemical Society* 2006, **153**(9)**:** A1732-A1740.
31. J. Durst, A. Siebel, C. Simon, F. Haschéé, J. Herranz, H. Gasteiger. New insights into the electrochemical hydrogen oxidation and evolution reaction mechanism. *Energy & Environmental Science* 2014(7)**:** 2255-2260.
32. L.I. Krishtalik. Frumkin Memorial Medal Lecture: Studies in the mechanisms of charge transfer reactions. *Electrochimica Acta* 2002, **48**(2)**:** 181-190.
33. L.L. Swette, A.B. LaConti, S.A. McCatty. Proton-exchange membrane regenerative fuel cells. *Journal of Power Sources* 1994, **47**(3)**:** 343-351.
34. T. Ioroi, N. Kitazawa, K. Yasuda, Y. Yamamoto, H. Takenaka. Iridium Oxide/Platinum Electrocatalysts for Unitized Regenerative Polymer Electrolyte Fuel Cells. *Journal of the Electrochemical Society* 2000, **147**(6)**:** 2018-2022.
35. T. Ioroi, T. Oku, K. Yasuda, N. Kumagai, Y. Miyazaki. Influence of PTFE coating on gas diffusion backing for unitized regenerative polymer electrolyte fuel cells. *Journal of Power Sources* 2003, **124**(2)**:** 385-389.

36. K. Sasaki, J.X. Wang, M. Balasubramanian, J. McBreen, F. Uribe, R.R. Adzic. Ultra-low platinum content fuel cell anode electrocatalyst with a long-term performance stability. *Electrochimica Acta* 2004, **49**(22-23)**:** 3873-3877.
37. K. Sasaki, Y. Mo, J.X. Wang, M. Balasubramanian, F. Uribe, J. McBreen, R.R. Adzic. Pt submonolayers on metal nanoparticles - novel electrocatalysts for H-2 oxidation and O-2 reduction. *Electrochimica Acta* 2003, **48**(25-26)**:** 3841-3849.
38. S.R. Brankovic, J. McBreen, R.R. Adzic. Spontaneous deposition of Pt on the Ru(0001) surface. *Journal of Electroanalytical Chemistry* 2001, **503**(1-2)**:** 99-104.
39. S.R. Brankovic, J.X. Wang, R.R. Adzic. New methods of controlled monolayer-to-multilayer deposition of Pt for designing electrocatalysts at an atomic level. *Journal of the Serbian Chemical Society* 2001, **66**(11-12)**:** 887-898.
40. J.X. Wang, S.R. Brankovic, Y. Zhu, J.C. Hanson, R.R. Adzic. Kinetic characterization of PtRu fuel cell anode catalysts made by spontaneous Pt deposition on Ru nanoparticles. *Journal of the Electrochemical Society* 2003, **150**(8)**:** A1108-A1117.
41. J. Greeley, T.F. Jaramillo, J. Bonde, I. Chorkendorff, J.K. Norskov. Computational high-throughput screening of electrocatalytic materials for hydrogen evolution. *Nature Materials* 2006, **5**(11)**:** 909-913.
42. O. Aaboubi. Hydrogen evolution activity of Ni-Mo coating electrodeposited under magnetic field control. *International Journal of Hydrogen Energy* 2011, **36**(8)**:** 4702-4709.
43. A. Misra, J. Giri, C. Daraio. Hydrogen Evolution on Hydrophobic Aligned Carbon Nanotube Arrays. *Acs Nano* 2009, **3**(12)**:** 3903-3908.
44. P.S. Fernández, E.B. Castro, S.G. Real, M.E. Martins. Electrochemical behaviour of single walled carbon nanotubes - Hydrogen storage and hydrogen evolution reaction. *International Journal of Hydrogen Energy* 2009, **34**(19)**:** 8115-8126.
45. A. Abbaspour, E. Mirahmadi. Electrocatalytic hydrogen evolution reaction on microwave assisted sol-gel-derived carbon ceramic electrodes modified with metalophthalocyanines. *Journal of Electroanalytical Chemistry* 2011, **652**(1-2)**:** 32-36.
46. T.F. Jaramillo, K.P. Jørgensen, J. Bonde, J.H. Nielsen, S. Horch, I. Chorkendorff. Identification of Active Edge Sites for Electrochemical H2 Evolution from MoS2 Nanocatalysts. *Science* 2007, **317**(5834)**:** 100-102.
47. J. Kibsgaard, Z. Chen, B.N. Reinecke, T.F. Jaramillo. Engineering the surface structure of MoS2 to preferentially expose active edge sites for electrocatalysis. *Nature Materials* 2012, **11**(11)**:** 963-969.
48. A.B. Laursen, S. Kegnaes, S. Dahl, I. Chorkendorff. Molybdenum sulfides-efficient and viable materials for electro - and photoelectrocatalytic hydrogen evolution. *Energy & Environmental Science* 2012, **5**(2)**:** 5577-5591.
49. B. Cao, G.M. Veith, J.C. Neuefeind, R.R. Adzic, P.G. Khalifah. Mixed close packed cobalt molybdenum nitrides as non-noble metal electrocatalysts for the hydrogen evolution reaction. *Journal of the American Chemical Society* 2013, **135**(51)**:** 19186-19192.
50. W.-F. Chen, K. Sasaki, C. Ma, A.I. Frenkel, N. Marinkovic, J.T. Muckerman, Y. Zhu, R.R. Adzic. Hydrogen-Evolution Catalysts Based on Non-Noble Metal Nickel–

Molybdenum Nitride Nanosheets. *Angewandte Chemie International Edition* 2012, **51**(25)**:** 6131-6135.
51. W.F. Chen, C.H. Wang, K. Sasaki, N. Marinkovic, W. Xu, J.T. Muckerman, Y. Zhu, R.R. Adzic. Highly active and durable nanostructured molybdenum carbide electrocatalysts for hydrogen production. *Energy & Environmental Science* 2013, **6**(3)**:** 943-951.
52. D.V. Esposito, J.G. Chen. Monolayer platinum supported on tungsten carbides as low-cost electrocatalysts: opportunities and limitations. *Energy & Environmental Science* 2011, **4**(10)**:** 3900-3912.
53. D.V. Esposito, S.T. Hunt, Y.C. Kimmel, J.G. Chen. A New Class of Electrocatalysts for Hydrogen Production from Water Electrolysis: Metal Monolayers Supported on Low-Cost Transition Metal Carbides. *Journal of the American Chemical Society* 2012, **134**(6)**:** 3025-3033.
54. T.G. Kelly, J.G. Chen. Metal overlayer on metal carbide substrate: unique bimetallic properties for catalysis and electrocatalysis. *Chemical Society Reviews* 2012, **41**(24)**:** 8021-8034.
55. N.A. Anastasijević, V. Vesović, R.R. Adžić. Determination of the kinetic parameters of the oxygen reduction reaction using the rotating ring-disk electrode: Part I. Theory. *Journal of Electroanalytical Chemistry and Interfacial Electrochemistry* 1987, **229**(1-2)**:** 305-316.
56. N.A. Anastasijevic, V. Vesovic, R.R. Adzic. Determination of the Kinetic Parameters of the Oxygen Reduction Reaction Using the Rotating-Ring-Disk Electrode .2. Applications. *Journal of Electroanalytical Chemistry* 1987, **229**(1-2)**:** 317-325.
57. R. Adzic. *Recent Advances in the Kinetics of Oxygen Reduction*. Wiley-VCH: New York, 1998.
58. H.A. Gasteiger, S.S. Kocha, B. Sompalli, F.T. Wagner. Activity benchmarks and requirements for Pt, Pt-alloy, and non-Pt oxygen reduction catalysts for PEMFCs. *Applied Catalysis B-Environmental* 2005, **56**(1-2)**:** 9-35.
59. R. Srivastava, P. Mani, N. Hahn, P. Strasser. Efficient Oxygen Reduction Fuel Cell Electrocatalysis on Voltammetrically Dealloyed Pt–Cu–Co Nanoparticles. *Angewandte Chemie International Edition* 2007, **46**(47)**:** 8988-8991.
60. H.A. Gasteiger, Y. Liu, D. Baker, W. Gu. Kinetics and Kinetically Limited Performance in PEMFCs and DMFCs with State-of-the-Art Catalysts. In: S. Kakaç, A. Pramuanjaroenkij, L. Vasiliev (eds). *Mini-Micro Fuel Cells*. Springer Netherlands, 2008, pp 209-224.
61. H.J. Zhou, W.P. Zhou, R.R. Adzic, S.S. Wong. Enhanced Electrocatalytic Performance of One-Dimensional Metal Nanowires and Arrays Generated via an Ambient, Surfactantless Synthesis. *Journal of Physical Chemistry C* 2009, **113**(14)**:** 5460-5466.
62. C. Koenigsmann, W.P. Zhou, R.R. Adzic, E. Sutter, S.S. Wong. Size-Dependent Enhancement of Electrocatalytic Performance in Relatively Defect-Free, Processed Ultrathin Platinum Nanowires. *Nano Letters* 2010, **10**(8)**:** 2806-2811.
63. S. Sun, G. Zhang, D. Geng, Y. Chen, R. Li, M. Cai, X. Sun. A Highly Durable Platinum Nanocatalyst for Proton Exchange Membrane Fuel Cells: Multiarmed Starlike Nanowire Single Crystal. *Angewandte Chemie International Edition* 2011, **50**(2)**:** 422-426.

64. Z. Chen, M. Waje, W. Li, Y. Yan. Supportless Pt and PtPd Nanotubes as Electrocatalysts for Oxygen-Reduction Reactions. *Angewandte Chemie International Edition* 2007, **46**(22)**:** 4060-4063.
65. H.M. Chen, R.S. Liu, M.Y. Lo, S.C. Chang, L.D. Tsai, Y.M. Peng, J.F. Lee. Hollow platinum spheres with nano-channels: Synthesis and enhanced catalysis for oxygen reduction. *Journal of Physical Chemistry C* 2008, **112**(20)**:** 7522-7526.
66. Y. Liu, C. Ji, W. Gu, J. Jorne, H.A. Gasteiger. Effects of Catalyst Carbon Support on Proton Conduction and Cathode Performance in PEM Fuel Cells. *Journal of the Electrochemical Society* 2011, **158**(6)**:** B614-B621.
67. B. Wu, Y. Kuang, X. Zhang, J. Chen. Noble metal nanoparticles/carbon nanotubes nanohybrids: Synthesis and applications. *Nano Today* 2011, **6**(1)**:** 75-90.
68. G. Sevjidsuren, S. Zils, S. Kaserer, A. Wolz, F. Ettingshausen, D. Dixon, A. Schoekel, C. Roth, P. Altantsog, D. Sangaa, C. Ganzorig. Effect of different support morphologies and pt particle sizes in electrocatalysts for fuel cell applications. *J. Nanomaterials* 2010, **2010:** 1-9.
69. J. Rooke, C.d.M. Passos, M. Chatenet, R. Sescousse, T. Budtova, S. Berthon-Fabry, R. Mosdale, F. Maillard. Synthesis and Properties of Platinum Nanocatalyst Supported on Cellulose-Based Carbon Aerogel for Applications in PEMFCs. *Journal of the Electrochemical Society* 2011, **158**(7)**:** B779-B789.
70. S.-H. Liu, C.-C. Chiang, M.-T. Wu, S.-B. Liu. Electrochemical activity and durability of platinum nanoparticles supported on ordered mesoporous carbons for oxygen reduction reaction. *International Journal of Hydrogen Energy* 2010, **35**(15)**:** 8149-8154.
71. Z. Wen, J. Liu, J. Li. Core/Shell Pt/C Nanoparticles Embedded in Mesoporous Carbon as a Methanol-Tolerant Cathode Catalyst in Direct Methanol Fuel Cells. *Advanced Materials* 2008, **20**(4)**:** 743-747.
72. V.R. Stamenkovic, B. Fowler, B.S. Mun, G. Wang, P.N. Ross, C.A. Lucas, N.M. Marković. Improved Oxygen Reduction Activity on Pt3Ni(111) via Increased Surface Site Availability. *Science* 2007, **315**(5811)**:** 493-497.
73. V. Stamenkovic, B.S. Mun, K.J.J. Mayrhofer, P.N. Ross, N.M. Markovic, J. Rossmeisl, J. Greeley, J.K. Nørskov. Changing the Activity of Electrocatalysts for Oxygen Reduction by Tuning the Surface Electronic Structure. *Angewandte Chemie* 2006, **118**(18)**:** 2963-2967.
74. GreeleyJ, I.E.L. Stephens, A.S. Bondarenko, T.P. Johansson, H.A. Hansen, T.F. Jaramillo, RossmeislJ, ChorkendorffI, J.K. Nørskov. Alloys of platinum and early transition metals as oxygen reduction electrocatalysts. *Nature Chemistry* 2009, **1**(7)**:** 552-556.
75. C. Chen, Y. Kang, Z. Huo, Z. Zhu, W. Huang, H.L. Xin, J.D. Snyder, D. Li, J.A. Herron, M. Mavrikakis, M. Chi, K.L. More, Y. Li, N.M. Markovic, G.A. Somorjai, P. Yang, V.R. Stamenkovic. Highly Crystalline Multimetallic Nanoframes with Three-Dimensional Electrocatalytic Surfaces. *Science* 2014, **343**(6177)**:** 1339-1343.
76. P. Strasser, S. Koh, J. Greeley. Voltammetric surface dealloying of Pt bimetallic nanoparticles: an experimental and DFT computational analysis. *Physical Chemistry Chemical Physics* 2008, **10**(25)**:** 3670-3683.

77. P. Strasser, S. Koh, T. Anniyev, J. Greeley, K. More, C.F. Yu, Z.C. Liu, S. Kaya, D. Nordlund, H. Ogasawara, M.F. Toney, A. Nilsson. Lattice-strain control of the activity in dealloyed core-shell fuel cell catalysts. *Nature Chemistry* 2010, **2**(6)**:** 454-460.
78. K.C. Neyerlin, R. Srivastava, C.F. Yu, P. Strasser. Electrochemical activity and stability of dealloyed Pt-Cu and Pt-Cu-Co electrocatalysts for the oxygen reduction reaction (ORR). *Journal of Power Sources* 2009, **186**(2)**:** 261-267.
79. S. Koh, P. Strasser. Electrocatalysis on bimetallic surfaces: Modifying catalytic reactivity for oxygen reduction by voltammetric surface dealloying. *Journal of the American Chemical Society* 2007, **129**(42)**:** 12624-12625.
80. E. Antolini, J.R.C. Salgado, M.J. Giz, E.R. Gonzalez. Effects of geometric and electronic factors on ORR activity of carbon supported Pt-Co electrocatalysts in PEM fuel cells. *International Journal of Hydrogen Energy* 2005, **30**(11)**:** 1213-1220.
81. C. Wang, D. van der Vliet, K.L. More, N.J. Zaluzec, S. Peng, S. Sun, H. Daimon, G. Wang, J. Greeley, J. Pearson, A.P. Paulikas, G. Karapetrov, D. Strmcnik, N.M. Markovic, V.R. Stamenkovic. Multimetallic Au/FePt3 Nanoparticles as Highly Durable Electrocatalyst. *Nano Letters* 2010, **11**(3)**:** 919-926.
82. V.R. Stamenkovic, B.S. Mun, M. Arenz, K.J.J. Mayrhofer, C.A. Lucas, G. Wang, P.N. Ross, N.M. Markovic. Trends in electrocatalysis on extended and nanoscale Pt-bimetallic alloy surfaces. *Nature Materials* 2007, **6**(3)**:** 241-247.
83. S. Chen, P.J. Ferreira, W. Sheng, N. Yabuuchi, L.F. Allard, Y. Shao-Horn. Enhanced Activity for Oxygen Reduction Reaction on "Pt3Co" Nanoparticles: Direct Evidence of Percolated and Sandwich-Segregation Structures. *Journal of the American Chemical Society* 2008, **130**(42)**:** 13818-13819.
84. L. Dubau, F. Maillard, M. Chatenet, L. Guetaz, J. Andre, E. Rossinot. Durability of Pt3Co/C Cathodes in a 16 Cell PEMFC Stack: Macro/Microstructural Changes and Degradation Mechanisms. *Journal of the Electrochemical Society* 2010, **157**(12)**:** B1887-B1895.
85. S. Koh, N. Hahn, C. Yu, P. Strasser. Effects of Composition and Annealing Conditions on Catalytic Activities of Dealloyed Pt--Cu Nanoparticle Electrocatalysts for PEMFC. *Journal of the Electrochemical Society* 2008, **155**(12)**:** B1281-B1288.
86. T.-Y. Jeon, S.J. Yoo, Y.-H. Cho, S.H. Kang, Y.-E. Sung. Effect of de-alloying of Pt-Ni bimetallic nanoparticles on the oxygen reduction reaction. *Electrochemistry Communications* 2010, **12**(12)**:** 1796-1799.
87. J. Wu, J. Zhang, Z. Peng, S. Yang, F.T. Wagner, H. Yang. Truncated Octahedral Pt3Ni Oxygen Reduction Reaction Electrocatalysts. *Journal of the American Chemical Society* 2010, **132**(14)**:** 4984-4985.
88. C. Cui, L. Gan, M. Heggen, S. Rudi, P. Strasser. Compositional segregation in shaped Pt alloy nanoparticles and their structural behaviour during electrocatalysis. *Nature Materials* 2013, **12**(8)**:** 765-771.
89. P. Mani, R. Srivastava, P. Strasser. Dealloyed binary PtM3 (M = Cu, Co, Ni) and ternary PtNi3M (M = Cu, Co, Fe, Cr) electrocatalysts for the oxygen reduction reaction: Performance in polymer electrolyte membrane fuel cells. *Journal of Power Sources* 2011, **196**(2)**:** 666-673.

90. J. Zhang, Y. Mo, M.B. Vukmirovic, R. Klie, K. Sasaki, R.R. Adzic. Platinum monolayer electrocatalysts for O-2 reduction: Pt monolayer on Pd(111) and on carbon-supported Pd nanoparticles. *Journal of Physical Chemistry B* 2004, **108**(30)**:** 10955-10964.
91. R.R. Adzic, J. Zhang, K. Sasaki, M.B. Vukmirovic, M. Shao, J.X. Wang, A.U. Nilekar, M. Mavrikakis, J.A. Valerio, F. Uribe. Platinum monolayer fuel cell electrocatalysts. *Topics in Catalysis* 2007, **46**(3-4)**:** 249-262.
92. M.H. Shao, K. Sasaki, R.R. Adzic. Pd-Fe nanoparticles as electrocatalysts for oxygen reduction. *Journal of the American Chemical Society* 2006, **128**(11)**:** 3526-3527.
93. M.H. Shao, P. Liu, J.L. Zhang, R. Adzic. Origin of enhanced activity in palladium alloy electrocatalysts for oxygen reduction reaction. *Journal of Physical Chemistry B* 2007, **111**(24)**:** 6772-6775.
94. M.H. Shao, T. Huang, P. Liu, J. Zhang, K. Sasaki, M.B. Vukmirovic, R.R. Adzic. Palladium monolayer and palladium alloy electrocatalysts for oxygen reduction. *Langmuir* 2006, **22**(25)**:** 10409-10415.
95. B. Wang. Recent development of non-platinum catalysts for oxygen reduction reaction. *Journal of Power Sources* 2005, **152**(1)**:** 1-15.
96. Y.J. Feng, N. Alonso-Vante. Nonprecious metal catalysts for the molecular oxygen-reduction reaction. *Physica Status Solidi B-Basic Solid State Physics* 2008, **245**(9)**:** 1792-1806.
97. B. Winther-Jensen, O. Winther-Jensen, M. Forsyth, D.R. MacFarlane. High Rates of Oxygen Reduction over a Vapor Phase–Polymerized PEDOT Electrode. *Science* 2008, **321**(5889)**:** 671-674.
98. A. Morozan, B. Jousselme, S. Palacin. Low-platinum and platinum-free catalysts for the oxygen reduction reaction at fuel cell cathodes. *Energy & Environmental Science* 2011, **4**(4)**:** 1238-1254.
99. F.d.r. Jaouen, J. Herranz, M. Lefèvre, J.-P. Dodelet, U.I. Kramm, I. Herrmann, P. Bogdanoff, J. Maruyama, T. Nagaoka, A. Garsuch, J.R. Dahn, T. Olson, S. Pylypenko, P. Atanassov, E.A. Ustinov. Cross-Laboratory Experimental Study of Non-Noble-Metal Electrocatalysts for the Oxygen Reduction Reaction. *ACS Applied Materials & Interfaces* 2009, **1**(8)**:** 1623-1639.
100. M. Lef èvre, E. Proietti, F. Jaouen, J.-P. Dodelet. Iron-Based Catalysts with Improved Oxygen Reduction Activity in Polymer Electrolyte Fuel Cells. *Science* 2009, **324**(5923)**:** 71-74.
101. R. Bashyam, P. Zelenay. A class of non-precious metal composite catalysts for fuel cells. *Nature* 2006, **443**(7107)**:** 63-66.
102. E. Proietti, F. Jaouen, M. Lef èvre, N. Larouche, J. Tian, J. Herranz, J.-P. Dodelet. Iron-based cathode catalyst with enhanced power density in polymer electrolyte membrane fuel cells. *Nat Commun* 2011, **2:** 416.
103. G. Wu, K.L. More, C.M. Johnston, P. Zelenay. High-Performance Electrocatalysts for Oxygen Reduction Derived from Polyaniline, Iron, and Cobalt. *Science* 2011, **332**(6028)**:** 443-447.
104. D. Wang, C.V. Subban, H. Wang, E. Rus, F.J. DiSalvo, H.D. Abruña. Highly Stable and CO-Tolerant Pt/Ti0.7W0.3O2 Electrocatalyst for Proton-Exchange Membrane Fuel Cells. *Journal of the American Chemical Society* 2010, **132**(30)**:** 10218-10220.

105. A. Ishihara, Y. Shibata, S. Mitsushima, K. Ota. Partially oxidized tantalum carbonitrides as a new nonplatinum cathode for PEFC-1-. *Journal of the Electrochemical Society* 2008, **155**(4)**:** B400-B406.
106. B. Cao, J.C. Neuefeind, R.R. Adzic, P.G. Khalifah. Molybdenum Nitrides as Oxygen Reduction Reaction Catalysts: Structural and Electrochemical Studies. *Inorganic Chemistry* 2015, **54**(5)**:** 2128-2136.
107. B. Cao, G.M. Veith, R.E. Diaz, J. Liu, E.A. Stach, R.R. Adzic, P.G. Khalifah. Cobalt Molybdenum Oxynitrides: Synthesis, Structural Characterization, and Catalytic Activity for the Oxygen Reduction Reaction. *Angewandte Chemie International Edition* 2013, **52**(41)**:** 10753-10757.
108. M.-R. Gao, J. Jiang, S.-H. Yu. Solution-Based Synthesis and Design of Late Transition Metal Chalcogenide Materials for Oxygen Reduction Reaction (ORR). *Small* 2012, **8**(1)**:** 13-27.
109. Y. Li, W. Zhou, H. Wang, L. Xie, Y. Liang, F. Wei, J.-C. Idrobo, S.J. Pennycook, H. Dai. An oxygen reduction electrocatalyst based on carbon nanotube-graphene complexes. *Nat Nano* 2012, **7**(6)**:** 394-400.
110. R.R. Adzic, S. Strbac, N. Anastasijevic. Electrocatalysis of oxygen on single crystal gold electrodes. *Materials Chemistry and Physics* 1989, **22**(3-4)**:** 349-375.
111. J.S. Spendelow, A. Wieckowski. Electrocatalysis of oxygen reduction and small alcohol oxidation in alkaline media. *Physical Chemistry Chemical Physics* 2007, **9**(21)**:** 2654-2675.
112. L. Tammeveski, H. Erikson, A. Sarapuu, J. Kozlova, P. Ritslaid, V. Sammelselg, K. Tammeveski. Electrocatalytic oxygen reduction on silver nanoparticle/multi-walled carbon nanotube modified glassy carbon electrodes in alkaline solution. *Electrochemistry Communications* 2012, **20**(0)**:** 15-18.
113. Y.L. Cao, H.X. Yang, X.P. Ai, L.F. Xiao. The mechanism of oxygen reduction on MnO2-catalyzed air cathode in alkaline solution. *Journal of Electroanalytical Chemistry* 2003, **557:** 127-134.
114. F.H.B. Lima, M.L. Calegaro, E.A. Ticianelli. Electrocatalytic activity of manganese oxides prepared by thermal decomposition for oxygen reduction. *Electrochimica Acta* 2007, **52**(11)**:** 3732-3738.
115. J. Suntivich, H.A. Gasteiger, N. Yabuuchi, H. Nakanishi, J.B. Goodenough, Y. Shao-Horn. Design principles for oxygen-reduction activity on perovskite oxide catalysts for fuel cells and metal–air batteries. *Nature Chemistry* 2011, **3**(7)**:** 546-550.
116. H.T. Chung, J.H. Won, P. Zelenay. Active and stable carbon nanotube/nanoparticle composite electrocatalyst for oxygen reduction. *Nat Commun* 2013, **4:** 1922.
117. M.S. Ahmed, H.S. Han, S. Jeon. One-step chemical reduction of graphene oxide with oligothiophene for improved electrocatalytic oxygen reduction reactions. *Carbon* 2013, **61**(0)**:** 164-172.
118. I.-Y. Jeon, S. Zhang, L. Zhang, H.-J. Choi, J.-M. Seo, Z. Xia, L. Dai, J.-B. Baek. Edge-Selectively Sulfurized Graphene Nanoplatelets as Efficient Metal-Free Electrocatalysts for Oxygen Reduction Reaction: The Electron Spin Effect. *Advanced Materials* 2013, **25**(42)**:** 6138-6145.

119. S.R. Brankovic, J.X. Wang, R.R. Adzic. Metal monolayer deposition by replacement of metal adlayers on electrode surfaces. *Surface Science* 2001, **474**(1-3)**:** L173-L179.
120. J. Zhang, F.H.B. Lima, M.H. Shao, K. Sasaki, J.X. Wang, J. Hanson, R.R. Adzic. Platinum monolayer on nonnoble metal-noble metal core-shell nanoparticle electrocatalysts for O-2 reduction. *Journal of Physical Chemistry B* 2005, **109**(48)**:** 22701-22704.
121. J. Zhang, M.B. Vukmirovic, K. Sasaki, F. Uribe, R.R. Adzic. Platinum monolayer electro catalysts for oxygen reduction: effect of substrates, and long-term stability. *Journal of the Serbian Chemical Society* 2005, **70**(3)**:** 513-525.
122. J.L. Zhang, M.B. Vukmirovic, Y. Xu, M. Mavrikakis, R.R. Adzic. Controlling the catalytic activity of platinum-monolayer electrocatalysts for oxygen reduction with different substrates. *Angewandte Chemie-International Edition* 2005, **44**(14)**:** 2132-2135.
123. F.H.B. Lima, J. Zhang, M.H. Shao, K. Sasaki, M.B. Vukmirovic, E.A. Ticianelli, R.R. Adzic. Catalytic activity-d-band center correlation for the O-2 reduction reaction on platinum in alkaline solutions. *Journal of Physical Chemistry C* 2007, **111**(1)**:** 404-410.
124. M. Shao, K. Sasaki, N.S. Marinkovic, L. Zhang, R.R. Adzic. Synthesis and characterization of platinum monolayer oxygen-reduction electrocatalysts with Co-Pd core-shell nanoparticle supports. *Electrochemistry Communications* 2007, **9**(12)**:** 2848-2853.
125. M.H. Shao, K. Sasaki, P. Liu, R.R. Adzic. Pd3Fe and Pt Monolayer-Modified Pd3Fe Electrocatalysts for Oxygen Reduction. *Zeitschrift für Physikalische Chemie* 2007, **221**(9-10)**:** 1175-1190.
126. M.B. Vukmirovic, J. Zhang, K. Sasaki, A.U. Nilekar, F. Uribe, M. Mavrikakis, R.R. Adzic. Platinum monolayer electrocatalysts for oxygen reduction. *Electrochimica Acta* 2007, **52**(6)**:** 2257-2263.
127. F.H.B. Lima, J. Zhang, M.H. Shao, K. Sasaki, M.B. Vukmirovic, E.A. Ticianelli, R.R. Adzic. Pt monolayer electrocatalysts for O-2 reduction: PdCo/C substrate-induced activity in alkaline media. *Journal of Solid State Electrochemistry* 2008, **12**(4)**:** 399-407.
128. K. Sasaki, R.R. Adzic. Monolayer-level Ru- and NbO2-supported platinum electrocatalysts for methanol oxidation. *Journal of the Electrochemical Society* 2008, **155**(2)**:** 180-186.
129. W.P. Zhou, X.F. Yang, M.B. Vukmirovic, B.E. Koel, J. Jiao, G.W. Peng, M. Mavrikakis, R.R. Adzic. Improving Electrocatalysts for O-2 Reduction by Fine-Tuning the Pt-Support Interaction: Pt Monolayer on the Surfaces of a Pd3Fe(111) Single-Crystal Alloy. *Journal of the American Chemical Society* 2009, **131**(35)**:** 12755-12762.
130. R.R. Adzic, F.H.B. Lima. Platinum monolayer oxygen reduction electrocatalysts. *Handbook of Fuel Cells*. John Wiley & Sons, Ltd, 2010.
131. T. Ghosh, M.B. Vukmirovic, F.J. DiSalvo, R.R. Adzic. Intermetallics as Novel Supports for Pt Monolayer O-2 Reduction Electrocatalysts: Potential for Significantly Improving Properties. *Journal of the American Chemical Society* 2010, **132**(3)**:** 906-907.
132. K. Gong, W.-F. Chen, K. Sasaki, D. Su, M.B. Vukmirovic, W. Zhou, E.L. Izzo, C. Perez-Acosta, P. Hirunsit, P.B. Balbuena, R.R. Adzic. Platinum-monolayer electrocatalysts: Palladium interlayer on IrCo alloy core improves activity in oxygen-reduction reaction. *Journal of Electroanalytical Chemistry* 2010, **649**(1-2)**:** 232-237.

133. K. Gong, D. Su, R.R. Adzic. Platinum-Monolayer Shell on AuNi0.5Fe Nanoparticle Core Electrocatalyst with High Activity and Stability for the Oxygen Reduction Reaction. *Journal of the American Chemical Society* 2010, **132**(41)**:** 14364-14366.
134. S. Knupp, M. Vukmirovic, P. Haldar, J. Herron, M. Mavrikakis, R. Adzic. Platinum Monolayer Electrocatalysts for O2 Reduction: Pt Monolayer on Carbon-Supported PdIr Nanoparticles. *Electrocatalysis* 2010, **1**(4)**:** 213-223.
135. K. Sasaki, H. Naohara, Y. Cai, Y.M. Choi, P. Liu, M.B. Vukmirovic, J.X. Wang, R.R. Adzic. Core-Protected Platinum Monolayer Shell High-Stability Electrocatalysts for Fuel-Cell Cathodes. *Angew Chem Int Ed* 2010, **49**(46)**:** 8602-8607.
136. K. Sasaki, M.B. Vukmirovic, J.X. Wang, R.R. Adzic. Platinum Monolayer Electrocatalysts: Improving Structure and Activity. *Fuel Cell Science*. John Wiley & Sons, Inc., 2010, pp 215-236.
137. K. Sasaki, J.X. Wang, H. Naohara, N. Marinkovic, K. More, H. Inada, R.R. Adzic. Recent advances in platinum monolayer electrocatalysts for oxygen reduction reaction: Scale-up synthesis, structure and activity of Pt shells on Pd cores. *Electrochimica Acta* 2010, **55**(8)**:** 2645-2652.
138. M. Shao, A. Peles, K. Shoemaker, M. Gummalla, P.N. Njoki, J. Luo, C.-J. Zhong. Enhanced Oxygen Reduction Activity of Platinum Monolayer on Gold Nanoparticles. *The Journal of Physical Chemistry Letters* 2010, **2**(2)**:** 67-72.
139. M. Shao, K. Shoemaker, A. Peles, K. Kaneko, L. Protsailo. Pt monolayer on porous Pd-Cu alloys as oxygen reduction electrocatalysts. *Journal of the American Chemical Society* 2010, **132**(27)**:** 9253-9255.
140. Y. Xing, Y. Cai, M.B. Vukmirovic, W.-P. Zhou, H. Karan, J.X. Wang, R.R. Adzic. Enhancing Oxygen Reduction Reaction Activity via Pd−Au Alloy Sublayer Mediation of Pt Monolayer Electrocatalysts. *The Journal of Physical Chemistry Letters* 2010, **1**(21)**:** 3238-3242.
141. W.P. Zhou, K. Sasaki, D. Su, Y.M. Zhu, J.X. Wang, R.R. Adzic. Gram-Scale-Synthesized Pd2Co-Supported Pt Monolayer Electrocatalysts for Oxygen Reduction Reaction. *Journal of Physical Chemistry C* 2010, **114**(19)**:** 8950-8957.
142. Y. Cai, R.R. Adzic. Platinum Monolayer Electrocatalysts for the Oxygen Reduction Reaction: Improvements Induced by Surface and Subsurface Modifications of Cores. *Advances in Physical Chemistry* 2011, **2011:** 1-16.
143. Y. Cai, C. Ma, Y. Zhu, J.X. Wang, R.R. Adzic. Low-Coordination Sites in Oxygen-Reduction Electrocatalysis: Their Roles and Methods for Removal. *Langmuir* 2011, **27**(13)**:** 8540-8547.
144. K. Gong, M.B. Vukmirovic, C. Ma, Y. Zhu, R.R. Adzic. Synthesis and catalytic activity of Pt monolayer on Pd tetrahedral nanocrystals with CO-adsorption-induced removal of surfactants. *Journal of Electroanalytical Chemistry* 2011.
145. C. Koenigsmann, A.C. Santulli, K. Gong, M.B. Vukmirovic, W.-p. Zhou, E. Sutter, S.S. Wong, R.R. Adzic. Enhanced Electrocatalytic Performance of Processed, Ultrathin, Supported Pd–Pt Core–Shell Nanowire Catalysts for the Oxygen Reduction Reaction. *Journal of the American Chemical Society* 2011, **133** (25)**:** 9783–9795.

146. A.U. Nilekar, K. Sasaki, C.A. Farberow, R.R. Adzic, M. Mavrikakis. Mixed-Metal Pt Monolayer Electrocatalysts with Improved CO Tolerance. *Journal of the American Chemical Society* 2011, **133**(46)**:** 18574-18576.
147. K. Sasaki, K. Kuttiyiel, D. Su, R. Adzic. Platinum Monolayer on IrFe Core–Shell Nanoparticle Electrocatalysts for the Oxygen Reduction Reaction. *Electrocatalysis* 2011, **2**(2)**:** 134-140.
148. M. Shao, A. Peles, K. Shoemaker. Electrocatalysis on Platinum Nanoparticles: Particle Size Effect on Oxygen Reduction Reaction Activity. *Nano Letters* 2011, **11**(9)**:** 3714-3719.
149. R.R. Adzic. Platinum Monolayer Electrocatalysts: Tunable Activity, Stability, and Self-Healing Properties. *Electrocatalysis* 2012, **3**(3-4)**:** 163-169.
150. K. Gong, Y. Choi, M.B. Vukmirovic, P. Liu, C. Ma, D. Su, R.R. Adzic. Tetrahedral Palladium Nanocrystals: A New Support for Platinum Monolayer Electrocatalysts with High Activity and Stability in the Oxygen Reduction Reaction. *Zeitschrift für Physikalische Chemie* 2012.
151. H.I. Karan, K. Sasaki, K. Kuttiyiel, C.A. Farberow, M. Mavrikakis, R.R. Adzic. Catalytic Activity of Platinum Monolayer on Iridium and Rhenium Alloy Nanoparticles for the Oxygen Reduction Reaction. *ACS Catalysis* 2012, **2**(5)**:** 817-824.
152. C. Koenigsmann, E. Sutter, R.R. Adzic, S.S. Wong. Size- and Composition-Dependent Enhancement of Electrocatalytic Oxygen Reduction Performance in Ultrathin Palladium–Gold (Pd1–xAux) Nanowires. *The Journal of Physical Chemistry C* 2012, **116**(29)**:** 15297-15306.
153. K.A. Kuttiyiel, K. Sasaki, Y. Choi, D. Su, P. Liu, R.R. Adzic. Bimetallic IrNi core platinum monolayer shell electrocatalysts for the oxygen reduction reaction. *Energy & Environmental Science* 2012, **5**(1)**:** 5297-5304.
154. M. Li, P. Liu, R.R. Adzic. Platinum Monolayer Electrocatalysts for Anodic Oxidation of Alcohols. *The Journal of Physical Chemistry Letters* 2012, **3**(23)**:** 3480-3485.
155. K. Sasaki, H. Naohara, Y. Choi, Y. Cai, W.-F. Chen, P. Liu, R.R. Adzic. Highly stable Pt monolayer on PdAu nanoparticle electrocatalysts for the oxygen reduction reaction. *Nat Commun* 2012, **3:** 1115.
156. M.B. Vukmirovic, Y. Cai, S.T. Bliznakov, K. Sasaki, J.X. Wang, R.R. Adzic. Platinum Monolayer Electrocatalysts for the Oxygen Reduction Reaction. *ECS Transactions* 2012, **45**(2)**:** 15-23.
157. L. Yang, M.B. Vukmirovic, D. Su, K. Sasaki, J. Herron, M. Mavrikakis, S. Liao, R.R. Adzic. Tuning the Catalytic Activity of Ru@Pt Core-Shell Nanoparticles for the Oxygen Reduction Reaction by Varying the Shell Thickness. *The Journal of Physical Chemistry C* 2012, **117**(4)**:** 1748-1753.
158. K. Gong, J. Park, D. Su, R. Adzic. Metalizing carbon nanotubes with Pd–Pt core–shell nanowires enhances electrocatalytic activity and stability in the oxygen reduction reaction. *Journal of Solid State Electrochemistry* 2014, **18**(5)**:** 1171-1179.
159. C. Koenigsmann, D.B. Semple, E. Sutter, S.E. Tobierre, S.S. Wong. Ambient Synthesis of High-Quality Ruthenium Nanowires and the Morphology-Dependent Electrocatalytic Performance of Platinum-Decorated Ruthenium Nanowires and Nanoparticles in the

Methanol Oxidation Reaction. *ACS Applied Materials & Interfaces* 2013, **5**(12)**:** 5518-5530.

160. K.A. Kuttiyiel, K. Sasaki, D. Su, M.B. Vukmirovic, N.S. Marinkovic, R.R. Adzic. Pt monolayer on Au-stabilized PdNi core–shell nanoparticles for oxygen reduction reaction. *Electrochimica Acta* 2013, **110:** 267-272.
161. M. Shao, B. Smith, S. Guerrero, L. Protsailo, D. Su, K. Kaneko, J.H. Odell, M. Humbert, K. Sasaki, J. Marzullo, R. Darling. Core-Shell Catalysts Consisting of Nanoporous Cores for Oxygen Reduction Reaction. *Physical Chemistry Chemical Physics* 2013, **15**(36)**:** 15078-15090.
162. S. Kumar, S. Zou. Electrooxidation of Carbon Monoxide and Methanol on Platinum-Overlayer-Coated Gold Nanoparticles: Effects of Film Thickness. *Langmuir* 2007, **23**(13)**:** 7365-7371.
163. Y. Choi, K. Kuttiyiel, J. Labis, K. Sasaki, G.-G. Park, T.-H. Yang, R. Adzic. Enhanced Oxygen Reduction Activity of IrCu Core Platinum Monolayer Shell Nano-electrocatalysts. *Topics in Catalysis* 2013, **56**(12)**:** 1059-1064.
164. M.B. Vukmirovic, Y. Zhang, J.X. Wang, D. Buceta, L. Wu, R.R. Adzic. Pt monolayer shell on hollow Pd core electrocatalysts: Scale up synthesis, structure, and activity for the oxygen reduction reaction. *Journal of the Serbian Chemical Society* 2013, **78**(12)**:** 1983-1992.
165. M.F. Mrozek, Y. Xie, M.J. Weaver. Surface-Enhanced Raman Scattering on Uniform Platinum-Group Overlayers: Preparation by Redox Replacement of Underpotential-Deposited Metals on Gold. *Analytical Chemistry* 2001, **73**(24)**:** 5953-5960.
166. S. Park, P. Yang, P. Corredor, M.J. Weaver. Transition Metal-Coated Nanoparticle Films: Vibrational Characterization with Surface-Enhanced Raman Scattering. *Journal of the American Chemical Society* 2002, **124**(11)**:** 2428-2429.
167. S.H. Yoo, S. Park. Platinum-Coated, Nanoporous Gold Nanorod Arrays: Synthesis and Characterization. *Advanced Materials* 2007, **19**(12)**:** 1612-1615.
168. D. Gokcen, S.-E. Bae, S.R. Brankovic. Stoichiometry of Pt Submonolayer Deposition via Surface-Limited Redox Replacement Reaction. *Journal of The Electrochemical Society* 2010, **157**(11)**:** D582-D587.
169. D.F. Yancey, E.V. Carino, R.M. Crooks. Electrochemical synthesis and electrocatalytic properties of Au@ Pt dendrimer-encapsulated nanoparticles. *J. Am. Chem. Soc* 2010, **132:** 10988-10989.
170. S. Yang, N.-Y. Park, J.W. Han, C. Kim, S.-C. Lee, H. Lee. A distinct platinum growth mode on shaped gold nanocrystals. *Chemical Communications* 2012, **48**(2).
171. D. Gokcen, S.-E. Bae, S.R. Brankovic. Reaction kinetics of metal deposition via surface limited red-ox replacement of underpotentially deposited metal monolayers. *Electrochimica Acta* 2011, **56**(16)**:** 5545-5553.
172. N. Jayaraju, D. Vairavapandian, Y.G. Kim, D. Banga, J.L. Stickney. Electrochemical Atomic Layer Deposition (E-ALD) of Pt Nanofilms Using SLRR Cycles. *Journal of The Electrochemical Society* 2012, **159**(10)**:** D616-D622.
173. Y. Jin, Y. Shen, S. Dong. Electrochemical Design of Ultrathin Platinum-Coated Gold Nanoparticle Monolayer Films as a Novel Nanostructured Electrocatalyst for Oxygen Reduction. *Journal of Physical Chemistry B* 2004, **108**(24)**:** 8142-8147.

174. A.U. Nilekar, Y. Xu, J.L. Zhang, M.B. Vukmirovic, K. Sasaki, R.R. Adzic, M. Mavrikakis. Bimetallic and ternary alloys for improved oxygen reduction catalysis. *Topics in Catalysis* 2007, **46**(3-4)**:** 276-284.
175. C. Koenigsmann, E. Sutter, T.A. Chiesa, R.R. Adzic, S.S. Wong. Highly Enhanced Electrocatalytic Oxygen Reduction Performance Observed in Bimetallic Palladium-Based Nanowires Prepared under Ambient, Surfactantless Conditions. *Nano Letters* 2012, **12**(4)**:** 2013-2020.
176. M. Humbert, B. Smith, Q. Wang, S. Ehrlich, M. Shao. Synthesis and Characterization of Palladium–Platinum Core–Shell Electrocatalysts for Oxygen Reduction. *Electrocatalysis* 2012**:** 1-6.
177. J.L. Zhang, M.B. Vukmirovic, K. Sasaki, A.U. Nilekar, M. Mavrikakis, R.R. Adzic. Mixed-metal Pt monolayer electrocatalysts for enhanced oxygen reduction kinetics. *Journal of the American Chemical Society* 2005, **127**(36)**:** 12480-12481.
178. R. Rettew, S. Cheng, M. Sauerbrey, T. Manz, D. Sholl, C. Jaye, D. Fischer, F. Alamgir. Near Surface Phase Transition of Solute Derived Pt Monolayers. *Topics in Catalysis* 2013, **56**(12)**:** 1065-1073.
179. Y.-G. Kim, J.Y. Kim, D. Vairavapandian, J.L. Stickney. Platinum Nanofilm Formation by EC-ALE via Redox Replacement of UPD Copper: Studies Using in-Situ Scanning Tunneling Microscopy. *The Journal of Physical Chemistry B* 2006, **110**(36)**:** 17998-18006.
180. M. Vukmirovic, S. Bliznakov, K. Sasaki, J.X. Wang, R.R. Adzic. Electrodeposition of Metals in Catalyst Synthesis: The Case of Platinum Monolayer Electrocatalysts. *Interface* 2011, **20**(2)**:** 33.
181. L. Sheridan, J. Czerwiniski, N. Jayaraju, D. Gebregziabiher, J. Stickney, D. Robinson, M. Soriaga. Electrochemical Atomic Layer Deposition (E-ALD) of Palladium Nanofilms by Surface Limited Redox Replacement (SLRR), with EDTA Complexation. *Electrocatalysis* 2012, **3**(2)**:** 96-107.
182. L.B. Sheridan, Y.-G. Kim, B.R. Perdue, K. Jagannathan, J.L. Stickney, D.B. Robinson. Hydrogen Adsorption, Absorption, and Desorption at Palladium Nanofilms formed on Au(111) by Electrochemical Atomic Layer Deposition (E-ALD): Studies using Voltammetry and In Situ Scanning Tunneling Microscopy. *The Journal of Physical Chemistry C* 2013, **117**(30)**:** 15728-15740.
183. M. Fayette, Y. Liu, D. Bertrand, J. Nutariya, N. Vasiljevic, N. Dimitrov. From Au to Pt via Surface Limited Redox Replacement of Pb UPD in One-Cell Configuration. *Langmuir* 2011, **27**(9)**:** 5650-5658.
184. D. Vairavapandian, J.L. Stickney. Formation of Platinum films by Electrochemical Atomic Layer Deposition (ALD) via Redox Replacement of UPD: Studies of Pb UPD as a Sacrificial Metal. *ECS Transactions* 2007, **3**(25)**:** 329-336.
185. A. Zolfaghari, B.E. Conway. Electroless deposition of Pt at a Pd electrode by reaction with sorbed H in Pd/H. *Journal of Electroanalytical Chemistry* 2000, **488**(2)**:** 151-153.
186. J. Nutariya, M. Fayette, N. Dimitrov, N. Vasiljevic. Growth of Pt by surface limited redox replacement of underpotentially deposited hydrogen. *Electrochimica Acta* 2013, **112:** 813-823.

187. S. Brimaud, R.J. Behm. Electrodeposition of a Pt Monolayer Film: Using Kinetic Limitations for Atomic Layer Epitaxy. *Journal of the American Chemical Society* 2013, **135**(32)**:** 11716-11719.
188. Y. Wang, N. Toshima. Preparation of Pd−Pt Bimetallic Colloids with Controllable Core/Shell Structures. *J. Phys. Chem. B* 1997, **101**(27)**:** 5301-5306.
189. S.I. Sanchez, M.W. Small, J.-m. Zuo, R.G. Nuzzo. Structural Characterization of Pt−Pd and Pd−Pt Core−Shell Nanoclusters at Atomic Resolution. *Journal of the American Chemical Society* 2009, **131**(24)**:** 8683-8689.
190. J. Wang, R. Adzic. Hydrogen absorption induced metal deposition on palladium and palladium-alloy particles. WO Patent 2006/135396; 2006.
191. A. Henglein. Preparation and Optical Aborption Spectra of AucorePtshell and PtcoreAushell Colloidal Nanoparticles in Aqueous Solution. *The Journal of Physical Chemistry B* 2000, **104**(10)**:** 2201-2203.
192. F. Taufany, C.-J. Pan, J. Rick, H.-L. Chou, M.-C. Tsai, B.-J. Hwang, D.-G. Liu, J.-F. Lee, M.-T. Tang, Y.-C. Lee, C.-I. Chen. Kinetically Controlled Autocatalytic Chemical Process for Bulk Production of Bimetallic Core–Shell Structured Nanoparticles. *Acs Nano* 2011, **5**(12)**:** 9370-9381.
193. C.H.L. Goodman, M.V. Pessa. Atomic layer epitaxy. *Journal of Applied Physics* 1986, **60**(3)**:** R65-R82.
194. S.M. George. Atomic Layer Deposition: An Overview. *Chemical Reviews* 2009, **110**(1)**:** 111-131.
195. T. Suntola. Atomic layer epitaxy. *Materials Science Reports* 1989, **4**(5)**:** 261-312.
196. C. Marichy, M. Bechelany, N. Pinna. Atomic Layer Deposition of Nanostructured Materials for Energy and Environmental Applications. *Advanced Materials* 2012, **24**(8)**:** 1017-1032.
197. C. Detavernier, J. Dendooven, S. Pulinthanathu Sree, K.F. Ludwig, J.A. Martens. Tailoring nanoporous materials by atomic layer deposition. *Chemical Society Reviews* 2011, **40**(11)**:** 5242-5253.
198. X. Jiang, H. Huang, F.B. Prinz, S.F. Bent. Application of Atomic Layer Deposition of Platinum to Solid Oxide Fuel Cells. *Chemistry of Materials* 2008, **20**(12)**:** 3897-3905.
199. J.H. Shim, X. Jiang, S.F. Bent, F.B. Prinz. Catalysts with Pt Surface Coating by Atomic Layer Deposition for Solid Oxide Fuel Cells. *Journal of the Electrochemical Society* 2010, **157**(6)**:** B793-B797.
200. J.W. Elam, A.V.V. Zinovev, M.J. Pellin, D.J. Comstock, M.C. Hersam. Nucleation and Growth of Noble Metals on Oxide Surfaces Using Atomic Layer Deposition. *ECS Transactions* 2007, **3**(15)**:** 271-278.
201. T. Aaltonen, M. Ritala, T. Sajavaara, J. Keinonen, M. Leskelä Atomic Layer Deposition of Platinum Thin Films. *Chemistry of Materials* 2003, **15**(9)**:** 1924-1928.
202. J.W. Elam, A. Zinovev, C.Y. Han, H.H. Wang, U. Welp, J.N. Hryn, M.J. Pellin. Atomic layer deposition of palladium films on Al2O3 surfaces. *Thin Solid Films* 2006, **515**(4)**:** 1664-1673.
203. T. Aaltonen, P. Alén, M. Ritala, M. Leskelä Ruthenium Thin Films Grown by Atomic Layer Deposition. *Chemical Vapor Deposition* 2003, **9**(1)**:** 45-49.

204. S.K. Kim, S.Y. Lee, S.W. Lee, G.W. Hwang, C.S. Hwang, J.W. Lee, J. Jeong. Atomic Layer Deposition of Ru Thin Films Using 2,4-(Dimethylpentadienyl)(ethylcyclopentadienyl)Ru by a Liquid Injection System. *Journal of the Electrochemical Society* 2007, **154**(2)**:** D95-D101.
205. T. Aaltonen, M. Ritala, V. Sammelselg, M. Leskelä. Atomic Layer Deposition of Iridium Thin Films. *Journal of the Electrochemical Society* 2004, **151**(8)**:** G489-G492.
206. T. Aaltonen, M. Ritala, M. Leskelä. ALD of Rhodium Thin Films from Rh(acac)3 and Oxygen. *Electrochemical and Solid-State Letters* 2005, **8**(8)**:** C99-C101.
207. X. Jiang, T.M. Gür, F.B. Prinz, S.F. Bent. Atomic Layer Deposition (ALD) Co-Deposited Pt−Ru Binary and Pt Skin Catalysts for Concentrated Methanol Oxidation. *Chemistry of Materials* 2010, **22**(10)**:** 3024-3032.
208. S.T. Christensen, J.W. Elam. Atomic Layer Deposition of Ir−Pt Alloy Films. *Chemistry of Materials* 2010, **22**(8)**:** 2517-2525.
209. I.J. Hsu, D.A. Hansgen, B.E. McCandless, B.G. Willis, J.G. Chen. Atomic Layer Deposition of Pt on Tungsten Monocarbide (WC) for the Oxygen Reduction Reaction. *The Journal of Physical Chemistry C* 2011, **115**(9)**:** 3709-3715.
210. J. Lu, B. Fu, M.C. Kung, G. Xiao, J.W. Elam, H.H. Kung, P.C. Stair. Coking- and Sintering-Resistant Palladium Catalysts Achieved Through Atomic Layer Deposition. *Science* 2012, **335**(6073)**:** 1205-1208.
211. W. Setthapun, W.D. Williams, S.M. Kim, H. Feng, J.W. Elam, F.A. Rabuffetti, K.R. Poeppelmeier, P.C. Stair, E.A. Stach, F.H. Ribeiro. Genesis and Evolution of Surface Species during Pt Atomic Layer Deposition on Oxide Supports Characterized by in Situ XAFS Analysis and Water− Gas Shift Reaction. *The Journal of Physical Chemistry C* 2010, **114**(21)**:** 9758-9771.
212. S.T. Christensen, J.W. Elam, F.A. Rabuffetti, Q. Ma, S.J. Weigand, B. Lee, S. Seifert, P.C. Stair, K.R. Poeppelmeier, M.C. Hersam, M.J. Bedzyk. Controlled Growth of Platinum Nanoparticles on Strontium Titanate Nanocubes by Atomic Layer Deposition. *Small* 2009, **5**(6)**:** 750-757.
213. J.S. King, A. Wittstock, J. Biener, S.O. Kucheyev, Y.M. Wang, T.F. Baumann, S.K. Giri, A.V. Hamza, M. Baeumer, S.F. Bent. Ultralow Loading Pt Nanocatalysts Prepared by Atomic Layer Deposition on Carbon Aerogels. *Nano Letters* 2008, **8**(8)**:** 2405-2409.
214. J. Li, X. Liang, D.M. King, Y.-B. Jiang, A.W. Weimer. Highly dispersed Pt nanoparticle catalyst prepared by atomic layer deposition. *Applied Catalysis B: Environmental* 2010, **97**(1–2)**:** 220-226.
215. C. Liu, C.-C. Wang, C.-C. Kei, Y.-C. Hsueh, T.-P. Perng. Atomic Layer Deposition of Platinum Nanoparticles on Carbon Nanotubes for Application in Proton-Exchange Membrane Fuel Cells. *Small* 2009, **5**(13)**:** 1535-1538.
216. H. Feng, J.W. Elam, J.A. Libera, W. Setthapun, P.C. Stair. Palladium catalysts synthesized by atomic layer deposition for methanol decomposition. *Chemistry of Materials* 2010, **22**(10)**:** 3133-3142.
217. H. Feng, J.A. Libera, P.C. Stair, J.T. Miller, J.W. Elam. Subnanometer Palladium Particles Synthesized by Atomic Layer Deposition. *ACS Catalysis* 2011, **1**(6)**:** 665-673.

218. J. Lu, P.C. Stair. Low-Temperature ABC-Type Atomic Layer Deposition: Synthesis of Highly Uniform Ultrafine Supported Metal Nanoparticles. *Angewandte Chemie International Edition* 2010, **49**(14)**:** 2547-2551.
219. M. Lashdaf, A.O.I. Krause, M. Lindblad, M. Tiitta, T. Venäläinen. Behaviour of palladium and ruthenium catalysts on alumina and silica prepared by gas and liquid phase deposition in cinnamaldehyde hydrogenation. *Applied Catalysis A: General* 2003, **241**(1–2)**:** 65-75.
220. R.J. Silvennoinen, O.J.T. Jylhä, M. Lindblad, H. Österholm, A.O.I. Krause. Supported iridium catalysts prepared by atomic layer deposition: effect of reduction and calcination on activity in toluene hydrogenation. *Catalysis Letters* 2007, **114**(3-4)**:** 135-144.
221. D.C. Cronauer, G. Jacobs, L. Linganiso, A.J. Kropf, J.W. Elam, S.T. Christensen, C.L. Marshall, B.H. Davis. CO Hydrogenation: Exploring Iridium as a Promoter for Supported Cobalt Catalysts by TPR-EXAFS/XANES and Reaction Testing. *Catalysis Letters* 2011, **141**(7)**:** 968-976.
222. S.T. Christensen, H. Feng, J.L. Libera, N. Guo, J.T. Miller, P.C. Stair, J.W. Elam. Supported Ru−Pt Bimetallic Nanoparticle Catalysts Prepared by Atomic Layer Deposition. *Nano Letters* 2010, **10**(8)**:** 3047-3051.
223. A. Santasalo-Aarnio, E. Sairanen, R.M. Arán-Ais, M.C. Figueiredo, J. Hua, J.M. Feliu, J. Lehtonen, R. Karinen, T. Kallio. The activity of ALD-prepared PtCo catalysts for ethanol oxidation in alkaline media. *Journal of Catalysis* 2014, **309**(0)**:** 38-48.
224. Y. Lei, B. Liu, J. Lu, R.J. Lobo-Lapidus, T. Wu, H. Feng, X. Xia, A.U. Mane, J.A. Libera, J.P. Greeley, J.T. Miller, J.W. Elam. Synthesis of Pt–Pd Core–Shell Nanostructures by Atomic Layer Deposition: Application in Propane Oxidative Dehydrogenation to Propylene. *Chemistry of Materials* 2012, **24**(18)**:** 3525-3533.
225. Y. Xia, Y. Xiong, B. Lim, S.E. Skrabalak. Shape-Controlled Synthesis of Metal Nanocrystals: Simple Chemistry Meets Complex Physics? *Angewandte Chemie International Edition* 2009, **48**(1)**:** 60-103.
226. L. Zhang, W. Niu, G. Xu. Synthesis and applications of noble metal nanocrystals with high-energy facets. *Nano Today* 2012, **7**(0)**:** 586-605.
227. B. Wu, N. Zheng. Surface and interface control of noble metal nanocrystals for catalytic and electrocatalytic applications. *Nano Today* 2013, **8**(2)**:** 168-197.
228. N.R. Jana, L. Gearheart, C.J. Murphy. Evidence for Seed-Mediated Nucleation in the Chemical Reduction of Gold Salts to Gold Nanoparticles. *Chemistry of Materials* 2001, **13**(7)**:** 2313-2322.
229. B. Nikoobakht, M.A. El-Sayed. Preparation and Growth Mechanism of Gold Nanorods (NRs) Using Seed-Mediated Growth Method. *Chemistry of Materials* 2003, **15**(10)**:** 1957-1962.
230. A. Gole, C.J. Murphy. Seed-Mediated Synthesis of Gold Nanorods: Role of the Size and Nature of the Seed. *Chemistry of Materials* 2004, **16**(19)**:** 3633-3640.
231. B. Lim, J.G. Wang, P.H.C. Camargo, M.J. Jiang, M.J. Kim, Y.N. Xia. Facile synthesis of bimetallic nanoplates consisting of Pd cores and Pt shells through seeded epitaxial growth. *Nano Letters* 2008, **8**(8)**:** 2535-2540.
232. S.E. Habas, H. Lee, V. Radmilovic, G.A. Somorjai, P. Yang. Shaping binary metal nanocrystals through epitaxial seeded growth. *Nature Materials* 2007, **6**(9)**:** 692-697.

233. M. Jiang, B. Lim, J. Tao, P.H.C. Camargo, C. Ma, Y. Zhu, Y. Xia. Epitaxial overgrowth of platinum on palladium nanocrystals. *Nanoscale* 2010, **2**(11)**:** 2406-2411.
234. C.-W. Yang, K. Chanda, P.-H. Lin, Y.-N. Wang, C.-W. Liao, M.H. Huang. Fabrication of Au–Pd Core–Shell Heterostructures with Systematic Shape Evolution Using Octahedral Nanocrystal Cores and Their Catalytic Activity. *Journal of the American Chemical Society* 2011, **133**(49)**:** 19993-20000.
235. F. Wang, C. Li, L.-D. Sun, H. Wu, T. Ming, J. Wang, J.C. Yu, C.-H. Yan. Heteroepitaxial Growth of High-Index-Faceted Palladium Nanoshells and Their Catalytic Performance. *Journal of the American Chemical Society* 2010, **133**(4)**:** 1106-1111.
236. K. Tedsree, T. Li, S. Jones, C.W.A. Chan, K.M.K. Yu, P.A.J. Bagot, E.A. Marquis, G.D.W. Smith, S.C.E. Tsang. Hydrogen production from formic acid decomposition at room temperature using a Ag-Pd core-shell nanocatalyst. *Nat Nano* 2011, **6**(5)**:** 302-307.
237. B. Rodriguez-Gonzalez, A. Burrows, M. Watanabe, C.J. Kiely, L.M. Liz Marzan. Multishell bimetallic AuAg nanoparticles: synthesis, structure and optical properties. *Journal of Materials Chemistry* 2005, **15**(17)**:** 1755-1759.
238. M. Min, C. Kim, Y. In Yang, J. Yi, H. Lee. Surface-specific overgrowth of platinum on shaped gold nanocrystals. *Physical Chemistry Chemical Physics* 2009, **11**(42)**:** 9759-9765.
239. B. Lim, M.J. Jiang, P.H.C. Camargo, E.C. Cho, J. Tao, X.M. Lu, Y.M. Zhu, Y.N. Xia. Pd-Pt Bimetallic Nanodendrites with High Activity for Oxygen Reduction. *Science* 2009, **324**(5932)**:** 1302-1305.
240. H. Kobayashi, B. Lim, J. Wang, P.H.C. Camargo, T. Yu, M.J. Kim, Y. Xia. Seed-mediated synthesis of Pd–Rh bimetallic nanodendrites. *Chemical Physics Letters* 2010, **494**(4–6)**:** 249-254.
241. B. Lim, M. Jiang, J. Tao, P.H.C. Camargo, Y. Zhu, Y. Xia. Shape-Controlled Synthesis of Pd Nanocrystals in Aqueous Solutions. *Advanced Functional Materials* 2009, **19**(2)**:** 189-200.
242. Y. Yu, Q. Zhang, B. Liu, J.Y. Lee. Synthesis of Nanocrystals with Variable High-Index Pd Facets through the Controlled Heteroepitaxial Growth of Trisoctahedral Au Templates. *Journal of the American Chemical Society* 2010, **132**(51)**:** 18258-18265.
243. G. Krylova, L.J. Giovanetti, F.G. Requejo, N.M. Dimitrijevic, A. Prakapenka, E.V. Shevchenko. Study of Nucleation and Growth Mechanism of the Metallic Nanodumbbells. *Journal of the American Chemical Society* 2012, **134**(9)**:** 4384-4392.
244. Y. Xia, X. Xia, Y. Wang, S. Xie. Shape-controlled synthesis of metal nanocrystals. *MRS Bulletin* 2013, **38**(04)**:** 335-344.
245. W. Niu, W. Zhang, S. Firdoz, X. Lu. Dodecahedral Gold Nanocrystals: The Missing Platonic Shape. *Journal of the American Chemical Society* 2014, **136**(8)**:** 3010-3012.
246. A. Tao, P. Sinsermsuksakul, P. Yang. Tunable plasmonic lattices of silver nanocrystals. *Nature Nanotechnology* 2007, **2**(7)**:** 435-440.
247. A. Ruditskiy, S.-I. Choi, H.-C. Peng, Y. Xia. Shape-controlled metal nanocrystals for catalytic applications. *MRS Bulletin* 2014, **39**(08)**:** 727-737.
248. J. Solla-Gullon, F.J. Vidal-Iglesias, J.M. Feliu. Shape dependent electrocatalysis. *Annu. Rep. Prog. Chem., Sect. C: Phys. Chem.* 2011, **107**(0)**:** 263-297.

249. M. Shao, J. Odell, M. Humbert, T. Yu, Y. Xia. Electrocatalysis on Shape-Controlled Palladium Nanocrystals: Oxygen Reduction Reaction and Formic Acid Oxidation. *Journal of Physical Chemistry C* 2013, **117**(8)**:** 4172-4180.
250. J. Wang, J. Gong, Y. Xiong, J. Yang, Y. Gao, Y. Liu, X. Lu, Z. Tang. Shape-dependent electrocatalytic activity of monodispersed gold nanocrystals toward glucose oxidation. *Chemical Communications* 2011, **47**(24)**:** 6894-6896.
251. J. Zhang, M.R. Langille, M.L. Personick, K. Zhang, S. Li, C.A. Mirkin. Concave Cubic Gold Nanocrystals with High-Index Facets. *Journal of the American Chemical Society* 2010, **132**(40)**:** 14012-14014.
252. G.H. Jeong, M. Kim, Y.W. Lee, W. Choi, W.T. Oh, Q.H. Park, S.W. Han. Polyhedral Au Nanocrystals Exclusively Bound by {110} Facets: The Rhombic Dodecahedron. *Journal of the American Chemical Society* 2009, **131**(5)**:** 1672-1673.
253. H. Erikson, A. Sarapuu, K. Tammeveski, J. Solla-Gullón, J.M. Feliu. Shape-Dependent Electrocatalysis: Oxygen Reduction on Carbon-Supported Gold Nanoparticles. *ChemElectroChem* 2014, **1**(8)**:** 1338-1347.
254. F.-S. Ke, B. Solomon, Y. Ding, G.-L. Xu, S.-G. Sun, Z.L. Wang, X.-D. Zhou. Enhanced electrocatalytic activity on gold nanocrystals enclosed by high-index facets for oxygen reduction. *Nano Energy* 2014, **7:** 179-188.
255. C. Buso-Rogero, V. Grozovski, F.J. Vidal-Iglesias, J. Solla-Gullon, E. Herrero, J.M. Feliu. Surface structure and anion effects in the oxidation of ethanol on platinum nanoparticles. *Journal of Materials Chemistry A* 2013, **1**(24)**:** 7068-7076.
256. Z.-Y. Zhou, S.-J. Shang, N. Tian, B.-H. Wu, N.-F. Zheng, B.-B. Xu, C. Chen, H.-H. Wang, D.-M. Xiang, S.-G. Sun. Shape transformation from Pt nanocubes to tetrahexahedra with size near 10 nm. *Electrochemistry Communications* 2012, **22:** 61-64.
257. C. Wang, H. Daimon, T. Onodera, T. Koda, S. Sun. A General Approach to the Size- and Shape-Controlled Synthesis of Platinum Nanoparticles and Their Catalytic Reduction of Oxygen. *Angew. Chem. Int. Ed.* 2008, **47**(19)**:** 3588-3591.
258. C. Coutanceau, P. Urchaga, S. Brimaud, S. Baranton. Colloidal Syntheses of Shape- and Size-Controlled Pt Nanoparticles for Electrocatalysis. *Electrocatalysis* 2012, **3**(2)**:** 75-87.
259. F.J. Vidal-Iglesias, R.M. Arán-Ais, J. Solla-Gullón, E. Herrero, J.M. Feliu. Electrochemical Characterization of Shape-Controlled Pt Nanoparticles in Different Supporting Electrolytes. *ACS Catalysis* 2012, **2**(5)**:** 901-910.
260. M.J.S. Farias, F.J. Vidal-Iglesias, J. Solla-Gullón, E. Herrero, J.M. Feliu. On the behavior of CO oxidation on shape-controlled Pt nanoparticles in alkaline medium. *Journal of Electroanalytical Chemistry*.
261. F. Vidal-Iglesias, A. López-Cudero, J. Solla-Gullón, A. Aldaz, J. Feliu. Pd-Modified Shape-Controlled Pt Nanoparticles Towards Formic Acid Electrooxidation. *Electrocatalysis* 2012, **3**(3-4)**:** 313-323.
262. M. Duca, P. Rodriguez, A. Yanson, M.M. Koper. Selective Electrocatalysis on Platinum Nanoparticles with Preferential (100) Orientation Prepared by Cathodic Corrosion. *Topics in Catalysis* 2013**:** 1-10.
263. G. Chen, Y. Tan, B. Wu, G. Fu, N. Zheng. Carbon monoxide-controlled synthesis of surface-clean Pt nanocubes with high electrocatalytic activity. *Chemical Communications* 2012, **48**(22)**:** 2758-2760.

264. H. Erikson, A. Sarapuu, N. Alexeyeva, K. Tammeveski, J. Solla-Gullón, J.M. Feliu. Electrochemical reduction of oxygen on palladium nanocubes in acid and alkaline solutions. *Electrochimica Acta* 2012, **59:** 329-335.
265. M. Shao, T. Yu, J.H. Odell, M. Jin, Y. Xia. Structural dependence of oxygen reduction reaction on palladium nanocrystals. *Chemical Communications* 2011, **47**(23)**:** 6566-6568.
266. H.-X. Zhang, H. Wang, Y.-S. Re, W.-B. Cai. Palladium nanocrystals bound by {110} or {100} facets: from one pot synthesis to electrochemistry. *Chemical Communications* 2012, **48**(67)**:** 8362-8364.
267. N. Arjona, M. Guerra-Balcazar, L.A. Ortiz-Frade, G. Osorio-Monreal, L. Alvarez-Contreras, J. Ledesma-Garcia, L.G. Arriaga. Electrocatalytic Activity of Well-Defined and Homogeneous Cubic-Shaped Pd Nanoparticles. *Journal of Materials Chemistry A* 2013, **1**(48)**:** 15524-15529.
268. M. Jin, H. Zhang, Z. Xie, Y. Xia. Palladium nanocrystals enclosed by {100} and {111} facets in controlled proportions and their catalytic activities for formic acid oxidation. *Energy & Environmental Science* 2012, **5**(4)**:** 6352-6357.
269. S. Hebié, K.B. Kokoh, K. Servat, T. Napporn. Shape-dependent electrocatalytic activity of free gold nanoparticles toward glucose oxidation. *Gold Bulletin* 2013, **46**(4)**:** 311-318.
270. X. Min, Y. Chen, M. Kanan. Alkaline O2 Reduction on Oxide-Derived Au: High Activity and 4e- Selectivity without (100) Facets. *Physical Chemistry Chemical Physics* 2014, **16:** 13601-13604.
271. C. Buso-Rogero, M.S.J. Farias, J.V. Perales-Rondon, F.J. Vidal-Iglesias, J. Solla-Gullon, E. Herrero, J.M. Feliu. Formic acid electrooxidation on thallium-decorated shape-controlled platinum nanoparticles: an improvement on electrocatalytic activity. *Physical Chemistry Chemical Physics* 2014, **16**(27)**:** 13616-13624.
272. J. Solla-Gullon, P. Rodriguez, E. Herrero, A. Aldaz, J.M. Feliu. Surface characterization of platinum electrodes. *Physical Chemistry Chemical Physics* 2008, **10**(10)**:** 1359-1373.
273. Q.S. Chen, Z.Y. Zhou, F.J. Vidal-Iglesias, J. Solla-Gullon, J.M. Feliu, S.G. Sun. Significantly Enhancing Catalytic Activity of Tetrahexahedral Pt Nanocrystals by Bi Adatom Decoration. *Journal of the American Chemical Society* 2011, **133**(33)**:** 12930-12933.
274. J. Hernández, J. Solla-Gullón, E. Herrero, A. Aldaz, J.M. Feliu. Electrochemistry of Shape-Controlled Catalysts: Oxygen Reduction Reaction on Cubic Gold Nanoparticles. *Journal of Physical Chemistry C* 2007, **111**(38)**:** 14078-14083.
275. X. Xia, S.-I. Choi, J.A. Herron, N. Lu, J. Scaranto, H.-C. Peng, J. Wang, M. Mavrikakis, M.J. Kim, Y. Xia. Facile Synthesis of Palladium Right Bipyramids and Their Use as Seeds for Overgrowth and as Catalysts for Formic Acid Oxidation. *Journal of the American Chemical Society* 2013, **135**(42)**:** 15706-15709.
276. F.J. Vidal-Iglesias, J. Solla-Gullón, P. Rodríguez, E. Herrero, V. Montiel, J.M. Feliu, A. Aldaz. Shape-dependent electrocatalysis: ammonia oxidation on platinum nanoparticles with preferential (100) surfaces. *Electrochemistry Communications* 2004, **6**(10)**:** 1080-1084.
277. Y. Zhang, F. Lu, K.G. Yager, D. van der Lelie, O. Gang. A general strategy for the DNA-mediated self-assembly of functional nanoparticles into heterogeneous systems. *Nat Nano* 2013(8)**:** 865-872.

278. M. Crespo-Quesada, J.-M. Andanson, A. Yarulin, B. Lim, Y. Xia, L. Kiwi-Minsker. UV–Ozone Cleaning of Supported Poly(vinylpyrrolidone)-Stabilized Palladium Nanocubes: Effect of Stabilizer Removal on Morphology and Catalytic Behavior. *Langmuir* 2011, **27**(12)**:** 7909-7916.
279. J. Monzó, M.T.M. Koper, P. Rodriguez. Removing Polyvinylpyrrolidone from Catalytic Pt Nanoparticles without Modification of Superficial Order. *ChemPhysChem* 2012, **13**(3)**:** 709-715.
280. J.N. Kuhn, C.-K. Tsung, W. Huang, G.A. Somorjai. Effect of organic capping layers over monodisperse platinum nanoparticles upon activity for ethylene hydrogenation and carbon monoxide oxidation. *Journal of Catalysis* 2009, **265**(2)**:** 209-215.
281. D. Li, C. Wang, D. Tripkovic, S. Sun, N.M. Markovic, V.R. Stamenkovic. Surfactant Removal for Colloidal Nanoparticles from Solution Synthesis: The Effect on Catalytic Performance. *ACS Catalysis* 2012, **2**(7)**:** 1358-1362.
282. T. Ming, W. Feng, Q. Tang, F. Wang, L. Sun, J. Wang, C. Yan. Growth of Tetrahexahedral Gold Nanocrystals with High-Index Facets. *Journal of the American Chemical Society* 2009, **131**(45)**:** 16350-16351.
283. J.A. Lopez-Sanchez, N. Dimitratos, C. Hammond, G.L. Brett, L. Kesavan, S. White, P. Miedziak, R. Tiruvalam, R.L. Jenkins, A.F. Carley, D. Knight, C.J. Kiely, G.J. Hutchings. Facile removal of stabilizer-ligands from supported gold nanoparticles. *Nature Chemistry* 2011, **3**(7)**:** 551-556.
284. J. Solla-Gullón, V. Montiel, A. Aldaz, J. Clavilier Synthesis and Electrochemical Decontamination of Platinum-Palladium Nanoparticles Prepared by Water-in-Oil Microemulsion. *Journal of the Electrochemical Society* 2003, **150**(2)**:** E104-E109.
285. A. Jackson, V. Viswanathan, A.J. Forman, J. Nørskov, T.F. Jaramillo. Effects of a New Electrochemical Cleaning Protocol on Ru@Pt Core-Shell ORR Catalysts. *ECS Transactions* 2013, **58**(1)**:** 929-936.
286. J. Solla-Gullón, V. Montiel, A. Aldaz, J. Clavilier. Electrochemical characterisation of platinum nanoparticles prepared by microemulsion: how to clean them without loss of crystalline surface structure. *Journal of Electroanalytical Chemistry* 2000, **491**(1–2)**:** 69-77.
287. F.J. Vidal-Iglesias, J. Solla-Gullón, E. Herrero, V. Montiel, A. Aldaz, J.M. Feliu. Evaluating the ozone cleaning treatment in shape-controlled Pt nanoparticles: Evidences of atomic surface disordering. *Electrochemistry Communications* 2011, **13**(5)**:** 502-505.
288. K. Winkler, T. Wojciechowski, M. Liszewska, E. Gorecka, M. Fialkowski. Morphological changes of gold nanoparticles due to adsorption onto silicon substrate and oxygen plasma treatment. *RSC Advances* 2014, **4**(25)**:** 12729-12736.
289. G.-R. Zhang, B.-Q. Xu. Surprisingly strong effect of stabilizer on the properties of Au nanoparticles and Pt^Au nanostructures in electrocatalysis. *Nanoscale* 2010, **2**(12)**:** 2798-2804.
290. H. Yang. Platinum-Based Electrocatalysts with Core–Shell Nanostructures. *Angew. Chem. Int. Ed.* 2011, **50**(12)**:** 2674-2676.
291. H.A. Gasteiger, J.E. Panels, S.G. Yan. Dependence of PEM fuel cell performance on catalyst loading. *Journal of Power Sources* 2004, **127**(1-2)**:** 162-171.

292. K.C. Neyerlin, W. Gu, J. Jorne, H.A. Gasteiger. Study of the Exchange Current Density for the Hydrogen Oxidation and Evolution Reactions. *J. Electrochem. Soc.* 2007, **154**(7)**:** B631-B635.
293. S.J. Lee, S. Mukerjee, E.A. Ticianelli, J. McBreen. Electrocatalysis of CO tolerance in hydrogen oxidation reaction in PEM fuel cells. *Electrochimica Acta* 1999, **44**(19)**:** 3283-3293.
294. S.J.C. Cleghorn, X. Ren, T.E. Springer, M.S. Wilson, C. Zawodzinski, T.A. Zawodzinski, S. Gottesfeld. PEM fuel cells for transportation and stationary power generation applications. *International Journal of Hydrogen Energy* 1997, **22**(12)**:** 1137-1144.
295. E. Antolini. The problem of Ru dissolution from Pt-Ru catalysts during fuel cell operation: analysis and solutions. *Journal of Solid State Electrochemistry* 2011, **15**(3)**:** 455-472.
296. M.K. Debe, A.K. Schmoeckel, G.D. Vernstrorn, R. Atanasoski. High voltage stability of nanostructured thin film catalysts for PEM fuel cells. *Journal of Power Sources* 2006, **161**(2)**:** 1002-1011.
297. M.K. Debe, S.M. Hendricks, G.D. Vernstrom, M. Meyers, M. Brostrom, M. Stephens, Q. Chan, J. Willey, M. Hamden, C.K. Mittelsteadt, C.B. Capuano, K.E. Ayers, E.B. Anderson. Initial Performance and Durability of Ultra-Low Loaded NSTF Electrodes for PEM Electrolyzers. *Journal of the Electrochemical Society* 2012, **159**(6)**:** K165.
298. Y. Zhang, Y.-C. Hsieh, K. Sasaki, N.S. Marinkovic, V. Volkov, Y. Zhu, J.X. Wang, R.R. Adzic. *In preparation*.
299. Y.-C. Hsieh, Y. Zhang, D. Su, V. Volkov, R. Si, L. Wu, Y. Zhu, W. An, P. Liu, P. He, S. Ye, R.R. Adzic, J.X. Wang. Ordered bilayer ruthenium–platinum core-shell nanoparticles as carbon monoxide-tolerant fuel cell catalysts. *Nat Commun* 2013, **4:** 2466.
300. J.X. Wang, P. He, Y. Zhang, S. Ye. Can CO-Tolerant Anodes be Economically Viable for PEMFC Applications with Reformates? *ECS Transactions* 2014, **64**(3)**:** 121-127.
301. J.X. Wang, Y. Zhang, C.B. Capuano, K.E. Ayers. *Submitted*.
302. A. Schlapka, M. Lischka, A. Groß, U. Käsberger, P. Jakob. Surface Strain versus Substrate Interaction in Heteroepitaxial Metal Layers: Pt on Ru(0001). *Physical Review Letters* 2003, **91**(1)**:** 016101.
303. P. Jakob, A. Schlapka, P. Gazdzicki. Oxygen adsorption on Pt/Ru(0001) layers. *The Journal of Chemical Physics* 2011, **134**(22)**:** 224707.
304. S. Alayoglu, A.U. Nilekar, M. Mavrikakis, B. Eichhorn. Ru-Pt core-shell nanoparticles for preferential oxidation of carbon monoxide in hydrogen. *Nature Materials* 2008, **7**(4)**:** 333-338.
305. S. Alayoglu, P. Zavalij, B. Eichhorn, Q. Wang, A.I. Frenkel, P. Chupas. Structural and Architectural Evaluation of Bimetallic Nanoparticles: A Case Study of Pt-Ru Core-Shell and Alloy Nanoparticles. *Acs Nano* 2009, **3**(10)**:** 3127-3137.
306. M. Oezaslan, F. Hasché, P. Strasser. Pt-Based Core–Shell Catalyst Architectures for Oxygen Fuel Cell Electrodes. *Journal of Physical Chemistry Letters* 2013, **4**(19)**:** 3273-3291.
307. F. Calle-Vallejo, M.T.M. Koper, A.S. Bandarenka. Tailoring the catalytic activity of electrodes with monolayer amounts of foreign metals. *Chemical Society Reviews* 2013, **42**(12)**:** 5210-5230.

308. Y. Zhang, Y.-C. Hsieh, V. Volkov, D. Su, W. An, R. Si, Y. Zhu, P. Liu, J.X. Wang, R.R. Adzic. High Performance Pt Monolayer Catalysts Produced via Core-Catalyzed Coating in Ethanol. *ACS Catalysis* 2014, **4**(3)**:** 738-742.
309. Y. Zhang, C. Ma, Y. Zhu, R. Si, Y. Cai, J.X. Wang, R.R. Adzic. Hollow core supported Pt monolayer catalysts for oxygen reduction. *Catalysis Today* 2013, **202:** 50-54.
310. Y. Yamada, C.K. Tsung, W. Huang, Z.Y. Huo, S.E. Habas, T. Soejima, C.E. Aliaga, G.A. Somorjai, P.D. Yang. Nanocrystal bilayer for tandem catalysis. *Nature Chemistry* 2011, **3**(5)**:** 372-376.
311. I. Katsounaros, W.B. Schneider, J.C. Meier, U. Benedikt, P.U. Biedermann, A. Cuesta, A.A. Auer, K.J.J. Mayrhofer. The impact of spectator species on the interaction of H2O2 with platinum - implications for the oxygen reduction reaction pathways. *Physical Chemistry Chemical Physics* 2013, **15**(21)**:** 8058-8068.
312. M. Haruta. Size- and support-dependency in the catalysis of gold. *Catalysis Today* 1997, **36**(1)**:** 153-166.
313. A.S.K. Hashmi, G.J. Hutchings. Gold Catalysis. *Angewandte Chemie International Edition* 2006, **45**(47)**:** 7896-7936.
314. M. Turner, V.B. Golovko, O.P. Vaughan, P. Abdulkin, A. Berenguer-Murcia, M.S. Tikhov, B.F. Johnson, R.M. Lambert. Selective oxidation with dioxygen by gold nanoparticle catalysts derived from 55-atom clusters. *Nature* 2008, **454**(7207)**:** 981-983.
315. N.M. Markovic, R.R. Adzic, V.B. Vesovic. Structural effects in electrocatalysis: Oxygen reduction on the gold single crystal electrodes with (110) and (111) orientations. *J. Electroanal. Chem.* 1984, **165**(1-2)**:** 121-133.
316. R.R. Adzic, N.M. Markovic, V.B. Vesovic. Structural effects in electrocatalysis: Oxygen reduction on the Au (100) single crystal electrode. *J. Electroanal. Chem.* 1984, **165**(1-2)**:** 105-120.
317. S. Strbac, R.R. Adzic. The influence of OH- chemisorption on the catalytic properties of gold single crystal surfaces for oxygen reduction in alkaline solutions. *Journal of Electroanalytical Chemistry* 1996, **403**(1-2)**:** 169-181.
318. F. Lu, Y. Zhang, D. Lu, D. Su, M. Liu, Y. Zhang, J.X. Wang, R.R. Adzic, O. Gang. *Submitted*.
319. J. Kim, A.A. Gewirth. Mechanism of Oxygen Electroreduction on Gold Surfaces in Basic Media. *The Journal of Physical Chemistry B* 2006, **110**(6)**:** 2565-2571.
320. J.K. Nørskov, J. Rossmeisl, A. Logadottir, L. Lindqvist, J.R. Kitchin, T. Bligaard, H. Jónsson. Origin of the Overpotential for Oxygen Reduction at a Fuel-Cell Cathode. *The Journal of Physical Chemistry B* 2004, **108**(46)**:** 17886-17892.
321. V. Viswanathan, H.A. Hansen, J. Rossmeisl, J.K. Nørskov. Unifying the 2e– and 4e– Reduction of Oxygen on Metal Surfaces. *The Journal of Physical Chemistry Letters* 2012, **3**(20)**:** 2948-2951.
322. T. Chierchie, C. Mayer. Voltammetric Study of the Underpotential Deposition of Copper on Polycrystalline and Single-Crystal Palladium Surfaces. *Electrochimica Acta* 1988, **33**(3)**:** 341-345.
323. E. Herrero, L.J. Buller, H.D. Abruña. Underpotential Deposition at Single Crystal Surfaces of Au, Pt, Ag and Other Materials. *Chemical Reviews* 2001, **101**(7)**:** 1897-1930.

324. J. Suntivich, H.A. Gasteiger, N. Yabuuchi, Y. Shao-Horn. Electrocatalytic Measurement Methodology of Oxide Catalysts Using a Thin-Film Rotating Disk Electrode. *Journal of the Electrochemical Society* 2010, **157**(8)**:** B1263-B1268.
325. N.M. Marković, B.N. Grgur, P.N. Ross. Temperature-Dependent Hydrogen Electrochemistry on Platinum Low-Index Single-Crystal Surfaces in Acid Solutions. *J. Phys. Chem. B* 1997, **101**(27)**:** 5405-5413.
326. H.A. Gasteiger, N.M. Markovic, P.N. Ross. H2 and CO Electrooxidation on Well-Characterized Pt, Ru, and Pt-Ru. 1. Rotating Disk Electrode Studies of the Pure Gases Including Temperature Effects. *The Journal of Physical Chemistry* 1995, **99**(20)**:** 8290-8301.
327. S. Chen, A. Kucernak. Electrocatalysis under Conditions of High Mass Transport: Investigation of Hydrogen Oxidation on Single Submicron Pt Particles Supported on Carbon. *J. Phys. Chem. B* 2004, **108**(37)**:** 13984-13994.
328. J. Durst, C. Simon, F. Hasché, H.A. Gasteiger. Hydrogen Oxidation and Evolution Reaction Kinetics on Carbon Supported Pt, Ir, Rh, and Pd Electrocatalysts in Acidic Media. *Journal of the Electrochemical Society* 2015, **162**(1)**:** F190-F203.
329. C.M. Zalitis, D. Kramer, A.R. Kucernak. Electrocatalytic performance of fuel cell reactions at low catalyst loading and high mass transport. *Physical Chemistry Chemical Physics* 2013, **15**(12)**:** 4329-4340.
330. Y. Liang, Y. Li, H. Wang, J. Zhou, J. Wang, T. Regier, H. Dai. Co3O4 nanocrystals on graphene as a synergistic catalyst for oxygen reduction reaction. *Nature Materials* 2011, **10**(10)**:** 780-786.
331. F. Opekar, P. Beran. Rotating disk electrodes. *J. Electroanal. Chem.* 1976, **69**(1)**:** 1-105.
332. K.E. Gubbins, J. Robert D. Walker. The Solubility and Diffusivity of Oxygen in Electrolytic Solutions. *Journal of the Electrochemical Society* 1965, **112**(5)**:** 469-471.
333. U.A. Paulus, T.J. Schmidt, H.A. Gasteiger, R.J. Behm. Oxygen reduction on a high-surface area Pt/Vulcan carbon catalyst: a thin-film rotating ring-disk electrode study. *Journal of Electroanalytical Chemistry* 2001, **495**(2)**:** 134-145.
334. W.M. Haynes, D.R. Lide, ed. *CRC Handbook of Chemistry and Physics*, 94th (Internet Version) edn. CRC Press/Taylor and Francis: Boca Raton, FL, 2014.
335. R.E. Davis, G.L. Horvath, C.W. Tobias. The solubility and diffusion coefficient of oxygen in potassium hydroxide solutions. *Electrochimica Acta* 1967, **12**(3)**:** 287-297.
336. B. Ravel, M. Newville. ATHENA, ARTEMIS, HEPHAESTUS: data analysis for X-ray absorption spectroscopy using IFEFFIT. *Journal of synchrotron radiation* 2005, **12**(4)**:** 537-541.
337. S. Hillyard, J. Silcox. Detector geometry, thermal diffuse scattering and strain effects in ADF STEM imaging. *Ultramicroscopy* 1995, **58**(1)**:** 6-17.
338. C.C. Ahn. *Transmission Electron Energy Loss Spectrometry in Materials Science and the EELS Atlas*, 2nd edn. Wiley-VCH: Weinheim, 2004.
339. K. Sun, J. Liu, N. Nag, N.D. Browning. Studying the Metal-Support Interaction in Pd/γ-Al2O3 Catalysts by Atomic-Resolution Electron Energy-Loss Spectroscopy. *Catalysis Letters* 2002, **84**(3)**:** 193-199.
340. G. Kresse, J. Hafner. Abinitio Molecular-Dynamics for Liquid-Metals. *Phys. Rev. B* 1993, **47**(1)**:** 558-561.

341. G. Kresse, J. Furthmuller. Efficient iterative schemes for ab initio total-energy calculations using a plane-wave basis set. *Phys. Rev. B* 1996, **54**(16)**:** 11169-11186.
342. P.E. Blochl. Projector Augmented-Wave Method. *Phys. Rev. B* 1994, **50**(24)**:** 17953-17979.
343. G. Kresse, D. Joubert. From ultrasoft pseudopotentials to the projector augmented-wave method. *Phys. Rev. B* 1999, **59**(3)**:** 1758-1775.
344. J.P. Perdew, J.A. Chevary, S.H. Vosko, K.A. Jackson, M.R. Pederson, D.J. Singh, C. Fiolhais. Atoms, Molecules, Solids, and Surfaces - Applications of the Generalized Gradient Approximation for Exchange and Correlation. *Physical Review B* 1992, **46**(11)**:** 6671-6687.
345. J.P. Perdew, J.A. Chevary, S.H. Vosko, K.A. Jackson, M.R. Pederson, D.J. Singh, C. Fiolhais. Atoms, Molecules, Solids, and Surfaces - Applications of the Generalized Gradient Approximation for Exchange and Correlation (Vol 46, Pg 6671, 1992). *Physical Review B* 1993, **48**(7)**:** 4978-4978.
346. H.J. Monkhorst, J.D. Pack. Special Points for Brillouin-Zone Integrations. *Physical Review B* 1976, **13**(12)**:** 5188-5192.
347. M. Methfessel, A.T. Paxton. High-Precision Sampling for Brillouin-Zone Integration in Metals. *Phys. Rev. B* 1989, **40**(6)**:** 3616-3621.
348. http://accelrys.com/products/materials-studio
349. G. Kresse, J. Furthmüller. Efficiency of ab-initio total energy calculations for metals and semiconductors using a plane-wave basis set. *Computational Materials Science* 1996, **6**(1)**:** 15-50.
350. G. Karp. *Cell and Molecular Biology*, 5th Ed. edn. Wiley, 2008.
351. T. Vitova, S. Mangold, C. Paulmann, M. Gospodinov, V. Marinova, B. Mihailova. X-ray absorption spectroscopy of Ru-doped relaxor ferroelectrics with a perovskite-type structure. *Physical Review B* 2014, **89**(14)**:** 144112.
352. I. Arčon, A. Benčan, A. Kodre, M. Kosec. X-ray absorption spectroscopy analysis of Ru in La2RuO5. *X-Ray Spectrometry* 2007, **36**(5)**:** 301-304.
353. J. Zhou, Y. Zu, A.J. Bard. Scanning electrochemical microscopy: Part 39. The proton/hydrogen mediator system and its application to the study of the electrocatalysis of hydrogen oxidation. *Journal of Electroanalytical Chemistry* 2000, **491**(1–2)**:** 22-29.
354. C.G. Zoski. Scanning Electrochemical Microscopy: Investigation of Hydrogen Oxidation at Polycrystalline Noble Metal Electrodes. *The Journal of Physical Chemistry B* 2003, **107**(26)**:** 6401-6405.
355. Y.C. Hsieh, L.C. Chang, P.W. Wu, Y.M. Chang, J.F. Lee. Displacement reaction of Pt on carbon-supported Ru nanoparticles in hexachloroplatinic acids. *Applied Catalysis B-Environmental* 2011, **103**(1-2)**:** 116-127.
356. B.J. Hwang, L.S. Sarma, C.H. Chen, C. Bock, F.J. Lai, S.H. Chang, S.C. Yen, D.G. Liu, H.S. Sheu, J.F. Lee. Controlled Synthesis and Characterization of Ru-core-Pt-shell Bimetallic Nanoparticles. *Journal of Physical Chemistry C* 2008, **112**(50)**:** 19922-19929.
357. A.R. Denton, N.W. Ashcroft. VEGARD LAW. *Physical Review A* 1991, **43**(6)**:** 3161-3164.
358. C. Pan, F. Dassenoy, M.J. Casanove, K. Philippot, C. Amiens, P. Lecante, A. Mosset, B. Chaudret. A new synthetic method toward bimetallic ruthenium platinum nanoparticles;

composition induced structural changes. *Journal of Physical Chemistry B* 1999, **103**(46)**:** 10098-10101.
359. A.D. Smigelskas, E.O. Kirkendall. Zinc Diffusion in Alpha-Brass. *Transactions of the American Institute of Mining and Metallurgical Engineers* 1947, **171:** 130-142.
360. A.V. Ruban, H.L. Skriver, J.K. Norskov. Surface segregation energies in transition-metal alloys. *Physical Review B* 1999, **59**(24)**:** 15990.
361. H.E. Hoster, A. Bergbreiter, P.M. Erne, T. Hager, H. Rauscher, R.J. Behm. Pt(x)Ru(1-x)/Ru(0001) surface alloys - formation and atom distribution. *Physical Chemistry Chemical Physics* 2008, **10**(25)**:** 3812-3823.
362. P. Liu, A. Logadottir, J.K. Nørskov. Modeling the electro-oxidation of CO and H2/CO on Pt, Ru, PtRu and Pt3Sn. *Electrochimica Acta* 2003, **48**(25–26)**:** 3731-3742.
363. A.U. Nilekar, S. Alayoglu, B. Eichhorn, M. Mavrikakis. Preferential CO Oxidation in Hydrogen: Reactivity of Core-Shell Nanoparticles. *Journal of the American Chemical Society* 2010, **132**(21)**:** 7418-7428.
364. S. Satyapal. Fuel Cell Technologies Update, in Hydrogen and Fuel Cell Technical Advisory Committee Meeting, Washington, DC. 2013.
365. A. Fukuoka, J.I. Kimura, T. Oshio, Y. Sakamoto, M. Ichikawa. Preferential oxidation of carbon monoxide catalyzed by platinum nanoparticles in mesoporous silica. *Journal of the American Chemical Society* 2007, **129**(33)**:** 10120-10125.
366. K. Liu, A.Q. Wang, T. Zhang. Recent Advances in Preferential Oxidation of CO Reaction over Platinum Group Metal Catalysts. *Acs Catalysis* 2012, **2**(6)**:** 1165-1178.
367. S. Gottesfeld, J. Pafford. A NEW APPROACH TO THE PROBLEM OF CARBON-MONOXIDE POISONING IN FUEL-CELLS OPERATING AT LOW-TEMPERATURES. *Journal of the Electrochemical Society* 1988, **135**(10)**:** 2651-2652.
368. M. Mavrikakis, B. Hammer, J.K. Norskov. Effect of strain on the reactivity of metal surfaces. *Physical Review Letters* 1998, **81**(13)**:** 2819-2822.
369. H. Hartmann, T. Diemant, J. Bansmann, R.J. Behm. Interaction of CO and deuterium with bimetallic, monolayer Pt-island/film covered Ru(0001) surfaces. *Physical Chemistry Chemical Physics* 2012, **14**(31)**:** 10919-10934.
370. R. Borup, J. Meyers, B. Pivovar, Y.S. Kim, R. Mukundan, N. Garland, D. Myers, M. Wilson, F. Garzon, D. Wood, P. Zelenay, K. More, K. Stroh, T. Zawodzinski, J. Boncella, J.E. McGrath, M. Inaba, K. Miyatake, M. Hori, K. Ota, Z. Ogumi, S. Miyata, A. Nishikata, Z. Siroma, Y. Uchimoto, K. Yasuda, K.I. Kimijima, N. Iwashita. Scientific aspects of polymer electrolyte fuel cell durability and degradation. *Chemical Reviews* 2007, **107**(10)**:** 3904-3951.
371. T.T.H. Cheng, N.Y. Jia, P. He. Characterization of the Degree of Ru Crossover and Its Performance Implications in Polymer Electrolyte Membrane Fuel Cells. *Journal of the Electrochemical Society* 2010, **157**(5)**:** B714-B718.
372. P. He, T.T.H. Cheng, R. Bashyam, Y.A. P., K. S. Relative Humidity Effect on Anode Durability in PEMFC Startup/Shutdown Processes. *ECS Transactions*: The Electrochemical Society; 2010. pp. 1273-1279.
373. J.X. Wang, H. Inada, L.J. Wu, Y.M. Zhu, Y.M. Choi, P. Liu, W.P. Zhou, R.R. Adzic. Oxygen Reduction on Well-Defined Core-Shell Nanocatalysts: Particle Size, Facet, and

Pt Shell Thickness Effects. *Journal of the American Chemical Society* 2009, **131**(47)**:** 17298-17302.
374. A. Frenkel. Solving the 3D structure of metal nanoparticles. *Zeitschrift für Kristallographie* 2007, **222**(11/2007)**:** 605-611.
375. K. Sasaki, K.A. Kuttiyiel, L. Barrio, D. Su, A.I. Frenkel, N. Marinkovic, D. Mahajan, R.R. Adzic. Carbon-Supported IrNi Core–Shell Nanoparticles: Synthesis, Characterization, and Catalytic Activity. *The Journal of Physical Chemistry C* 2011, **115**(20)**:** 9894–9902.
376. D. Glasner, A.I. Frenkel. Geometrical characteristics of regular polyhedra: application to EXAFS studies of nanoclusters. *X-Ray Absorption Fine Structure--XAFS 13* 2007, **882:** 746-748.
377. K. Kunimatsu, H. Uchida, M. Osawa, M. Watanabe. In situ infrared spectroscopic and electrochemical study of hydrogen electro-oxidation on Pt electrode in sulfuric acid. *Journal of Electroanalytical Chemistry* 2006, **587**(2)**:** 299-307.
378. R. Aydın, F. Köleli. Hydrogen evolution on conducting polymer electrodes in acidic media. *Progress in Organic Coatings* 2006, **56**(1)**:** 76-80.
379. Y.D. Yin, R.M. Rioux, C.K. Erdonmez, S. Hughes, G.A. Somorjai, A.P. Alivisatos. Formation of hollow nanocrystals through the nanoscale Kirkendall Effect. *Science* 2004, **304**(5671)**:** 711-714.
380. S.E. Davis, M.S. Ide, R.J. Davis. Selective oxidation of alcohols and aldehydes over supported metal nanoparticles. *Green Chem* 2013, **15**(1)**:** 17-45.
381. T. Mallat, A. Baiker. Oxidation of Alcohols with Molecular Oxygen on Solid Catalysts. *Chemical Reviews* 2004, **104**(6)**:** 3037-3058.
382. M. Li, A. Kowal, K. Sasaki, N. Marinkovic, D. Su, E. Korach, P. Liu, R.R. Adzic. Ethanol oxidation on the ternary Pt-Rh-SnO2/C electrocatalysts with varied Pt:Rh:Sn ratios. *Electrochimica Acta* 2010, **55**(14)**:** 4331-4338.
383. J.W. Hong, S.W. Kang, B.-S. Choi, D. Kim, S.B. Lee, S.W. Han. Controlled Synthesis of Pd–Pt Alloy Hollow Nanostructures with Enhanced Catalytic Activities for Oxygen Reduction. *Acs Nano* 2012, **6**(3)**:** 2410-2419.
384. H. Zhang, M. Jin, J. Wang, W. Li, P.H.C. Camargo, M.J. Kim, D. Yang, Z. Xie, Y. Xia. Synthesis of Pd−Pt Bimetallic Nanocrystals with a Concave Structure through a Bromide-Induced Galvanic Replacement Reaction. *Journal of the American Chemical Society* 2011, **133**(15)**:** 6078-6089.
385. S.M. Alia, K.O. Jensen, B.S. Pivovar, Y. Yan. Platinum-Coated Palladium Nanotubes as Oxygen Reduction Reaction Electrocatalysts. *Acs Catal* 2012, **2**(5)**:** 858-863.
386. R.E. Benfield. Mean Coordination Numbers and the Non-metal-Metal Transition in Clusters. *Journal of the Chemical Society-Faraday Transactions* 1992, **88**(8)**:** 1107-1110.
387. J.M. Montejano-Carrizales, F. Aguilera-Granja, J.L. Morán-López. Direct enumeration of the geometrical characteristics of clusters. *Nanostructured Materials* 1997, **8**(3)**:** 269-287.
388. E.V. Carino, H.Y. Kim, G. Henkelman, R.M. Crooks. Site-Selective Cu Deposition on Pt Dendrimer-Encapsulated Nanoparticles: Correlation of Theory and Experiment. *Journal of the American Chemical Society* 2012, **134**(9)**:** 4153-4162.

389. T.J. Schmidt, H.A. Gasteiger, G.D. Stab, P.M. Urban, D.M. Kolb, R.J. Behm. Characterization of high-surface area electrocatalysts using a rotating disk electrode configuration. *Journal of the Electrochemical Society* 1998, **145**(7)**:** 2354-2358.
390. X. Lu, M. McKiernan, Z. Peng, E.P. Lee, H. Yang, Y. Xia. Noble-Metal Nanotubes Prepared via a Galvanic Replacement Reaction Between Cu Nanowires and Aqueous HAuCl4, H2PtCl6, or Na2PdCl4. *Science of Advanced Materials* 2010, **2**(3)**:** 413-420.
391. K.J.J. Mayrhofer, D. Strmcnik, B.B. Blizanac, V. Stamenkovic, M. Arenz, N.M. Markovic. Measurement of oxygen reduction activities via the rotating disc electrode method: From Pt model surfaces to carbon-supported high surface area catalysts. *Electrochimica Acta* 2008, **53**(7)**:** 3181-3188.
392. J.X. Wang, C. Ma, Y. Choi, D. Su, Y. Zhu, P. Liu, R. Si, M.B. Vukmirovic, Y. Zhang, R.R. Adzic. Kirkendall Effect and Lattice Contraction in Nanocatalysts: A New Strategy to Enhance Sustainable Activity. *Journal of the American Chemical Society* 2011, **133**(34)**:** 13551-13557.
393. S.G. Rinaldo, J.r. Stumper, M. Eikerling. Physical Theory of Platinum Nanoparticle Dissolution in Polymer Electrolyte Fuel Cells. *Journal of Physical Chemistry C* 2010, **114**(13)**:** 5773-5785.
394. V. Komanicky, K.C. Chang, A. Menzel, N.M. Markovic, H. You, X. Wang, D. Myers. Stability and Dissolution of Platinum Surfaces in Perchloric Acid. *Journal of the Electrochemical Society* 2006, **153**(10)**:** B446-B451.
395. Y. Xu, A.V. Ruban, M. Mavrikakis. Adsorption and dissociation of O-2 on Pt-Co and Pt-Fe alloys. *Journal of the American Chemical Society* 2004, **126**(14)**:** 4717-4725.
396. J.X. Wang, F.A. Uribe, T.E. Springer, J.L. Zhang, R.R. Adzic. Intrinsic kinetic equation for oxygen reduction reaction in acidic media: the double Tafel slope and fuel cell applications. *Faraday Discussions* 2008, **140:** 347-362.
397. J.X. Wang, N.M. Markovic, R.R. Adzic. Kinetic analysis of oxygen reduction on Pt(111) in acid solutions: Intrinsic kinetic parameters and anion adsorption effects. *Journal of Physical Chemistry B* 2004, **108**(13)**:** 4127-4133.
398. J. Greeley, J.K. Norskov, M. Mavrikakis. Electronic structure and catalysis on metal surfaces. *Annual Review of Physical Chemistry* 2002, **53:** 319-348.
399. J.R. Kitchin, J.K. Norskov, M.A. Barteau, J.G. Chen. Modification of the surface electronic and chemical properties of Pt(111) by subsurface 3d transition metals. *Journal of Chemical Physics* 2004, **120**(21)**:** 10240-10246.
400. P. Mani, R. Srivastava, P. Strasser. Dealloyed Pt-Cu core-shell nanoparticle electrocatalysts for use in PEM fuel cell cathodes. *Journal of Physical Chemistry C* 2008, **112**(7)**:** 2770-2778.
401. L.A. Kibler, A.M. El-Aziz, R. Hoyer, D.M. Kolb. Tuning Reaction Rates by Lateral Strain in a Palladium Monolayer. *Angewandte Chemie International Edition* 2005, **44**(14)**:** 2080-2084.
402. S.E. Skrabalak, L. Au, X. Li, Y. Xia. Facile synthesis of Ag nanocubes and Au nanocages. *Nat. Protocols* 2007, **2**(9)**:** 2182-2190.
403. S. Guo, S. Dong, E. Wang. A General Method for the Rapid Synthesis of Hollow Metallic or Bimetallic Nanoelectrocatalysts with Urchinlike Morphology. *Chemistry – A European Journal* 2008, **14**(15)**:** 4689-4695.

404. M.R. Kim, D.K. Lee, D.-J. Jang. Facile fabrication of hollow Pt/Ag nanocomposites having enhanced catalytic properties. *Applied Catalysis B: Environmental* 2011, **103**(1-2)**:** 253-260.
405. H.J. Fan, U. Gosele, M. Zacharias. Formation of nanotubes and hollow nanoparticles based on Kirkendall and diffusion processes: A review. *Small* 2007, **3**(10)**:** 1660-1671.
406. M. Ibáñez, J. Fan, W. Li, D. Cadavid, R. Nafria, A. Carrete, A. Cabot. Means and Limits of Control of the Shell Parameters in Hollow Nanoparticles Obtained by the Kirkendall Effect. *Chemistry of Materials* 2011, **23**(12)**:** 3095-3104.
407. C.M. Cobley, Y. Xia. Engineering the properties of metal nanostructures via galvanic replacement reactions. *Materials Science and Engineering: R: Reports* 2010, **70**(3-6)**:** 44-62.
408. M.E. Glicksman. *Diffusion in Solids: Field Theory, Solid-State Principles, and Applications*. Wiley, 2000.
409. X. Lu, J. Chen, S.E. Skrabalak, Y. Xia. Galvanic replacement reaction: a simple and powerful route to hollow and porous metal nanostructures. *Proceedings of the Institution of Mechanical Engineers, Part N: Journal of Nanoengineering and Nanosystems* 2007, **221**(1)**:** 1-16.
410. J. Philibert. *Atom movements: diffusion and mass transport in solids*. Les Editions de Physique: France, 1991.
411. E.G. Seebauer, C.E. Allen. ESTIMATING SURFACE-DIFFUSION COEFFICIENTS. *Progress in Surface Science* 1995, **49**(3)**:** 265-330.
412. I. Beszeda, E.G. Gontier-Moya, D.L. Beke. Investigation of mass transfer surface self-diffusion on palladium. *Surface Science* 2003, **547**(1-2)**:** 229-238.
413. G.E. Rhead. Diffusion on surfaces. *Surface Science* 1975, **47**(1)**:** 207-221.
414. A.J. Bard, R. Parsons, J. Jordan. *Standard potentials in aqueous solution*. M. Dekker: New York, 1985.
415. P.R. Selvakannan, M. Sastry. Hollow gold and platinum nanoparticles by a transmetallation reaction in an organic solution. *Chemical Communications* 2005(13)**:** 1684-1686.
416. F. Lu, Y. Zhang, L. Zhang, Y. Zhang, J.X. Wang, R.R. Adzic, E.A. Stach, O. Gang. Truncated ditetragonal gold prisms as nanofacet activators of catalytic platinum. *Journal of the American Chemical Society* 2011, **133**(45)**:** 18074-18077.
417. F. Lu, Y. Tian, M. Liu, D. Su, H. Zhang, A.O. Govorov, O. Gang. Discrete Nanocubes as Plasmonic Reporters of Molecular Chirality. *Nano Letters* 2013, **13**(7)**:** 3145-3151.
418. W.X. Niu, S.L. Zheng, D.W. Wang, X.Q. Liu, H.J. Li, S.A. Han, J. Chen, Z.Y. Tang, G.B. Xu. Selective Synthesis of Single-Crystalline Rhombic Dodecahedral, Octahedral, and Cubic Gold Nanocrystals. *Journal of the American Chemical Society* 2009, **131**(2)**:** 697-703.
419. A.R. Tao, S. Habas, P. Yang. Shape Control of Colloidal Metal Nanocrystals. *Small* 2008, **4**(3)**:** 310-325.
420. C.J. Johnson, E. Dujardin, S.A. Davis, C.J. Murphy, S. Mann. Growth and form of gold nanorods prepared by seed-mediated, surfactant-directed synthesis. *Journal of Materials Chemistry* 2002, **12**(6)**:** 1765-1770.

421. J. Henzie, M. Grünwald, A. Widmer-Cooper, P.L. Geissler, P. Yang. Self-assembly of uniform polyhedral silver nanocrystals into densest packings and exotic superlattices. *Nature Materials* 2012, **11**(2)**:** 131-137.
422. A. Hamelin, M.J. Sottomayor, F. Silva, S.-C. Chang, M.J. Weaver. Cyclic voltammetric characterization of oriented monocrystalline gold surfaces in aqueous alkaline solution. *J. Electroanal. Chem.* 1990, **295**(1-2)**:** 291-300.
423. J.X. Wang, R.R. Adzic, B.M. Ocko. X-ray Scattering Study of Tl Adlayers on the Au(111) Electrode in Alkaline Solutions: Metal Monolayer, OH- Coadsorption, and Oxide Formation. *Journal of Physical Chemistry* 1994, **98**(29)**:** 7182-7190.
424. R.R. Adzic, A.V. Tripkovic, N.M. Markovic. Structural effects in electrocatalysis: Oxidation of formic acid and oxygen reduction on single-crystal electrodes and the effects of foreign metal adatoms. *J. Electroanal. Chem.* 1983, **150**(1-2)**:** 79-88.
425. H.G. Fritsche, R.E. Benfield. Exact analytical formulae for mean coordination numbers in clusters. *Zeitschrift fur Physik D (Atoms, Molecules and Clusters)* 1993, **26:** 15-17.
426. M.T.M. Koper. Structure sensitivity and nanoscale effects in electrocatalysis. *Nanoscale* 2011, **3**(5)**:** 2054-2073.
427. G.A. Somorjai. Centenary Lecture. Molecular ingredients of heterogeneous catalysis. *Chemical Society Reviews* 1984, **13**(3)**:** 321-349.
428. E. Yeager. Dioxygen electrocatalysis: mechanisms in relation to catalyst structure. *Journal of Molecular Catalysis* 1986, **38**(1–2)**:** 5-25.
429. J.L. Fernandez, D.A. Walsh, A.J. Bard. Thermodynamic guidelines for the design of bimetallic catalysts for oxygen electroreduction and rapid screening by scanning electrochemical microscopy. M-Co (M : Pd, Ag, Au). *Journal of the American Chemical Society* 2005, **127**(1)**:** 357-365.
430. S. Singh, S. Li, R. Carrasquillo-Flores, A.C. Alba-Rubio, J.A. Dumesic, M. Mavrikakis. Formic acid decomposition on Au catalysts: DFT, microkinetic modeling, and reaction kinetics experiments. *AIChE Journal* 2014, **60**(4)**:** 1303-1319.
431. P. Vassilev, M.T.M. Koper. Electrochemical Reduction of Oxygen on Gold Surfaces: A Density Functional Theory Study of Intermediates and Reaction Paths. *J Phys Chem C* 2007, **111**(6)**:** 2607-2613.
432. Y. Xu, M. Mavrikakis. Adsorption and Dissociation of O2 on Gold Surfaces: Effect of Steps and Strain. *The Journal of Physical Chemistry B* 2003, **107**(35)**:** 9298-9307.
433. N. Ramaswamy, S. Mukerjee. Influence of Inner- and Outer-Sphere Electron Transfer Mechanisms during Electrocatalysis of Oxygen Reduction in Alkaline Media. *J Phys Chem C* 2011, **115**(36)**:** 18015-18026.
434. J. Saavedra, H.A. Doan, C.J. Pursell, L.C. Grabow, B.D. Chandler. The critical role of water at the gold-titania interface in catalytic CO oxidation. *Science* 2014, **345**(6204)**:** 1599-1602.
435. G.M. Mullen, J. Gong, T. Yan, M. Pan, C.B. Mullins. The Effects of Adsorbed Water on Gold Catalysis and Surface Chemistry. *Top Catal* 2013, **56**(15-17)**:** 1499-1511.
436. T. Fujitani, I. Nakamura, M. Haruta. Role of Water in CO Oxidation on Gold Catalysts. *Catalysis Letters* 2014, **144**(9)**:** 1475-1486.

437. S.A. Wasileski, M.J. Janik. A first-principles study of molecular oxygen dissociation at an electrode surface: a comparison of potential variation and coadsorption effects. *Physical Chemistry Chemical Physics* 2008, **10**(25)**:** 3613-3627.
438. V. Tripković, E. Skúlason, S. Siahrostami, J.K. Nørskov, J. Rossmeisl. The oxygen reduction reaction mechanism on Pt(111) from density functional theory calculations. *Electrochimica Acta* 2010, **55**(27)**:** 7975-7981.

APPENDIX: List of Collaborators

I am sincerely grateful for the scientific expertise and technical support from all the collaborators shown as follows.

TEM and STEM measurements (Sections 3.1 – 3.5) ‡
Bingfei Cao,[a,b] Chao Ma,[c,d] Dong Su,[e] Vyacheslav Volkov,[c] Lijun Wu,[c] Yimei Zhu[c]
XRD measurements (Sections 3.1 – 3.4)
Bingfei Cao,[a,b] Rui Si[a]
Methodology develop for GDE measurements and data analyses (Section 3.1, 3.2)
Jia X. Wang[a]
Guidance with XAS measurements and data analyses (Section 3.1)
Yu-Chi Hsieh,[a] Kotaro Sasaki,[a] Nebojsa S. Marinkovic[f]
DFT calculations (Sections 3.2, 3.3, 3.5)
Wei An,[a] Ping Liu,[a] Deyu Lu[e]
Methodology develop for syntheses of Ru@Pt and Pd@Pt catalysts (Section 3.2, 3.3)
Yu-Chi Hsieh,[a] Jia X. Wang[a]
Fuel cell tests (Section 3.2)
Ping He,[g] Siyu Ye[g]
Water electrolyzer tests (Section 3.2)
Katherine E. Ayers,[h] Christopher B. Capuano[h]
Syntheses of $Pd_9Au@Pt_{ML}$ and $Pd_9Au(hollow)@Pt_{ML}$ catalysts (Section 3.4)
Yun Cai[a]
Synthesis of Au monofaceted nanocrystals (Section 3.5)
Oleg Gang,[e] Fang Lu,[e] Yugang Zhang[e]
Concentration quantification of Au nanocrystals (Section 3.5)
Mingzhao Liu[e]

Affiliations:
[a] Chemistry Department, Brookhaven National Laboratory, Upton, New York 11793, USA
[b] Chemistry Department, Stony Brook University, Stony Brook, New York 11794, USA
[c] Condensed Matter Physics & Materials Science Department, Brookhaven National Laboratory, New York 11793, USA
[d] Beijing National Laboratory for Condensed Matter Physics, Institute of Physics, Chinese Academy of Sciences, Beijing 100190, China
[e] Center for Functional Nanomaterials, Brookhaven National Laboratory, Upton, New York 11973, USA
[f] Department of Chemical Engineering, University of Delaware, Newark, Delaware 19716, USA
[g] Ballard Power Systems, 9000 Glenlyon Parkway, Burnaby, BC, V5J 5J8, Canada
[h] Proton OnSite, 10 Technology Drive, Wallingford, CT 06492, USA

‡ **Note:**
All the collaborators are listed alphabetically.